

TECHNISCHE UNIVERSITÄT MÜNCHEN

TUM SCHOOL OF NATURAL SCIENCES

**Realization and characterization of topological phases
of matter on a digital quantum computer**

Yujie Liu

Vollständiger Abdruck der von der TUM School of Natural Sciences der Technischen Universität München zur Erlangung des akademischen Grades eines **Doktors der Naturwissenschaften (Dr. rer. nat.)** genehmigten Dissertation.

Vorsitz: Prof. Dr. Alexander Holleitner

Prüfer der Dissertation:

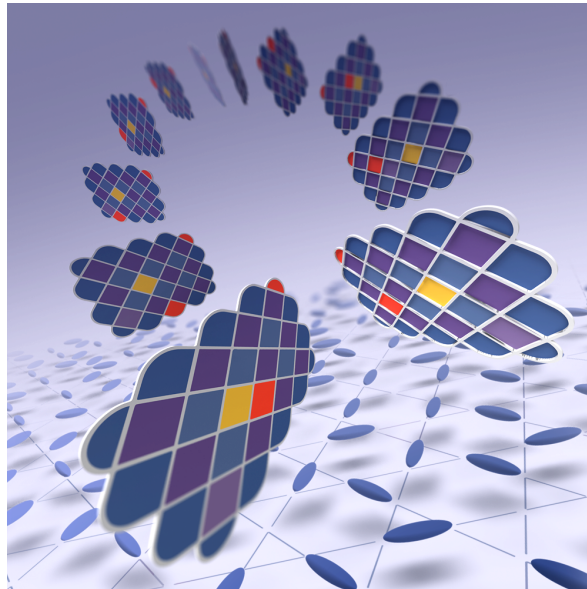
1. Prof. Dr. Frank Pollmann
2. Prof. Dr. Johannes Knolle

Die Dissertation wurde am 25.07.2024 bei der Technischen Universität München eingereicht und durch die TUM School of Natural Sciences am 02.09.2024 angenommen.

REALIZATION AND CHARACTERIZATION OF TOPOLOGICAL PHASES OF MATTER ON A DIGITAL QUANTUM COMPUTER

Dissertation

Yu-Jie Liu



Chair of Theoretical Solid-State Physics
TUM School of Natural Sciences, Physics Department
Technical University of Munich

Abstract

The discovery of topological order has revised the understanding of quantum matter and provided the theoretical foundation for many quantum error-correcting codes. Finding physical realizations of topologically ordered states in experimental settings, from condensed matter to synthetic quantum systems, has been the main challenge en route to utilizing their unconventional properties. In this thesis, we explore the realization and characterization of topological order on synthetic quantum systems. We present a theoretical proposal based on unitary quantum circuits to realize a large class of topologically ordered states and simulate their quasiparticle excitations on a digital (gate-based) quantum computer. To achieve this we design a set of linear-depth quantum circuits to generate ground states of general string-net models together with efficient unitary string-like operators for creation and manipulation of abelian and non-abelian anyons. Our scheme allows us to directly probe characteristic topological properties, including topological entanglement entropy, braiding statistics, and fusion channels of anyons. We demonstrate the efficacy of the scheme by a successful realization of a 31-qubit ground state with \mathbb{Z}_2 topological order on the Google Sycamore quantum processor. Following the state preparation, in the next part of the thesis, we propose a method to detect the quantum phases of matter from the wavefunction via a model-independent training of quantum convolutional neural networks, allowing for efficient characterization of quantum phases of matter on the prepared state. At the end, we also briefly explain another possible approach for detecting topological quantum phase transition based on the framework of quantum error correction. In the last part of the thesis, we show how tensor-network states provide simple solutions to ground states across symmetry-enriched topological (SET) phase transitions. Inspired by this, we further show how to realize quantum phase transitions between states with distinct SET order by using the new class of isometric tensor-network states (isoTNS). Using the proposed scheme, we proposed two experimental protocols for realization and detection of an SET phase transition on near-term digital quantum processors. One is based on the lattice realization of the isoTNS with efficient quantum circuits, the other approach is based on the holographic realization of the isoTNS.

Kurzfassung

Die Entdeckung der topologischen Ordnung hat das Verständnis der Quantenmaterie verändert und die theoretische Grundlage für viele Quantenfehlerkorrekturcodes geschaffen. Die größte Herausforderung auf dem Weg zur Nutzung ihrer unkonventionellen Eigenschaften war es, im Experiment physikalische Realisierungen topologisch geordneter Zustände zu finden, von kondensierter Materie bis hin zu synthetischen Quantensystemen. In dieser Arbeit untersuchen wir die Realisierung und Charakterisierung der topologischen Ordnung in synthetischen Quantensystemen. Wir präsentieren einen theoretischen Vorschlag, der auf unitären Quantenschaltkreisen basiert, um eine große Klasse topologisch geordneter Zustände zu realisieren und ihre Quasiteilchenanregungen auf einem digitalen (quantengatterbasierten) Quantencomputer zu simulieren. Um dies zu erreichen, entwerfen wir eine Reihe von Quantenschaltungen mit linearer Tiefe, um Grundzustände allgemeiner String-Net-Modelle zusammen mit effizienten unitären stringähnlichen Operatoren zur Erzeugung und Manipulation von abelschen und nichtabelschen Anyonen zu erzeugen. Unser Schema ermöglicht es uns, charakteristische topologische Eigenschaften, einschließlich topologischer Verschränkungsentropie, Vertauschungsstatistiken und Fusionskanälen von Anyonen, direkt zu untersuchen. Wir veranschaulichen die Wirksamkeit des Schemas durch die erfolgreiche Realisierung eines 31-Qubit-Grundzustands mit der topologischen Ordnung \mathbb{Z}_2 auf dem Quantenprozessor Google Sycamore. Nach der Zustandsvorbereitung schlagen wir im nächsten Teil der Arbeit eine Methode zur Erkennung von Quantenphasen von Materie aus der Wellenfunktion über ein modellunabhängiges Training von Quantum Convolutional Neural Networks vor, die eine effiziente Charakterisierung der Quantenphasen der Materie im präparierten Zustand ermöglicht. Abschließend erläutern wir einen weiteren möglichen Ansatz zur Erkennung topologischer Quantenphasenübergänge basierend auf dem Rahmenkonzept der Quantenfehlerkorrektur. Im letzten Teil der Arbeit zeigen wir, wie Tensor-Netzwerkzustände einfache Lösungen für Grundzustände über symmetriereichere topologische (SET) Phasenübergänge hinweg bereitstellen. Davon inspiriert zeigen wir außerdem, wie Quantenphasenübergänge zwischen Zuständen mit unterschiedlicher SET-Ordnung mithilfe der neuen Klasse isometrischer Tensor-Netzwerk-Zustände (isoTNS) realisiert werden können. Unter Verwendung des vorgeschlagenen Schemas haben wir zwei experimentelle Protokolle zur Realisierung und Erkennung eines SET-Phasenübergangs auf zeitnah verfügbaren digitalen Quantenprozessoren vorgeschlagen. Eines basiert auf der Gitterrealisierung des isoTNS mit effizienten Quantenschaltkreisen, das andere auf der holographischen Umsetzung des isoTNS.

Publications

This thesis contains extended versions of published works in peer-reviewed journals and works uploaded to the open-access repository arXiv.

Works contained in this thesis:

1. **Yu-Jie Liu**, Kirill Shtengel, and Frank Pollmann: “Topological quantum phase transitions in 2D isometric tensor networks”, [arXiv:2312.05079](#) (2023) [1].
YJL developed the details of the construction and performed the calculation. FP conceived the project. All authors contributed to the discussion and analysis of the results.
2. **Yu-Jie Liu**, Adam Smith, Michael Knap and Frank Pollmann: “Model-Independent Learning of Quantum Phases of Matter with Quantum Convolutional Neural Networks”, [Phys. Rev. Lett. 130, 220603](#) (2023) [2].
YJL performed the calculations and the analysis. All authors contributed to the discussion of the results and writing of the manuscript. MK and FP supervised the project.
3. Lukas Haller*, Wen-Tao Xu*, **Yu-Jie Liu** and Frank Pollmann: “Quantum phase transition between symmetry enriched topological phases in tensor-network states”, [Phys. Rev. Research 5, 043078](#) (2023) [3].
LH and WTX performed the numerical simulation. YJL developed the parent Hamiltonian and supervised LH together with FP. FP conceived the project. All authors contributed to the writing of the manuscript.
4. **Yu-Jie Liu**, Kirill Shtengel, Adam Smith and Frank Pollmann: “Methods for simulating string-net states and anyons on a digital quantum computer”, [PRX Quantum 3 \(4\), 040315](#) (2022) [4].
YJL developed the construction and wrote the manuscript. All authors contributed to the discussion of the results and to revising the manuscript. AS and FP supervised the project.
5. Kevin Satzinger, **Yu-Jie Liu**, Adam Smith, Christina Knapp et al: “Realizing topologically ordered states on a quantum processor”, [Science 374 \(6572\), 1237-1241](#) (2021) [5].
AS, MK, FP, KS., YJL, CK, and PR. designed the experiment. KS. and PR performed the experiment. KS. and YJL analyzed the data and wrote the supplement. YJL, AS, CK, MK, FP, and KS. provided theoretical support and analysis. CK, KS., YJL, AS, MK, FP, and PR wrote the manuscript. All authors contributed to revising the manuscript and supplement. All authors contributed to the experimental and theoretical infrastructure to enable the experiment.

A manuscript under preparation is also mentioned in the thesis:

1. In collaboration with Wen-Tao Xu, Michael Knap and Frank Pollmann: “Detection of emergent 1-form symmetry and 2D topological quantum phase transition with

active quantum error correction”, (manuscript in preparation)
WTX performed the numerical simulations. YJL designed the detection protocol.
MK and FP supervised the project.

Works conducted during the doctoral study but not contained in this thesis:

1. Simon Lieu*, **Yu-Jie Liu*** and Alexey Gorshkov: “Candidate for a passively protected quantum memory in two dimensions”, [Phys. Rev. Lett. 133, 030601](#) (2024) [6].
2. **Yu-Jie Liu** and Simon Lieu: “Dissipative phase transitions and passive error correction”, [Phys. Rev. A 109, 022422](#) (2024) [7].
3. Oles Shtanko*, **Yu-Jie Liu***, Simon Lieu, Alexey Gorshkov and Vicotr Albert: “Bounds on Autonomous Quantum Error Correction”, [arXiv:2308.16233](#) (2023) [8].
4. Rohit Dilip, **Yu-Jie Liu**, Adam Smith and Frank Pollmann: “Data compression for quantum machine learning”, [Phys. Rev. Research 4, 043007](#) (2022) [9].

*Equally contributed.

Acknowledgements

The past four years have been quite an experience for me. I am deeply grateful to lots of people, who have helped and supported me in the past four years.

First and foremost, I want to thank my supervisor Frank Pollmann. When I started my PhD at the end of 2019, I was looking forward to the experience of doing proper research. Then, Covid hit in early 2020 and suddenly everything was out of order. The frequent outbreak of the pandemic and lockdown of the workspace lasted for almost one and a half years before everything started to come back to a normal pace. As the “Covid generation”, it took some time for me to really get into the PhD mode. I am deeply grateful for the patience and flexibility you have provided during the special period, and also throughout the course of my PhD. Thank you for your physical insights, your positive attitude and your guidance on doing research and more importantly, how to be an independent physicist.

I am also deeply grateful to Michael Knap, who has been a mentor to me. You have provided invaluable advice on both the research and my scientific career. I am always impressed by and have always admired how dedicated you are. It has been a joyful experience to collaborate with you and I learned a lot from these collaborations.

I have really enjoyed the stay in the condensed matter theory (CMT) group and made lots of good friends. I am very grateful for conducting my PhD study in the group. It has been quite a pleasure to work and share many inspiring discussions with my colleagues here (or who were here) at the CMT group. Special thanks go to Pablo, Adam, Wilhelm, Johannes (Feldmeier), Sanjay, Clemens, Yanbai, Melissa, Hongzhen, Gibaik, Yahui, Shenghsuan, Raul, Bernhard, Lukas, Wentao, Rao, Julian and Wonjune for numerous discussions. I learned quite a lot from them. The ping-pong matches in the physics building with Pablo and Raul have been a great way to close a day of work. It has always been fun to see the lunch “parade” formed by the ever-growing CMT group. I also want to thank all the CMT staff members who ensured that everything ran smoothly.

I would also like to express my gratitude to one of my best friends, Simon Lieu, who recently moved from University of Maryland to AWS quantum. We knew each other after a seminar talk during the pandemic lockdown. You brought me into the fascinating world of open quantum systems. It has been great fun discussing physics, not just for producing results, but also for sharing the excitement with friends. I would also like to thank Alexey Gorshkov. You have effectively been another mentor for me. You showed me how a mature scientist would handle things. I am very proud of the results we have achieved together.

I am lucky to have many friends who helped me maintain good work-life balance and a positive attitude throughout the years: Zhiyuan, Sirui, Yilun, Bingxin, Xingyan, Xiehang, Xin Chen and Man Luo. You have been an important part of my life.

Finally, I want to thank my parents Ling Li and Bin Liu, who have always been there for me no matter what. I want to thank my fiance, Anqi Xu, for her love and infinite patience. Your support means everything to me. Without your support and sacrifice, none of this would be possible.

Contents

Abstract

Kurzfassung

Publications

Acknowledgements

Contents

1. Introduction	1
I. Realizing topologically ordered states on digital quantum computers	5
Overview of Part I	7
2. A short review of topologically ordered quantum phases of matter and their characterization	9
2.1. Topological entanglement entropy	11
2.2. Anyonic braiding and fusion channel	12
2.3. Exactly solvable model: The toric code	14
2.4. The string-net model	16
3. Theoretical proposals for realizations of abelian and non-abelian topologically ordered states with gate-based quantum computers	21
3.1. Preparation of the toric code ground state	22
3.2. Preparation of the double semion ground state	23
3.3. Preparation of general string-net ground states	24
3.4. Creating and moving anyons in the string-net model	27
3.4.1. Locating the quasiparticles	28
3.4.2. Unitary string operators for the abelian anyons	29
3.4.3. The difficulty of manipulating non-abelian anyons	29
3.4.4. Unitary string operators for non-abelian anyons	30
3.5. Explicit quantum circuits for the string-net states and their anyons	31
3.5.1. Quasiparticle string operators	31
3.5.2. Quantum circuits for string operators and $C\text{-}\hat{B}_p$	33
3.5.3. An example: Quantum circuits for double Fibonacci model	36
3.6. Discussion and conclusion	37
4. Experimental realization of the \mathbb{Z}_2 toric code ground state on a programmable quantum processor	39
4.1. Realizing the ground state of the toric code	39
4.2. Measuring topological entanglement entropy	41
4.2.1. Randomized measurement of second Renyi entropy	42
4.2.2. Error mitigated estimation of the second Renyi entropy	43

4.3. Simulating and extracting the anyonic braiding statistics	44
4.4. Logical state injection and readout	47
4.5. Discussion and conclusion	49
II. Detecting quantum phases of matter on digital quantum computers	51
Overview of Part II	53
5. Quantum convolutional neural networks and quantum phase classifications	55
5.1. Quantum convolutional neural networks and the problem setup	56
5.2. Model-independent training of QCNN for 1D quantum phases of matter . .	57
5.3. Recognizing time-reversal symmetric quantum phases in 1D	57
5.3.1. Training of the QCNN	58
5.3.2. Testing of the trained QCNN on physical ground states	59
5.4. Recognizing 1D $\mathbb{Z}_2 \times \mathbb{Z}_2^T$ symmetric quantum phases	62
5.5. Non-existence of QCNN solution under random noise without additional symmetries	63
5.5.1. Non-existence result for \mathbb{Z}_2^T symmetry	64
5.5.2. Non-existence result for $\mathbb{Z}_2 \times \mathbb{Z}_2^T$ symmetry	64
5.5.3. Non-existence result for $\mathbb{Z}_2 \times \mathbb{Z}_2$ symmetry	65
5.5.4. Interpretation of the Lemmas for string order parameters	66
5.5.5. Circumventing the non-existence results	67
5.6. Discussion and conclusion	68
III. Realizing 2D topological quantum phase transition on digital quantum computers	71
Overview of Part III	73
6. A short review of tensor-network states and their preparation	75
6.1. Matrix-product states in 1D	75
6.1.1. Equivalence to sequential quantum circuits	76
6.2. Tensor-network states in 2D	77
6.2.1. Isometric tensor networks and sequential quantum circuits	78
7. Quantum phase transition between symmetry enriched topological phases in tensor-network states	81
7.1. Quantum phase transitions in tensor-network states	82
7.1.1. 1D \mathbb{Z}_2^T -symmetric SPT phase transition in matrix product states . .	82
7.1.2. 2D toric code with string tension	83
7.2. Decorating the toric code	84
7.3. Tensor-network representation of the SET path	85
7.4. Parent Hamiltonian	86
7.5. Phase diagram and order parameters	88
7.6. Discussion and conclusion	90
8. Efficient quantum circuits and holographic quantum algorithms for simulating topological quantum phase transitions from 2D isometric tensor networks	93
8.1. Isometric tensor networks and classical partition functions	94

8.2.	A continuous isoTNS path between symmetry-enriched topological phases crossing a quantum critical point	95
8.3.	Power-law correlation at the critical isoTNS	97
8.4.	Anisotropic correlation at the quantum critical point	99
8.5.	Realizing 2D quantum phase transition based on holographic duality of isoTNS	100
8.5.1.	Quantum circuit representation	100
8.5.2.	Simulating the isoTNS via holographic duality	101
8.5.3.	Probing the SET transition	102
8.6.	Discussion and conclusion	104
9.	Summary and outlook	105
A.	Appendix: Theoretical proposals for simulating string-net states and anyons on gate-based quantum computers	109
A.1.	Isometry Property of Plaquette Operator \hat{B}_p^s and the Open String Operator	109
A.2.	Determine the S -matrix from Measurement	110
B.	Appendix: Experimental realization of topologically ordered states on a programmable quantum processor	111
B.1.	Linear quantum circuit for the toric code	111
B.1.1.	Matching boundary conditions	112
B.1.2.	Mixed boundary conditions (logical states)	112
B.1.3.	Circuit compilation and optimization	114
B.2.	Readout error mitigation	116
B.3.	Measuring topological entanglement entropy	118
B.3.1.	Randomized measurement of second Rényi entropy	119
B.3.2.	Extended experimental details	120
B.4.	Simulating braiding	124
B.4.1.	Interferometry	124
B.4.2.	Randomized compiling	125
B.5.	Logical qubit states	129
B.5.1.	Logical state measurement	129
B.5.2.	Dynamical decoupling	129
B.5.3.	Extended experimental results	130
B.6.	Experimental details	133
C.	Appendix: QCNN and quantum phase classifications	135
C.1.	QCNN prediction with modified training setup	135
C.2.	Training with $\mathbb{Z}_2 \times \mathbb{Z}_2^T$ symmetry	135
C.3.	Results for uniform QCNN	138
C.4.	Extended numerical results	138
C.5.	Making predictions with weak disorder	138
C.6.	Alternating-bond Heisenberg model	139
C.7.	Symmetrization of local quantum gates for generic symmetry groups	140
C.8.	The error probability for a majority vote	141
D.	Appendix: Symmetry-enriched topological phase transitions in 2D tensor-network states	143
D.1.	Parent Hamiltonians away from the fixed points	143
D.1.1.	Warm-up: 1D case	143
D.1.2.	2D parent Hamiltonian	144

Contents

D.2. $U(1)$ pivot symmetry at $g = 0$	145
D.2.1. $U(1)$ pivot symmetry for 1D Hamiltonian	145
D.2.2. $U(1)$ pivot symmetry for 2D parent Hamiltonian	146
D.3. Mapping the SET TNS norm to a partition function	147
D.4. 2D $\mathbb{Z}_2 \times \mathbb{Z}_2^T$ SPT states and corresponding partition function	149
D.5. Real symmetric tensors and symmetry fractionalization	150
D.6. CTMRG and correlation length	151
D.7. Calculation of membrane order parameters using tensor networks	152
D.8. Degeneracy of entanglement spectrum and calculation of TEE using tensor networks	156
E. Appendix: Efficient quantum circuits and quantum algorithms for simulating topological quantum phase transitions in 2D isometric tensor networks	159
E.1. The plumbing construction in 1D MPS	159
E.2. Quantum-classical correspondence	160
E.3. A parent Hamiltonian for the isoTNS path between SET phases	160
Bibliography	165

1. Introduction

It doesn't matter how beautiful your theory is, it doesn't matter how smart you are. If it doesn't agree with experiment, it's wrong.

Richard P. Feynman

Matter in nature exists in different phases, such as liquid and solid, resulting from the interaction of many microscopic constituent particles. The many-body phenomena, ranging from spontaneous symmetry breaking and topological phases of matter, to the universality of phase transitions and non-equilibrium dynamics, have been a central focus of condensed matter physics. The quantum phases of matter, i.e. the phases of matter at zero temperature, exhibit rich and fascinating phenomena due to the many-body interaction and strong quantum fluctuation. Various exotic quantum phases of matter have been predicted or discovered to exist, including the symmetry-breaking phases [10, 11], the symmetry-protected topological (SPT) phases [12–18], intrinsically topological phases [19–21] and more generally the symmetry-enriched topological (SET) phases [22–30]. Unfortunately, quantum phases of matter are challenging to understand—they are described by exponentially growing Hilbert space as the system size increases. While powerful classical computational methods exist, e.g. Density Matrix Renormalization Group (DMRG) [31, 32] and Quantum Monte Carlo (QMC) [33], they are applicable to quantum systems in low dimensions or to a very restricted class of problems. The simulation of general quantum many-body systems remains a major challenge.

The advent of programmable quantum hardware provides an unprecedented access to novel quantum states and represents a new avenue for probing the exotic quantum phases of matter beyond classical computing power. On the other hand, quantum simulation has become a language that bridges the theorists and experimentalists—the models that are theoretically predicted to exist but are hardly seen in nature can find realizations via synthetic quantum systems. A central goal of the thesis is to study the use of synthetic quantum systems in realizing and characterizing exotic *topological* quantum phases of matter, by providing both the theoretical framework and the experimental demonstration.

The quest for quantum simulation began with a simple question: is it possible to simulate a quantum system with another quantum system? A quantum system naturally serves as a machine capable of storing exponentially large Hilbert space without exponentially many physical resources! The notion of a “quantum computer” was envisaged by Yuri Manin and Richard Feynman in early 1980s. This theoretical idea sparked further interest when quantum algorithms were subsequently discovered that outperformed all classical algorithms, e.g. Deutsch’s algorithm [34] and Simon’s algorithm [35] (which later inspired the famous Shor’s algorithm [36] for the problem of factoring). Enormous efforts have therein been devoted to building a functioning quantum computer. In 2018, the quantum team at Google announced the realization of a carefully designed sampling task on a 54-qubit superconducting quantum processor that is beyond the reach of any classical computing power at that time [37]—achieving the so-called quantum supremacy¹. Limited by the sizes and the noise, these noisy intermediate-scale quantum (NISQ) computers

¹Due to the low fidelity of the experimental signals, it is still debated whether Google has convincingly demonstrated a task that cannot be simulated classically on a short timescale, see e.g. Refs. [38–40].

are still far from practical use. However, with rapid advances in hardware, the control of the quantum devices has matured enough to allow for proof-of-principle demonstration of quantum simulation of quantum many-body systems. Among the first quantum simulations, the seminal work by Greiner et al in 2002 demonstrated the realization of a quantum phase transition from a superfluid to a Mott insulator using cold atoms confined on optical lattices [41]. Since then, a plethora of experimental demonstrations have been made, and new physical phenomena have also been discovered from quantum simulations, e.g. the many-body quantum scars were discovered on the 51-atom Rydberg quantum simulator [42]. Nowadays, various controlled quantum platforms have become available, such as the superconducting qubits, the Rydberg atom array, the trapped ions, ultracold atoms and so on. A pressing question is therefore how we can already make use of these NISQ platforms to start studying interesting quantum many-body systems.

Topologically ordered phases of matter are among the most exotic quantum phases of matter. Despite tremendous progress in their theoretical understanding, the experimental realization remains a significant challenge. Topologically ordered systems exhibit general robustness against any zero-temperature perturbation to the system. Moreover, they have energetically gapped ground states with degeneracies that depend on their boundary conditions. The non-local nature of these states makes them particularly attractive platforms for fault-tolerant quantum computation, since quantum information encoded in locally indistinguishable ground states is robust to local perturbations [43, 44]. This is the underlying principle of topological quantum error-correcting codes, where the logical codespace corresponds to the degenerate ground state subspace of a lattice model [45–47]. Before the advent of quantum simulation, the only unambiguous solid-state system with topological order is where this phenomenon was originally discovered—the fractional quantum Hall effect (FQHE) [48]. Although there are many candidate materials with topological order, it has been notoriously hard to provide conclusive evidence for their nature. On the other hand, the use of model wavefunction has played a key role in the development of the theory of topological order. They do not capture all the microscopic physical details of the system, yet they capture the essential features of the quantum phases and are easy to analyze and understand. Early examples include the valence-bond solid state [49] and later the Laughlin state [50]. Other examples are found later, such as the Rokhsar-Kivelson wavefunction [51], the toric code state [43] and its generalization to the string-net states [52]. Because of their simplicity, simple model wavefunctions have become the focus for early proof-of-principle demonstrations of quantum simulations of topologically ordered systems. Small-scale experimental realizations of the toric code state [53–63] and the Laughlin state [64] on synthetic quantum systems have been extensively investigated.

Despite these efforts, the experimental realization of topologically ordered states on synthetic quantum systems remains a major challenge, requiring the generation of long-range entanglement. Probing the non-local topological properties of such a state on an array of qubits requires high-fidelity gates and a sufficiently large two-dimensional lattice. An important question is therefore how to achieve quantum simulation of topologically ordered systems with high quality and convincing evidence of their topological nature. Currently, the methods for the realization of topologically ordered systems can be roughly categorized into three classes: (1) **Hamiltonian engineering (analog approach)**. The realization is achieved by engineering the background many-body Hamiltonian of the system and the ground states are prepared by an adiabatic protocol. This method is general and is important for the future application of quantum computers in quantum many-body physics, but it is currently very challenging to achieve experimentally except for some limited class of models. Experiments in, e.g. Refs [58, 64–66] are based on this method. (2) **Ground-state realization by unitary quantum circuits (gate-based approach)**. The method uses explicit unitary quantum circuits to generate the ground states of the system without a

background Hamiltonian². This circuit could be obtained either variationally or analytically for specific models. The method has the advantage of being feasible on near-term quantum devices and serves as an important subroutine for general quantum simulation of many-body systems. Experiments in, e.g. Refs [5, 67–69] are based on this method. (3) **Ground-state realization by measurements and feedback.** The method is similar to 2 in that it relies on gate-based quantum platforms and it also only realizes the ground states without a background Hamiltonian. But the preparation of the states involves mid-circuit measurements and feedback control, which in some cases can speed up the preparation procedure and reduce the resource required. The extent to which this method helps in the preparation of general ground states is an open question that is being actively investigated. For example, the experiment in Ref [70] is based on this method. While each of the three schemes has its own merits, the future quantum simulation of topologically ordered systems is likely to utilize a highly optimized hybrid method.

In this thesis, we will focus on the Method 2 using gate-based quantum computers for physical realization and will aim to address three important questions:

- (i) How do we realize a topologically ordered system on currently available quantum computers?
- (ii) Once we have realized a topologically ordered system, how do we experimentally detect the quantum phases of matter it belongs to?
- (iii) Can we go beyond the realization of specific topologically ordered systems, and realize quantum phase transitions between topologically ordered systems?

The three questions cover a broad and active area of research. We will present our findings as we address each of the questions. Centering around the three questions, the thesis consists of three parts. Part I is about the realization of topologically ordered states using digital quantum computers. We review the concept of topological order and present our proposal of an efficient theoretical protocol for simulating topologically ordered ground states on digital quantum computers. We conclude the part with an experimental demonstration of the protocol, where we achieved the realization of \mathbb{Z}_2 topologically ordered states. Part II explores the question of how to characterize the quantum phases of matter generated on a quantum computer. We make use of the stability of perturbed quantum phases of matter and present a method based on efficient data generation for quantum machine learning. We also briefly mention another idea of quantum phase detection based on active quantum error correction. Finally, in Part III, we show that how we can go beyond the realization scheme for specific topologically ordered states presented in Part I, i.e. to achieve a quantum phase transition between distinct topologically ordered phases of matter on a quantum computer. We first briefly review the concept of tensor networks, which is a major ingredient for the proposed scheme. We motivate the scheme by studying tensor-network representation of a symmetry-enriched topological phase transition. Later, we restrict the tensor networks to the subclass of isometric tensor networks, which leads to efficient experimental protocols for physical realization: one is the lattice realization based on the efficient quantum circuits of the states, the other one is the holographic realization based on the causal structure of the states.

²Quantum phases of matter are generally defined with respect to some Hamiltonian. However, topologically ordered systems are characterized by long-range entanglement, which is a ground-state property. While the ground-state realizations are certainly important, whether a realization without the Hamiltonian is considered to be a realization of the topological order depends on how one defines the topological order. Indeed, whether a single ground state contains all the data necessary to define a topological phase is an interesting open question.

Part I.

Realizing topologically ordered
states on digital quantum
computers

Overview of Part I

In this opening part of the thesis, we present methods for quantum simulation of gapped topological phases of matter. Using the proposed method, we achieve one of the first direct experimental realizations of topologically ordered ground states supported by measurements of topological entanglement entropy on an actual digital quantum hardware. In particular, we focus on the fixed points of gapped topologically ordered phases of matter under the real-space renormalization group [12, 71–74]. These states are representative ground states of topological phases with zero correlation length. The realization of them marks an important first step towards the quantum simulation of generic topologically ordered systems.

In Chapter 2, we briefly review the concept of *intrinsic* topological order with an emphasis on their relation to long-range entanglement. We also discuss the direct approaches for characterizing the topological order from the ground states and review the exactly solvable model of the toric code and string-net models. In Chapter 3, we present general methods for efficiently engineering topologically ordered ground states and their exotic quasiparticle excitations on a gate-based quantum computer. This chapter is based on the work [4]. The proposed method leads to the successful experimental demonstration of the realization of topological states in the next chapter. In Chapter 4, we present the experimental results for the realization of a 31-qubit \mathbb{Z}_2 topologically ordered ground state on the Google Sycamore quantum processor. We further demonstrate various aspects of the topological nature of the prepared states, including the measurement of a non-trivial topological entanglement entropy, the simulation of anyonic braiding and active quantum error correction as a surface code. This chapter is based on the publication [5].

2. A short review of topologically ordered quantum phases of matter and their characterization

There are two ways of doing calculations in theoretical physics. One way, and this is the way I prefer, is to have a clear physical picture of the process you are calculating. The other way is to have a precise and self-consistent mathematical formalism.

Enrico Fermi

Starting with the discovery of the fractional quantum Hall effect ((FQHE) [48], a rich zoo of topologically ordered phases of matter has been discovered. The conventional Landau paradigm of symmetry breaking [10, 11] provides a systematic way to understand phases and phase transitions where distinct phases of matter are characterized by local order parameters. Nonetheless, topologically ordered phases of matter are zero-temperature quantum phases of matter without any local order parameters, and therefore do not fall into the conventional Landau paradigm. The development of the theory for topological phases of matter dated back to late 1980s, when the notion of chiral spin liquids was introduced in an attempt to explain the phenomena of high-temperature superconductivity [51, 75–78]. These constructions turned out later to be incorrect for high-temperature superconductivity but they can be used as a theory for FQHE [78, 79], or more generally the topological order [19–21]. Around the same time, several authors also started to explore the abstract theory of anyons—point-like particles living in (2+1)D systems which have more general spin statistics than bosons and fermions. Beginning with Leinaas and Myrheim [80], and later Goldin et al [81] and Wilczek [82, 83], the general theory of anyons was further explored and developed [84–91] under different contexts. The anyon theory (i.e. the topological quantum field theory (TQFT)) provides a general low-energy effective theory for (2+1)D topologically ordered systems [92].

Topologically ordered phases of matter are characterized by their long-range entanglement in the ground state¹, which can be seen from the consideration of the adiabatic theorem [93]. Formally speaking, the Hamiltonians H_0 and H_1 belong to the same gapped quantum phase of matter if there exists a smooth path $H(s)$ connecting the two Hamiltonians such that $H(s)$ remains gapped along the entire path². The adiabatic theorem implies that the ground states $|\psi_0\rangle$ and $|\psi_1\rangle$ within the same phase of matter are related via an adiabatic time evolution. From this definition, it immediately follows that if two ground states cannot be mapped to each other by an adiabatic time evolution, they must belong to distinct quantum phases of matter! Therefore, distinct quantum phases of matter can be understood as different equivalence classes under the adiabatic evolution [93]. For instance, if we additionally impose symmetries on the adiabatic paths, we obtain phases

¹The systems are said to have *intrinsic* topological order. This is to be differentiated from topological phases based on symmetry protection, i.e. the symmetry-protected topological (SPT) phases, whose ground states are short-range entangled.

²Note that the parameter $s \in \mathbb{R}$ can be chosen to lie within $[0, 1]$. The adiabatic path corresponds to slowly varying s to sweep through this interval.

that are separated by quantum phase transitions due to the presence of symmetries, e.g. the symmetry-breaking phases and the phases with unbroken symmetries.

Are there distinct quantum phases of matter without any symmetry? In other words, is there a ground state of some Hamiltonian H that cannot be deformed to the product state, e.g. $|00\cdots 0\rangle$ by any adiabatic evolution? The answer is yes. This class of ground states are said to possess long-range entanglement and ground states with topological order lie precisely in this class³. The adiabatic evolution can be well approximated by a finite-depth local unitary quantum circuit [93, 95], which provides a conceptually clearer picture for the causal structure and the entanglement pattern of the states. Within this picture, a topologically ordered state cannot be mapped to a product state by any finite-depth local quantum circuits, i.e. it is the fundamentally different entanglement pattern that distinguishes the topological ground states from the simple product state. For this reason, they are sometimes said to have intrinsic topological order. Unlike symmetry-breaking phases, topological phases are stable without the presence of any symmetries.

The long-range entanglement manifests in a few defining features of the low-energy physics of topologically ordered systems

1. **Robust topology-dependent ground-state degeneracy:** If the system is defined on a closed manifold, the ground-state degeneracy of the system depends only on the topology of the manifold and is robust against arbitrary small local perturbation to the Hamiltonian. No local operators can cause tunnelling between the degenerate ground states, i.e. $\langle\psi_i|\hat{O}|\psi_j\rangle = C\delta_{ij}$, where \hat{O} is a local operator⁴ and i, j label the orthogonal ground states. The constant C is independent of i and j .
2. **Non-local excitations:** On a closed manifold, no local operators can create or annihilate a single excitation above the ground state. In (2+1)D topologically ordered systems, these excitations are point-like particles called *anyons*. Unlike bosons and fermions with exchange statistics ± 1 , anyons are emergent quasiparticles with fractional exchange statistics and non-trivial mutual statistics. These exotic statistics are key data in the classification of topological order.

In this thesis, we focus on (2+1)D bosonic topologically ordered systems. Similar to the classification of symmetry-breaking phases of matter based on group theory, the classification of topologically ordered phases of matter relies on a branch of mathematics, i.e. the tensor category theory. In particular, it is strongly believed that distinct (2+1)D bosonic topological order is classified by the braiding of the anyons, i.e. distinct sets of self and mutual statistics of anyons which are solutions to some consistency equations. These data are encoded in the modular S and T matrices in the unitary modular tensor category. The mathematical details behind the classification of topological order are beyond the scope of this thesis. Thorough discussions of the relevant topics can be found in e.g. Refs. [92, 97, 98].

An interesting and important question is how to characterize topological order in a physical quantum many-body ground state. Below we describe two direct approaches involving probing the long-range entanglement and the braiding statistics of the anyons

³A simple quantum state with a long-range entanglement is the Greenberger–Horne–Zeilinger (GHZ) state $(|00\cdots 0\rangle + |11\cdots 1\rangle)\sqrt{2}$. However, the GHZ state is not topological. It corresponds to the ground state that spontaneously breaks the \mathbb{Z}_2 symmetry. The long-range entanglement of symmetry-breaking and topological phases can be further distinguished by the stability under local imaginary-time evolution (or sometimes called stochastic local transformation [94]). The long-range entanglement in topological phases is stable under such perturbation and it is unstable in the symmetry-breaking phases.

⁴Here we are considering a thermodynamic system. For a finite system, locality means that \hat{O} is geometrically local and the support of \hat{O} is small compared to the total system size. This condition is called the Knill-Laflamme condition in the quantum error correction community [96]. This is closely related to the fact that topological ground states can be interpreted as quantum error correcting codes.

of the system; these quantities constitute the fundamental data for the topological order. Then we will review some exactly solvable lattice models with non-trivial topological order.

2.1. Topological entanglement entropy

Topologically ordered states in 2D systems exhibit long-range quantum entanglement. A smoking gun for topological order is a direct measurement of such long-range entanglement. The entanglement entropy of subsystem A is defined as the von Neumann entropy $S_A = -\text{tr}(\rho_A \ln \rho_A)$, where ρ_A is the reduced density matrix of the subsystem A . If we consider a disk with boundary length L and compute the entanglement entropy for the region enclosed by the disk, it is expected to follow $S = \alpha L - \gamma + \dots$, where α and γ are constants. The rest of the terms vanish as $L \rightarrow \infty$. This so-called *area law* has been proven for 1D gapped local Hamiltonian [99] and conjectured to hold for higher dimensions.

The constant α is non-universal and depends on the details of the Hamiltonian, but $\gamma (\geq 0)$ is a universal quantity that cannot be changed unless a quantum phase transition occurs. The negativity of $-\gamma$ and the positivity of von Neumann entropy prevent one from smoothly connecting the state to a product state without changing γ (via a quantum phase transition), indicating an intrinsic long-range entanglement. This universal quantity $S_{\text{topo}} = -\gamma$ is dubbed the *topological entanglement entropy* (TEE) [100, 101] and can be determined in a model-independent way via a subtraction procedure

$$S_{\text{topo}} = S_A + S_B + S_C - S_{AB} - S_{BC} - S_{AC} + S_{ABC}, \quad (2.1)$$

where A, B and C are simply connected domains (Fig. 2.1a) and they are assumed to be large compared to the correlation length. The TEE is an invariant in the sense that it does not change when A, B, C are smoothly deformed. For sufficiently large A, B and C , it is easy to see that any finite-depth local quantum circuit leaves TEE invariant, consistent with the stability of topological phases. The TEE, as an invariant of the phases, is determined by the underlying anyon theory that describes the topological order, i.e. $S_{\text{topo}} = -\ln \mathcal{D}$, where \mathcal{D} is the *total quantum dimension* of the anyon theory [102, 103]. It therefore serves as a useful probe to characterize a topological order in the ground state of the system, i.e. the measurement of $S_{\text{topo}} \neq 0$ provides strong evidence for the topological nature of the ground state.

On a programmable quantum platform, we can extract the TEE from the system by performing a full quantum state tomography (QST). This is generally impractical for large system size as it involves reconstructing the reduced density matrices by measuring a complete set of observables. A nice feature of the string-net states is that their TEE remains unchanged if the von Neumann entropy is replaced by the Rényi entropy of arbitrary order [104]. This provides an alternative approach to accessing TEE via randomized measurements [105, 106]. The protocol allows for a direct access to the entropy without reconstructing the state, which significantly reduces the necessary measurements needed for statistical averaging. When operating on NISQ devices, the randomized measurements can be performed together with the state-of-art error-mitigation technique to produce an unbiased estimator for the TEE, as successfully demonstrated for subsystems up to nine qubits in Ref. [5].

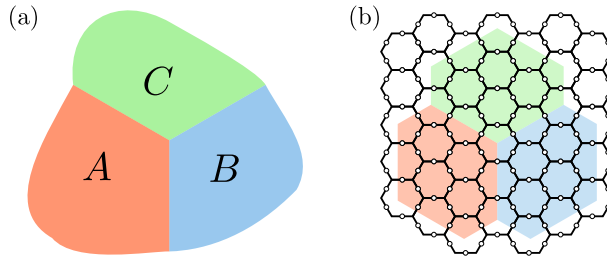


Figure 2.1.: Probing the TEE on a quantum computer. (a) The simply connected domains A, B and C are used in the subtraction procedure given in Eq. (2.1); the exterior is the rest of the system. (b) An example for extracting TEE from a connected domain on a honeycomb lattice with degrees of freedom on the links. The domain includes the sites on the external links, while the sites on the boundary of two domains are shared by both sides.

2.2. Anyonic braiding and fusion channel

Anyons emerge as the non-local excitations of topologically ordered phase. They are quasi-particles that obey fractionalized statistics. Two key quantities of the underlying anyonic theories are the twist factors θ_a and modular S -matrix. They can be used to classify the theory down to finitely many possibilities [107] (up to gauge equivalence). The measurement of these data serves as another useful tool to characterize the topological order experimentally [108].

The anyonic twist factor θ_a is defined to be the phase accumulated when a particle is rotated by 2π about itself. For abelian anyons (including bosons and fermions), the twist factor determines their braiding statistics, i.e. the phase resulting from exchanging two identical particles. Whereas $\theta_a = \pm 1$ for bosons and fermions, it can take other rational phases for generic anyons. To obtain the twist factor, we first create a pair of anyons, a and \bar{a} (particle and anti-particle), from the ground state and then move particle a to the final position with unitary \hat{U}_a along a twisted path as shown in Fig. 2.2b. The twist factor is the phase relative to the state with the particle moved to the same location along a path without a twist. We denote the unitary that drags particle a along this alternative (untwisted) path as \hat{V}_a .

The modular S -matrix captures the mutual statistics between the anyons. In the abelian case, the matrix elements encode the phase accumulated when one anyon winds around another. In the non-abelian case, the winding induces a non-trivial transformation in the subspace formed by these anyonic particles⁵. To measure the S -matrix, we first create two pairs of anyons a, \bar{a}, b, \bar{b} from the ground state (the vacuum for the quasiparticles) and then intertwine a and b with unitary \hat{U}_{ab} (see Fig. 2.2a). Next we consider another path corresponding to moving these anyons to the same location without crossing each other along the way; we denote the unitary for this path as \hat{V}_{ab} . Matrix element S_{ab} is obtained by measuring the overlap between the final states in the two scenarios above. The twist factor θ_a and the S -matrix are expressed in terms of expectation of unitaries \hat{V}_a, \hat{U}_a and $\hat{U}_{ab}, \hat{V}_{ab}$ as follows:

$$\begin{aligned}\theta_a &= \langle \psi_{a\bar{a}} | \hat{V}_a^\dagger \hat{U}_a | \psi_{a\bar{a}} \rangle, \\ M_{ab} &= \langle \psi_{a\bar{a}b\bar{b}} | \hat{V}_{ab}^\dagger \hat{U}_{ab} | \psi_{a\bar{a}b\bar{b}} \rangle.\end{aligned}\tag{2.2}$$

Here M_{ab} is the monodromy matrix [109] and it is related to the S -matrix via $S_{ab} = (d_a d_b / \mathcal{D}) M_{ab}$, where $d_{a,b}$ is the quantum dimension of anyons a, b and $\mathcal{D} = \sqrt{\sum_a d_a^2}$ is the

⁵More precisely, the braiding statistics for non-abelian anyons are described by some multi-dimensional irreducible representations of the braid group.

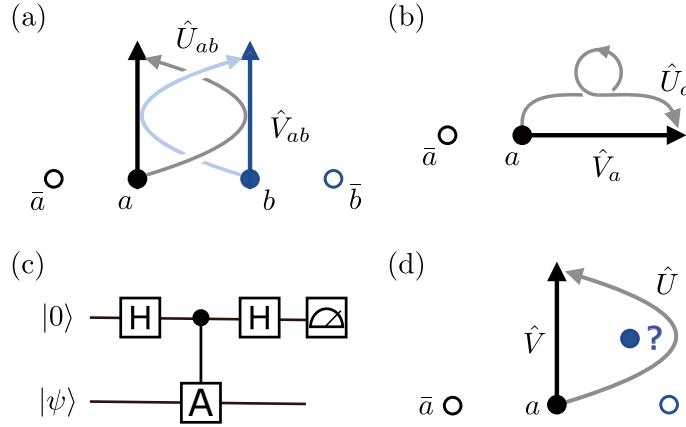


Figure 2.2.: Probing braiding statistics by interferometry. The unitary paths \hat{V} and \hat{U} for obtaining (a) S_{ab} and (b) the twist factor θ_a . (c) A simple circuit for measuring the expectation $\langle\psi|\hat{A}|\psi\rangle$, where \hat{A} is a unitary operator acting on $|\psi\rangle$ and the ancilla qubit is initially prepared in $|0\rangle$. At the end of the circuit, the ancillary qubit is measured to obtain $\langle Z - iY \rangle$. The expectation of \hat{A} follows from $\langle\psi|\hat{A}|\psi\rangle = \langle Z - iY \rangle$. (d) An alternative path to measure the S -matrix. The path can be used to measure an unknown anyon (blue) at a fixed position by braiding with anyons of known species (black).

total quantum dimension. $|\psi_{a\bar{a}}\rangle$ is the wavefunction with a pair of anyons a, \bar{a} and $|\psi_{a\bar{a}b\bar{b}}\rangle$ is the wavefunction with two anyon pairs a, \bar{a}, b, \bar{b} . Once we know how to implement \hat{U} and \hat{V} , the expectation value can be efficiently measured by a simple Hadamard-test quantum circuit with one ancilla qubit as shown in Fig. 2.2c. The number of local gates needed to perform the measurement will scale linearly with the number of qudits supported by the unitary being measured. The costs come from the long-range controlled gates from the ancilla qubit to the support of the unitary. The procedure is a typical example of Mach-Zehnder or Ramsey type interferometry for measuring the braiding statistics [109, 110] where the anyonic statistics results from the interference of paths \hat{V} and \hat{U} .

Notice that the details of the paths in Fig. 2.2a-b are not important, any paths that can be continuously deformed to them are considered equivalent. Some non-universal phases can emerge locally along the paths (e.g. geometric phases). Nevertheless, the braiding phase can still be determined by splitting a single path into multiple segments. These segments of paths can be implemented in different order to create trajectories with and without the particle braiding, the interference of which determines the statistics [111]. If the exact creation and annihilation operators for the anyons are known (e.g. using the approach described in Section 3.4), we do not encounter these non-universal phases.

A measurement of the monodromy matrix alone is sufficient for determining the modular S -matrix for the anyon theory (i.e. a unitary modular tensor category). This is because the modular S -matrix is required to satisfy certain constraints, e.g. the modular S -matrix is symmetric and unitary, and satisfies the Verlinde formula [112]. These stringent constraints do not only allow us to directly infer the modular S -matrix from the monodromy matrix measured from the experiments,

$$S_{ab} = \sqrt{\frac{(M^{-1})_{ba}^*}{M_{ab}}} M_{ab}, \quad (2.3)$$

where M^{-1} is the inverse of M . Due to the structure of the S -matrix, the monodromy M_{ab} should satisfy a set of constraints in order to yield a physical S -matrix. For example, by definition we have $S_{ab} = S_{ba}$, this suggests $M_{ab} = M_{ba}$. The list of constraints is not

exhausted. Other constraints can come from, e.g. the Verlinde formula [112] or being (together with the twist factors) the generator for the modular group [109]. In practice, these stringent constraints are helpful in benchmarking the experimental data and identifying the correct S -matrix for the underlying modular tensor category from the noisy data.

Measurement of these interfered paths also provides access to the *fusion channel*. If we bring two abelian anyons together, they can be regarded as a single particle of a unique type. Abelian anyons have a unique fusion channel whereas non-abelian anyons have multiple fusion channels by definition. For non-abelian anyons, combining them can result in a particle of multiple types. Suppose that we have an unknown anyonic state $|\psi\rangle = \sum_i p_i |i\rangle$ at a fixed position, where i labels all the possible anyons and p_i are some complex amplitudes. We can prepare a known anyon a and braid it around the unknown anyon (Fig. 2.2d); interfering this winding path with the path without winding gives the same quantity as the S -matrix element in (2.2), i.e. $\langle\psi_a|\hat{V}^\dagger\hat{U}|\psi_a\rangle = \mathcal{D}\sum_i |p_i|^2 S_{ai}/d_a d_i$, where $|\psi_a\rangle$ is $|\psi\rangle$ with a pair of a, \bar{a} created and \hat{U}, \hat{V} are the unitaries for the two paths. The probability amplitudes $|p_i|^2$ are determined by inverting the matrix $S_{ai}/d_a d_i$. Measurement of the fusion results allows us to directly access the fundamental algebraic relation underlying the topological quantum field theory (TQFT) [113].

2.3. Exactly solvable model: The toric code

We conclude the review section by discussing some exactly solvable lattice models realizing topological order. The simplest topologically ordered lattice model is the toric code model [43] (see also [114]) with a \mathbb{Z}_2 topological order. The simplicity of the model makes it one of the most widely studied toy models for topologically ordered systems. The model can be defined on a square lattice with each spin-1/2 (or qubit) degree of freedom on the links. The Hamiltonian reads

$$H = -\sum_p B_p - \sum_s A_s, \quad (2.4)$$

where $B_p = \prod_{i \in p} X_i$ is the product of Pauli X operators around each plaquette p and $A_s = \prod_{i \in s} Z_i$ is the product of Pauli Z operators around each star (vertex) s . One can check that the plaquette and star operators all commute with each other, the ground state $|GS\rangle$ therefore satisfies $A_s |GS\rangle = B_p |GS\rangle = |GS\rangle$ for all p and s . To understand the ground state, it is convenient to regard the link state $|0\rangle$ as empty and link state $|1\rangle$ as occupied. Within this picture, the star operators A_s constraint the ground state to contain only closed loop configurations. On the other hand, the plaquette operators B_p provide some “kinematics” for the loop configuration and prefer a state with randomly fluctuating loops. Together, the ground state $|GS\rangle$ is simply an equal-weight superposition of all the closed loop configurations.

Quasiparticle excitations. The elementary excitations of the toric code are generated by Pauli strings. For example, if we apply a Pauli string of X , the plaquette and star operators along the bulk of the Pauli string are preserved, while the star operators at the endpoints of the Pauli string are flipped, i.e. $\langle A_s \rangle = -1$. This excitation is called the electric charge e in connection to lattice gauge theory. Analogously, if we apply a Pauli string of Z , only the plaquette operators at the endpoints of the string are flipped, i.e. $\langle B_p \rangle = -1$, this excitation is called the magnetic charge m . We can also compose an e and an m particle together by bringing the endpoints of a Pauli X string and Pauli Z string close to each other, they form a composite particle denoted by ψ . Together with the trivial particle $\mathbb{1}$, the set $\{\mathbb{1}, e, m, \psi\}$ describes the full set of anyons emerging as excitations of the toric code. Since all the non-trivial anyons appear at the endpoints of string-like Pauli operators, on a closed manifold the anyons always come in pairs and no local operators

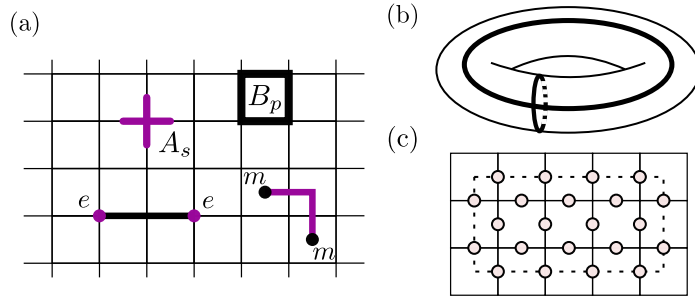


Figure 2.3.: The toric code model on a square lattice. (a) The star operators A_s and the plaquette operators B_p . The excitations generated by Pauli strings of X (black) or Pauli strings of Z (purple). The endpoints of the Pauli strings either violate the star constraint or the plaquette constraint on the ground state. They correspond to the e and m excitation, respectively. (b) On the torus, there are two types of non-contractible loops. (c) The topological entanglement entropy of the toric code ground state can be obtained by computing the subsystem (shaded qubits) entanglement entropy. The dashed line marks the boundary of the subsystem.

can generate a single anyon⁶. Note that the two anyons in the toric code fuse uniquely to another anyon and the two identical anyons fuse to the vacuum. The toric code therefore has an abelian \mathbb{Z}_2 topological order.

Braiding statistics. By knowing the explicit string operators for the anyons, the braiding statistics for the anyons can be explicitly worked out as described in Section 2.2. We get

$$\theta_1 = 1, \quad \theta_e = 1, \quad \theta_m = 1, \quad \theta_\psi = -1. \quad (2.5)$$

While three of the particles are bosonic, the composite anyon ψ has fermionic self-statistics! This explicitly illustrates the surprising fact that a fermionic excitation can emerge from a system of completely bosonic degrees of freedom (qubits). The mutual statistics (S -matrix) can also be easily obtained

$$S_{em} = S_{me} = S_{e\psi} = S_{\psi e} = S_{m\psi} = S_{\psi m} = -\frac{1}{2}, \quad (2.6)$$

and the rest of the elements in the S -matrix are all $1/2$ ⁷. The S -matrix reveals the exotic anyonic nature of these quasiparticles—unlike conventional bosons and fermions, braiding one anyon over the another anyon can lead to a non-trivial phase of -1 .

Topology-dependent ground-state degeneracy. The toric code has a ground-state degeneracy that depends only on the topology of the system. Consider the toric code on a torus, i.e. with periodic boundary condition. It is easy to verify that the Hamiltonian commutes with the global loop operators

$$\bar{X}_{\text{hor}} = \prod_{i \in C_h} X_i, \quad \bar{X}_{\text{ver}} = \prod_{i \in C_v} X_i, \quad \bar{Z}_{\text{hor}} = \prod_{i \in L_h} Z_i, \quad \bar{Z}_{\text{ver}} = \prod_{i \in L_v} Z_i, \quad (2.7)$$

where C_h (C_v) denotes a horizontal (vertical) non-contractible loop⁸ on the torus along which a Pauli X string is applied (see Fig. 2.3b). Similarly, L_h (L_v) denotes a horizontal

⁶This is possible with a non-local operator. E.g. an infinitely long Pauli string such that one endpoint (anyon) stays in the bulk, but the other endpoint extends to the infinity.

⁷As shown in Section 2.2, we need to account for the quantum dimension d for each anyon. For abelian anyon, they have unique fusion channel and therefore $d = 1$ for all the anyons.

⁸This means that there is no continuous way to shrink the loop to a point.

(vertical) non-contractible loop along which a Pauli Z string is applied (note that the Pauli X string and Z string are applied along paths as in Fig. 2.3a). Or equivalently, these string operators are formed by creating a pair of anyons locally, then dragging them away and annihilating them on the other end of the torus. Since there are no endpoints of the string operators, they commute with all the terms in the Hamiltonian H . This means that we can always choose a ground state such that

$$\bar{Z}_{\text{hor}} |GS\rangle = \bar{Z}_{\text{ver}} |GS\rangle = |GS\rangle. \quad (2.8)$$

Since $\{\bar{X}_{\text{hor}}, \bar{Z}_{\text{ver}}\} = \{\bar{X}_{\text{ver}}, \bar{Z}_{\text{hor}}\} = 0$, we see that the ground states are in fact four-fold degenerate! The four ground states are generated as $\bar{X}_{\text{hor}}^n \bar{X}_{\text{ver}}^m |GS\rangle$ for $n, m \in \{0, 1\}$ and they are labelled by the eigenvalues under \bar{Z}_{ver} and \bar{Z}_{hor} . The ground-state degeneracy is counted by drawing different non-contractible loops on the surface where we define the system. More generally, the toric code has 2^{2g} degenerate ground states on a closed surface with genus g . The topology-dependent ground-state degeneracy is not a fine-tuned property of the toric code model, they are proven to be robust under arbitrary small local perturbation at the thermodynamic limit [43, 115].

Topological entanglement entropy. The entanglement of the toric code ground state was first investigated by Hamma, Ionicioiu and Zanardi [116]. The subleading correction to the entanglement entropy of a subsystem is later understood to be the topological entanglement entropy S_{topo} [100, 101], providing a topological invariant for topologically ordered ground states. Consider a disk-like subsystem in the toric code ground state (see Fig. 2.3c). The reduced density matrix of the subsystem takes a very simple form

$$\rho \propto \sum_{\{i_b\}} |\{i_b\}\rangle \langle \{i_b\}|, \quad (2.9)$$

where the state $|\{i_b\}\rangle$ is the toric code ground state with any possible boundary qubit configuration $\{i_b\}$. More precisely, the state $|\{i_b\}\rangle$ satisfies all the terms in H which lie entirely within the boundary formed by the boundary qubits (see Fig. 2.3c). The entanglement between the subsystem and rest of the system entirely concentrates on the boundary between the two regions. This is the so-called area-law entanglement as mentioned in Section 2.1. Next, we note that due to the closed loop constraint on the ground state, only boundary qubit configurations $\{i_b\}$ with an even number of states $|1\rangle$ are allowed. It follows that the entanglement entropy of ρ gives

$$S = -\text{Tr}(\rho \ln \rho) = L \ln 2 - \ln 2, \quad (2.10)$$

where L is the number of boundary qubits for the subsystem. The first term growing with L corresponds to the area-law contribution. From the second term we have $S_{\text{topo}} = \ln 2$. Recall that $S_{\text{topo}} = \ln \mathcal{D}$, where \mathcal{D} is the total quantum dimension of the anyon theory. For abelian anyons, we simply have $\mathcal{D} = \sqrt{\#\text{anyons}}$. Since the toric code has four different anyons, we indeed arrive at $S_{\text{topo}} = \ln 2$.

2.4. The string-net model

String-net models are a class of exactly solvable models generalizing the toric code model and they realize a large class of topologically ordered phases with low-energy theories described by doubled TQFT [52]. A string-net model is specified by a set of branching rules and self-consistent local constraints. The branching rules are all the triplets of string types $\{a, b, c\}$ that are allowed to meet at each trivalent vertex while open-ended strings are prohibited. For example, in the toric code model, the branching rules only allow qubits

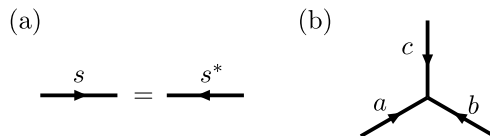


Figure 2.4.: (a) Inverting a string s is the same as changing to the dual string s^* . (b) The orientation convention for branching at a vertex.

that add up to 0 (mod 2) to meet at the vertex. On the other hand, the local constraints ensure that any string configurations that can be smoothly deformed to each other have the same weight in the ground state. As a result, the system describes a fixed point of the real-space renormalization group flow [117, 118].

We review the string-net model introduced in Ref. [52]. There exist generalizations beyond the original construction [119–121]. In this chapter we focus on the original construction in (2+1)D with rotational invariance.

The string-net models are defined on a 2D trivalent graph where each edge is associated with a string. We label the strings by $s = 0, 1, 2, \dots, N$ where N is the total number of nontrivial string types in the model, with $s = 0$ labeling the absence of any strings. The strings are generally oriented, each string s has a dual string s^* which points to the opposite direction (see Fig. 2.4a). As a result, the unoriented string satisfies $s = s^*$. The branching rule is the set of triplets of strings $\{a, b, c\}$ allowed to meet at the vertex, with the orientation convention shown in Fig. 2.4b. We define the branching delta $\delta_{abs} = 1$ if the branching $\{a, b, c\}$ is allowed, and zero otherwise. The null string $s = 0$ is associated with the branching rule $\delta_{0ss^*} = 1$ for any string type s . In the abelian string-net model (the excitations are abelian anyons), if two strings a, b meet (branch) at a vertex, then the third string c at the same vertex is uniquely determined [121], we denote this by $c^* = a \times b$. For a continuous string $\{0, s, s^*\}$ we have $s = s \times 0$. For general non-abelian string-net models, the third string c is not uniquely determined.

The string-net ground state is the state that satisfies a set of local rules. More precisely, let us consider a configuration X in the ground state wavefunction, its amplitude is denoted by $\Phi(X)$. The ground state is the weighted superpositions of string configurations $|\psi\rangle = \sum_X \Phi(X) |X\rangle$, The set of local rules relate the weights of the configurations that only differ locally

$$\begin{aligned} \Phi\left(\begin{array}{c} i \quad k \quad j \\ \circlearrowleft \\ l \end{array}\right) &= \delta_{ij} \frac{v_k v_l}{v_i} \Phi\left(\begin{array}{c} i \\ \text{---} \\ \end{array}\right), \\ \Phi\left(\begin{array}{c} i \quad l \\ \diagdown \quad \diagup \\ j \quad k \end{array}\right) &= \sum_n F_{kln}^{ijm} \Phi\left(\begin{array}{c} i \quad l \\ \diagdown \quad \diagup \\ j \quad k \end{array}\right), \end{aligned} \quad (2.11)$$

where $v_s = \sqrt{\pm d_s}$ with $d_s > 0$ being the quantum dimension of string s , they also satisfy $v_0 = 1$ and $v_s = v_{s^*}$. The rank-six tensor F is called the F -symbol. For convenience we usually define F_{kln}^{ijm} to be zero if the corresponding diagram has forbidden branching. By setting $i = j = 0$, we see that a type- s loop carries a weight of $b_s = v_s^2 \in \mathbb{R}$. These rules completely determine the ground state wavefunction in the sense that the amplitude of any configuration can be reduced to the amplitude of trivial configuration $|00\dots 0\rangle$ by applying these rules (neglecting the boundary conditions).

Because one configuration can be related to the same configuration by applying the local rules in different order, they therefore satisfy the so-called pentagon equation:

$$\sum_n F_{kp^*n}^{mlq} F_{mns^*}^{jip} F_{lkr^*}^{js^*n} = F_{q^*kr^*}^{jip} F_{mls^*}^{riq^*}. \quad (2.12)$$

In addition, it can be shown that in order for the string-net model to be physical and

self-consistent, F -symbol should satisfy

$$\begin{aligned} F_{k^*l^*n^*}^{i^*j^*m^*} &= \left(F_{kln}^{ijk} \right)^*, \\ F_{j^*i^*0}^{ijm} &= \frac{v_m}{v_i v_j} \delta_{ijm}, \\ F_{kln}^{ijm} &= F_{jin}^{lkm^*} = F_{lkn^*}^{jim} = F_{k^*nl}^{imj} \frac{v_m v_n}{v_j v_l}, \end{aligned} \quad (2.13)$$

where the star $*$ on the scalar denotes the complex conjugate of that number. The algebraic object (F_{kln}^{ijk}, b_s) that satisfies the constraints above is what defines a string-net model. Using the equations from above, we can derive one of the most useful properties of the F -symbol that underlines the unitarity of our construction

$$\sum_n F_{kln}^{ijm} \left(F_{kln}^{ijm'} \right)^* = \delta_{mm'} \delta_{ijm} \delta_{klm^*}. \quad (2.14)$$

Another useful identity that can be derived from Eqs. (2.12) and (2.13) is

$$\sum_s \delta_{abc^*} d_c = d_a d_b, \quad (2.15)$$

where $d_s = |v_s|^2 > 0$ turns out to be the quantum dimension of the anyon realized by the type- s simple string operator.

The Hamiltonian of the general string-net model generalizes the form of the one for the toric code, consisting of commuting projectors

$$\hat{H} = - \sum_v \hat{Q}_v - \sum_p \hat{B}_p, \quad (2.16)$$

where \hat{Q}_v projects the triplet of strings at each vertex v onto the allowed branching, $\hat{B}_p = \sum_s a_s \hat{B}_p^s$ is the plaquette projector with a_s being some real coefficients determined by specific string-net models. \hat{B}_p^s is a plaquette operator for each string type s , it acts on the plaquette p and its six external legs. By construction all the terms commute with each other. For the topological phase to have a continuum limit, a_s is chosen to be $a_s = b_s / \sum_s b_s^2$. With this choice of a_s , \hat{B}_p becomes a projector. Each \hat{B}_p^s physically corresponds to adding a type- s loop to a plaquette and fusing it into the lattice based on the local rules Eq. (2.11). With this graphical picture, one can work out the general matrix element for \hat{B}_p^s in terms of the F -symbol

$$\begin{aligned} & \left\langle \begin{array}{c} b \quad h' \quad c \\ \swarrow \quad \downarrow \quad \searrow \\ a \quad g \quad i' \\ \swarrow \quad \downarrow \quad \searrow \\ l' \quad k' \quad e \end{array} \right| \hat{B}_p^s \left| \begin{array}{c} b \quad h \quad c \\ \swarrow \quad \downarrow \quad \searrow \\ a \quad g \quad i \\ \swarrow \quad \downarrow \quad \searrow \\ f \quad k \quad e \end{array} \right\rangle \\ &= F_{s^*h'g'l'^*}^{bg^*h} F_{s^*i'h'^*}^{ch^*i} F_{s^*j'i'^*}^{di^*j} F_{s^*k'j'^*}^{ej^*k} F_{s^*l'k'^*}^{fk^*l} F_{s^*g'l'^*}^{al^*g}. \end{aligned} \quad (2.17)$$

Note that the spins on the six external legs are not changed upon the application of \hat{B}_p^s . The operators of any string types and on any plaquettes commute, i.e. $[\hat{B}_{p_1}^{s_1}, \hat{B}_{p_2}^{s_2}] = 0$ for any s_1, s_2 and p_1, p_2 .

Each quasiparticle excitation of the Hamiltonian (3.4) corresponds to a closed string operator. The string should not be observable, only the endpoints of the string (quasiparticles) are. For this reason, the closed string operator should commute with the Hamiltonian. A type- s string operator that fulfills the requirements has the matrix element from i to i'

$$W_{i_1 i_2 \dots}^{i'_1 i'_2 \dots}(e) = \left(\prod_k F_{s^*i'_{k-1}i_k^*}^{e_{k-1}i_k^*} \right) \left(\prod_k \omega_k \right), \quad (2.18)$$

where i_1, i_2, \dots are the spins along the closed string, e is the set of external legs along the path of the string operator (e.g. see Fig. 3.4a). The closed string operator W only changes the spins along the path but not the ones on external legs. The quantity ω is defined as

$$\omega_k = \begin{cases} \frac{v_{i_k} v_s}{v_{i'_k}} \omega_{i_k}^{i'_k}, & \text{if before/after } i_k, \text{ it turns right/left,} \\ \frac{v_{i_k} v_s}{v_{i'_k}} \bar{\omega}_{i_k}^{i'_k}, & \text{if before/after } i_k, \text{ it turns left/right,} \\ 1, & \text{otherwise.} \end{cases} \quad (2.19)$$

where ω_j^i and $\bar{\omega}_j^i$ are phase factors satisfying Eq. (2.20). Notice that when W acts on a plaquette p , it should correspond to adding a type- s string loop and fusing it into the plaquette, i.e. it is equivalent to applying \hat{B}_p^s .

The solutions of ω are solved from a set of consistency equations by imposing the commutativity of the string operators with the Hamiltonian

$$\begin{aligned} \bar{\omega}_i^j &= \sum_n \omega_{i^*}^k F_{i^* s j^*}^{i s^* k}, \\ \frac{v_s v_j}{v_m} \bar{\omega}_j^m F_{k j m^*}^{s l^* i} \omega_j^l &= \sum_n F_{s^* n l^*}^{j i^* k} \omega_k^n F_{k s m^*}^{j l^* n}. \end{aligned} \quad (2.20)$$

The string operator of this form is called the *simple string operator*. The product of two simple string operators $W_1 W_2$ results in another string operator for the composite quasiparticle. The simple string operators form a large subclass of the general string operators, they describe many interesting anyonic quasiparticles that are relevant for physical realizations, such as the anyons in the toric code model and the non-abelian double Fibonacci model (see Section 3.5.3).

3. Theoretical proposals for realizations of abelian and non-abelian topologically ordered states with gate-based quantum computers

While the search for physical systems hosting topological order and methods of its detection remains an active area of research, another route toward realizing topological states is through their simulation in suitable quantum systems. To this end, exactly solvable models play a special role; they can serve as a test bed for calibrating the system in order to realize the established properties before venturing into the unknown. A quintessential example of soluble models of topological order is provided by string-net models [52]. These are lattice models, the low-energy physics of which is described by a non-chiral doubled topological quantum field theory (TQFT) [122, 123]. String-nets also have an intimate connection to quantum computation: Abelian string-net models can be regarded as a family of quantum error-correcting codes and certain non-abelian string-net models can be used for universal quantum computation in relation to Turaev-Viro codes [124].

In this chapter, we show that generic string-net (ground) states can be efficiently realized and manipulated on a digital quantum computer with shallow unitary circuits. Our protocol allows a preparation of topologically ordered states with $\mathcal{O}(l)$ -depth quantum circuits of local gates, where l is the smaller of the width and the height of the system. The algorithm thus saturates the circuit complexity lower bound for preparing topologically ordered ground state [125]. Moreover, it is possible to characterize the topological order of the prepared states by entanglement and braiding statistics measurements. The creation and manipulation of the localized anyonic quasiparticles in the abelian and non-abelian phases rely on string-like quantum circuits. The depth of the required circuits is constant for abelian anyons and scales linearly with the separation of the non-abelian anyons. Based on the anyonic braiding, the fusion of anyons can be determined by efficient interferometry measurements. This completes a toolkit for simulating the underlying TQFT of the string-net model. As a result, the scheme can be viewed as an efficient mapping from the gate-based computation to an anyon-based computation [126]. Due to the inherent noise of NISQ devices, efficient algorithms become particularly important for obtaining reliable results. A special case of our protocol has already been used to realize \mathbb{Z}_2 topological order on the 31-qubit Sycamore quantum processor [5] (see also Chapter 4).

It is worth mentioning that other explicit unitary constructions for string-net states are known. Letting L be the perimeter of the system, a depth- $\mathcal{O}(L \log L)$ quantum circuit can be derived from entanglement renormalization [117, 127]. The isometric tensor network representation [128] of the string-net states can be regarded as a local quantum circuit of depth $\mathcal{O}(L)$ [129–131]. A subclass of the string-net model, the quantum double model and its anyonic excitations [43] can be simulated without the presence of a background Hamiltonian by involving measurement operations [132, 133]. Additionally, there are alternative protocols for extracting anyon statistics based on wavefunction overlaps [134], or using defects and lattice deformation such as in [124].

3.1. Preparation of the toric code ground state

We begin by presenting the preparation algorithm for the toric code (TC) ground state (see Section 2.3). For the convenience of later generalization, we consider the toric code on a honeycomb lattice. But the algorithm can be easily adapted to arbitrary lattice structure. The model consists of spin-1/2 degrees of freedom on the links of a honeycomb lattice with Hamiltonian

$$\hat{H}_{TC} = - \sum_s \hat{Q}_s^{(TC)} - \sum_p \hat{B}_p^{(TC)}. \quad (3.1)$$

The commuting projectors $\hat{Q}_s^{(TC)} = \frac{1}{2}(1 + \prod_{j \in s} Z_j)$ contain a product of Pauli matrices Z around each vertex s and $\hat{B}_p^{(TC)} = \frac{1}{2}(1 + \prod_{j \in p} X_j)$ contains a product of Pauli matrices X around each plaquette p , as shown in Fig. 3.1a. Throughout this chapter we consider open boundary conditions, as in Fig. 3.1a, which are most relevant for experimental realization of the states on NISQ devices.

In the Pauli- z basis, we regard the qubit state $|1\rangle$ as being occupied and state $|0\rangle$ as unoccupied. Similar to the TC on a square lattice, the vertex and the plaquette projectors, \hat{Q}_s and \hat{B}_p , constrain the ground state to be an equal-weight superposition of all the closed loop configurations. A ground state can be compactly written as a product of the plaquette projectors over the product state, neglecting the normalization:

$$|GS\rangle_{TC} \propto \prod_p \left(1 + \prod_{j \in p} X_j \right) |000 \cdots 0\rangle. \quad (3.2)$$

With the choice of open boundary conditions, Eq. (3.2) is the unique ground state of the Hamiltonian (3.1)¹. A similar idea can be adapted to periodic boundary conditions, where the ground state of the Hamiltonian becomes fourfold degenerate.

The compact form of Eq. (3.2) motivates an efficient quantum circuit construction for the ground state, which is as follows:

1. Prepare an initial product state. We associate a representative qubit with each plaquette and they are initialized as $|+\rangle = (|0\rangle + |1\rangle)/\sqrt{2}$ (blue in Fig. 3.1c). The rest of the qubits are initialized as $|0\rangle$ (red in Fig. 3.1c).
2. Perform $C-\hat{B}_p$ over all the plaquettes in parallel on each row and iterate this from the bottom row to the top row. Where the controlled- \hat{B}_p operation ($C-\hat{B}_p$ for short) applies CNOT gates controlled by the representative qubit to the rest of the qubits in the same plaquette, shown in Fig. 3.1b.

The depth of the quantum circuit built from this algorithm is linear in the number of plaquette rows in the system. Graphical illustrations of the steps are shown in Fig. 3.1b-c. The $C-\hat{B}_p$ operator plays a central role in our construction of the quantum circuit. It flips all the rest of the qubits in the plaquette if the representative qubit is $|1\rangle$, otherwise it acts trivially. The algorithm therefore has a nice interpretation that, each operation $C-\hat{B}_p$, together with the initialization of the representative qubit for plaquette p , splits the state into an equal-weight superposition of being acted on by the identity or $\prod_{j \in p} X_j$. Iterating this set of operations over all the plaquettes yields the ground state of the form given in Eq. (3.2). If we follow this row-wise construction in Fig. 3.1c and step 2, the circuit can be designed to have a depth that scales proportional to the smallest linear dimension of the

¹To be more precise, under this open boundary condition, some vertices on the boundary are only connected to two spins. The vertex operators \hat{Q} on these vertices thus consist of Pauli matrices on two spins instead of three as in the bulk.

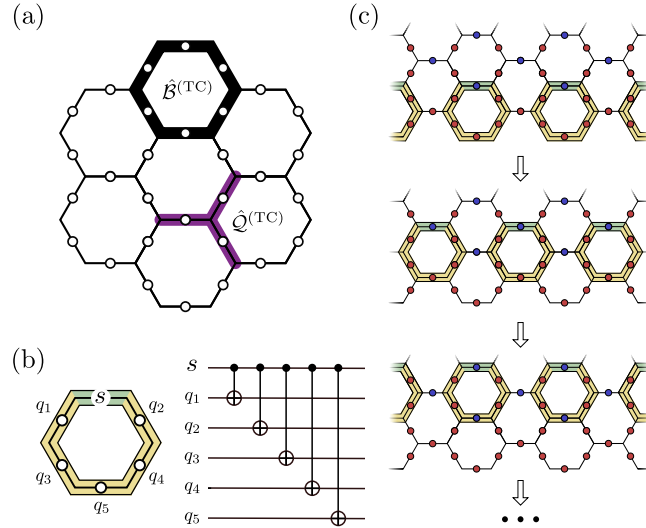


Figure 3.1.: The construction of the toric code ground state. (a) The honeycomb lattice with qubits on the edges that contains a plaquette (black) and a vertex (purple); The vertices on the boundary only have two incoming legs. (b) The quantum gate $C-\hat{B}_p$ that is controlled by the representative qubit and targets the rest. The green marks the control qubits (unchanged upon $C-\hat{B}_p$), the yellow marks the target qubits (changed); (c) A graphical illustration of the algorithm. Prepare the red qubits in $|0\rangle$ and the blue qubits in $|+\rangle = (|0\rangle + |1\rangle)/\sqrt{2}$. Then apply $C-\hat{B}_p$ on each plaquette in parallel for each row.

system. A concrete experimental implementation of this algorithm can be found in Ref. [5] and Chapter 4.

The algorithm can be extended beyond the row-wise construction to other geometries, e.g. to periodic boundary conditions. However, the order must be such that each representative qubit is used as a control qubit before it is part of the targets of the $C-\hat{B}_p$ gate. That is, before applying the $C-\hat{B}_p$ gate, we require the representative qubit for that plaquette not to be entangled with the rest of the system. If the choice of representative qubits and the order in which the $C-\hat{B}_p$ gates are applied satisfy this constraint, then we say that the order is *permissible*. The row operation in step 2 of the algorithm can be replaced with other protocols following any permissible order. In general, the algorithm yields a parallel quantum circuit of depth that is at most linear in the perimeter of the system. We will see that this statement holds true for all the string-net models.

3.2. Preparation of the double semion ground state

Before moving on to general string-net models, let us consider another spin-1/2 example—the double semion (DS). This model can support semions and their chiral partners as excitations with an exchange phase of $\pm i$ [123]. The Hamiltonian of the DS takes a form similar to Eq. (3.1), with $\hat{Q}_s^{(\text{TC})}$ replaced by $\hat{Q}_s^{(\text{DS})}$ and $\hat{B}_p^{(\text{TC})}$ by $\hat{B}_p^{(\text{DS})}$. The vertex projector $\hat{Q}_s^{(\text{DS})}$ projects onto the space where an even number of strings meet on each vertex s (i.e. the same as the TC). The plaquette projector takes the form $\hat{B}_p^{(\text{DS})} = \frac{1}{2}(1 - \hat{B}_p^1)$, where \hat{B}_p^1 flips all the qubits in the plaquette p and associates a phase $+1(-1)$ to the configuration if the total number of loops in that configuration is changed (unchanged) after the flip. Note that in the literature, the factor of -1 in the DS model is typically associated with a change in the number of loops, but here we have an additional minus sign in front of \hat{B}_p^1 ,

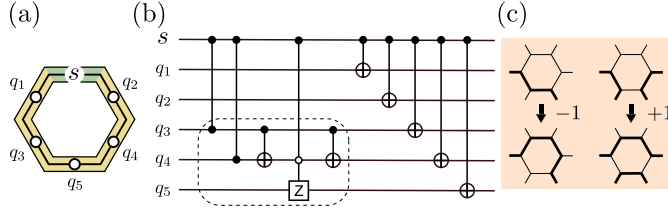


Figure 3.2.: Construction of the double semion ground state. We implement the algorithm as in analogy to Fig. 3.1c: the representative qubits (blue) are initialized in $|-\rangle = (|0\rangle - |1\rangle)/\sqrt{2}$, and the rest of the qubits (red) are $|0\rangle$. (a) The construction consists of parallel application of $C\hat{B}_p$ on each row. (b) The circuit diagram for $C\hat{B}_p$ is shown. The two-qubit gate symbolised by two solid dots connected by a line is a controlled- Z gate. The three-qubit gate applies Pauli Z to the third qubit if the solid and hollow control qubits are 1 and 0, respectively, otherwise it does nothing. The dashed box in the circuit diagram contains the unitary that gives a phase $+1(-1)$ if the number of loops changes (unchanged) when a TC plaquette operator is applied (as shown in (c)).

corresponding to the choice of $|-\rangle = (|0\rangle - |1\rangle)/\sqrt{2}$ for the representative qubits. This is only a matter of convention; we keep the minus sign here for later generalizations.

Similarly to the TC, the resulting DS ground state can be obtained by applying a product of plaquette projectors $\hat{B}_p^{(DS)}$:

$$|GS\rangle_{DS} \propto \prod_p \hat{B}_p^{(DS)} |000\dots 0\rangle. \quad (3.3)$$

The DS ground state is a superposition of all the closed loop configurations with weights $(-1)^C$, where C is the total number of closed loops in that configuration.

To construct the wavefunction given in Eq. (3.3), we translate the same procedure from the TC construction:

1. We assign a representative qubit to each plaquette and initialize them in $|-\rangle = (|0\rangle - |1\rangle)/\sqrt{2}$, the rest of the qubits are initialized in $|0\rangle$.
2. Then apply the $C\hat{B}_p$ operator over the plaquettes row by row in parallel as in Fig. 3.1c.

Notice the difference with the TC case: we initialize the representative qubits in the $|-\rangle$ state instead of $|+\rangle$. We also employ a different $C\hat{B}_p$, which applies \hat{B}_p^1 to the other qubits in the plaquette if the representative qubit is $|1\rangle$ and acts trivially otherwise. An explicit circuit for the $C\hat{B}_p$ is shown in Fig. 3.2. Again during the construction, the order in which we apply $C\hat{B}_p$ is important. We can choose the same row iteration as in the TC case, and then the depth of the circuits constructed row-wise scales linearly with the smallest linear dimension of the system. More generally we can follow any permissible order, as defined in Section 3.1.

3.3. Preparation of general string-net ground states

A general string-net model can be defined on a honeycomb (or any trivalent) lattice with local spins located on the edges (see Section 2.4 for a review). These spin degrees of freedom correspond to different *string types* at that edge. The strings are oriented in general, we use i^* to denote the string i with inverted orientation, with $i^* \neq i$ for oriented strings. String-net models describe a large class of topologically ordered phases the low-energy

3.3. Preparation of general string-net ground states

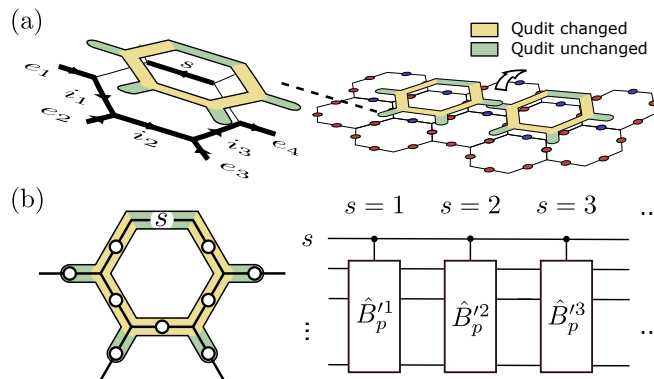


Figure 3.3.: The construction for general string-net models. (a) During the construction, $C\text{-}\hat{B}_p^s$ only acts on the subspace shown on the left, here $i_1, i_2, i_3, e_1, e_2, e_3, e_4$ labels all the allowed strings under branching rules. s is the state of the representative qudit. The arrows indicate the convention for the string orientation. One can prepare general string-net states on the honeycomb lattice by applying $C\text{-}\hat{B}_p$ row by row. Despite the overlap of the gates, they can be decomposed for parallel implementation on each row. The $C\text{-}\hat{B}_p$ gate is controlled by the green qudits and alters the yellow ones. The representative qudits (blue) are initialized in $\mathcal{D} \sum_i a_i |i\rangle$. (b) The gate structure of $C\text{-}\hat{B}_p$: If the representative qudit is in state $|s\rangle$, it applies \hat{B}_p^s to the rest of the spins within the plaquette. This gate satisfies Eq. (3.6). We provide an explicit circuit for the gate in Section 3.5.2

physics of which gives rise to a doubled TQFT [52]. On a quantum computing platform, the spins (or strings of different types) are encoded as *qudits*, a generalization of qubits with more than two levels, which in practice could correspond to multiple physical qubits.

For a model with N nontrivial string types, we can define an orthonormal basis $\{|s\rangle\}$, i.e. $(N+1)$ -level qudit states, for string $s = 0, 1 \dots N$ where each qudit state $|s\rangle$ labels an edge occupied by a string s . The label $s = 0$ is reserved for the vacuum or null string. The Hamiltonian of the general string-net model generalizes the form of TC and DS, consisting of commuting projectors

$$\hat{H} = - \sum_v \hat{Q}_v - \sum_p \hat{B}_p, \quad (3.4)$$

where \hat{Q}_v projects the triplet of strings at each vertex v onto the allowed branching, $\hat{B}_p = \sum_s a_s \hat{B}_p^s$ is the plaquette projector with a_s being some real coefficients determined by specific string-net models. \hat{B}_p^s is a plaquette operator for each string type s , it acts on the plaquette p and its six external legs (see Section 2.4 for a detailed definition). By construction all the terms commute with each other.

Notice that the TC and DS in the previous sections are special cases of Eq. (3.4) with $a_0 = a_1 = 1/2$ and $a_0 = -a_1 = 1/2$ respectively. The plaquette operators are $\hat{B}_p^0 = 1$ and the non-trivial plaquette operator \hat{B}_p^1 in each case. The coefficients a_s are related to the *total quantum dimension* \mathcal{D} of the underlying anyonic theory through $\mathcal{D} = 1/\sum_i a_s^2$.

A ground state of the general string-net model can be conveniently written as a product of projectors over the zero product state

$$|GS\rangle \propto \prod_p \hat{B}_p |000 \dots 0\rangle = \prod_p \left(\sum_s a_s \hat{B}_p^s \right) |000 \dots 0\rangle. \quad (3.5)$$

The state preparation is a direct generalization of the case for the DS, with the $C\text{-}\hat{B}_p$ (DS)

operator acting on qubits replaced by the new $C-\hat{B}_p$ operator acting on qudits. Similar to controlled operations on qubits, this controlled operation applies a unitary to the target qudits if the control qudit is in a particular state s , as shown in Fig. 3.3.

For simplicity, we focus on the same row-wise construction as in the previous sections. A generalization to any permissible order is straightforward. When $C-\hat{B}_p$ operations are performed from the bottom to the top row during the row-wise construction, the qudit subspace on which the qudit gates act is shown in Fig. 3.3a. The shape of general $C-\hat{B}_p$ generalizes those for the TC and DS; there are four additional qudits covered by the gates and the states of these qudits are unchanged upon the application of the gate. Despite the shared bond between the neighbouring operations, similar to the CNOT decomposition for the TC construction in Fig. 3.1c, the $C-\hat{B}_p$ gate can be decomposed into a sequence of smaller controlled qudit gates around a plaquette. This allows for parallel implementation of the gates to all the plaquettes along each row (see details in Section 3.5.2).

We can therefore adopt the following steps to construct a general string-net ground state:

1. We assign a representative spin for each plaquette and initialize them in a state $\sqrt{\mathcal{D}} \sum_s a_i |s\rangle$. The rest of the spins are initialized to be $|0\rangle$.
2. We then iteratively apply the $C-\hat{B}_p$ on each row of plaquettes.

Here operators $C-\hat{B}_p$ for the row construction satisfy

$$\begin{aligned}
 C-\hat{B}_p \left| \begin{array}{c} \text{---} s \text{---} \\ \nearrow \quad \searrow \\ e_1 \quad i_1 \quad e_4 \\ \leftarrow \quad \rightarrow \\ e_2 \quad i_2 \quad e_3 \end{array} \right\rangle &= \hat{B}_p^{s} \left| \begin{array}{c} \text{---} s \text{---} \\ \nearrow \quad \searrow \\ e_1 \quad i_1 \quad e_4 \\ \leftarrow \quad \rightarrow \\ e_2 \quad i_2 \quad e_3 \end{array} \right\rangle \\
 &= \hat{B}_p^s \left| \begin{array}{c} \text{---} \quad \text{---} \\ \nearrow \quad \searrow \\ e_1 \quad i_1 \quad e_4 \\ \leftarrow \quad \rightarrow \\ e_2 \quad i_2 \quad e_3 \end{array} \right\rangle .
 \end{aligned} \tag{3.6}$$

Thin unlabeled edges stand for the vacuum $|0\rangle$, while the set of labels $\{i\}$ and $\{e\}$ are arbitrary qudit configurations satisfying the branching rules of the string-net ground state. Edges with arrows indicate a convention that we use to label an oriented string with the qudit state. Operator \hat{B}_p^{s} is implicitly defined by Eq. 3.6 and takes into account that the representative qubit starts in the state s , such that its action corresponds to applying plaquette operator \hat{B}_p^s to that plaquette. We indicate the strings with a particular convention for the orientation. However, for models with only unoriented strings, no convention needs to be chosen. This includes all the spin-1/2 string-net models, the TC, the DS, and the double Fibonacci model discussed in Section 3.5.3. The $C-\hat{B}_p$ operation is controlled by the representative qudit: if the qudit is $|s\rangle$, \hat{B}_p^{s} is applied to the rest of the qudits in the same plaquette p (see Fig. 3.3b), which is the same as acting with \hat{B}_p^s on the state with a trivial representative qudit. It is also possible to implement the $C-\hat{B}_p$ operations in a different permissible order other than the row-wise construction above. To do this, a more generic definition of $C-\hat{B}_p$ is needed whereby the subspace of the initial qudit configurations is more general than that shown in Fig. 3.3a and Eq. (3.6). In Appendix A.1, we give a more general subspace of qudit configurations for defining $C-\hat{B}_p$ that can be used for any permissible order. The operator $C-\hat{B}_p$ is well defined due to the isometry condition of \hat{B}_p^s restricting to the subspace where at least one of the qudit states on the plaquette edge is trivial $|0\rangle$. A proof of the isometry property is given in Appendix A.1.

The construction prepares any given string-net ground states from $\mathcal{O}(l)$ layers of parallel local quantum gates, where l is the smallest linear dimension of the system. The circuit depth shows explicitly that the lower bound of the circuit scaling provided in Ref. [125] is optimal for string-net states.

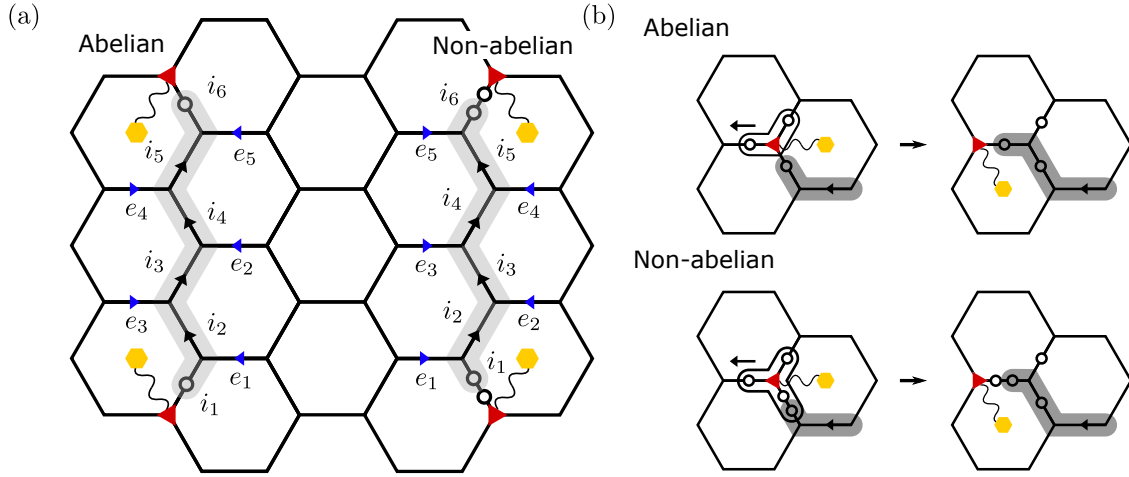


Figure 3.4.: Prepare and move anyons with unitary string operators. (a) Open string operators for abelian (left) and non-abelian (right) anyons. The operators act on the set of labeled qudits $\{i\}$ along the path and $\{e\}$ of the legs. Only the states of the qudits $\{i\}$ along the path are changed by the operator. Each quasiparticle has an associated vertex (red) and plaquette (yellow). Before the string operators are applied, the ancillary qudits in the non-abelian case are initialized to align with the other qudits on the same edge. (b) The endpoint quasiparticles can be moved by extending the string operator sequentially with unitary gates. The dark gray marks the existing string, The enclosed qudits on the left are acted on by the endpoint-moving unitary gates, which correspond to an exact (modified) form of the unitary string operators for abelian (non-abelian) case. The plaquette-vertex labels are used to locate the quasiparticle. When extending the string operator, they trace the motion of the quasiparticle. Note that the ancillary qudit in the non-abelian case can be moved without physically displacing the qudits. See Sections 3.5.1 and 3.5.2 for more details.

3.4. Creating and moving anyons in the string-net model

In this section, we describe how abelian anyons can be created and braided using quantum circuits of a constant depth, whereas braiding of non-abelian anyons requires linear-depth (in anyon–anyon separation) quantum circuits due to their non-unique fusion.

The quasiparticles in the string-net model are identified with closed string (Wilson loop) operators that commute with the string-net Hamiltonian. When a closed string operator is broken to have open ends, the quasiparticle and the corresponding anti-quasiparticle emerge as defects localized at the endpoints of the open string operator applied to the string-net states [52]. The string operators connecting the two endpoints can be thought of as a trajectory traced by the quasiparticle at one end while the other is at rest. As a result, the braiding events can be simulated by realizing the open string operators with a sequence of unitary gates.

The precise details of how the closed string operators are broken into open strings are not essential for our purpose. Braiding is described by the relative motion between different quasiparticles. In other words, the braidings are captured by how the open string operators cross each other away from their endpoints (see Fig. 2.2). We require the open string operators to have the exact same bulk form as the closed string operators given in Ref. [52], but at the same time to be unitary. These string operators are generally isometries, but can be promoted to a unitary form. Such *unitary string operators* allow the manipulation

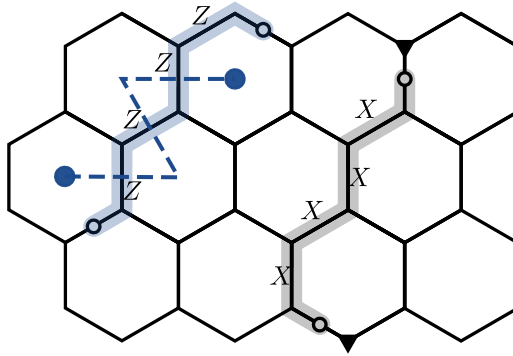


Figure 3.5.: The string operators for toric code. The endpoints can be labeled by a plaquette or vertex that corresponds to exactly the microscopic excitation in Eq. (3.1). The dashed line indicates the path that the plaquette excitation takes as the Wilson string is generated.

of anyons by decomposition into a sequence of smaller gates.

To simplify the discussion, we focus on the string-net models where quasiparticles correspond to either a simple string operator or a product of simple string operators. This is not a very restrictive condition and, for instance, includes all of the spin-1/2 string-net models originally considered in Ref. [52] and non-abelian anyons beyond spin-1/2 lattice such as the Ising anyon. A string operator being *simple* means that it can be assigned a unique basis string label $s \in \{0, 1, \dots, N\}$ and it characterizes an irreducible quasiparticle in the model (see Section 2.4 for details). We give a definition of the open simple string operators that can be promoted to a unitary in Section 3.5.1. The shapes of the operators are depicted in Fig. 3.4a for general abelian and non-abelian cases. The string operator changes the qudit states $\{i\}$ along its path and leaves the states $\{e\}$ on the legs unchanged. The orientation of the path along the string is indicated with arrows. The quasiparticles at the endpoints of the open string can be moved by deforming the string operator with some local unitary gates (see Fig. 3.4b). The product of simple strings can be implemented by multiple simple strings with non-overlapping endpoints.

3.4.1. Locating the quasiparticles

The braiding interferometry in Section 2.2 assumes the quasiparticle configurations at the end of the interfered paths to be identical. To unambiguously locate a quasiparticle at the endpoint of a string operator, we label each endpoint with a vertex and a plaquette. If the string operator turns left (right) before the spin at the endpoint, then the associated plaquette is on the left (right) of the endpoint. The associated vertex is the vertex away from the endpoint of the string operator. The plaquette-vertex pair labels the location and orientation of the quasiparticle (see Fig. 3.4a). The motion of the quasiparticle can be visualized as moving the pair of labels as shown in Fig. 3.4b. Note that the plaquette/vertex label does not necessarily coincide with the actual plaquette-vertex violation that appears as excitation in the microscopic string-net Hamiltonian. In some cases, they can be chosen to coincide. An example is the TC excitations which are created by a string of Pauli X along the vertex labels and a string of Pauli Z along the plaquette labels (Fig. 3.5). Each string operator thus only needs one of the plaquette or vertex labels and the other one becomes irrelevant.

3.4. Creating and moving anyons in the string-net model

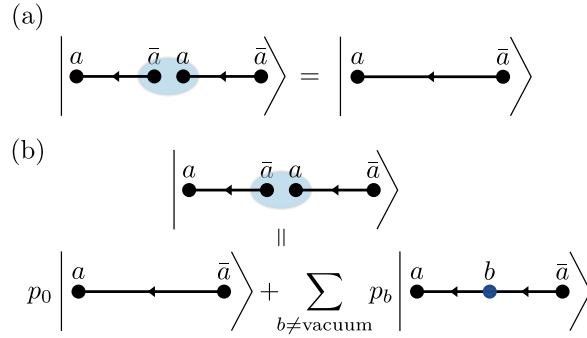


Figure 3.6: The manipulation of abelian and non-abelian anyons. (a) Two separate abelian anyons a, \bar{a} can be created by a sequence of multiple local anyon-antianyon pairs. The intermediate quasiparticles fuse to the vacuum. (b) If a, \bar{a} are non-abelian anyons, the transport of the anyon is no longer equivalent to local pair creation and pair annihilation of a and \bar{a} . The fusion yields a superposition of the vacuum and some other non-trivial anyon species b , with amplitudes p_b .

3.4.2. Unitary string operators for the abelian anyons

If the quasiparticle describes an abelian anyon, the trajectory represented by the string operator can be interpreted as a chain of anyon–antianyon pair creations. Since the abelian anyon and its antianyon are guaranteed to fuse into the vacuum, the result will be the same as having one quasiparticle at each end of this chain, as depicted in Fig. 3.6a.

This shows that a long unitary string operator for the abelian anyons is a product of disjoint short unitary string operators. As seen in the circuit decomposition of the string operator as shown in Fig. 3.4b, an abelian open string operator can be extended by one more site, with a two-qudit quantum gate that does not overlap with the existing string operator. In this case, this two-qudit gate corresponds to a unitary open string operator in Fig. 3.4a with one endpoint slightly modified. To create a long string operator of the form in Fig. 3.4a, we can apply a short string operator (a three-qudit quantum gate) and extend it to a longer string as schematically illustrated in Fig. 3.7a. Since none of the gates overlap with each other, the circuit can be implemented with a constant depth. Further details of the two- and three-qudit gates are given in Section 3.5.1.

3.4.3. The difficulty of manipulating non-abelian anyons

The argument given for the abelian anyons no longer holds when we consider the non-abelian case. The fusion of two non-abelian anyons along the chain does not give only the vacuum, but in general a superposition of fusion channels (see Section 2.2 and Fig. 3.6b). To create two separated non-abelian anyons from the local pairs, additional projections are needed around the anyon-antianyon pair to ensure that they fuse to the vacuum.

Therefore, a unitary (and hence reversible) movement of non-abelian anyons can only be achieved sequentially, requiring at least a number of time steps that scales with the separation between the anyons. In the language of field theories, this amounts to the necessity of path-ordering in the Wilson loop operator for non-abelian anyons. This intuition implies that at least a linear-depth quantum circuit is needed to implement a unitary string operator that describes the movement of non-abelian anyons. A recent work [135] has proved this lower bound in the context of the quantum double model.

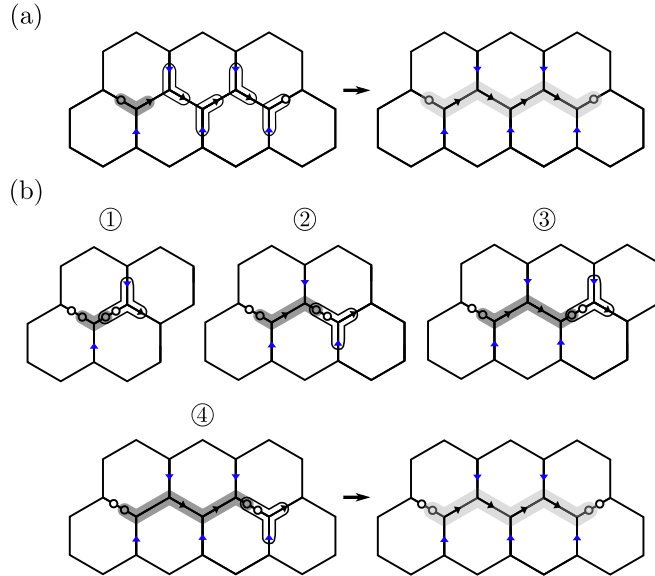


Figure 3.7.: The decomposed string operators using the movements from Fig. 3.4b. (a) For the abelian string operators, an initial short string (dark gray) can be extended to a long string operator (light gray) by a constant-depth local quantum circuit. (b) A sequentially applied quantum circuit is required for extending a short non-abelian string, resulting in a linear-depth quantum circuit. We show the details of the circuits, including the short string initialization in Section 3.5.1.

3.4.4. Unitary string operators for non-abelian anyons

To define a unitary string operator for the non-abelian anyons, we introduce an additional qudit at each endpoint of the string as shown in Fig. 3.4a. This additional degree of freedom at the string endpoints is motivated by the diagrammatic calculus of the string operators in the Appendix D of Ref. [52]. In the diagrammatic approach, an endpoint of a string operator will carry a simple string label and split the edge it touches (represented by a physical qudit) into two edges; One of the edges still retains the original qudit state, and the other edge now stores the new qudit state obtained from applying the string operator. In our protocol, we introduce the additional qudit to take into account this additional split edge so that we can keep the full information about the open string endpoint, making the unitary construction of the operator possible.

As depicted in Fig. 3.4b, a non-abelian open string operator can be extended by one site with a four-qudit quantum gate. In contrast with the abelian case, the gate that extends the string operator needs to involve the qudits at the endpoint of the existing string operator, and the gate itself cannot be regarded as a short unitary open string operator. To create a long string operator, we first implement a short unitary string operator of the form in Fig. 3.4a (in the non-abelian case, this is achieved by a four-qudit quantum gate as explained in Section 3.5.1), the short string is extended using a sequence of four-qudit gates in Fig. 3.4b. An explicit procedure is depicted in Fig. 3.7b, which is a quantum circuit the depth of which grows linearly with the separation of the string endpoints. Note that the resulting unitary string operators satisfy the optimal scaling of the circuit depth argued above. The existence of the efficient string operator decomposition allows for manipulation of non-abelian anyons without the need of any projection.

When simulating the non-abelian strings, the additional ancillary qudits should always be placed at the endpoints of the current string operators. This can be achieved by swapping the ancilla states through the lattice without physically displacing the qudits. We

3.5. Explicit quantum circuits for the string-net states and their anyons

provide full details of the protocol together with explicit quantum circuits in Sections 3.5.1 and 3.5.2. Alternatively, we can simply place two qudits on each edge instead of only one. Despite doubling the number of qudits, the alternative approach retains the translational and rotational invariance of the lattice.

3.5. Explicit quantum circuits for the string-net states and their anyons

In this section, we provide the explicit quantum circuits for the preparation algorithm and for the quasiparticle braiding above the string-net states. The readers who wish to skip the technical details can directly jump to Section 3.6 for the discussion and conclusion.

3.5.1. Quasiparticle string operators

The anyonic excitations in the string-net models are localized at the endpoints of the open string operators. There is no unique way to define the endpoints (excitations) of these open string operators. However, the topological properties of these quasiparticles are independent of such details. Here we give a definition of the open string operator (corresponding to a type- s string of length L) in the string-net model, its matrix element from initial spins i_1, i_2, \dots to i'_1, i'_2, \dots can be written as

$$W_{i_1 i_2 \dots i_L}^{i'_1 i'_2 \dots i'_L}(e) = \frac{v_{i'_1}}{v_{i_1} v_s} \left(\prod_{k=2}^L F_{s^* i_{k-1} i_k}^{e_{k-1} i_k} \right) \left(\prod_{k=2}^{L-1} \omega_k \right), \quad (3.7)$$

where $e = \{e_1, e_2, \dots, e_{L-1}\}$ is the set of external legs along the string (see Fig. 3.4a). The complex numbers v_i and rank-six tensor F are the data that define the given string-net model (see Section 2.4). ω is defined in Eq. (2.19).

This open string operator has the property that creating a type- s string along $\{i_1, i_2, \dots, i_L\}$ is the same as creating a type- s^* string along $\{i_L, \dots, i_2, i_1\}$. In addition, the open string operator satisfies an isometry condition that underlies the unitary decomposition of the operator as discussed below.

Abelian quasiparticle strings: In the abelian theory, we can move the abelian anyon by applying the open string operator that connects between the anyons at the initial and final position. That is, we change the position of the endpoint by joining two open strings together to form a new open string. This is possible because abelian anyons have a unique fusion channel. When two endpoints (anyons) join, the anyon and its anti-partner combine (fuse) to vacuum.

Since we can move the anyon using a sequence of local unitary, it is convenient to initialize a short open string operator and move the anyons (endpoints) apart from each other later. We can prepare a pair of abelian anyons (that corresponds to an type- s string) by a three-qudit unitary having the matrix elements in (3.7) for $L = 2$

$$\left| \begin{array}{c} \text{Diagram 1: A vertex with three legs } e, q_1, q_2. \end{array} \right\rangle = \frac{v_{q'_1}}{v_{q_1} v_s} F_{s^* q'_1 q'_2}^{e q_1} \left| \begin{array}{c} \text{Diagram 2: A vertex with three legs } e, q'_1, q'_2. \end{array} \right\rangle, \quad (3.8)$$

where $q'_{1,2} = s \times q_{1,2}$ and $\{e, q_1, q_2^*\}$ is an allowed branching. The dark path on the right hand side indicates the path created by the string operator. We use an arrow along the string to indicate the orientation convention following Fig. 3.4a. In abelian theory, the non-trivial values in F -symbol become phase factors (see Section 2.4). This operator initializes a string of length two on the lattice. Note that we could have set the phase $v_{q'_1}/v_{q_1} v_s$ to

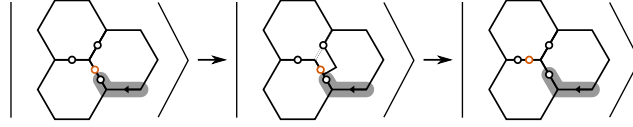


Figure 3.8.: A local change of registered connectivity—to make sure the endpoint of the string can land at an edge with two qudits. No physical gates are needed here.

1 by local unitary in this abelian case, but in non-abelian theory this factor is no longer a phase and it becomes important for preserving the isometry property of the open string operator.

The abelian anyon at the end of the string can be moved using a two-qudit unitary that satisfies

$$\left| \begin{array}{c} \text{hexagon} \\ \text{hexagon} \\ \text{hexagon} \end{array} \right\rangle = \omega_{p',p} F_{s^* p' q'^*}^{e q^* p} \left| \begin{array}{c} \text{hexagon} \\ \text{hexagon} \\ \text{hexagon} \end{array} \right\rangle, \quad (3.9)$$

again here $p = e^* \times q$, $p' = s \times p$ and $q' = s \times q$. We also define $\omega_{p',p}$ to be the same as ω_k in Eq. (2.20) by replacing $i'_k = p'$ and $i_k = p$. A schematic diagram of the unitary is shown in Fig. 3.9. We give an example of the circuit realization for Eq. (3.8) and Eq. (3.9) in Section 3.5.2.

Non-abelian quasiparticle strings: By placing one additional qudit at each end of the string operator, we can prepare a length-two non-abelian open string (corresponds to type- s string) similar to the abelian case

$$\left| \begin{array}{c} \text{hexagon} \\ \text{hexagon} \\ \text{hexagon} \end{array} \right\rangle = \sum_{q'_1, q'_2} \frac{v_{q'_1}}{v_{q_1} v_s} F_{s^* q'_1 q'_2}^{e q_2^* q_1} \left| \begin{array}{c} \text{hexagon} \\ \text{hexagon} \\ \text{hexagon} \end{array} \right\rangle. \quad (3.10)$$

This four-qudit unitary uses two ancillary qudits to create a non-abelian string with two qudits along the path. The orange color highlights the qudits that store the ancillary qudit states.

We can further define local unitary to move an existing non-abelian anyon at the endpoints of an open string. A key difference between the non-abelian and the abelian cases is that unitarily encoding non-abelian anyons with open string operators requires an additional ancillary qudit at the endpoint. In order to implement non-abelian strings, we need to ensure the endpoint of the string operator always lands on an edge that has an ancillary qudit. This can be achieved by placing one additional qudit on each edge. Alternatively, we can adapt the following strategy that only requires two additional qudits for implementing one open string operator.

For a given configuration, we first perform a local lattice distortion as shown in Fig. 3.8. Such distortion does not require any physical quantum operation, one can simply register such change, e.g. on a classical computer. This step makes sure the endpoint of the string will land at an edge with two qudits. Following this virtual lattice distortion, we implement a four-qudit unitary that satisfies

$$\left| \begin{array}{c} \text{hexagon} \\ \text{hexagon} \\ \text{hexagon} \end{array} \right\rangle = \omega_{q_1, q_2} \sum_{q'_2} F_{s^* q_1 q'_2}^{e q_3^* q_2} \left| \begin{array}{c} \text{hexagon} \\ \text{hexagon} \\ \text{hexagon} \end{array} \right\rangle. \quad (3.11)$$

The operators for creating and moving the anyons are schematically shown in Fig. 3.10. with a circuit in terms of qudit quantum gates. Notice that a long abelian string costs a constant depth quantum circuit while a linear-depth is required for the non-abelian strings.

3.5. Explicit quantum circuits for the string-net states and their anyons

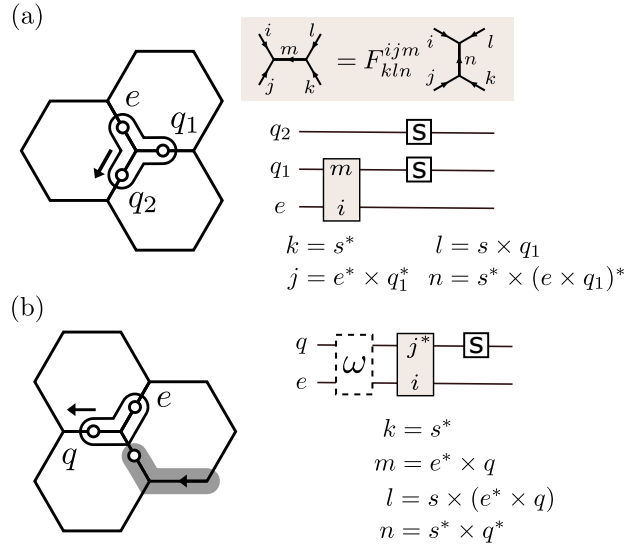


Figure 3.9.: The quantum circuits for abelian open string operators. (a) A circuit realization for preparing abelian anyons. The shaded box shows the F -move defined by the F -symbol in the abelian model, together with the labeling convention for the F -symbol. We define the shaded circuit element to associate the qudit state with an F -symbol phase. This phase is computed based on the F -symbol labels assigned in the circuit diagram (see also the discussion in Section 3.5.2). (b) A circuit realization for moving the abelian anyons by extending the string operator (dark grey).

3.5.2. Quantum circuits for string operators and $C-\hat{B}_p$

In this section, we provide some examples of quantum circuits for the string operators, which also lead to a quantum circuit for the $C-\hat{B}_p$. Since all the open string operators satisfy isometry condition, there are certain degrees of freedom in defining the unitary to realize them. What we show here is one realization of such unitary.

We encode the spin state on each site in a qudit. As a result, the quantum gates become qudit gates in general. For example, we can generalize the two-qubit CNOT gate to two-qudit CNOT by modular arithmetic, i.e. for $(N+1)$ -level qudit, $\text{CNOT}_{\text{qudit}} |a, b\rangle = |a, b+a\rangle$ in mod $N+1$. Another example is the qudit SWAP gate that swaps the two states of two qudits, $\text{SWAP}_{\text{qudit}} |a, b\rangle = |b, a\rangle$. We will use the same circuit symbol for qudit CNOT and SWAP as for qubit CNOT and SWAP. For clarification, let us consider the case for abelian and non-abelian strings separately.

The abelian open string operators (i.e. each non-trivial value in the F -symbol is a phase), such as for the toric code, take a particularly simple form due to the fusion constraints (see Section 2.4). A quantum circuit implementation of a type- s string in terms of qudit gates are shown in Fig. 3.9, where we define the colored circuit element in Fig. 3.9 as a two-qudit gate that associates each state with an F -symbol phase. Explicitly, they map $|eq_1\rangle \rightarrow F_{klm}^{ijn} |eq_1\rangle$ or $|eq\rangle \rightarrow F_{klm}^{ijn} |eq\rangle$ depending on which of two the labels i, j, k, m, n, l in F_{klm}^{ijn} are assigned to the input qudits according to the circuit diagram. The rest of the four unknown labels in the F -symbol are uniquely determined by fusion in the abelian model. The other qudit gates we used can be found in Table. 3.11. In the string preparation stage, we simplify the circuits by removing the phase in Eq. (3.8) as discussed in Section 3.5.1. The string preparation gate thus satisfies $\hat{U}_{\text{prep}}^s |eq_1q_2\rangle = F_{s^*q_1'q_2'}^{eq_2q_1} |eq_1'q_2'\rangle$, which is equivalent to Eq. (3.8) up to an overall phase.

The non-abelian string circuits are shown in Fig. 3.10, where we have used the qudit

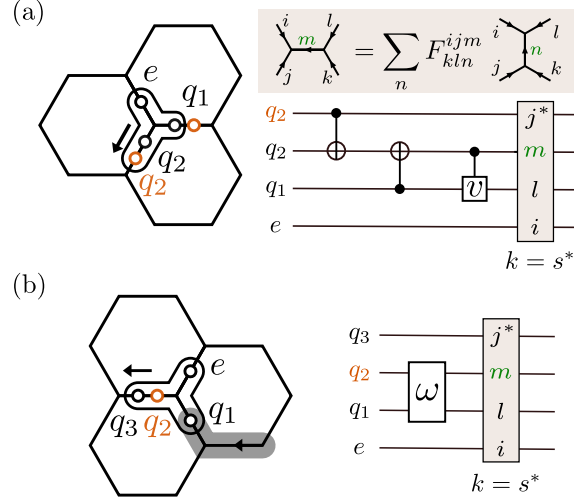


Figure 3.10.: The quantum circuits for the non-abelian open string operators. The orange color highlights the qudits that store the ancillary qudit states. (a) A circuit realization for preparing non-abelian anyons. The shaded box shows the F -move defined by the F -symbol in the non-abelian model, together with the labeling convention for the F -symbol. The shaded circuit elements are qudit quantum gates that perform the F -move. The gates are controlled single-qudit rotations that change the state of the green qudit labeled with m . The gates are controlled by the states of the other input qudits, each of which is assigned with a label in the F -symbol according to the circuit diagram. (b) A circuit realization for moving the non-abelian anyons by extending the open string operator (dark grey).

CNOT introduced above. The colored gate in this case implements the F -move to the state according to the assigned labels in the circuit diagram. Unlike the abelian case, the gate changes the state of the qudit assigned with green label m in Fig. 3.10. The definition for other qudit gates can be found in Table. 3.11.

Next, we use the circuits for the string operators to construct a circuit for the $C-\hat{B}_p$. The controlled gate $C-\hat{B}_p$ can be seen as applying a type- s string operator around the plaquette if the control qudit of the gate (i.e. the representative qudit for the plaquette) is in state $|s\rangle$. It thus follows that we can decompose $C-\hat{B}_p$ into a sequence of local controlled gates that prepare and deform the string operator as in Fig. 3.9 and Fig. 3.10. We show how this can be done for the non-abelian case, the abelian case follows straightforwardly. Note

$ a\rangle \text{---} \boxed{S} \text{---}$	$ a\rangle \rightarrow s \times a\rangle$	$ a\rangle \text{---} \bullet \text{---}$ $ a\rangle \text{---} \boxed{U} \text{---}$	$ a, a\rangle \rightarrow \sum_{a'} \delta_{aa's} \frac{v_{a'}}{v_a v_s} a, a'\rangle$
$ a\rangle \text{---} \times \text{---}$ $ b\rangle \text{---} \times \text{---}$	$ a, b\rangle \rightarrow b, a\rangle$	$ a\rangle \text{---} \text{---} \omega \text{---} \text{---}$ $ b\rangle \text{---} \text{---} \omega \text{---} \text{---}$	$ a, b\rangle \rightarrow \omega_{a \times b^* \times s^*, a^* \times b} a, b\rangle$
$ a\rangle \text{---} \bullet \text{---}$ $ b\rangle \text{---} \oplus \text{---}$	$ a, b\rangle \rightarrow a, b + a\rangle$	$ a\rangle \text{---} \text{---} \omega \text{---} \text{---}$ $ b\rangle \text{---} \text{---} \omega \text{---} \text{---}$	$ a, b\rangle \rightarrow \omega_{b, a} a, b\rangle$

Figure 3.11.: Definition for the qudit gates used in the construction of the open string operators, where s is the label for the corresponding simple string operator. The quantity $\omega_{p', p}$ is the phase ω_k in Eq. (2.20) with $i'_k = p'$ and $i_k = p$, and the orientation is to be identified from the direction of the string operators in the circuit diagrams, such as in Fig. 3.9 and 3.10.

3.5. Explicit quantum circuits for the string-net states and their anyons

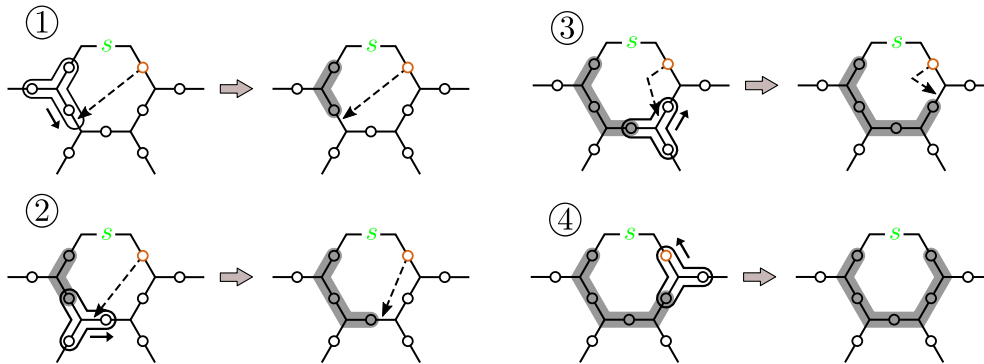


Figure 3.12.: A circuit decomposition for $C\hat{B}_p$ gate using the labeling convention in Eq. (3.12). All the gate operations are controlled by the qudit on the top bond (the green s). The dashed arrows show the virtual location of the ancillary qudit state, which is stored in the initially disentangled qudit (orange) throughout the steps. In step 1, the qudit gate is a qudit CNOT followed by Fig. 3.10a. The CNOT aligns the $|0\rangle$ qudit (orange) with the qudit at the endpoint of the string operator which is to be initialized. In step 2 and 3, the qudit gate is the same as Fig. 3.10b followed by a SWAP gate that keeps the ancillary qudit state in the orange qudit. The step 4 is similar to step 2 and 3, except that we adapt the circuit slightly since no ancillary qudit is required at the last step. The explicit circuit diagrams are given by Fig. 3.13.

that the subspace $C\hat{B}_p$ acts on is

$$\begin{array}{c}
 \begin{array}{ccc}
 & s & \\
 & \downarrow & \\
 |0\rangle & \text{---} & |0\rangle \\
 \uparrow & & \downarrow \\
 e_1 & & e_4 \\
 \downarrow & & \downarrow \\
 i_1 & & i_3 \\
 \downarrow & & \downarrow \\
 e_2 & & e_3 \\
 & & .
 \end{array}
 \end{array}
 \quad (3.12)$$

Our goal is to apply a type- s string operator around the plaquette, where $|s\rangle$ is the state of the control qudit at the top.

A schematic of the circuit is shown in Fig. 3.12. To construct $C\hat{B}_p$, we first initialize a length-two string using the circuits in Fig. 3.10a. In this step, we use one of the initially disentangled qudits, which is chosen to be the one on the right in this example, to store the ancillary qudit state. Next, we extend the string around the plaquette by applying the circuit in Fig. 3.10b followed by a qudit SWAP gate that ensures the ancillary qudit state is always stored in the same qudit throughout. In the last step, the endpoint of the string is going to land at the qudit that stores the ancillary qudit state. We do this with a slight adaptation of the circuit by fixing the state q_3 to $|0\rangle$ in Fig. 3.10b. In other words, since the ancillary qudit is supposed to store the initial state of the endpoint qudit before the string operator is applied, the use of the ancillary qudits becomes unnecessary if that initial qudit is disentangled $|0\rangle$. The resulting explicit circuit diagrams for the decomposition are depicted in Fig. 3.13 for both abelian and non-abelian cases. One can check that for the case $s = 0$, the circuit operates an identity on the input state.

We note that all the qudit gates that implement the corresponding F -symbol can be realized as a multi-controlled qudit gate. The gate applies a single-qudit rotation on the qudit marked by a green label depending on the states of the other qudits. We illustrate this in the next section with an explicit example.

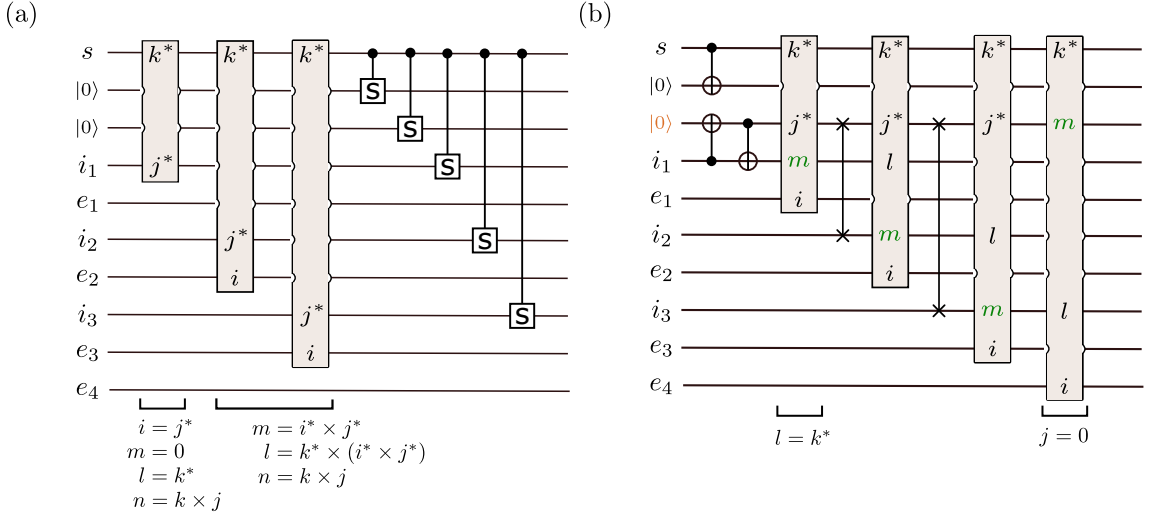


Figure 3.13.: Explicit circuit diagrams for Fig. 3.12. The qudits are labeled by Eq. (3.12). (a) The $C-\hat{B}_p$ for the abelian case. Here we have used the controlled fusion gate C-S, which performs the unitary $C-S|s, i\rangle = |s, s \times i\rangle$. (b) The circuit for the non-abelian case, the qudit used to store the ancillary state is marked orange.

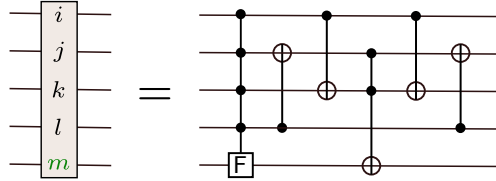


Figure 3.14.: A quantum circuit for the F -symbol given in Ref. [136], where all the gates are qubit gates. Here we have used a four-qubit controlled rotation gate, i.e. a single-qubit rotation is applied to the fifth qubit if the qubits at the solid dots are $|1\rangle$, otherwise no operation will be performed. The single-qubit rotation is defined in Eq. (3.13).

3.5.3. An example: Quantum circuits for double Fibonacci model

The double Fibonacci model is a string-net model that hosts a non-abelian topological order. The model can be defined on a honeycomb lattice with qubit ($|0\rangle$ or $|1\rangle$) correspond to string-0 and string-1) on each site. The strings are unoriented with branching rules given by $\delta_{111} = \delta_{110} = \delta_{000} = 1$. The F -symbol is defined by the Fibonacci unitary tensor category

$$\begin{aligned}
 v_0 &= 1, & v_1 &= \phi^{\frac{1}{2}}, \\
 F_{110}^{111} &= \phi^{-\frac{1}{2}}, & F_{111}^{111} &= -\phi^{-1}, \\
 F_{110}^{110} &= \phi^{-1}, & F_{111}^{110} &= \phi^{-\frac{1}{2}},
 \end{aligned} \tag{3.13}$$

where $\phi = \frac{1+\sqrt{5}}{2}$ is the golden ratio [52]. All the other non-zero values in F -symbol are 1.

As mentioned in the last section, a circuit implementation of the F -move can be realized by a multi-controlled qubit gate. For the double Fibonacci model this gate can be decomposed as shown in Fig. 3.14 [136], where the single-qubit rotation is given by the F -symbol in Eq. (3.13) as $(F)_{ij} = F_{11j}^{11i}$.

We can insert the circuit of the F -move into Fig. 3.10 and 3.13b to obtain a set of circuits that efficiently simulates the double Fibonacci model on a digital quantum computer. Although the circuit has not yet been optimized for practical implementation (this depends on the connectivity of the device), we can still roughly estimate the resources needed for the simulation by counting the number of CNOT gates needed to do a $C\text{-}\hat{B}_p$ and perform an anyon movement. The multi-controlled F gate in Fig. 3.14 can be broken down into 30 CNOT gates [137]. The Toffoli gate can be further decomposed into 6 CNOT gates [138], together with the other 4 CNOT we have 40 CNOT gates in total. For the $C\text{-}\hat{B}_p$ operator in Fig. 3.13b, the first and last F -move unitary can be simplified exploiting the fact that we are not using the full F -symbol. In the first F -move, the four-qubit controlled gate in Fig. 3.14 becomes a three-qubit controlled gate by identifying $l = k$, which can be decomposed into 13 CNOT [137], altogether the first F -move consists of 23 CNOT. Similarly for the last F -move, by setting $j = 0$, the circuit in Fig. 3.14 can be simplified to 8 CNOT. Taking into account these consideration, there are in total 120 CNOT gates (without any circuit optimization).

The counting above does not take into account any circuit parallelization. In practice, many of the gates can be operated in parallel to improve the efficiency, and circuit simplification may be exploited. For example, the continuity of the strings on the subspace in Eq. 3.12 implies $e_1 = i_1$ and $i_3 = e_4$, this can be used to further reduce the number of gates needed in Fig. 3.13.

3.6. Discussion and conclusion

In light of the ground state structure of the string-net models, we develop a set of efficient quantum circuits for preparing the topological string-net states with depth that scales linearly as the minimum width of the system. The implementation offers substantial practical advantages compared to the previously known unitary constructions [117, 129]. The prepared topological states serve as platforms supporting abelian or non-abelian anyons, which are braided by the unitary string operators. Although we focus our discussion on the honeycomb lattice, the implementation of the protocol can easily be run on the heavy-hexagon lattice [139], which is available in current quantum computing platforms. The construction also straightforwardly generalizes to any other 2D trivalent lattices compatible with the architecture of the devices, rendering further reduction on the number of qudits needed. The explicit quantum gates that we use during the construction are local within each plaquette on the lattice (e.g. Fig. 3.3). In practice, the implementation of these gates needs to be optimized based on specific device connectivity, as has been done in Ref. [5] for the square lattice.

The circuit construction can be extended to other topological states or quantum stabilizer codes that share a similar ground state structure. An example is Kitaev's quantum double model [43], which can be defined on any lattice embedded in 2D orientable surface with orthonormal basis $\{|g\rangle | g \in G\}$ labeled by the elements of a finite group G . The Hamiltonian also takes the form as a sum of commuting local projectors on vertices and plaquettes. We can use similar idea to obtain a linear quantum circuit for its ground state with the representative spin in each plaquette initialized as $\frac{1}{|G|} \sum_{g \in G} |g\rangle$. This is not surprising as it is known that quantum double models can be mapped to a subclass of string-net models [140, 141]. The same scheme can also be used to prepare any states that are related to the string-net states by a finite-depth quantum circuit, the corresponding quasiparticle string operators being smeared out with support bounded by the light cone of the finite circuit. The states of this form (often with a finite correlation length) will exhibit the same topological order [93], making them valuable computing resources for the study of correlated quantum many-body physics with controlled quantum systems.

The preparation scheme can be exploited as an efficient generator for a family of 2D quantum datasets on the digital quantum computers. It would be interesting to use these exotic states for benchmarking various protocols where the non-trivial order of the states are relevant. Some examples include quantum phase recognition [142, 143], quantum tomography for weakly entangled states [144–146] or entanglement measurements [106, 147–149], which have so far mostly only been illustrated on 1D cases. These quantum data can also be efficiently generated on a photonic quantum computer [150].

Another exciting direction to be explored is fault-tolerant quantum computation. The circuits realize an efficient unitary encoding of the logical information in planar geometry with suitable boundary conditions, i.e. the surface code protocol [47, 151, 152]. Despite not being intrinsically fault-tolerant, small-scale unitary encoding already provides useful insights into the logical state injection and logical error dynamics [5]. An alternative approach to achieve fault-tolerance is the topological quantum computation (TQC) [113], where logical information is encoded in non-abelian anyons. A key advantage of TQC compared to the surface code protocol is that it allows for *universal* fault-tolerant computation by anyonic braiding. While universal computation is possible in surface code, it requires a costly state distillation process. The unitary quasiparticle string provides a unitary encoding scheme for TQC (e.g. based on Fibonacci anyons). The braiding is accomplished by a sequence of local gates, which can also be used to determine the fusion of the anyons. However, whether all these anyonic operations can be performed fault-tolerantly, e.g., by introducing syndrome measurements [136, 153] or anyon distillation [154], remains an interesting open question for future work.

4. Experimental realization of the \mathbb{Z}_2 toric code ground state on a programmable quantum processor

In the previous chapter, we develop the method for realizing and characterizing the topological order of the string-net states on a digital quantum computer. While the state preparation protocol is efficient (i.e. the circuit depth scales linearly with the system size), it had remained an open question whether this can be achieved experimentally with the currently available quantum devices. In this chapter, we utilize the method from the last chapter and demonstrate the realization of the \mathbb{Z}_2 topologically ordered ground state on a programmable quantum processor. More specifically, we develop an optimized efficient quantum circuit to prepare the toric code ground state on a lattice of 31 superconducting qubits. We then experimentally establish the topological nature of the state by measuring the topological entanglement entropy. By simulating interferometry of toric code excitations, we fully determine their associated braiding statistics. Furthermore, we prepare logical states of the distance-5 surface code on 25 qubits and demonstrate error correction of logical measurements [47, 151]. While a meaningful implementation of active error correction on these states is beyond current experimental capabilities, we realize these states without stabilizer circuitry, providing a scheme to characterize and understand errors of logical qubits.

4.1. Realizing the ground state of the toric code

We realize the toric code ground state, depicted in Fig. 4.1A, by implementing a shallow quantum circuit on a Sycamore quantum processor [37]. The toric code Hamiltonian (see also Section 2.3 for more details)

$$H = - \sum_s A_s - \sum_p B_p \quad (4.1)$$

is defined in terms of qubits living on the edges of a square lattice. The “star” operators $A_s = \prod_{i \in s} Z_i$ are products of Pauli Z operators touching each star (+, blue). The “plaquette” operators $B_p = \prod_{j \in p} X_j$ are products of Pauli X operators on each plaquette (\square , purple). For the boundary conditions shown in Fig. 4.1A, there is a unique toric code ground state $|G\rangle$, with parity +1 for all star and plaquette operators: $A_s |G\rangle = B_p |G\rangle = +1 |G\rangle$.

Rather than realizing the Hamiltonian explicitly, we directly prepare the ground state using the algorithm depicted in Fig. 4.1B. This algorithm is motivated by the observation that the ground state is an equal superposition of all possible “plaquette configurations” and can be written as

$$|G\rangle = \frac{1}{\sqrt{2^{12}}} \prod_p (\mathbb{1} + B_p) |0\rangle^{\otimes 31}, \quad (4.2)$$

where $|0\rangle^{\otimes 31}$ is the product of single-qubit states $|0\rangle$, and the product is over the 12 plaquettes. We begin in the trivial state $|0\rangle^{\otimes 31}$, where all $\langle A_s \rangle = 1$ and $\langle B_p \rangle = 0$. For each plaquette B_p , we perform a Hadamard on the upper qubit, preparing $(|0\rangle + |1\rangle)/\sqrt{2}$,

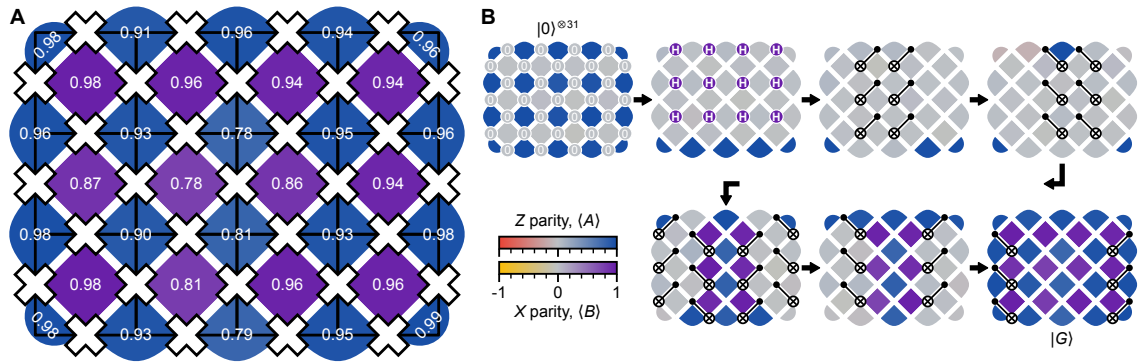


Figure 4.1.: **Toric code ground state.** (A) Experimentally-measured parity values for a 31-qubit lattice in the toric code ground state $|G\rangle$. Qubits (x) are drawn on the standard toric code lattice, touching star (A_s , +, blue tile) and plaquette (B_p , \square , purple tile) operators. We compute each parity from a measured probability distribution (measuring each A_s and B_p separately, 10^4 repetitions), which we correct for readout error using iterative Bayesian methods [155] (see Appendix B2). Mean parity: 0.92 ± 0.06 (1σ). (B) Quantum circuit to prepare $|G\rangle$, with quantum gates superimposed on experimentally-measured parity values following each step. The circuit consists of Hadamard (H) and CNOT gates, which we compile into CZ gates.

and then perform CNOT gates to the other qubits on the plaquette, effectively realizing $\mathbb{I} + B_p$. These operations are carefully ordered, starting in the middle and working outward, to avoid conflict between plaquettes while minimizing circuit depth. The 12 Hadamards create a superposition of 2^{12} bitstrings, and the CNOTs transform each of those bitstrings into a configuration where the Z parity on each star is +1; the final superposition has X parity +1 on each plaquette. This circuit exhibits optimal scaling, with depth *linear* in system width [125], specifically $3 + 2\lfloor(N - 1)/2\rfloor$ nearest-neighbor CNOT layers for a lattice N plaquettes wide.

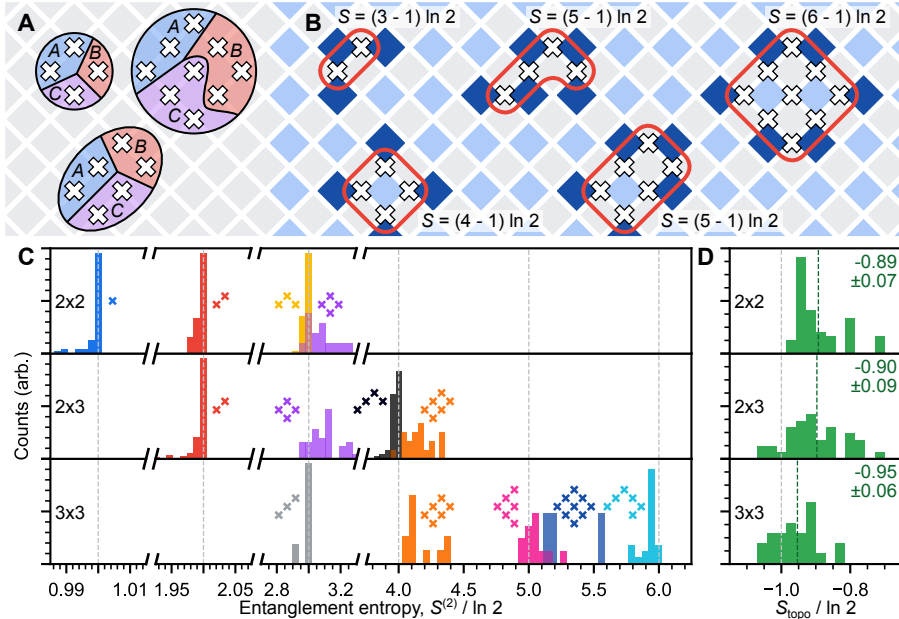


Figure 4.2.: **Topological entanglement entropy.** (A) Schematic identifying the subsystems A , B , and C used to measure topological entanglement entropy S_{topo} on 4-, 6-, and 9-qubit systems within the toric code lattice. (B) Illustration identifying the expected entanglement entropy S for groups of qubits in the toric code. We draw a red perimeter around each group and count the number k of star operators (blue tiles) it crosses. $S = k \ln 2 + S_{\text{topo}} = (k - 1) \ln 2$. (C) Experimental second Rényi entropy $S^{(2)}$ distributions measured on the 31-qubit toric code ground state. There is a histogram for each subsystem shape. Dashed gray lines indicate the predicted integer values for $|G\rangle$. (D) Topological entanglement entropy $S_{\text{topo}}/\ln 2$ (ideal value -1) computed from the entropies in C. We evaluate each dataset in all possible orientations of the subsystems in A (2×2 : 4, 2×3 : 2, 3×3 : 8). Upper right: mean (dark green line) and distribution standard deviation.

4.2. Measuring topological entanglement entropy

The topological entanglement entropy provides a “smoking gun” order parameter for the topological nature of the ground state (see Section 2.1). To extract S_{topo} , a linear combination of subsystem entropies can be constructed such that the local contributions cancel. For the subsystems depicted in Fig. 4.2A,

$$S_{\text{topo}} = S_A + S_B + S_C - S_{AB} - S_{BC} - S_{AC} + S_{ABC}, \quad (4.3)$$

where AB indicates the union of A and B . The structure of toric code eigenstates implies that S_{topo} can be inferred from small subsystems. For the toric code ground state, $S_{\text{topo}} = -\ln 2$, reflecting the total quantum dimension of \mathbb{Z}_2 topological order [156], while $S_{\text{topo}} = 0$ in the absence of topological order.

The structure of the toric code Hamiltonian results in entanglement characterized by integer multiples of $\ln 2$, scaling with the number of star operators A_s intersecting the subsystem boundary [116], as illustrated in in Fig. 4.2B. To compute S_{topo} , one can measure the second Rényi entropy $S^{(2)} = -\ln[\text{Tr}(\rho^2)]$, where ρ is density matrix, for each subsystem in Eq. (4.3). Recently-introduced randomized methods enable efficient measurement of Rényi entanglement entropies, requiring a smaller number of measurements for large subsystems compared to full quantum state tomography [147, 149, 157]. This

enables accurate entropy measurement when tomography is intractable, such as the 9-qubit subsystem in Fig. 4.2A. We apply random single-qubit unitaries to the subsystem of interest and sample the probability distribution of the bitstrings. Analyzing statistical correlations across many random instances allows us to compute the second Rényi entropy. We use an iterative Bayesian scheme [155] to mitigate measurement errors and remove under-sampling bias (see Appendix B3, where we also compare randomized measurement with tomography results).

Figure 4.2C shows distributions of the measured entanglement entropies for subsystems of 2×2 , 2×3 , and 3×3 qubits within the toric code ground state. For a subsystem with n qubits, the entanglement entropy ranges from 0 for a product state up to $n \ln 2$. In the toric code, subsystems with no interior have the maximum value $n \ln 2$; in those cases, we measure a narrow distribution centered just below the ideal value. For subsystems with an interior, we measure a wider distribution centered slightly above the predicted value. This is consistent with unitary error and decoherence slightly mixing the system with its environment, which increases entanglement entropies that are not yet at their maximal value.

We compute S_{topo} from the subsystem entropies using Eq. (4.3) for 14 different 2×2 arrays, 20 different 2×3 arrays, and 3 different 3×3 arrays. Each randomized measurement on the qubit array yields several S_{topo} estimates from different orientations of the partitions A, B, C . Distributions of measured S_{topo} are shown in Figure 4.2D, with mean values $S_{\text{topo}}/\ln 2 = -0.89, -0.90, \text{ and } -0.95$ for the $2 \times 2, 2 \times 3, \text{ and } 3 \times 3$ qubit arrays, respectively. The distributions provide strong evidence for the non-trivial topological nature of the state, closely approaching the ideal value of $S_{\text{topo}} = -\ln 2$, completely distinct from the trivial state value of zero.

4.2.1. Randomized measurement of second Rényi entropy

In this section, we provide further details for the experimental measurement of S_{topo} . Measuring the entropy of a system is experimentally challenging: one often needs the density matrix ρ , from which one can extract the von Neumann entropy

$$S = -\text{Tr} [\rho \ln \rho], \quad (4.4)$$

or n -th order Rényi entropy

$$S^{(n)} = \frac{1}{1-n} \ln (\text{Tr} \rho^n). \quad (4.5)$$

The entropy cannot be measured directly, but can be accessed through quantum state tomography of the density matrix. Full quantum state tomography is resource intensive, with cost typically scaling exponentially with the subsystem size. Moreover, tomography produces a biased estimator [158], which can sometimes be tricky to account for.

The topological entanglement entropy is defined using von Neumann entanglement entropies for the subsystems [100, 101]. In the case of abelian topological order (such as the toric code), the same equation holds when the von Neumann entropies are replaced by second Rényi entropies [103, 104]. This equivalence is helpful when investigating larger system sizes, as we can extract the second Rényi entropies from the statistical correlations of the subsystems using the technique of randomized measurement (RM). A main advantage of this protocol is the direct access to the entropy without reconstructing the full state, significantly reducing the required number of measurements. It also provides a simpler way to remove the bias and understand the statistical errors for the estimation.

4.2. Measuring topological entanglement entropy

The RM protocol measures the second Rényi entropy by using single-qubit random unitary. Consider a subsystem A , whose purity is given by

$$\text{Tr}(\rho_A^2) = 2^{N_A} \sum_{s,s'} (-2)^{-H(s,s')} \overline{P(s)P(s')}, \quad (4.6)$$

where N_A, ρ_A is the number of qubits and the density matrix of A . The average is over the tensor product of single-qubit random unitaries which act on the qubits in A and are independently drawn from the circular unitary ensemble (CUE). s, s' are the binary strings in the computational basis with $H(s, s')$ outputting the hamming distance between them, and $P(s)$ denotes the probability of observing s . The second Rényi entropy is given by $S^{(2)}(\rho_A) = -\ln(\text{Tr}(\rho_A^2))$. A nice feature of the randomized method is that the same set of measurement data can be used to compute the entropies for multiple subsystems at the same time. This renders particular convenience in measuring the S_{topo} , which is inferred from a linear combination of the entropies from different partitions. In the experiment, we only have to measure the entropy of the subsystems themselves, from which S_{topo} can be obtained by calculating all the entropies for different partition using the same data. This avoids having several randomized measurements on the subsystem partitions and the large statistical errors built up from adding and subtracting these independently-measured entropies.

In practice, $P(s)^2$ is a biased estimator for $\mathbb{E}(P(s))^2$ and needs to be replaced with an unbiased estimator

$$P \rightarrow P \times \frac{nP - 1}{n - 1}, \quad (4.7)$$

where n is the number of measurements used to determine $P(s)$ [159]. The random unitaries can be drawn from the continuous (Haar) measure. However, on many current devices it is more desirable to use a given finite set of pre-calibrated quantum gates. This is made possible by approximating the ensemble (up to certain statistical moment) using a unitary 3-design, e.g. the Clifford group [160, 161]. The single-qubit random unitary can be implemented as random single-qubit Clifford gates.

In the setting of RM, averaging over the tensor product of single-qubit Clifford gates is equivalent to averaging over all the Pauli basis measurement [106]. This can be seen by noting the qubit measurement projects the state onto Pauli Z basis, i.e. $|0\rangle\langle 0| = (1 + Z)/2$ and $|1\rangle\langle 1| = (1 - Z)/2$. The single-qubit Clifford gates send the Pauli Z to any other non-identity Pauli gates with equal frequency, $U^\dagger Z U = \pm P$, where $U \in \text{Cliff}(2)$ and $P \in \{X, Y, Z\}$. One can then go back to the Pauli Z basis as in the usual Pauli measurements. The mapping with phase -1 corresponds to a bit-flip when transforming back to the Pauli Z basis. The Hamming prefactor in Eq. (4.6) is preserved under bit-flip on s, s' , hence the equivalence follows.

4.2.2. Error mitigated estimation of the second Renyi entropy

A subtlety arises when applying the error unfolding in RM of the entropy, which is estimated from a list of cross-probabilities $P(s)P(s')$ between two bit-strings s, s' . However, the multinomial nature indicates finite covariance between $P(s)$ and $P(s')$. In other words, the estimation of $P(s)P(s')$ becomes biased:

$$\mathbb{E}[P(s)P(s')] - \mathbb{E}[P(s)]\mathbb{E}[P(s')] = \text{cov}(P(s), P(s')). \quad (4.8)$$

In practice, an unbiased estimator for the cross-probability is used to remove this bias. That only allows us to remove the bias in the estimation based on the observed data, but not the error-mitigated data after the iterative Bayesian unfolding (IBU) [155]. To fix this deficiency, we need to simultaneously unfold the covariance during the iterative steps [162]

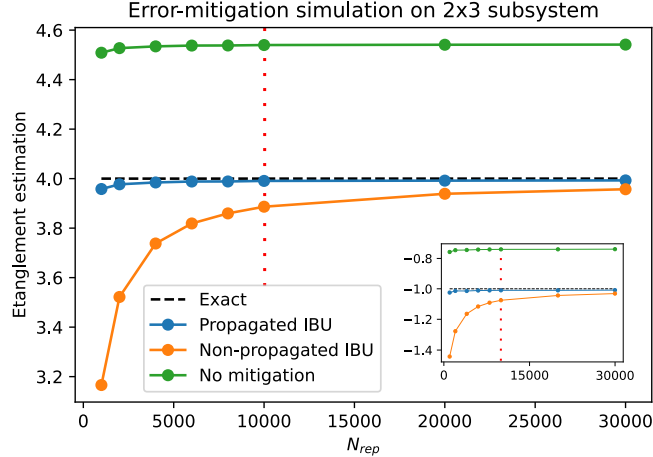


Figure 4.3.: **Classical Monte Carlo simulation of the error-mitigation for a 6-qubit subsystem (2×3 qubit array) in toric code.** Error mitigation can be applied to estimate non-linear quantities like entropy, but the induced bias needs to be removed by error-propagation. Here we show a simulation of entanglement entropy estimation for a 2×3 subsystem, using an uncorrelated noise model ($e_0 = 0.01$, $e_1 = 0.05$). The red dotted line highlights the number of repeated bitstring measurements used in the actual experiment. The inset shows a simulated estimation of $S_{\text{topo}}/\ln 2$.

and use the unfolded covariance to remove the bias in the error-mitigated estimation at the end.

In the experiment, the unfolding and the propagation of the covariance were performed using RooUnfold package [162]. The iterative steps are chosen to be 15, 50 and 50 for the 4-qubit, 6-qubit and 9-qubit systems.

To illustrate the effectiveness of the error-mitigation and the unfolding techniques, we classically simulate the 6-qubit experiment using an uncorrelated readout error model. The model assumes asymmetric error rates $e(0 \rightarrow 1) = 0.01$ and $e(1 \rightarrow 0) = 0.05$ during the readout procedure, while other sources of error such as decoherence and gate error are neglected. The randomized measurements are simulated by drawing sufficiently many single-qubit random unitaries (or equivalently, summing over the full Pauli basis rotations) and repeating the bitstring measurements N_{rep} times for each random unitary instance, where N_{rep} sweeps through a range of possible values. The results are shown in Fig. 4.3. Without taking error-propagation into account, a clear under-sampling bias is induced, where the estimated entropy will strongly depend on N_{rep} . Instead, when the error-propagation is taken into account, the bias is removed, allowing an accurate determination of the entropy for a wide range of bitstring samples N_{rep} .

4.3. Simulating and extracting the anyonic braiding statistics

Our approach of directly preparing the toric code ground state also allows us to simulate the exotic braiding statistics of its quasiparticle excitations (anyons). We utilize a mapping between the adiabatic evolution of toric code excitations and strings of Pauli operators applied to the ground state. With this framing, a controlled Pauli string implements an interferometry protocol through which we experimentally extract the mutual and exchange statistics corresponding to all combinations of excitations.

The quasiparticle excitations of the toric code are commonly denoted as “electric” e with $\langle A_s \rangle = -1$, and “magnetic” m with $\langle B_p \rangle = -1$, in connection to lattice gauge theory. The

4.3. Simulating and extracting the anyonic braiding statistics

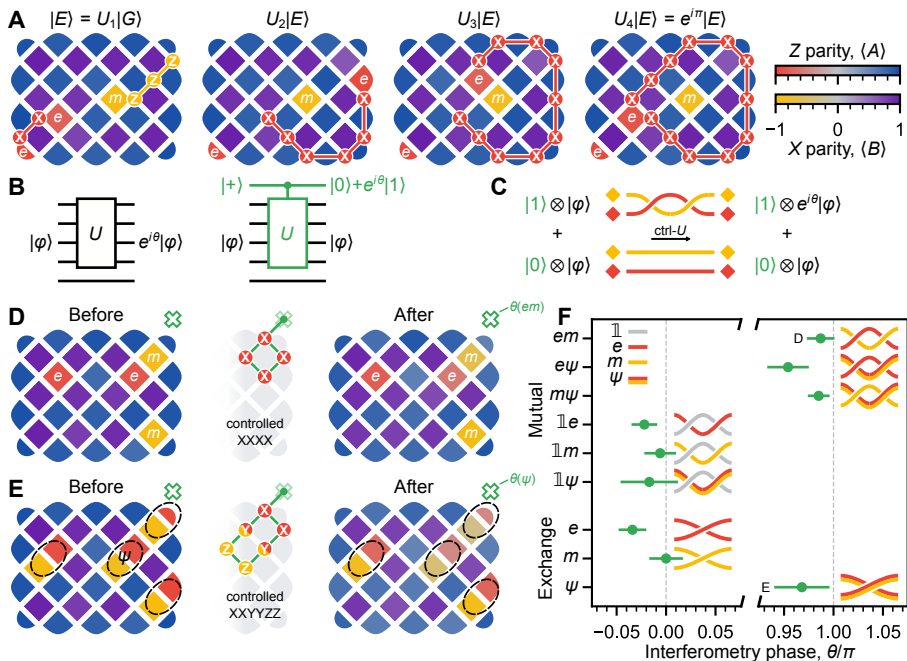


Figure 4.4.: **Extracting braiding statistics using Ramsey interferometry.** (A) Visualizing braiding with a toric code excited state $|E\rangle = U_1|G\rangle$ (excitations e (red) and m (yellow), experimentally-measured parities). We apply additional X gates (U_2, U_3, U_4) to visualize braiding an e around the m . (B) Quantum circuits with unitary U and an eigenstate $|\varphi\rangle$. Left: Direct application. Right: Extracting the phase θ using an auxiliary qubit (green). (C) Illustration of Ramsey interferometry for the case of braiding an e and m (state $|\varphi\rangle$) using an operator U . We visualize the superposition of two paths, with the braid operation U controlled by an auxiliary qubit in $|+\rangle$. (D) Extracting the mutual statistics for e and m . Left: initial excited eigenstate (similar to A). We implement controlled-XXXX with an auxiliary control qubit (green) starting in $|+\rangle$. Right: parity measurements after controlled-XXXX. (E) Extracting the fermion exchange statistics, analogous to D. We create two pairs of ψ (neighboring e and m) and implement controlled-XXYYZZ to measure the exchange phase. (F) Measured mutual and exchange phases, with braiding diagrams. Phases are from tomography on the auxiliary qubit, 18000 total repetitions per compiled instance. Standard error estimated with jackknife re-sampling over instances.

four distinct anyons of the toric code are $\mathbb{1}$ (the absence of an e or m), e , m , and ψ (an emergent fermion resulting from the combination of e and m) (see also Section 2.3). In the toric code, the mutual statistics are encoded in the phase accumulated when dragging one anyon around another anyon of different type, while the exchange statistics are phases arising from spatial interchange of two identical anyons. The toric code excited states can be created by applying a string of Pauli operators to the ground state: an X -string will result in the state with e excitations at each end, while a Z -string prepares the state with m excitations at each end. We visualize an example of $e - m$ mutual braiding in Fig. 4.4A with snapshots of experimentally-measured parity values, $\langle A_s \rangle$ and $\langle B_p \rangle$. We move an e around m with an X -string, eventually returning to its initial position. The initial and final states have the same parity values but differ by an overall phase, in this case π , which is not directly detectable.

To experimentally determine this phase, we employ multi-qubit Ramsey interferometry [110]. This protocol provides a scalable way to measure the overlap between the initial and final states, allowing experimental access to the accumulated phase θ . A key step in this protocol is the use of an auxiliary qubit and a controlled operation, effectively creating a superposition of the braided and non-braided states, as shown in Fig. 4.4B-C. This sequence imparts θ into a measurable rotation of the auxiliary qubit. We efficiently compile the multi-qubit controlled operations into CZ gates. Since the measured phases are sensitive to coherent and non-Markovian errors, we use randomized compiling to mitigate these errors [163]. See Appendix B4 for details.

Fig. 4.4D-E illustrate two examples of braiding interferometry. In Fig. 4.4D, we extract the $e - m$ mutual statistics, where the braiding path is a Pauli string $XXXX$, moving e around the plaquette that contains an m . Fig. 4.4E shows a similar example for the exchange statistics of two identical ψ excitations using a path of intertwining Pauli strings of $XXXX$ and $ZZZZ$, simplifying to $XXYYZZ$ (see Appendix B6 for details). The parity measurements show consistent values before and after the controlled-braiding operation, slightly fading due to decoherence and gate error. We measure the phases for the other mutual and exchange combinations, presenting the results in Fig. 4.4F. The phases are plotted alongside their corresponding braid diagrams, with the expected values 0 and π indicated by dashed gray lines.

Our measurements illuminate the non-trivial mutual and exchange statistics of the toric code. Braiding e around m results in a π phase, which does not occur for local bosons or fermions. Moreover, while e and m both satisfy bosonic exchange statistics, their combination ψ exhibits fermionic exchange statistics. The mutual and exchange statistics of the anyons, conventionally summarized in the modular \mathcal{S} and \mathcal{T} matrices, fully characterize the \mathbb{Z}_2 topological order [156].

Distinct topologically ordered ground states are locally indistinguishable, making them attractive logical qubits due to this immunity to local perturbations. The lattice of Fig. 4.1A has only one ground state under Eq. (4.1), but in Fig. 4.6A we use different boundary conditions where the toric code admits a ground state degeneracy, as proposed for the surface code [45, 46, 152]. We introduce *logical operators* Z_L and X_L which span across the lattice and commute with the Hamiltonian but anti-commute with each other.

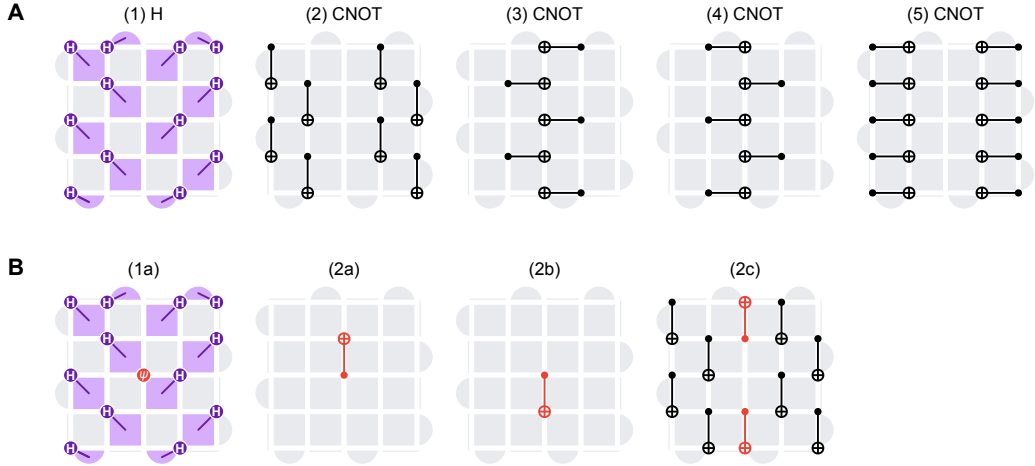


Figure 4.5.: **State preparation and injection circuits for 5×5 logical qubit states (mixed boundary)**. **(A)** Quantum circuit to transform $|0\rangle^{\otimes 25} \rightarrow |0_L\rangle$. This maintains $Z_L = +1$ (see Fig. 4.6A). To prepare $|+_L\rangle$, we rotate the circuit 90° and perform a transversal logical Hadamard at the end. **(B)** To inject an arbitrary logical state $\alpha|0_L\rangle + \beta|1_L\rangle$, we replace steps (1) and (2) from **A**, initializing the center qubit to the desired $|\psi\rangle = \alpha|0\rangle + \beta|1\rangle$.

4.4. Logical state injection and readout

We generalize the state preparation circuit of Fig. 4.1B to create the logical states $|0_L\rangle$ and $|+_L\rangle$, where $Z_L|0_L\rangle = +1|0_L\rangle$ and $X_L|+_L\rangle = +1|+_L\rangle$, on both 5×5 (distance-5) and 3×3 (distance-3) arrays. The explicit quantum circuit for the 5×5 code is shown in Fig. 4.5. The $|0_L\rangle$ and $|+_L\rangle$ preparations are closely related, connected by a logical Hadamard. We then use the logical operators, which are simply products of single-qubit gates, to realize $|1_L\rangle = X_L|0_L\rangle$ and $|-_L\rangle = Z_L|+_L\rangle$. See Appendix B1 for details on state preparation and logical operations.

The logical states are resilient to local errors, which we demonstrate with logical measurement with error correction, shown in Fig. 4.6B. Following surface code proposals, we perform a logical measurement by projectively measuring all the qubits in Z or X basis (for Z_L or X_L , respectively). Naively evaluating the parity of the logical operator is vulnerable to errors on any qubit along the operator, but errors can be detected by also evaluating the local parities (A_s or B_p) from the individual qubit measurements. By construction, we expect the local parities to be $+1$, so any -1 values indicate nearby errors. We find a minimal set of qubits to flip in order to recover $+1$ parities before evaluating the logical operator. This correction decreases the logical error significantly. Averaging logical preparation and measurement error over X_L and Z_L eigenstates, without correction, we observe 0.17 for distance-5 and 0.090 for distance-3, while with correction, we observe 0.030 for both, lower than the average physical qubit preparation and measurement error, 0.034. This is a simplified form of error correction compared to the repetitive stabilizer measurements of surface code proposals, where parity changes are matched together over space and time.

The logical subspace also admits arbitrary superposition states $\alpha|0_L\rangle + \beta|1_L\rangle$, which we realize with *state injection*, encoding a single physical qubit state into the logical qubit. For 5×5 state injection, we prepare the central qubit in $\alpha|0\rangle + \beta|1\rangle$ and then create a GHZ-like state $(\alpha\mathbb{1} + \beta X_L)|0\rangle^{\otimes 25}$ using three CZ layers. The toric code preparation circuit maps $|0\rangle^{\otimes 25} \rightarrow |0_L\rangle$ and $X_L|0\rangle^{\otimes 25} \rightarrow |1_L\rangle$, giving $\alpha|0_L\rangle + \beta|1_L\rangle$. For example, the states

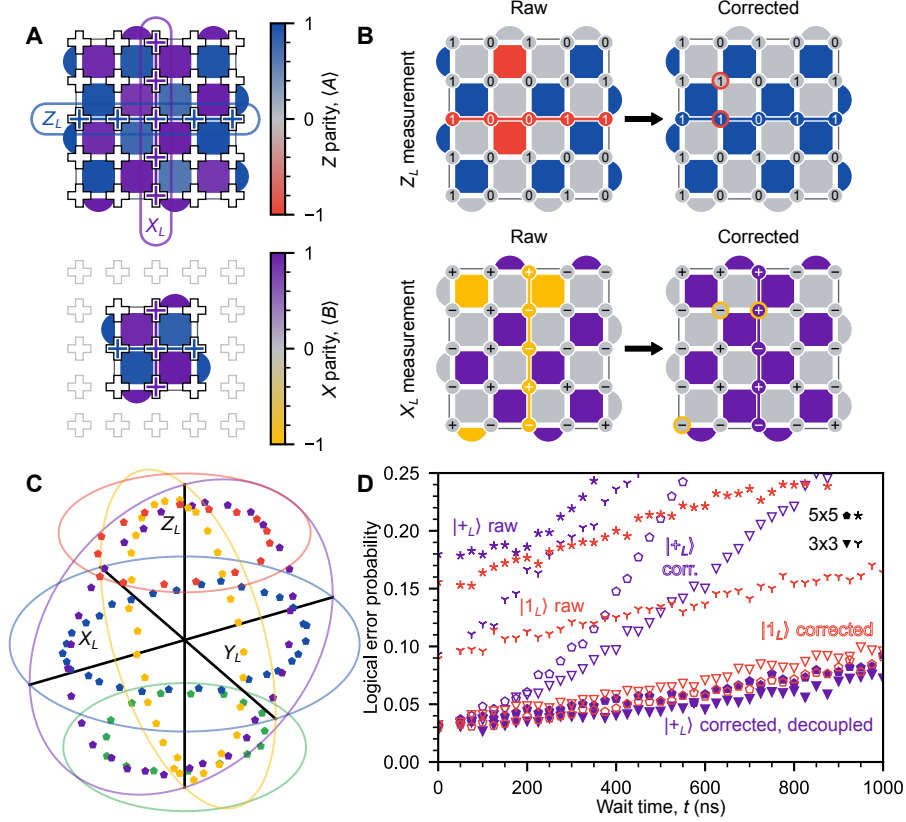


Figure 4.6.: **Surface code logical qubit states.** (A) Measured parity values for surface code logical qubit states $|T_L\rangle = (|0_L\rangle + e^{i\pi/4}|1_L\rangle)/\sqrt{2}$ on 5×5 and 3×3 qubit arrays. Logical operators Z_L and X_L span across each array. (B) Logical measurement with error correction. We measure a 25-qubit bitstring in X or Z basis and evaluate the local parities of the same basis. Negative parities indicate an error. We flip the circled qubits to restore positive parities. (C) Experimental logical qubit tomography immediately after state injection for 128 states (sweeping the initial state of the center qubit $|\alpha\rangle + |\beta\rangle$), plotted in the Bloch sphere (5×5). The ideal states lie on five planes: $x = 0$ (yellow), $y = 0$ (purple), $z = 1/\sqrt{2}$ (red), $z = 0$ (blue), $z = -1/\sqrt{2}$ (green). Mean Bloch vector length: 0.6 ± 0.1 (1σ). (D) We prepare logical states, wait for a time t , and then perform a logical measurement. We compare logical measurements for $|1_L\rangle$ (red) and $|+_L\rangle$ (purple), for both 5×5 (5-sided markers) and 3×3 (3-sided markers) states. Star markers: raw measurements. Hollow markers: corrected measurements. Filled markers: corrected measurements with dynamical decoupling during the wait time ($|+_L\rangle$ only, see main text). Each logical measurement uses 10^4 repetitions.

depicted in Fig. 4.6A are logical T states $|T_L\rangle = (|0_L\rangle + e^{i\pi/4}|1_L\rangle)/\sqrt{2}$, of interest for non-Clifford operations. We characterize injected states using logical tomography. Measuring Z_L and X_L is straightforward and robust, as discussed above. We measure Y_L by performing another logical gate, $X_L^{1/2} = (\mathbb{1} - iX_L)/\sqrt{2}$, decomposed into five CZ layers, and then measuring Z_L . We plot the resultant Bloch vectors for 128 injected states across the Bloch sphere in Fig. 4.6C. By measuring these non-local order parameters, we illuminate the logical degree of freedom that was invisible to the local parity measurements of Fig. 4.6A. Note that, in contrast to surface code proposals, our state preparation methods are not fault tolerant, though in principle states prepared in this way can be further

purified by distillation [47, 164, 165].

Finally, we investigate decoherence of Z_L and X_L eigenstates by plotting logical error versus wait time t in Fig. 4.6D. We reiterate the importance of measurement error correction by comparing raw and corrected data. Note that while distance-5 has significantly worse raw error, after correction it is modestly better than distance-3 for $|1_L\rangle$. However, observe that $|+_L\rangle$ decays much more quickly than $|1_L\rangle$, due to its sensitivity to Z errors (dephasing). We dynamically decouple the qubits from low-frequency noise with a simple sequence executing an X gate on each qubit at $t/4$ and $3t/4$, which brings $|+_L\rangle$ error slightly below $|1_L\rangle$ error, with distance-3 remaining slightly lower-error. $|1_L\rangle$ and $|0_L\rangle$ are not appreciably affected by this dynamical decoupling (see Appendix B5). Overall, the logical error increases linearly at 0.06 per microsecond. For active error correction with the surface code, we expect a few percent logical error per cycle at threshold [151]. Typical cycle durations are hundreds of nanoseconds [166], where the logical state suffers the decoherence studied here as well as gate errors, suggesting continued efforts to decrease the cycle duration and improve coherence.

4.5. Discussion and conclusion

In this chapter, we presented the results on the realization of the 31-qubit toric code ground state on the Google Sycamore quantum processor. We benchmarked the quality of the prepared ground state by measuring the stabilizer values on the ground state. We then provided strong evidence of the topological nature of the prepared ground state by performing, to our knowledge, one of the first direct measurements of the topological entanglement entropy of the state. Using the high-quality topological state, we further explored the error-correcting aspects of the surface code, including logical state injection and logical information readout. Our results not only represent a significant advance in the field of quantum simulation of topological phases of matter, it also sheds light into the future development of quantum error correction.

The experimental method employed can be used to realize more general topological ground states, including the string-net states as shown in the last chapter. Recently, the theoretical method has been used to successfully demonstrate the non-abelian anyonic braiding [68] and non-abelian ground states of the double Fibonacci model [69]. The quasi-static protocol using controlled Pauli strings to simulate braiding can be generalized to dynamical adiabatic braiding [167] by using deeper circuits in future devices. By encoding quantum information in the degenerate ground state manifold of the toric code, we provide a method for studying coherence properties of logical qubit states. This method could be used to identify and mitigate noise correlations in the system, with critical implications for future error correction experiments.

Part II.

Detecting quantum phases of
matter on digital quantum
computers

Overview of Part II

In Part I of the thesis, we discussed and presented the results on the realization of specific fixed-point ground states of gapped topological phases and the topological nature of the states is probed by measuring their topological entanglement entropy, which provides an order parameter for the topological phases. However, the measurement scheme used for the topological entanglement entropy is not scalable. i.e. the number of measurement samples required to achieve a given accuracy grows exponentially with the system size. This poses a significant challenge in characterizing the prepared topological ground states in large-scale experiments. An interesting and important question is thus whether there exist other order parameters for topological phases of matter that can be efficiently measured.

In Part II, we investigate the question within the framework of quantum machine learning. In Chapter 5, we propose a method to discover suitable order parameters by training a quantum convolutional neural network in a model-independent way. We demonstrate the effectiveness of the method on a few 1D quantum phases of matter. The method can also be easily extended to higher dimensional systems. This chapter is based on the publication [2]. At the end of the chapter, we also briefly comment on the possibility of using the framework of quantum error correction to detect emergent 1-form symmetries and 2D topological quantum phase transitions. This is a work under preparation (in collaboration with Wen-Tao Xu, Michael Knap and Frank Pollmann), in which we numerically benchmark the approach and demonstrate its success in the well-known phase diagram of the 2D toric code subject to both longitudinal and transverse fields.

5. Quantum convolutional neural networks and quantum phase classifications

A good idea has a way of becoming simpler and solving problems other than that for which it was intended.

Robert Tarjan

Phases of matter are traditionally identified by measuring order parameters, including local order parameters for symmetry-breaking phases, string order parameters for one-dimensional symmetry-protected topological (SPT) phases [13, 15, 168–171], or the topological entanglement entropy for topologically ordered systems in 2D as discussed in Chapter 2. Finding a suitable string order parameter can be difficult in general, in particular, without the presence of additional symmetries [172]. Nonetheless, non-local order parameters, utilizing multiple copies of the system, can directly extract the topological invariant of one-dimensional (1D) SPT phases for global symmetries [172, 173]. They can also be probed by randomized measurements [174] at a cost that scales exponentially with the subsystem size of interest.

Recently, classical and quantum machine learning approaches have been introduced to tackle the task of quantum phase classification; see e.g. Refs. [142, 175–182]. Quantum circuit classifiers, such as quantum convolutional neural networks (QCNNs) [142], as demonstrated experimentally in Ref. [183], naturally provide a quantum machine learning architecture to learn observables for the classification of phases. One advantage of these classifiers is, that the learned observable can be efficiently measured on a quantum device. Thus, an interesting question is to study whether a quantum machine learning approach, such as the training of a QCNN, can automate the discovery of (non-local) order parameters that characterize the phases and are efficient to measure experimentally. The training of a quantum classifier faces challenges. For example, a large amount of labelled training data, in the form of ground states, is needed. These states could be obtained by adiabatic [184, 185] or variational algorithms [186, 187]. However, the generation of a large amount of ground states can become infeasible, in particular, for noisy intermediate scale quantum devices. Another prominent obstacle is vulnerability or over-fitting of the QCNN, caused by training on a specific class of ground states.

In this chapter, we propose a model-independent quantum protocol for training QCNNs using minimal information about the gapped quantum phases, which includes the fixed-point wavefunctions and the symmetry group of the system [93, 94]. We train the QCNN with synthetic training data by first constructing the fixed-point wavefunctions, which are typically efficiently prepared [12, 71], and then apply a finite number of layers of random symmetric local gates. Each layer is translationally invariant and independently sampled. Randomness helps prevent the QCNN from learning local (non-universal) properties of the states by masking the local structure of the fixed-point. We will focus on quantum phases of matter in 1D, but the approach is applicable to finding order parameters for quantum phases in higher dimensions.

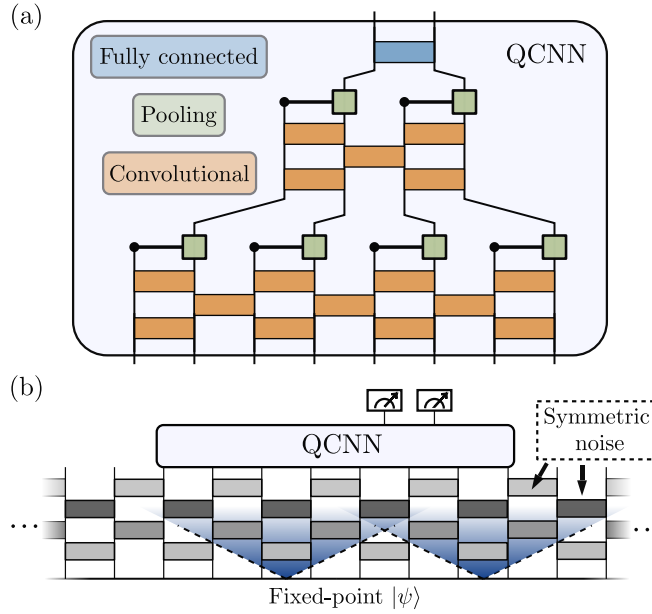


Figure 5.1.: Architecture of an 8-qubit QCNN and training data. (a) The QCNN consists of three building blocks [142]. Convolutional layers consist of two-qubit gates (orange). The pooling is achieved by a set of controlled rotations (green). The gates in the pooling and the convolutional layers can be either translation-invariant or independently parametrized. The fully connected layer in this case is a two-qubit gate (blue). (b) Random local symmetric two-qubit gates create finite correlations that mask the microscopic details of the state. In the shown example, four layers of symmetric noise ($L_{\text{noise}} = 4$) are applied to a fixed-point in the thermodynamic limit. Each layer is translationally invariant and independently sampled.

5.1. Quantum convolutional neural networks and the problem setup

The architecture of QCNNs consists of convolutional, pooling, and fully-connected layers [142], as shown in Fig. 5.1a. Each convolutional layer is a finite-depth circuit of local unitary gates. The pooling layer is a set of parallel controlled single-qubit rotations, where the control qubits are discarded. During the training, the controlled rotations can be absorbed into the convolutional layer. Originally, the unitary gates on the same circuit layer were chosen to be identical everywhere [142]. Besides this uniform ansatz, we also investigate independently parametrized gates. Despite having an extensive number of free parameters, and hence an increase in the difficulty of training, both the uniform and the generalized QCNN are barren-plateau free [188]. Before the readout, a fully connected layer “summarizes” the information into the measured qubits. This layer is a multi-qubit gate that acts on all the qubits at the final level of the network.

Here, we focus on 1D systems and consider the following task: Suppose we have M phases protected by a symmetry group G and a set $\Psi_G = \{|\psi_1\rangle, \dots, |\psi_M\rangle\}$, where each $|\psi_m\rangle \in \Psi_G$ is a fixed-point wavefunction for each phase under the real-space renormalization group flow [12, 71–74]. We aim to find a QCNN that predicts the phase of any input ground state $|\psi\rangle$ of a symmetric Hamiltonian.

We tackle the classification task by training an N -qubit QCNN that acts on an infinite system (Fig. 5.1b). We choose the number of readout qubits at the fully connected layer to be $\lceil \log_2 M \rceil$ and associate each phase with a bitstring label $s \in \{1, 2, \dots, M\}$. The

5.2. Model-independent training of QCNN for 1D quantum phases of matter

probability for each bitstring $|s\rangle$ is interpreted as the QCNN's confidence score for that phase, and the prediction is the phase with the largest probability. A quantum phase transition is marked by the change of the label with the highest probability. This contrasts the original QCNN considered in Ref. [142], which produces an order parameter that vanishes for one phase and is non-zero for the other phases.

5.2. Model-independent training of QCNN for 1D quantum phases of matter

To train an N -qubit QCNN, we use the stability of the quantum phases under finite-depth symmetric quantum circuits. Two ground states $|\psi_1\rangle, |\psi_2\rangle$ belong to the same phase if and only if they are related by a finite-depth local quantum circuit $|\psi_1\rangle \sim \prod_k \hat{U}^{(k)} |\psi_2\rangle$, where $\hat{U} = \prod_k \hat{U}^{(k)}$ is a product of layers of local unitaries that can be continuously connected to the identity [93, 94]. When the system has certain symmetries, \hat{U} needs to be symmetric as well.

We generate the training data with the following steps (sketched in Fig. 5.1b):

1. Randomly pick a label $m \in \{1, \dots, M\}$ and prepare the fixed-point wavefunction $|\psi_m\rangle \in \Psi_G$.
2. Apply L_{noise} layers of random symmetric local two-qubit gates, for $L_{\text{noise}} < N/2$.

The requirement of $L_{\text{noise}} < N/2$ comes from the finite size of the QCNN. Namely, if the correlation length created by the noise becomes comparable to the QCNN's size, the phases are no longer distinguishable by the QCNN. In practice, we first train the QCNN with a single layer of noise then increase the number of layers one-by-one as we achieve convergence. We continue until test accuracy falls below a threshold. We restrict ourselves to the simplest case of two-qubit gates for the noise. However, the scheme can be easily generalized to symmetric gates that act on more qubits.

5.3. Recognizing time-reversal symmetric quantum phases in 1D

To investigate the effectiveness of the protocol, we consider classification of gapped phases of 1D translationally invariant spin-1/2 chains with time-reversal symmetry generated by $T = (\prod_i X_i) K$, where X is the Pauli- X matrix and K is complex conjugation. We focus on the cases where the translation symmetry is not spontaneously broken. The system hosts three phases [15, 171]: (i) The symmetry-breaking (SB) phase, where T is spontaneously broken and the system has degenerate ground states; (ii) the trivial phase; and (iii) the SPT phase. In the thermodynamic limit, the ground state is unique for (ii) and (iii), but T is fractionalized trivially and non-trivially, respectively. A fixed-point wavefunction can be found for each phase

$$\begin{aligned} |\psi_{\text{SB}}\rangle &= \frac{1}{\sqrt{2}} (|\cdots 000 \cdots\rangle + |\cdots 111 \cdots\rangle), \\ |\psi_{\text{Trivial}}\rangle &= |\cdots + + + \cdots\rangle, \quad |\psi_{\text{SPT}}\rangle = |CS\rangle, \end{aligned} \quad (5.1)$$

where the basis $Z|0\rangle = |0\rangle, Z|1\rangle = -|1\rangle$ is used, and $|+\rangle = (|0\rangle + |1\rangle)/\sqrt{2}$. The state $|CS\rangle$ is the cluster state satisfying $Z_{i-1} X_i Z_{i+1} |CS\rangle = -|CS\rangle, \forall i$. The set of time-reversal symmetric two-qubit unitary gates that continuously connects to the identity forms a Lie group Q generated by the set of Pauli strings $P = \{iZ_1, iZ_2, iZ_1Y_2, iY_1Z_2, iZ_1X_2, iX_1Z_2\}$.

In Section 5.5, we prove that the QCNN that we aim to find does not exist without imposing translational invariance (TI), or other additional symmetries, on the input data. However, when we impose TI, there exists a set of observables that can be used to perfectly identify the phases in the thermodynamic limit (see Section 5.5.5 for details). Therefore, a QCNN for TI input states may be found and the prediction of the phase is obtained by applying a low-depth quantum circuit followed by local bitstring measurements.

In principle we allow TI for arbitrary size unit cells. Here, we impose TI with a two-site unit cell by using a single two-qubit gate per layer, which is repeated across the system, see Fig. 5.1b. The two-qubit gate is parametrized as $\exp(\sum_k \theta_k P_k)$, where $P_k \in P$, the set of generators for the symmetric noise, and each θ_k is randomly sampled from a uniform distribution. In the following, we will focus on the QCNN in which every gate is independently parametrized. To classify the three phases, the prediction is made by measuring two qubits at the end of the QCNN circuit. We assign labels to each bitstring output: 00 \rightarrow Trivial, 01 \rightarrow SB and 10 \rightarrow SPT. The bitstring 11 corresponds to an unsuccessful classification.

5.3.1. Training of the QCNN

We focus on a QCNN that acts on N qubits with $N = 4$ or 8 (see Fig. 5.1). During the training, the pooling layers are absorbed into the two-qubit gates at the end of the convolutional layers. A two-qubit gate is a 4×4 unitary parametrized by 15 parameters as $\exp\left(-\frac{i}{2} \sum_{\rho, \gamma \in \{0,1,2,3\}} \theta_{\rho, \gamma} \hat{O}^\rho \otimes \hat{O}^\gamma\right)$, with the matrices $\hat{O}^0 = \mathbf{I}$, $\hat{O}^1 = X$, $\hat{O}^2 = Y$ and $\hat{O}^3 = Z$. We set $\theta_{0,0} = 0$ to fix the phase degree of freedom of the gate.

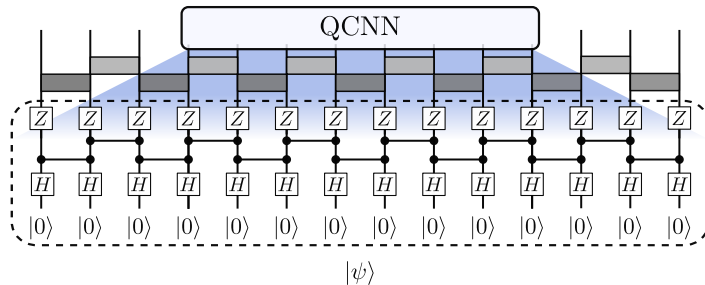


Figure 5.2.: To simulate an N -site QCNN with $N = 8$ and $L_{\text{noise}} = 2$, we use a 14-qubit system with the QCNN acting on the middle 8 qubits. This avoids the finite-size effects. The absence of the finite-size effects can be checked for the input fixed-point function, e.g. $|CS\rangle$ with $Z_{i-1}X_iZ_{i+1} = -|CS\rangle$ in the bulk as shown. The H -gate is the Hadamard gate and the line connected by two dots is the controlled- Z gate. The other fixed-point wavefunctions used in the work can also be verified to have no finite-size effects for the chosen QCNN.

We train the QCNN based on a log-softmax cross entropy loss function. Given a batch of $|B|$ input states and their labels $B = \{(\mathbf{p}, l)\}$, the loss function for the batch is defined by

$$L(B) = -\frac{1}{|B|} \sum_{(\mathbf{p}, l) \in B} \log \left(\frac{e^{Cp_l}}{\sum_j e^{Cp_j}} \right). \quad (5.2)$$

In the above equation, p_j is the j^{th} probability from the output bitstring distribution \mathbf{p} , C is a constant used to set the desired scale of probability difference between different labels. In our experiments, we set $C = 50$. Suppose the symmetric local unitary is generated by some Pauli strings P_k such that the unitary is parametrized as $\exp(\sum_k \theta_k P_k)$ for some $\theta_k \in \mathbb{R}$. We sample the symmetric unitary by uniformly sampling $\theta_k \in (-\pi, \pi]$.

5.3. Recognizing time-reversal symmetric quantum phases in 1D

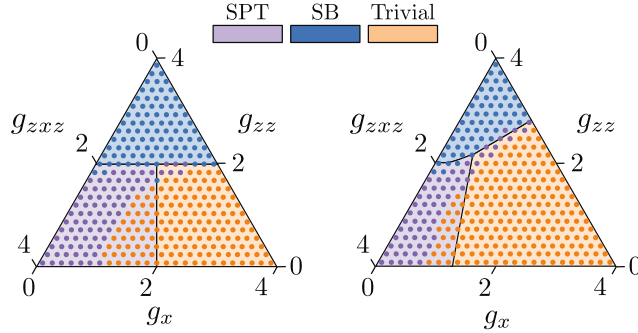


Figure 5.3.: Prediction of the phase diagram of the cluster-Ising model H_{CI} based on the 4-qubit QCNN (filled circles); see Eq. (5.3). The background and the boundaries are the theoretical phase diagram solved analytically. The right hand side shows the prediction on a perturbed cluster-Ising Hamiltonian. The theoretical phase diagram is obtained by an iDMRG algorithm.

To implement the proposed protocol, we generate the training data for each phase by applying $L_{\text{noise}} = 1$ or $L_{\text{noise}} = 2$ layers of random symmetric two-qubit unitary to a fixed-point wavefunction of the phase. The training is done as follows: we start with $L_{\text{noise}} = 1$ until we have reached 100% test accuracy and we use the output QCNN to continue the training on data with $L_{\text{noise}} = 2$. The optimization is performed using Adam optimizer [189], with a learning rate of 5×10^{-4} for $L_{\text{noise}} = 1$ and 1×10^{-4} for $L_{\text{noise}} = 2$. To ensure convergence, for each training session of the 4-qubit (8-qubit) QCNN we generate 30000 (60000) samples for training and 1000 samples for testing. The batch size is 30 (50) and the number of epochs is chosen to be at most 12000. Note that we have not optimized the choice of the training sample size here. We expect much fewer training samples can be used to produce less optimal, yet reasonable results.

In the simulation, we simulate the application of an N -qubit QCNN to an infinite system by including $L_{\text{noise}} + 1$ more qubits on the left and right of an N -qubit system, respectively. In total, the system contains $N + 2(L_{\text{noise}} + 1)$ qubits. An example of $N = 8$ and $L_{\text{noise}} = 2$ is depicted in Fig. 5.2, the system consists of 14 qubits in total. The QCNN only acts on the middle 8 qubits, such that any expectation values evaluated within these 8 qubits are the same as the expectation values evaluated in an infinite system. We can verify this with the circuit generating the cluster state as shown in Fig. 5.2.

The trained QCNN is tested on 10^5 synthetic data constructed with different L_{noise} to obtain a final test accuracy. We first train a 4-qubit QCNN. The test accuracy reached by the 4-qubit QCNN is 87.21% on the test data generated with $L_{\text{noise}} = 1$. This means that the 4-qubit QCNN is not able to perfectly distinguish the phases of a 4-qubit subsystem when the correlation length of the system is roughly two sites. For an 8-qubit QCNN, the performance is drastically improved and attains a test accuracy of 100% on engineered data with $L_{\text{noise}} = 1$ and of 97.37% on data with $L_{\text{noise}} = 2$.

In Appendix C, we also examine the ansatz with uniformly parametrized gates within the 8-qubit QCNN, which achieves similar performance to the non-uniform ansatz when increasing the depth of the convolutional layer from 3 to 5 in Fig. 5.1a. Despite the deeper circuit, the uniform ansatz has fewer free parameters.

5.3.2. Testing of the trained QCNN on physical ground states

We now test the trained QCNN on different time-reversal symmetric physical models.

We first consider a cluster-Ising model [143, 190, 191] where the phases are protected by

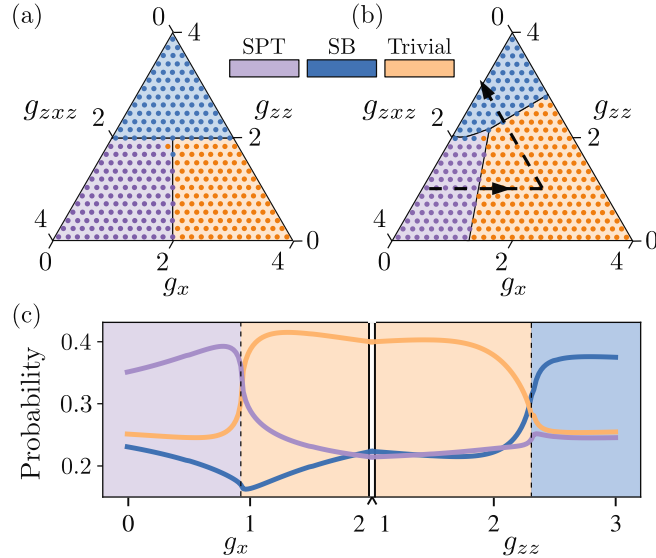


Figure 5.4.: (a) Prediction using the 8-qubit QCNN (b) QCNN prediction (filled circles) obtained for a perturbed cluster-Ising model H_{pCI} . (c) A zoom-in along the cut of the perturbed phase diagram in (b) indicated by the black dashed line. The QCNN prediction corresponds to the solid lines. The dashed vertical lines mark the location of the critical points predicted by iDMRG.

time-reversal symmetry $T = (\prod_i X_i) K$. The Hamiltonian of the system is

$$H_{CI} = g_{zxz} \sum_i Z_{i-1} X_i Z_{i+1} - g_{zz} \sum_i Z_i Z_{i+1} - g_x \sum_i X_i, \quad (5.3)$$

where $g_{zxz}, g_{zz}, g_x \geq 0$. Depending on the couplings, the symmetry protects three distinct phases—the trivial, the SB and the SPT phase. We test the QCNN over the phase diagram of H_{CI} in Eq. (5.3). We do this by first finding the ground states of H_{CI} using an infinite density matrix renormalization group algorithm (iDMRG) [32, 192], which are then input to the QCNN for classification.

We first show the results using the 4-qubit QCNN in Fig. 5.3. The background color marks the theoretical prediction, while the colored circles show the QCNN prediction. The theoretical phase diagram is obtained by mapping H_{CI} to a free-fermion chain [191]. As we can see, near the fixed points where the correlation length of the system is small, the QCNN does a good job. The prediction becomes incorrect quickly when approaching the phase boundaries. To test robustness, we add a perturbation $H_{pCI} = H_{CI} - g_x \sum_i X_i X_{i+1}$ that breaks the free-fermion mapping of the chain. The prediction of the same QCNN is shown in Fig. 5.3. In this case, the theoretical phase diagram is obtained by a transfer-matrix approach [172] based on iDMRG. The trivial phase is expanded in parameter space due to the additional coupling. The results based on the 8-qubit QCNN are shown in Fig. 5.4a. We see that the 8-qubit QCNN accurately predicts the phase diagram compared to the 4-qubit case. For the perturbed cluster-Ising model, the trained 8-qubit QCNN again accurately predicts the shifted phase boundary as shown in Fig. 5.4b. To take a closer look, in Fig. 5.4c we show the probability for the three phases given by the QCNN along a particular cut in the phase diagram (the black, dashed path with arrows in Fig. 5.4b).

The cluster-Ising model has the special property that the phase diagram contains the fixed-point wavefunctions Eq. (5.1), when only one of g_{zxz}, g_{zz}, g_x is non-zero. We remove this property by applying the trained 8-qubit QCNN to four additional time-reversal symmetric physical models that are previously unseen by the network.

5.3. Recognizing time-reversal symmetric quantum phases in 1D

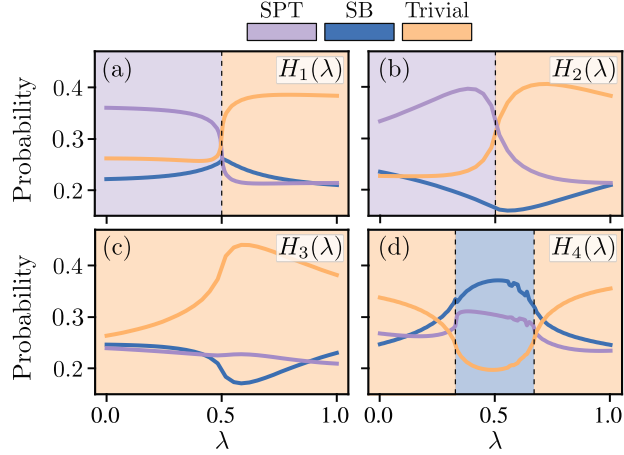


Figure 5.5.: QCNN prediction on various microscopic models. In (a) and (b), a transition between an SPT and the trivial phase is detected at $\lambda = 1/2$. (c) The system is predicted to lie entirely in the trivial phase. A phase transition protected by a different symmetry occurs at $\lambda = 1/2$. (d) The bond-alternating Heisenberg model for $\Delta = 4$. The antiferromagnetic order is correctly detected by the QCNN. Details can be found in the text.

To start, we consider a cluster model with a Y field, namely $H_1 = (1-\lambda) \sum_i Z_{i-1} X_i Z_{i+1} - \lambda \sum_i Y_i$. The model has a transition from the SPT phase to the trivial phase at $\lambda = 1/2$, which is accurately captured by the QCNN as shown in Fig. 5.5a. Similarly, we consider $H_2 = (1-\lambda) \sum_i Z_{i-1} Y_i Z_{i+1} - \lambda \sum_i Y_i$ with a modified cluster coupling term. The transition at $\lambda = 1/2$ is also identified by the QCNN as shown in Fig. 5.5b.

Next, we consider $H_3 = (1-\lambda) \sum_i X_{i-1} Y_i X_{i+1} + \lambda \sum_i Y_i$. This Hamiltonian illustrates an intricate example where the correlation length diverges at $\lambda = 1/2$, but the system never leaves the trivial phase with respect to the T symmetry. As shown in Fig. 5.5c, the QCNN trained based on the representation T correctly predicts the phase diagram. We emphasize that the system also has another time-reversal symmetry represented by $T' = (\prod_i Z_i) K$ which is responsible for a phase transition at $\lambda = 1/2$: Under T' , the system belongs to distinct phases for $\lambda > 1/2$ and $\lambda < 1/2$. Such a transition can be captured if the QCNN is trained based on the representation T' . This can be easily verified by noting H_2 , where the distinct phases are identified by the QCNN, is related to H_3 by a basis transformation.

The last example we consider is $H_4 = (1-\lambda) \sum_i H_{2i}^{\text{bond}} + \lambda \sum_i H_{2i+1}^{\text{bond}}$, describing an antiferromagnetic alternating-bond Heisenberg model. We denote the XXZ-coupling on each bond as $H_{2i}^{\text{bond}} = X_{2i} X_{2i+1} + Y_{2i} Y_{2i+1} + \Delta Z_{2i} Z_{2i+1}$. At the limit $\lambda = 0$ and $\lambda = 1$, the system is in two different dimerized states. Interestingly, the system has a time-reversal symmetry represented by an effective spin-1 π -rotation around the y -axis in the bulk followed by a complex conjugation [191], which protects the two dimerized limits as distinct phases. However, under the symmetry representation T , the two dimerized limits can be continuously connected without a phase transition and they both belong to the trivial phase (see Appendix C for more details). For sufficiently strong Δ , the model exhibits an antiferromagnetic ordering at intermediate λ . In Fig. 5.5d we show the case of $\Delta = 4$, exhibiting an intermediate SB phase in the vicinity of $\lambda = 1/2$. We note that the transition points predicted by the QCNN are slightly shifted away from the iDMRG phase boundary. This is reasonable given the relatively large correlation length near the phase boundary, which the 8-qubit QCNN cannot fully accommodate.

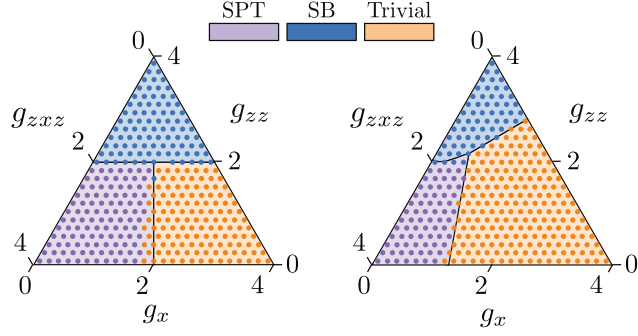


Figure 5.6.: Comparing the theoretical phase diagram and the phase diagram predicted by the 4-qubit QCNN trained based on $\mathbb{Z}_2 \times \mathbb{Z}_2^T$ symmetry.

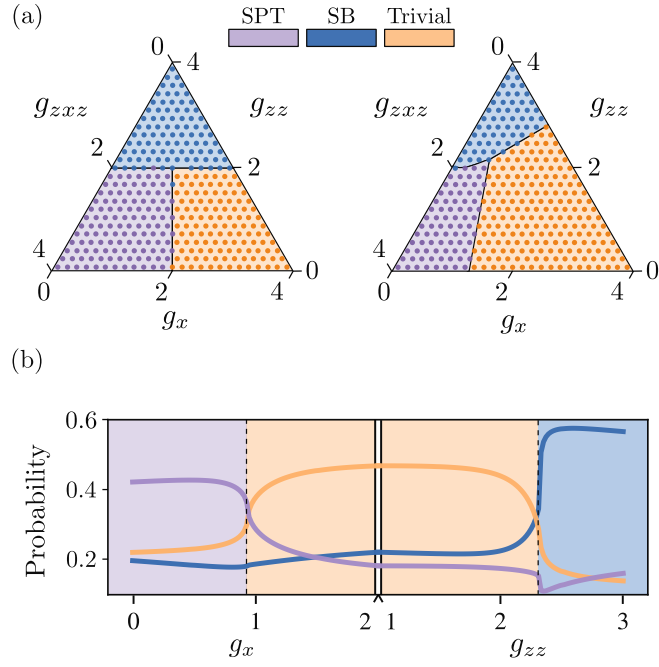


Figure 5.7.: The 8-qubit QCNN trained based on $\mathbb{Z}_2 \times \mathbb{Z}_2^T$ symmetry. Panel (b) shows the probability along the same path as in Fig. 5.4b.

5.4. Recognizing 1D $\mathbb{Z}_2 \times \mathbb{Z}_2^T$ symmetric quantum phases

The protocol we propose can be applied to generic 1D symmetric quantum phases (with additional symmetries, such as TI). The set of local symmetric unitary gates for a given symmetry representation forms a unitary Lie group and can be found by identifying all the symmetric generators of the group (see Appendix C). For example, the cluster-Ising model is also protected by a $\mathbb{Z}_2 \times \mathbb{Z}_2^T$ symmetry, i.e. the set of symmetries $\{I, \prod_i X_i, K, (\prod_i X_i) K\}$, where I is the identity. The symmetric two-qubit unitary is generated by iZ_1Y_2 and iY_1Z_2 . Using the fixed-points Eq. (5.1), we can also train a QCNN that accurately characterizes the cluster-Ising model.

We use the three fixed points provided in Section 5.3. Since $T \in \mathbb{Z}_2 \times \mathbb{Z}_2^T$, the system has more disconnected phases due to a larger symmetry group. Note that, by using only three fixed points, we restrict to the phases that contain the fixed points, which only cover a subset of all the phases protected by the symmetry (with TI). Unlike the time-reversal case, we found the training in this case converges much quicker. We do not need to split the entire training into sessions with different L_{noise} . Instead, we directly train on the data

5.5. Non-existence of QCNN solution under random noise without additional symmetries

with the prescribed L_{noise} . We used a training sample size of 30000 and a batch size of 30. Therefore, even though more fixed-points are required to fully cover all the phases, imposing more symmetry can simplify the training process.

In this case, the symmetric local unitary is generated by the Pauli strings iZ_1Y_2 and iY_1Z_2 . We first train a 4-qubit QCNN. The 4-qubit QCNN reaches a test accuracy of 99.98% for $L_{\text{noise}} = 1$. In Fig. 5.6, we show the phase diagram prediction similar to Fig. 5.4a and 5.4b using the 4-qubit QCNN. We see the QCNN does a nice job away from the phase boundary. Near the phase boundary, the QCNN again suffers from the large correlation length of the system and is less accurate.

Next, we train an 8-qubit QCNN and the QCNN reaches a test accuracy of 100% for both $L_{\text{noise}} = 1$ and 2. For $L_{\text{noise}} = 3$, the QCNN is not perfect and achieves 99.93% test accuracy. The phase diagram prediction is shown in Fig. 5.7. Compared to the 4-qubit case, we see that the 8-qubit QCNN indeed improves significantly. Near the phase boundary, the 8-qubit QCNN is able to distinguish the phases accurately.

The non-existence of a QCNN without additional symmetries, such as TI, can also be proven for 1D systems with $\mathbb{Z}_2 \times \mathbb{Z}_2^T$ or $\mathbb{Z}_2 \times \mathbb{Z}_2$ symmetry (see Section 5.5). The requirement of additional symmetries is thus potentially applicable to the classification task of general symmetric phases.

5.5. Non-existence of QCNN solution under random noise without additional symmetries

In this section, we prove three non-existence results for classifying phases with physical observables when no additional symmetries are present. This provides a theoretical support for imposing translational invariance (TI) on the training data as in Section 5.3. For systems with time-reversal symmetry only, we prove a non-existence result for a phase-classifying observable. We also prove that in general no QCNNs can classify systems with $\mathbb{Z}_2 \times \mathbb{Z}_2^T$ or $\mathbb{Z}_2 \times \mathbb{Z}_2$ symmetry, where \mathbb{Z}_2^T is an anti-unitary order-2 group.

Proposition 1. *Let $U \subseteq \mathbb{C}_{N \times N}$ be a compact unitary group and C_U be the centralizer of U in $\mathbb{C}_{N \times N}$. If $C_U \subseteq \{\lambda I | \lambda \in \mathbb{C}\}$, then for any $M \in \mathbb{C}_{N \times N}$*

$$\mathbf{E}_{\mu(u)} uMu^\dagger = \frac{\text{Tr}(M)}{N} I. \quad (5.4)$$

where the average is taken over the Haar measure μ of U .

Proof. We make use of the Haar integration. We have

$$A = \mathbf{E}_{\mu(u)} uMu^\dagger = \int uMu^\dagger d\mu(u). \quad (5.5)$$

Consider any $v \in U$, we have $vAv^\dagger = A$ based on the invariance of Haar integration. So $A \in C_U$ is proportional to the identity. Taking the trace on Eq. (5.5), we get $\text{Tr}(A) = \text{Tr}(M)$. Knowing that the matrix is $N \times N$, we have $A = \frac{\text{Tr}(M)}{N} I$. \square

Proposition 2. *Given two n -qubit states $|\psi_a\rangle, |\psi_b\rangle$, there does not exist an operator \hat{O} such that $\langle \phi | \hat{O} | \phi \rangle > 0, \forall |\phi\rangle \in S_a$ and $\langle \phi | \hat{O} | \phi \rangle \leq 0, \forall |\phi\rangle \in S_b$. The sets are defined as $S_a = \{u_1 \otimes u_2 \otimes \dots \otimes u_m |\psi_a\rangle | u_i \in U\}$ and $S_b = \{u_1 \otimes u_2 \otimes \dots \otimes u_m |\psi_b\rangle | u_i \in U\}$, where U is a compact group of unitary operators that act on k qubits and has the centralizer $C_U \subseteq \{\lambda I | \lambda \in \mathbb{C}\}$ and $mk = n$.*

Proof. The proof is adapted from Lemma 9 in Ref [180], by combining it with the Proposition 1. We elaborate the idea here. The result is established by contradiction. Suppose an operator \hat{O} exists for S_a and S_b such that $\langle \phi | \hat{O} | \phi \rangle > 0, \forall |\phi\rangle \in S_a$ and $\langle \phi | \hat{O} | \phi \rangle \leq 0, \forall |\phi\rangle \in S_b$. Next, we average over the Haar measure μ of U . From Proposition 1 this yields

$$\mathbf{E}_{\mu(u)} u_1^\dagger \otimes u_2^\dagger \otimes \cdots \otimes u_m^\dagger \hat{O} u_1 \otimes u_2 \otimes \cdots \otimes u_m = \frac{\text{Tr } \hat{O}}{2^n} I. \quad (5.6)$$

This follows by decomposing \hat{O} into a linear combination of the basis operators, each of which is a tensor product of local operators supported on each qubit. Note that for an operator \hat{o} , we can always define a basis in the Hilbert space such that $\hat{o} = \sum_{ij} o_{ij} |i\rangle\langle j|$ and o_{ij} is a matrix representation of \hat{o} , for which Proposition 1 applies. Since Haar integration is a linear map, Proposition 1 can be applied on each basis operator. Now we can define

$$o_a := \text{Inf}\{\langle \phi | \hat{O} | \phi \rangle \mid |\phi\rangle \in S_a\}, \quad (5.7)$$

$$o_b := \text{Sup}\{\langle \phi | \hat{O} | \phi \rangle \mid |\phi\rangle \in S_b\}. \quad (5.8)$$

Note that U is compact and therefore closed. Hence, the infimum and supremum can be attained by some elements in S_a and S_b , respectively. By definition, for $|\psi_a\rangle \in S_a$ and $|\psi_b\rangle \in S_b$ we have

$$\frac{\text{Tr } \hat{O}}{2^n} = \mathbf{E}_{\mu(u)} \langle \psi_a | u_1^\dagger \otimes u_2^\dagger \otimes \cdots \otimes u_m^\dagger \hat{O} u_1 \otimes u_2 \otimes \cdots \otimes u_m | \psi_a \rangle \geq o_a, \quad (5.9)$$

$$\frac{\text{Tr } \hat{O}}{2^n} = \mathbf{E}_{\mu(u)} \langle \psi_b | u_1^\dagger \otimes u_2^\dagger \otimes \cdots \otimes u_m^\dagger \hat{O} u_1 \otimes u_2 \otimes \cdots \otimes u_m | \psi_b \rangle \leq o_b. \quad (5.10)$$

Now since $o_a > 0$ and $o_b \leq 0$ by the assumption, we arrive at a contradiction that $\frac{\text{Tr } \hat{O}}{2^n} \leq o_b < o_a \leq \frac{\text{Tr } \hat{O}}{2^n}$. \square

5.5.1. Non-existence result for \mathbb{Z}_2^T symmetry

Lemma 1. Consider a time-reversal symmetry represented by $\prod_i X_i K$ and two n -qubit states $|\psi_a\rangle, |\psi_b\rangle$, there exists no operator \hat{O} such that $\langle \phi | \hat{O} | \phi \rangle > 0 \forall |\phi\rangle \in S_a$ and $\langle \phi | \hat{O} | \phi \rangle \leq 0 \forall |\phi\rangle \in S_b$, for the set $S_a = \{u_1 \otimes u_2 \otimes \cdots \otimes u_m | \psi_a\rangle \mid u_i \in Q\}$ and the set $S_b = \{u_1 \otimes u_2 \otimes \cdots \otimes u_m | \psi_b\rangle \mid u_i \in Q\}$, where u_i acts on neighboring two qubits and $n = 2m$ and Q is a symmetric unitary Lie group generated by $P = \{iZ_1, iZ_2, iZ_1Y_2, iY_1Z_2, iZ_1X_2, iX_1Z_2\}$.

Proof. Let $A \in \mathbb{C}_{4 \times 4}$, note that A commutes with all the elements of Q if and only if $[A, p] = 0 \forall p \in P$. Since A can be decomposed into a linear combination of $\sigma_1 \sigma_2$, with $\sigma_1, \sigma_2 \in \{I, X, Y, Z\}$. We first consider $p = iZ_1$ and iZ_2 . Commuting with Pauli- Z on two sites individually implies A is a linear combination of $I, Z_1, Z_2, Z_1 Z_2$. Since A also commutes with $Y_1 Z_2$ and $Z_1 Y_2$, A has to be proportional to the identity. Then by Proposition 2 we finish the proof. \square

If we consider any two states in the set of three fixed points considered in Section 5.3, Lemma 1 implies there exists no QCNN that can be used to classify the time-reversal symmetric phases. We now proceed to prove non-existence results for phases protected by $\mathbb{Z}_2 \times \mathbb{Z}_2^T$ and $\mathbb{Z}_2 \times \mathbb{Z}_2$ using a similar idea.

5.5.2. Non-existence result for $\mathbb{Z}_2 \times \mathbb{Z}_2^T$ symmetry

We first prove a non-existence result for distinguishing the SPT and the SB phases in systems protected by the symmetry $\mathbb{Z}_2 \times \mathbb{Z}_2^T$ generated via a global spin flip and the complex conjugation. More precisely, we have the following

5.5. Non-existence of QCNN solution under random noise without additional symmetries

Lemma 2. *Let $|\psi\rangle, |\psi'\rangle \in \{|\psi_{SB}\rangle, |\psi_{SPT}\rangle\}$ as defined in Section 5.3 and $|\psi\rangle \neq |\psi'\rangle$. Consider the set $S = \{u_1 \otimes u_2 \otimes \cdots \otimes u_m |\psi\rangle | u_i \in U\}$ and $S' = \{u_1 \otimes u_2 \otimes \cdots \otimes u_m |\psi'\rangle | u_i \in U\}$, where u_i acts on neighboring three qubits and $n = 3m$. U is a unitary Lie group generated by all the 3-qubit Pauli strings symmetric under $\mathbb{Z}_2 \times \mathbb{Z}_2^T$ symmetry generated by the global spin flip and complex conjugation. There does not exist an operator \hat{O} such that $\langle \phi | \hat{O} | \phi \rangle > 0 \forall |\phi\rangle \in S$ and $\langle \phi | \hat{O} | \phi \rangle \leq 0 \forall |\phi\rangle \in S'$. Furthermore, there does not exist a Hermitian operator \hat{D} with $\text{Tr} \hat{D} = 0$ and the number of supported qubits $n_{\hat{D}} < n$ such that $\langle \phi | \hat{D} | \phi \rangle \neq 0 \forall |\phi\rangle \in S$ or $\forall |\phi\rangle \in S'$.*

Proof. We use a similar idea of the proofs from above. Again we will establish the proof by contradiction. To prove the first statement, we suppose such \hat{O} exists.

Let U be the Lie group generated by all the anti-Hermitian Pauli matrices symmetric under $\mathbb{Z}_2 \times \mathbb{Z}_2^T$, namely up to permutation we have $iXYZ, iYZX, \dots$ and $iZYI, iZIY, \dots$. Since U is a compact Lie group, for any 8×8 complex matrix M we can define

$$A = \int u M u^\dagger d\mu(u), \quad (5.11)$$

where μ is the Haar measure of U . Consequently, $[A, u] = 0$ for $u \in U$. This is true if and only if A commutes with all the generators of U , which implies

$$A = c_0 I + c_1 X_1 X_2 X_3, \quad (5.12)$$

for some $c_0, c_1 \in \mathbb{C}$. Next, we consider the average

$$\hat{O}' = \mathbf{E}_{\mu(u)} u_1 \otimes u_2 \otimes \cdots \otimes u_m \hat{O} u_1^\dagger \otimes u_2^\dagger \otimes \cdots \otimes u_m^\dagger. \quad (5.13)$$

\hat{O} can be decomposed into a sum of at most 4^n Pauli strings. From Eq. (5.12) we deduce that \hat{O}' is a linear combination of Pauli strings of I or X . We note that any Pauli strings of I and X evaluate to the same value in $|\psi_{SPT}\rangle$ and $|\psi_{SB}\rangle$, so $\langle \psi_{SPT} | \hat{O}' | \psi_{SPT} \rangle = \langle \psi_{SB} | \hat{O}' | \psi_{SB} \rangle$. We can now apply exactly the same reasoning as in the proof of Proposition 2 to prove the first statement in the lemma.

Next we assume there exists an operator \hat{D} with $\text{Tr} \hat{D} = 0$ and the number of supported qubits $n_{\hat{D}} < n$ such that $\langle \phi | \hat{D} | \phi \rangle \neq 0 \forall |\phi\rangle \in S$ or $\forall |\phi\rangle \in S'$. Since $\text{Tr} \hat{D} = 0$ implies its Haar average \hat{D}' satisfies $\text{Tr} \hat{D}' = 0$. \hat{D}' is either 0 or consists of Pauli strings that have at least one X . Now knowing the support of \hat{D}' is smaller than the total number of qubits in the system, we have $\langle \psi_{SPT} | \hat{D}' | \psi_{SPT} \rangle = \langle \psi_{SB} | \hat{D}' | \psi_{SB} \rangle = 0$.

Finally, we note that U is connected and $\langle \phi | \hat{D} | \phi \rangle$ is real-valued, it follows that there exists some $u_1 \otimes u_2 \otimes \cdots \otimes u_m$ that attains the mean value, resulting in a contradiction since there is some $|\phi\rangle \in S$ and S' such that $\langle \phi | \hat{D} | \phi \rangle = 0$. \square

The lemma suggests that there exists no QCNN we can use to distinguish or recognize the SPT and the SB phases protected by $\mathbb{Z}_2 \times \mathbb{Z}_2^T$. Note that the requirement $\text{Tr} \hat{D} = 0$ is easy to meet. Since we can always remove the trace of an operator by redefining $\hat{D} - \frac{\text{Tr} \hat{D}}{2^n} I$. The identity shift will not be relevant to characterize different phases if $\text{Tr} \hat{D} / 2^n \rightarrow 0$ happens faster than $\langle \hat{D} \rangle \rightarrow 0$ as $n_{\hat{D}} \rightarrow \infty$. For the QCNN, we can distinguish the phases by choosing \hat{D} to be the observable $\hat{D} = \hat{U}(|s\rangle\langle s| - |s'\rangle\langle s'|)\hat{U}^\dagger$ for bitstrings s, s' , where \hat{U} is the QCNN circuit. We automatically have $\text{Tr} \hat{D} = 0$.

5.5.3. Non-existence result for $\mathbb{Z}_2 \times \mathbb{Z}_2$ symmetry

We proceed to the case of $\mathbb{Z}_2 \times \mathbb{Z}_2$, generated by the spin flip on the even and the odd sites in the system. Note that the cluster state $|\psi_{SPT}\rangle$ we defined in the Section 5.3 has an SPT order under the symmetry. We prove that a QCNN cannot recognize the SPT phase if no other symmetries are present.

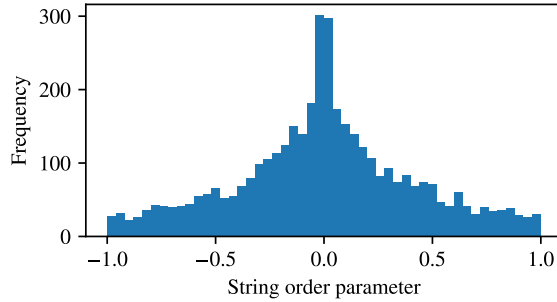


Figure 5.8.: A histogram that shows the evaluation of a string order parameter

$Z_1 Y_2 \left(\prod_{i=3}^{i=6} X_i \right) Y_7 Z_8$ on a cluster state subject to two layers of $\mathbb{Z}_2 \times \mathbb{Z}_2^T$ symmetric noise. A total of 4000 samples are taken.

Lemma 3. *Let $|\psi_{\text{SPT}}\rangle$ be the n -qubit cluster state. Consider the set $S = \{u_1 \otimes u_2 \otimes \cdots \otimes u_m |\psi_{\text{SPT}}\rangle |u_i \in U\}$, where u_i acts on neighboring two qubits and $n = 2m$. The group $U = \{e^{i\alpha I + i\beta X_1 + i\gamma X_2 + i\delta X_1 X_2} | \alpha, \beta, \gamma, \delta \in \mathbb{R}\}$ is symmetric under $\mathbb{Z}_2 \times \mathbb{Z}_2$ symmetry generated by spin flip on even/odd sites. There does not exist a Hermitian operator \hat{O} with $\text{Tr} \hat{O} = 0$ and the number of supported qubits $n_{\hat{O}} < n/2$ such that $\langle \phi | \hat{O} | \phi \rangle \neq 0 \forall |\phi\rangle \in S$.*

Proof. The proof is basically the same as Lemma 2. We prove by contradiction. Suppose such \hat{O} exists.

Since U is a compact Lie group, for any 4×4 complex matrix M we can define $A = \int u M u^\dagger d\mu(u)$, where μ is the Haar measure of U . Consequently, $[A, u] = 0$ for $u \in U$. This implies

$$A = c_0 I + c_1 X_1 + c_2 X_2 + c_3 X_1 X_2, \quad (5.14)$$

for some $c_0, c_1, c_2, c_3 \in \mathbb{C}$. Next, we define $\hat{O}' = \mathbf{E}_{\mu(u)} u_1 \otimes u_2 \otimes \cdots \otimes u_m \hat{O} u_1^\dagger \otimes u_2^\dagger \otimes \cdots \otimes u_m^\dagger$.

Again, we can decompose \hat{O} in the basis of $4^{n_{\hat{O}}}$ Pauli strings. From Eq. (5.14), we deduce that \hat{O}' is a linear combination of Pauli strings of I or X . Since $\text{Tr} \hat{O} = 0$ implies $\text{Tr} \hat{O}' = 0$, \hat{O}' contains Pauli strings that have at least one X . Now knowing the support of \hat{O}' is smaller than half the total number of qubits in the system, the Pauli strings do not contain any symmetry of the system (i.e. $\mathbb{Z}_2 \times \mathbb{Z}_2$). When they are applied to $|\psi_{\text{SPT}}\rangle$, the resulting state necessarily violates at least one of the cluster couplings so that $\hat{O}' |\psi_{\text{SPT}}\rangle$ is a linear combination of excited states for the cluster Hamiltonian and orthogonal to $|\psi_{\text{SPT}}\rangle$, we have $\langle \psi_{\text{SPT}} | \hat{O}' | \psi_{\text{SPT}} \rangle = 0$. Using the connectedness of U and knowing $\langle \phi | \hat{O} | \phi \rangle$ is real-valued, we know there exists some $u_1 \otimes u_2 \otimes \cdots \otimes u_m$ that attains the mean value, resulting in a contradiction, in that there is some $|\phi\rangle \in S$ such that $\langle \phi | \hat{O} | \phi \rangle = 0$. \square

5.5.4. Interpretation of the Lemmas for string order parameters

In this section, we clarify how to interpret the lemmas we prove in the context of physical observables. The lemmas show that an observable that perfectly classifies the phases cannot exist in general without additional symmetries such as translational invariance. This forms a non-existence result for an observable that extracts the topological invariant of the phases (without utilizing multiple copies of the system). However, the statement can be overly restrictive in the context of string order parameters.

The lemma says that there does not exist a string order parameter that is zero, say in phase A and strictly non-zero in a different phase B , i.e. there always exist some states in phase B where the string order parameter is zero. The set of states in phase B that have identically zero string order is measure-zero. This is because the vanishing of a string

5.5. Non-existence of QCNN solution under random noise without additional symmetries

order parameter relies on a set of selection rules [172] when the system is in phase A . Without the selection rules a string order parameter is generically non-zero. To verify this, we consider a cluster state at the thermodynamic limit and apply two layers of $\mathbb{Z}_2 \times \mathbb{Z}_2^T$ symmetric noise (each two-qubit gate is sampled as in one of the previous sections, but each two-qubit gate within a noise layer is now independently sampled). A string order parameter $Z_1 Y_2 \left(\prod_{i=3}^{i=6} X_i \right) Y_7 Z_8$ of length 8 is then measured. Without any noise, the string order parameter attains +1 at the cluster state. With the noise, the string order parameter can attain any values between +1 and -1, as shown in Fig. 5.8. In particular, only for some instances the string order parameter is strictly zero in noisy cluster states. Moreover, due to the randomness of the noise, the average string order parameter is zero. However, the variance of it remains finite in the noisy cluster state.

This suggests that a string order parameter can still be used to classify phases in practice, up to a small fraction of states whose string order is vanishingly small (e.g. the ones near the center of Fig. 5.8).

It is worth noting that, even though a string order parameter may exist and work well, we can neither directly use the string order to construct a cost function for optimization of a QCNN nor it is obvious how a QCNN that is linear in its input state and makes prediction based on a majority vote among the final measurement outcomes could reproduce the behavior of the string order parameter. An exception will be the existence of a string order that is zero in one phase and always non-negative (zero is only attained on a measure-zero set) in the other phase. However, this is excluded by the non-existence results we proved. When TI is enforced, it might be possible to find such string order parameters for unitary on-site symmetries. In this case, QCNNs that learn them could exist. However, finding a string order parameter is not so simple for SPTs protected only by time-reversal symmetry. In the next section we will show that, for both unitary on-site symmetries and (antiunitary) time-reversal symmetry, there exists a more complicated non-local order parameter and it detects the topological invariant of the SPTs (e.g. it yields +1/-1 in different phases). Therefore, a QCNN can in principle be found.

5.5.5. Circumventing the non-existence results

In Section 5.3, we claim that imposing a translational symmetry in addition to the time-reversal symmetry allows one to avoid the non-existence result by Lemma 1. To see this, let us first consider the case between the trivial and the SPT phases. Suppose A, B are two disjoint connected subregions in the unique ground state of a local and gapped 1D Hamiltonian. If A, B are separated from each other further than the correlation length of the system, the reduced density matrix satisfies $\rho_{AB} \approx \rho_A \otimes \rho_B$. In TI system, we can choose the two separated regions to be identical copies. In Ref. [172], an order parameter that dictates the topological invariants and requires two copies of the state is proposed for time-reversal systems: it attains different signs for the trivial and the SPT phases, and it vanishes in the SB phases. We can therefore use it for the phase classification task, as subsystems A and B serve as two copies of each other. A schematic diagram of this TI order parameter is shown in Fig. 5.9a. In the case of the SB phases, we can always find a local field Δ_i such that $\langle \psi | \Delta_i | \psi \rangle \neq 0$ ($\langle \psi | \Delta_i | \psi \rangle = 0$) if $|\psi\rangle$ breaks (respects) the symmetry. For TI-SB systems, the phase can be probed by a non-zero value of $\Delta_i \Delta_{i+L}$, which vanishes in the trivial and the SPT phases for $L \rightarrow \infty$. The same observable can also be used to avoid the non-existence results in Lemma 2 for $\mathbb{Z}_2 \times \mathbb{Z}_2^T$ with TI. While the observable constructed above has $\text{Tr} \hat{O} \neq 0$ in general, by enlarging the SWAP operator sequence in Fig. 5.9a, we can always define it in a way such that $\text{Tr} \hat{O}/2^n \rightarrow 0$ happens exponentially faster than $\langle \hat{O} \rangle \rightarrow 0$ when it is evaluated on either SPT or the trivial phase as $n \rightarrow \infty$.

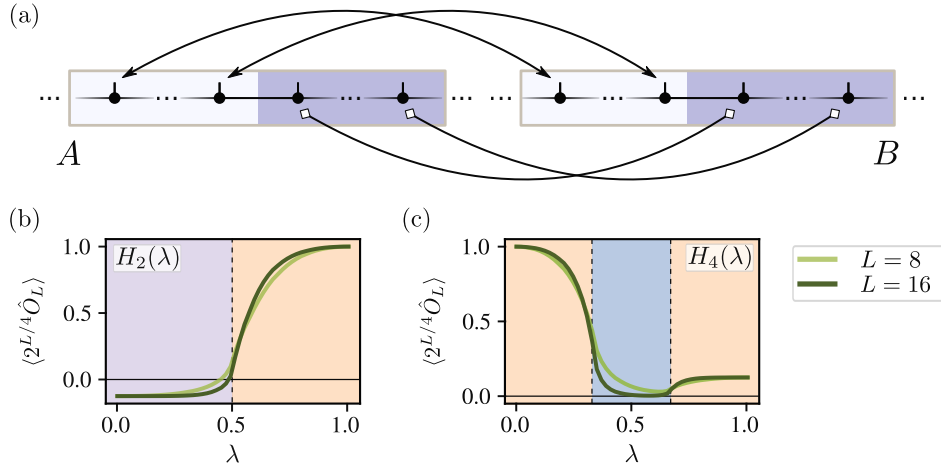


Figure 5.9.: In (a) we illustrate the order parameter for the TI time-reversal systems. The solid circles represent the qubits on the chain. The double-arrow represents an operator $R = \frac{1}{2} (|01\rangle\langle 01| + |10\rangle\langle 10| + |01\rangle\langle 10| + |10\rangle\langle 01|)$. The double-square is a SWAP operator. The operator R is applied between all the pairs across the light blue region of A, B , and the SWAP operator is applied between all the pairs across the light purple region of A, B . In (b) and (c), we verify the order parameter for TI time-reversal symmetric systems. We evaluate the order parameter on the ground states of H_2 and H_4 . The order parameter is multiplied by $2^{L/4}$ for an easy comparison between cases with different L .

We numerically verify the order parameter for the TI time-reversal SPT in Fig. 5.9b and 5.9c. The order parameter \hat{O}_L of length L consists of two operators proposed in Ref. [172] applied to two equally sized subsystems A, B that are next to each other on the chain. We checked that taking A, B apart from each other has little effects on the expectation value in the cases for which we will test it. We normalize the order parameter such that $\|\hat{O}_L\| = 1$, where $\|\cdot\|$ is the operator norm. We evaluate the operator on H_2 and H_4 , with $L = 8$ and 16. When L is much larger than the correlation length of the system, \hat{O}_L evaluates to 0 in the SB phase, and $\pm(\text{Tr} \Lambda^4)^3/2^{L/4}$ in the trivial and the SPT phase, respectively. Here Λ is the diagonal matrix whose diagonal entries are the Schmidt values obtained by cutting the chain into half. For cluster-state-like ground states, Λ has two equal entries $1/\sqrt{2}$, we therefore expect $\langle 2^{L/4} \hat{O}_L \rangle = -1/8$. For a product state, Λ only has one entry with value 1, we have $\langle 2^{L/4} \hat{O}_L \rangle = 1$. When the entanglement-cut crosses a singlet, Λ is doubly degenerate leading to $\langle 2^{L/4} \hat{O}_L \rangle = 1/8$. The plots give consistent results at these limits, as well as reasonable prediction of the critical points.

For the on-site symmetry $\mathbb{Z}_2 \times \mathbb{Z}_2$ with TI, the trivial and SPT phases can be detected by a traceless observable proposed in Ref. [173]. The TI circumvents the non-existence result by Lemma 3.

5.6. Discussion and conclusion

In this chapter, we proposed to train a QCNN with artificially created quantum states obtained from randomly perturbing the fixed points with finite-depth quantum circuits. The trained QCNN discovers order parameters that correctly identify different quantum phases of matter. We illustrated the effectiveness of the method by considering the example of 1D quantum phases protected by time-reversal symmetry and we showed the trained QCNN accurately predicted the theoretical phase diagram from the given ground states of the system in unknown quantum phases.

The proposed method is reminiscent of data augmentation in classical machine learning for reducing over-fitting [193]. A key difference is that our training data set is entirely generated with perturbation. This is possible due to the notion of quantum phases. Let δ be the finite gap between the largest probability and the other probabilities in the output distribution of a QCNN. In practice, δ not only ensures that the QCNN's prediction is robust under weak perturbation, it also provides an estimate of the number of projective measurements required to accurately determine the prediction of the QCNN based on a majority vote. An error probability of $\varepsilon < 1$ can be achieved with more than $2 \log \varepsilon / \log(1 - \delta^2)$ repetitions (see Appendix C for a proof).

The protocol can be further simplified by replacing the SB fixed-point, i.e. $\frac{1}{\sqrt{2}}(|\cdots 000 \cdots\rangle + |\cdots 111 \cdots\rangle)$ with the asymmetric product state $|\cdots 000 \cdots\rangle$ or $|\cdots 111 \cdots\rangle$ which are easier to prepare. In Appendix C, we show that such replacement does not affect the performance of the trained QCNN on the time-reversal symmetric phases.

While physical observables that characterize 1D SPT phases are relatively well understood, probing the SPT order in higher dimensions is much more challenging [16, 194]. One exciting question is whether the proposed protocol can discover such an observable. Another interesting direction is to discover phase-classifying observables for intrinsic topological order, knowing that their fixed points can be efficiently prepared on quantum hardware [4, 5, 195, 196]. Although it has been shown that such an observable cannot exist in general [180], it remains an open question whether imposing TI or other symmetries could help as for the 1D symmetric case discussed here.

Under the current setup, the proposed method is unable to detect hidden phases that are not known a priori. However, we observed that in some examples when a trained QCNN is implemented to classify an unknown phase, it gets confused by multiple phases with matching probability (see Appendix C). It would therefore be intriguing to see whether this behavior is generic at large system size and whether such confusion could be used to identify the existence of an unknown phase [197]. Another important question to study is the underlying principles for the phase detection behind a trained QCNN. Besides comparing it with some known analytical examples such as in Refs. [142, 198], a possible strategy would be to run the trained QCNN backward and use it as a generative model. Some properties of the trained QCNN may be inferred by examining the generated states. It will also be interesting to see whether the trainability of the classifiers can be improved by incorporating symmetry in the design of the classifiers [199, 200].

A novel approach to be explored. In this chapter, we presented a method to discover suitable order parameters for quantum phases of matter based on quantum machine learning. However, a disadvantage of that method is the lack of physical interpretation of the discovered observables. Due to the hardness in classically simulating 2D quantum systems, application of the proposed method to 2D quantum phases of matter, e.g. intrinsically topological phases of matter, requires implementation on actual quantum hardware. Below, we outline another idea of detecting quantum phases of matter based on the framework of *quantum error correction* [201]. This provides a method to *efficiently* detect 2D topological phases and transitions based on the physics of emergent 1-form symmetry.

In Part I, we showed how topological order can be characterized using the topological entanglement entropy. However, the measurement of topological entanglement entropy is not scalable in quantum experiments and requires a sample size that grows exponentially with the subsystem size of interest. Recently, it has been realized that topological order can be understood using higher-form symmetries [95, 202, 203]. A p -form symmetry applies on a $d - p$ dimensional sub-manifold of a quantum system in d spatial dimensions, 1-form symmetry generators of a 2D quantum system are loop-like objects. Topological order can be understood as spontaneous higher-form symmetry breaking [204–207]. Therefore, higher-form symmetry can be used as a probe for the topological phases and phase transi-

tions. However, higher-form symmetry exists as emergent symmetries [95, 205, 206, 208], which do not have a simple analytic form and it is unclear how they can be measured experimentally. There are some other proposals to detect topological phase transitions with physical order parameters (not from entanglement). For instance, the Fredenhagen-Marcu (FM) string order parameter [209, 210] has been used to detect the topological order realized by the Rydberg quantum simulator [65]. Unfortunately, the FM order parameter is obtained by taking the ratio between two exponentially small measured quantities, which makes it infeasible to be measured in a scalable experiment.

The recoverability in quantum error correction (QEC) and existence of an emergent 1-form symmetry are closely related. A remarkable property of 1-form symmetry is that it is emergent. While the usual on-site symmetry is fragile under local perturbation violating the symmetry, upon small perturbation that violates the exact 1-form symmetry, the system is still symmetric under an 1-form symmetry adiabatically connected to the original one. This is reminiscent of QEC based on surface code [47, 113, 151], i.e. under small local noise, the logical information encoded in global loop operators is no longer explicitly preserved. But there exists a recovery protocol to recover the logical information. If we regard the violation of an exact 1-form symmetry as noise in the context of quantum error correction, the emergence of the 1-form symmetry corresponds to the recoverability of some effective “logical information”. A noise threshold beyond which the logical information is no longer recoverable coincides with a critical perturbation strength for the breakdown of the emergent 1-form symmetry.

Using this connection, it is possible to (i) devise an order parameter for an emergent 1-form symmetry based on recoverability decided by the QEC protocol and (ii) detect 2D topological phase transition by first recovering the exact 1-form symmetry of the system using QEC protocol, and then measuring an order parameter for the transition valid only in the presence of an exact 1-form symmetry [211, 212]. In collaboration with Wen-Tao Xu, Michael Knap and Frank Pollmann, we numerically benchmark this idea against well-known phase diagrams for 2D topologically ordered systems. We show that indeed the method provides an efficient experimental protocol for measuring emergent 1-form symmetries and 2D topological quantum phase transitions.

Part III.

Realizing 2D topological quantum
phase transition on digital
quantum computers

Overview of Part III

In Part I and II, we focused on the realization and the characterization of fixed-point ground states of gapped quantum phases of matter. Can we go beyond these specific states and realize other many-body ground states away from the fixed points, or even across a quantum critical point? In this part of the thesis, we address the question of engineering topological quantum phase transitions on a programmable quantum computer with the method of tensor networks.

In Chapter 6, we review the important concept of tensor networks and isometric tensor networks, with an emphasis on the state preparation using efficient sequential quantum circuits. In Chapter 7, we show how 2D tensor-network states can describe exact ground states of some parametrized many-body Hamiltonian across a quantum phase transition between distinct 2D symmetry-enriched topological (SET) phases of matter. They therefore provide exactly solvable simple model states for the physical realization. This chapter is based on the publication [3]. In Chapter 8, we utilize the new class of isometric tensor-network states as a tool to design efficient quantum circuits for preparing ground states across the quantum phase transition between the distinct 2D SET phases. We further discuss the experimental strategies for realizing the proposed quantum phase transition on programmable quantum hardware, one method is based on the lattice realization and the other method is based on the holographic duality of the isometric tensor networks. The results are based on the preprint [1].

6. A short review of tensor-network states and their preparation

The behaviour of large and complex aggregates of elementary particles, it turns out, is not to be understood in terms of a simple extrapolation of the properties of a few particles. Instead, at each level of complexity entirely new properties appear, and the understanding of the new behaviours requires research what I think is as fundamental in nature as any other.

Philip W. Anderson

A significant challenge of understanding quantum many-body systems, both using analytical methods or computational methods, is rooted at their tensor product structure, i.e. they require exponentially large Hilbert space description as the number of particles increases. However, it was realized that a large class of physically relevant states, e.g. the ground states of a many-body system, has the feature of low entanglement. This common feature allows for an efficient description of the states without exponentially many parameters. Tensor-network representation provides a parametrization of the wavefunctions such that a good approximation to the wavefunctions can be obtained in a systematic way by keeping the parameters relevant for the entanglement of the state. In one dimension, tensor-network representation of the states is called the *matrix-product states* and has gained enormous success in the classical simulation of many-body ground states based on the Density Matrix Renormalization Group (DMRG) method [31, 32]. In higher dimensions, the tensor-network methods become more cumbersome in the numerical simulation, but they still serve as the state-of-the-art numerical methods for many-body problems [213, 214].

Apart from the application in the numerical simulation, tensor-network methods also have profound impact in the theoretical understanding of many-body systems, including the classification of quantum phases of matter in one and higher dimensions [15, 16, 171, 215–218]. In Part III, we use tensor-network representation as an analytical tool and investigate the application of the tensor-network methods in designing efficient protocols for engineering interesting classes of quantum many-body states on a programmable quantum computer. Below, we briefly review the concept of tensor-network states in 1D and 2D, and the efficient preparation of them using unitary quantum circuits.

6.1. Matrix-product states in 1D

Matrix-product states (MPS) are an ansatz class where the coefficients of a full n -qubit state ψ are decomposed into products of matrices. Explicitly,

$$|\psi\rangle = \sum_{\{j_k\}} \sum_{\{\alpha_i\}} B_{\alpha_1}^{[1]j_1} B_{\alpha_1\alpha_2}^{[2]j_2} \dots B_{\alpha_{n-1}}^{[n]j_n} |j_1, j_2, \dots, j_n\rangle, \quad (6.1)$$

where the $j_k \in \{0, 1\}$ indices are referred to as “physical” indices and the α indices are referred to as “virtual indices.” By convention, we refer to the dimension of the α indices as

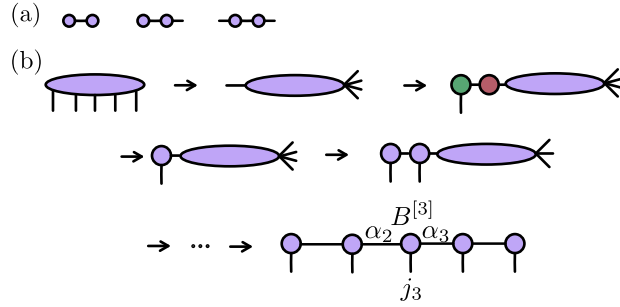


Figure 6.1.: (a) Basic MPS diagrammatic notation. Connected tensors represent summing over the index corresponding to the connected legs. From left to right, a vector inner product, a matrix-vector multiplication, and a matrix-matrix multiplication. (b) Converting a general vector into an MPS. A generic vector with size 2^N can be viewed as an N index tensor. We convert each vector into a product of matrices via a singular value decomposition, then truncate the singular value matrix (the red tensor) to the desired number of singular values (i.e., χ). By repeatedly applying this procedure, we decompose the original vector into a matrix-product state with bond dimension χ . To return to the vector representation, we would contract the MPS along the virtual indices α_j (albeit with some loss from the truncation).

the bond dimension χ . Without loss of generality, we may assign any MPS a single bond dimension χ corresponding to the largest bond dimension in the network (padding the others with zeros). In the above expression, each tensor $B^{[k]}$ for $k = 2, \dots, n-1$ contains three indices, two virtual and one physical. The boundary tensors $B^{[1]}$ and $B^{[n]}$ each contain two indices. We will often use a diagrammatic notation for tensor manipulations, where tensors are represented by symbols and each index is represented by a leg. Two connected legs represent summing over the corresponding index. See Fig. 6.1a for more details. The bond dimension χ controls the maximum amount of entanglement the system can have. More precisely, consider two subsystems A and B separated by a virtual bond, the entanglement entropy satisfies $S_A = S_B = -\text{Tr}(\rho_A \log \rho_A) \leq \log \chi$, where χ is the dimension of that virtual bond. To exactly represent the state, the bond dimension χ grows exponentially with the system size n . Remarkably, it has been shown that the ground states of 1D gapped local Hamiltonian are well approximated by an MPS with a low bond dimension [99].

A length 2^n vector can always be decomposed into a matrix-product state with n tensors; see Fig. 6.1b. Decomposing a vector in this way will guarantee that the tensors satisfy the isometry condition

$$\sum_{j_k} \sum_{\alpha_k} B_{\alpha_{k-1} \alpha_k}^{[k] j_k} \left(B_{\alpha'_{k-1} \alpha_k}^{[k] j_k} \right)^* = \delta_{\alpha_{k-1}, \alpha'_{k-1}}. \quad (6.2)$$

MPS satisfying this isometry condition is said to be in its (right) canonical form. Similarly, the MPS is in its left canonical form when the local tensors satisfy the isometry when contracted from the left. An extensive review of MPS can be found in Ref. [219].

6.1.1. Equivalence to sequential quantum circuits

Due to the isometry condition, a bond dimension χ MPS in the canonical form, i.e. where all the tensors satisfy Eq. (6.2), can be exactly mapped to a sequential quantum circuit with unitaries acting on $\log \chi + 1$ qubits [220], as shown in Fig. 6.2. MPS with length n

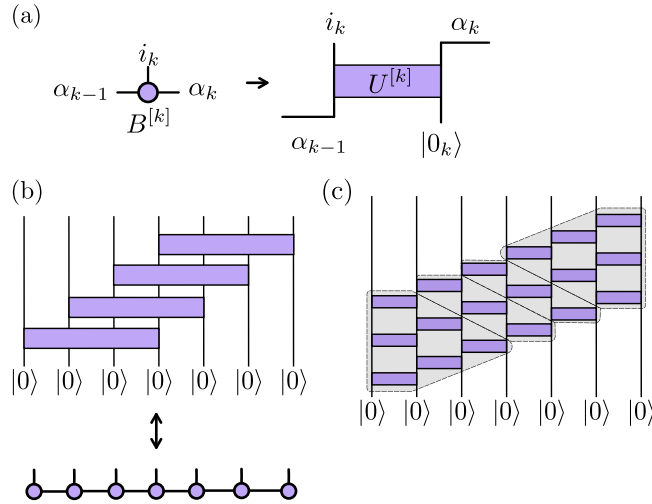


Figure 6.2.: (a) The mapping between an MPS tensor and a unitary matrix. The MPS tensors are used to define a unitary action on an additional set of qubits initialized to a product state, where the number of additional qubits depends on the bond dimension of the MPS. (b) An MPS with bond dimension χ is equivalent to a quantum circuit where each gate acts on $\log_2 \chi + 1$ qubits. (c) Every M -layer sequential quantum circuit with two qubit gates is a subset of the set of sequential quantum circuits with $(M + 1)$ qubit gates. Here, we show the equivalence for $M = 3$.

can therefore be efficiently prepared on a quantum computer with a circuit depth $O(n)$. For practical implementations, each unitary gate must be further decomposed into single and two-qubit gates. For a generic quantum gate acting on $\log_2 \chi + 1$ qubits, this requires $O(\text{poly}(\chi))$ single and two-qubit gates [201], resulting in a total cost of $O(\text{poly}(\chi)n)$ quantum operations.

The mapping, which is diagrammatically depicted in Fig 6.2a, is given by

$$B_{\alpha_{k-1}\alpha_k}^{[k]j_k} = \langle \alpha_k, j_k | U^{[k]} | 0_k, \alpha_{k-1} \rangle, \quad (6.3)$$

where $|0_k\rangle$ is a product state.

On the other hand, a sequential quantum circuit with M layers of two-qubit gates can be viewed as an equivalent sequential circuit with a single layer of $M + 1$ qubit gates (see Fig 6.2b). This circuit, in turn, can be mapped to an MPS with bond dimension $\chi = 2^M$. Every single-layer circuit thus has an exact $\chi = 2$ equivalence.

6.2. Tensor-network states in 2D

The generalization of MPS to higher-dimensional systems is straightforward. A 2D tensor-network state (TNS) (also known as Projected Entangled Pair States (PEPS) [213]) is obtained by contraction of local tensors. Each local tensor T_{ijmn}^σ consists of four virtual legs with bond dimension D and one physical leg with local physical dimension d . The wavefunction for an N -site state is

$$|\psi\rangle = \sum_{\{\sigma_s\}} \text{tTr} \left(T^{[1]\sigma_1} T^{[2]\sigma_2} \dots T^{[N]\sigma_N} \right) |\sigma_1, \sigma_2, \dots, \sigma_N\rangle, \quad (6.4)$$

where tTr denotes the 2D tensor contraction of the nearest neighbour virtual legs (see Fig. 6.3a). Again, any 2D wavefunctions can be written as 2D TNS with a bond dimension

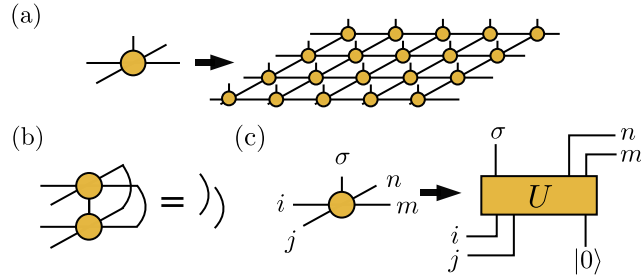


Figure 6.3.: The schematics for 2D TNS (a) The wavefunction is contracted from local tensors (yellow circles) with a finite bond dimension. (b) and (c) illustrate the isometric tensor networks. (b) shows the isometric condition on the local tensors. (c) Similar to how MPS is generated by a sequential quantum circuit obtained from its canonical form, an isoTNS can be sequentially generated by applying a unitary U sequentially to a product state $|0\rangle$ with ancillary qudits). This unitary is obtained by lifting the isometric local tensors to a full unitary.

exponentially large in the system size. It is believed that the ground states of local gapped 2D Hamiltonian can be well approximated by 2D TNS with a low bond dimension. For an extensive review of 2D TNS, see Ref. [214].

6.2.1. Isometric tensor networks and sequential quantum circuits

Unlike 1D MPS, generic 2D TNS do not have a well-defined canonical form and are hard to prepare on a quantum computer [221]. A subclass of general 2D TNS, the isometric tensor-network states (isoTNS) [128], shares the same property as 1D MPS that they can be efficiently prepared with a sequential quantum circuit with depth $O(L)$, where L is the linear size of the system. Surprisingly, despite being a subclass of general 2D TNS, isoTNS are expressive and are known to be able to exactly represent a large class of gapped many-body ground states, including the string-net states [52, 129] (which are representative models for topological phases of matter, see also Section 2.4) and ground states of various symmetry-protected quantum phases of matter [222]. For this reason, isoTNS serve as a valuable tool not only in the numerical method, but they can also be utilized to design efficient quantum circuits for interesting class of many-body ground states, as we will discuss in Section 8.

IsoTNS are 2D tensor-network states where the local tensors additionally satisfy an isometric condition, as depicted in Fig. 6.3b. Explicitly, we have

$$\sum_{m,n,\sigma} (T_{ijmn}^\sigma)^* T_{i'j'mn}^\sigma = \delta_{ii'} \delta_{jj'}, \quad (6.5)$$

where $\delta_{ii'}$ is the kronecker delta and takes 1 if $i = i'$ and zero otherwise. Similar to the canonical form of MPS, this isometric condition implies that each local tensor can be directly lifted to a local unitary which can be used to efficiently generate the isoTNS (see Fig. 6.3c).

We show how a simple sequential quantum circuit for general 2D isoTNS can be constructed. Suppose we want to prepare a finite 2D isoTNS with an open boundary condition. We begin with a square lattice with physical qudits (a d -level quantum system) at each vertex and ancillary qudits (a D -level quantum system, where D is the bond dimension of the TNS) on each link. We initialize the sequential circuit from the boundary closer to the input virtual legs of the lifted local unitary (left-pointing legs of Fig. 6.3c). The qudits on this boundary are initialized according to the chosen boundary condition. The rest of

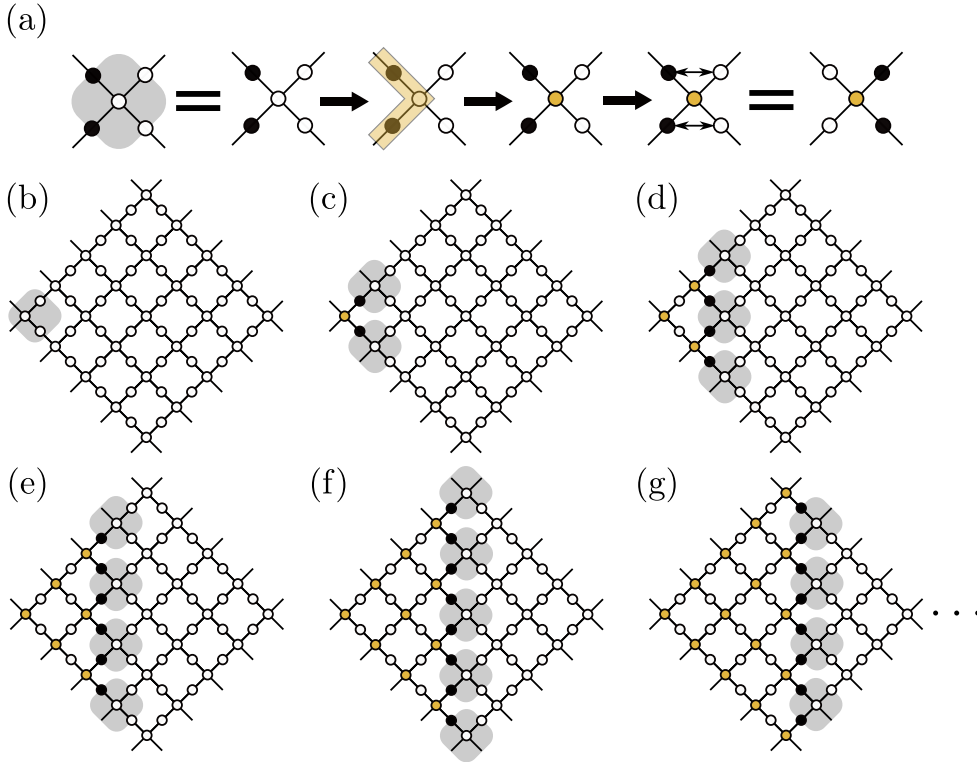


Figure 6.4.: A sequential quantum circuit for general isoTNS. The white circles are disentangled qudits in state $|0\rangle$. The black circles are the ancillary qudits storing the uncontracted virtual legs (legs i,j in Fig. 6.3c). The yellow circles are the entangled physical qudits of the prepared wavefunction. (a) At each step, a five-qudit gate is applied around each vertex. The gate first applies the lifted unitary (yellow block) in Fig. 6.3c, where the black qudit states on the links are taken as the input legs i,j . After the lifted unitary, the uncontracted virtual legs (legs m,n in Fig. 6.3c) are still stored in the black qudit states. Next, these ancillary states are swapped to the ancillary qudits on the right. (b)-(g) The isoTNS is generated by applying the unitary in (a) along each column of vertices sequentially. At the end of the circuit, the ancillary qudits are all in disentangled states $|0\rangle$ and the physical qudits store the isoTNS.

the qudits are all initialized in state $|0\rangle$. The isoTNS is generated by applying the vertex unitary in Fig. 6.4a sequentially to each column of the vertices (see Fig. 6.4b-g). The application of the gates across each column is effectively contracting the isoTNS tensors along the column. At each step, the ancillary qudits store the uncontracted virtual legs of the local tensors. They are disentangled back to states $|0\rangle$ at the end of the circuit.

The use of the ancillary qudits simplifies the structure of the circuit but they are not necessary for the preparation. The ancillary states can also be stored in the disentangled physical qudits that are not yet reached by the sequential circuit. With a careful design of the gates, the resulting sequential circuit without ancillary qudits also consists of $O(L)$ layers of local quantum gates [130].

7. Quantum phase transition between symmetry enriched topological phases in tensor-network states

Over the past decades, significant progress has been made in understanding quantum phases of matter [20, 48, 97]. In the absence of any symmetries, quantum systems in two or higher spatial dimensions can host distinct topologically ordered phases separated by quantum phase transitions (QPT) [223]. When (intrinsic) topological order is absent, the presence of symmetries alone can lead to different symmetry protected topological (SPT) phases [12–18]. If both topological order and symmetries are present, distinct *symmetry enriched topological* (SET) phases can emerge, which are characterized by how symmetry operations act on the anyonic quasiparticle excitations [22, 23]. A remarkable experimental manifestation of SET order is the $\nu = 1/3$ Laughlin’s fractional quantum Hall state [48, 50], where the anyons carry fractional charges under the global $U(1)$ symmetry. The classification and characterization of bosonic and fermionic SET phases have been intensively investigated [22–30]. Certain phase transitions between different SET phases can be understood via anyon condensation [216, 224, 225], or as SPT phase transitions after gauging the global symmetries [28, 226]. Simple toy models realizing different SET phases can be constructed in the following way: Starting from a \mathbb{Z}_2 topologically ordered system (for example, the toric code [43]), different SET phases protected by a global symmetry G can be constructed by decorating the loops in the topologically ordered state with one-dimensional (1D) SPT states protected by the symmetry G [227–230]. As illustrated in Fig. 7.1, the resulting state is a condensate of SPT loops and the symmetry will fractionalize between the anyons in a similar fashion as the symmetry fractionalizes at the boundaries of a 1D SPT chain with open boundary conditions [22, 227].

In this chapter, we follow this idea and construct a parameterized tensor-network solvable model that realizes a direct continuous transition between SET phases with an antiunitary time-reversal symmetry \mathbb{Z}_2^T . In particular, we derive a tunable model for which the ground state is given by a tensor-network state (TNS) [213, 231]. This family of exact TNS corresponds to states of decorated loops with string tension and a tunable internal parameter, which are able to describe two distinct \mathbb{Z}_2 topologically ordered SET phases with different symmetry fractionalization patterns and a continuous phase transition between them (Fig. 7.1). We numerically determine the phase diagram of the system by examining the correlation length, the topological entanglement entropy [100, 101] (see also Section 2.1), and a membrane order parameter [229]. Along the phase boundary between the two SET phases, the amplitudes of the wavefunction can be exactly mapped to the partition function of the classical $O(2)$ loop model in the dense loop phase, described by the compactified free boson conformal field theory (CFT) with central charge $c = 1$. The model exhibits an additional $U(1)$ symmetry at the $O(2)$ critical points. The additional $U(1)$ symmetry is an example of a pivot symmetry, which has recently been studied in the context of SPT phase transitions [232]. These transition points are, similar to the Rokhsar–Kivelson point on a square lattice [51], $(2 + 0)$ D conformal critical points [233, 234], which have also appeared in several Abelian and non-Abelian topological phase transitions described by TNS [235–241]. Finally, we discuss how the constructed example is dual to tensor-network solvable paths for the symmetry enriched double-semion model [52, 123] and $(2 + 1)$ D SPT states

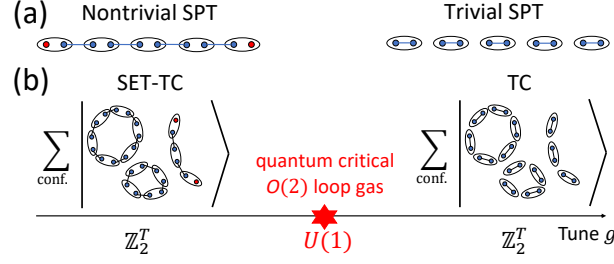


Figure 7.1.: Schematic illustration of distinct SET phases and the transition between them. (a) The symmetry fractionalizes over the edges in the 1D non-trivial SPT phase (red dots). By tuning a parameter g , the non-trivial SPT phase becomes trivial through a topological phase transition. (b) A state in the SET toric code (SET-TC) phase or toric code (TC) phase with a pair of charge excitations at the ends of the broken loops. The sum runs over all the configurations with closed SPT loops and a broken SPT loop whose two ends are fixed. The global symmetry fractionalizes over the charges. Notice that for the ground state on a closed manifold, the configurations only contain closed loops. Using the 1D SPT phase transition, we can construct a direct continuous phase transition from the SET-TC phase to the TC phase.

protected by $\mathbb{Z}_2 \times \mathbb{Z}_2^T$.

7.1. Quantum phase transitions in tensor-network states

In this section, we explain the two main ingredients for our construction. We begin by first reviewing the 1D SPT phase transition described by a family of 1D TNS, namely matrix-product states (MPS) that will be used for the decoration of the loops. We then recall the definition of the toric code model with a tunable string tension on a honeycomb lattice. In this paper, we use the standard notation $\{X, Z\}$ for Pauli matrices, and their eigenstates are denoted as $Z|0\rangle = |0\rangle$, $Z|1\rangle = -|1\rangle$, $X|\pm\rangle = \pm|+\rangle$, where $|\pm\rangle = (|0\rangle \pm |1\rangle)/\sqrt{2}$. The Greenberger–Horne–Zeilinger (GHZ) state is defined as $(|00\dots 0\rangle + |11\dots 1\rangle)/\sqrt{2}$.

7.1.1. 1D \mathbb{Z}_2^T -symmetric SPT phase transition in matrix product states

We consider the antiunitary \mathbb{Z}_2^T time-reversal symmetry $K \prod_i X_i$, which is a combination of the global spin flip operator and complex conjugation K . A Hamiltonian describing a phase transition between two 1D SPT phases protected by the \mathbb{Z}_2^T symmetry is [242]

$$H(g) = \sum_i [2(g^2 - 1)Z_i Z_{i+1} - (1 + g)^2 X_i + (1 - g)^2 Z_i X_{i+1} Z_{i+2}], \quad (7.1)$$

where $g \in [-1, 1]$ is the tuning parameter. When $g = 1$, $H = -4 \sum_i X_i$ and the ground state is a product state $|\psi(1)\rangle = \otimes_i |+\rangle_i$. When $g = -1$, H reduces to the cluster model $H = 4 \sum_i Z_{i-1} X_i Z_{i+1}$ with the ground state $|\psi(-1)\rangle = \prod_i C Z_{i,i+1} \prod_i Z_i |\psi(1)\rangle$, where the control Z gate $C Z_{i,i+1}$ acts on qubits i and $i+1$, and $C Z_{i,i+1} = -1$ if both qubits are 1 and $C Z_{i,i+1} = 1$ otherwise. The two limits $g = \pm 1$ exactly correspond to two fixed points of time-reversal symmetric SPT phases [15, 171]. A phase transition occurs at $g = 0$, which is a multi-critical point characterized by a dynamical critical exponent $z = 2$ [242, 243].

The ground states of this Hamiltonian are exactly described by a one-parameter family of MPS with bond dimension $\chi = 2$ [242]

$$|\psi(g)\rangle = \frac{1}{\sqrt{\mathcal{N}(g)}} \sum_{\{s_i\}} \text{Tr}(M^{[s_1]} M^{[s_2]} \dots M^{[s_N]}) |s_1, s_2, \dots, s_N\rangle, \quad (7.2)$$

7.1. Quantum phase transitions in tensor-network states

where the MPS tensors are given by

$$M^{[0]} = \begin{pmatrix} 0 & 0 \\ 1 & 1 \end{pmatrix}, \quad M^{[1]} = \begin{pmatrix} 1 & g \\ 0 & 0 \end{pmatrix}, \quad (7.3)$$

and $\mathcal{N}(g)$ is the normalization coefficient (or simply squared norm) of the MPS. Notice that at the phase transition point $g = 0$, the MPS becomes a GHZ state.

7.1.2. 2D toric code with string tension

Let us now consider a honeycomb lattice with qubits on the edges, as shown in Fig. 7.2. Each vertex v is a set of three edges and each plaquette p is a set of six edges. The toric code Hamiltonian is a sum of local and commuting projectors (see Section 2.3 for a review of the toric code)

$$H_{\text{TC}} = \sum_v A_v + \sum_p B_p, \quad (7.4)$$

where the star projector around each vertex v is $A_v = \frac{1}{2} (1 - \prod_{e \in v} Z_e)$. The plaquette projectors have the form $B_p = \frac{1}{2} (1 - \prod_{e \in p} X_e)$. The Hamiltonian has a ground state energy of zero. As shown in Fig. 7.2, an edge of state $|1\rangle$ is said to be occupied by a loop segment (or a string) and the state $|0\rangle$ is empty (vacuum). The ground state of the toric code is then an equal-weight superposition of closed-loop configurations on the edges of the lattice. The excitations in the toric code are denoted as electric \mathbf{e} with $\langle A_v \rangle = 1$ and magnetic \mathbf{m} with $\langle B_p \rangle = 1$. Their composite forms a fermion, which we denote by \mathbf{f} . We further denote the trivial (null) excitation as $\mathbf{1}$.

As we will discuss in Section 7.2, it turns out to be convenient to introduce a tunable string tension $\eta > 0$ on the loops in the toric code [244, 245]. The ground state is then modified to be a weighted superposition of closed-loop configurations

$$|\Psi(\eta)\rangle \propto \sum_C \eta^{L(C)} |C\rangle, \quad (7.5)$$

where C denotes the closed loop configurations on the honeycomb lattice and $L(C)$ is the total length of all loops in C . A parent Hamiltonian of the modified ground state is given in Section 7.4. For $\eta = 1$, we recover the toric code ground state $|\Psi(1)\rangle = |\Psi_{\text{TC}}\rangle$. At large string tension ($\eta \rightarrow 0$), the state becomes fully polarized. The amplitude $\eta^{L(C)}$ can be mapped to the Boltzmann weight of the 2D classical Ising model and the critical string tension can be identified from the critical temperature of the Ising model as $\eta_c = 3^{-1/4}$ [245].

Moreover, the one-parameter family of wavefunctions in Eq. (7.5) can be expressed in terms of the ‘‘single-line’’ TNS

$$|\Psi(\eta)\rangle = \frac{1}{\sqrt{\mathcal{N}(\eta)}} \sum_{\{s_e\}} \text{tTr} \left(\bigotimes_v V \bigotimes_e E^{[s_e]}(\eta) \right) |\dots s_e \dots\rangle \quad (7.6)$$

with bond dimension $D = 2$ [118], where the superscripts (subscripts) are the physical (virtual) indices which take 0 or 1, tTr denotes the tensor contraction over all virtual indices and

$$V_{\alpha\beta\gamma} = \delta_{\text{mod}(\alpha+\beta+\gamma, 2), 0}, \quad E_{\alpha\beta}^{[s]}(\eta) = \eta^s \delta_{\alpha\beta} \delta_{\alpha p}, \quad (7.7)$$

are tensors placed at the vertices and edges of the honeycomb lattice, respectively. $\mathcal{N}(\eta)$ is the squared norm of the TNS. The tensor V imposes the \mathbb{Z}_2 Gauss law on each vertex, and the tensor E promotes the virtual degrees of freedom to the physical level and implements the string tension.

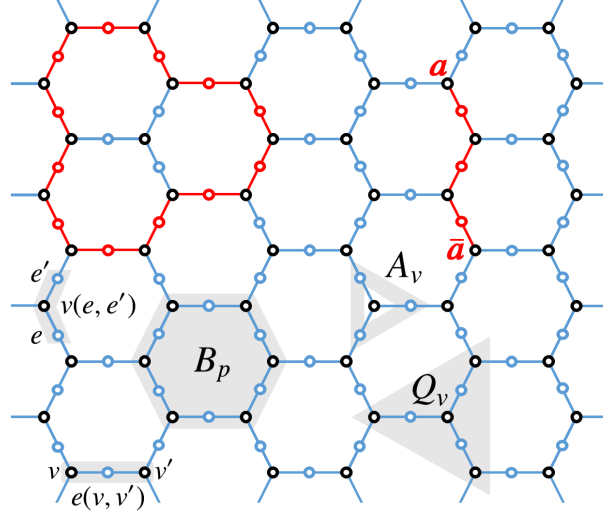


Figure 7.2.: A snapshot of an excited state. The system is defined on a honeycomb lattice, the circles are two sets of physical qubits on the edges and vertices, respectively. Red (blue) circles represent edge qubits in the state 1(0), and black circles are vertex qubits. A loop in the toric code is formed by a string of edge qubits with state 1 along which the 1D SPT states are decorated. Ends of open loops (the open loop can deform freely except the endpoints) correspond to anyons \mathbf{a} , which can be \mathbf{e} or \mathbf{f} anyons of the toric code. The qubits in the grey regions support the plaquette projector B_p , star projector A_v and vertex projector Q_v of the parent Hamiltonian (7.14), respectively.

7.2. Decorating the toric code

Next, we consider the same honeycomb lattice on which the toric code ground state with string tension $|\Psi(\eta)\rangle$ is prepared on the qubits at the edges of the lattice. To decorate the loops, we add to each vertex v a qubit as shown in Fig. 7.2. The decoration is carried out with a simple procedure: whenever a loop is formed on the edges, we contract the MPS tensors (7.3) on the vertices along the closed loop. The vertices away from the loops are set to the product state $|+\cdots+\rangle$. The resulting decorated 2D state $|\Psi(g, \eta)\rangle$ is thus a superposition of MPS-loop configurations and has a global \mathbb{Z}_2^T symmetry generated by $K \prod_v X_v$, i.e. global spin flips on all vertices followed by complex conjugation.

At $g = 1$ and $\eta = 1$ (no string tension), the ground state is a tensor product of the toric code ground state and a product state on all vertex qubits

$$|\Psi(g = 1, \eta = 1)\rangle = |\Psi_{\text{TC}}\rangle \otimes \left(\bigotimes_v |+\rangle_v \right), \quad (7.8)$$

which has a trivial SET order, where the time-reversal symmetry fractionalizes trivially over the anyons of the toric code. We will simply refer to the phase it belongs to as the toric code (TC) phase. At $g = -1$, the system can be obtained from the toric code limit by a constant-depth quantum circuit $|\Psi(-1, 1)\rangle = U|\Psi(1, 1)\rangle$, where U is defined as

$$U = \left(\prod_{\langle v, v' \rangle} CCZ_{vv'e(v, v')} \right) \left(\prod_{\langle e, e' \rangle} CCZ_{ee'v(e, e')} \right), \quad (7.9)$$

which is a 2D analogue of how we obtained $|\psi(-1)\rangle$ from $|\psi(1)\rangle$ in the 1D SPT model. The first product goes over all distinct pairs of nearest neighbouring vertices with $\langle v, v' \rangle =$

$\langle v', v \rangle$, and the second product goes over all different pairs of nearest neighbouring edges $\langle e, e' \rangle$. We use $e(v, v')$ (or $v(e, e')$) to denote the edge (or vertex) between the nearest neighbouring pair $\langle v, v' \rangle$ (or $\langle e, e' \rangle$), as shown in Fig. 7.2. The CCZ gate satisfies

$$CCZ_{abc} = \begin{cases} -1, & \text{if all qubits at } a, b, c \text{ are } 1, \\ 1, & \text{otherwise.} \end{cases} \quad (7.10)$$

The wavefunction $|\Psi(-1, 1)\rangle$ is the fixed point for a non-trivial SET phase, where the symmetry fractionalizes non-trivially over the \mathbf{e} and \mathbf{f} anyons of the toric code. We refer to the phase as SET-TC.

7.3. Tensor-network representation of the SET path

Away from the fixed points, the state $|\Psi(g, \eta)\rangle$ can be conveniently represented as a 2D TNS by decorating the MPS (7.3) onto the single-line TNS. The resulting decorated single-line TNS, similar to the TNS in Eq. (7.6), consists of tensors with a bond dimension of $D = 3$, which are placed at the vertices and edges of the honeycomb lattice. The virtual degrees of freedom are spanned by the basis $\{|0\rangle, |1\rangle, |2\rangle\}$. We apply a \mathbb{Z}_2 grading on this virtual space such that the parity of $|0\rangle$ is even and the parity of $|1\rangle$ and $|2\rangle$ is odd, so the dimension of the odd parity subspace is 2.

The decorated vertex tensor \tilde{V} is schematically shown in Fig. 7.3a. In contrast to the vertex tensor V in Eq. (7.7), the decorated vertex tensor \tilde{V} has a physical leg of dimension 2 corresponding to a vertex qubit. The \mathbb{Z}_2 Gauss law at the vertex tensor \tilde{V} implies that either the vertex is not covered by any string or the vertex is covered by a closed loop segment. In the former case, the physical vertex qubit is $\sqrt{2}|+\rangle$ and the three virtual legs are $|0\rangle$. In the latter case, the entries of \tilde{V} given by the physical leg together with the two odd virtual legs are exactly defined by the MPS tensor $M^{[i]}$, as shown in Fig. 7.3a. To construct the single-line TNS with a bond dimension $D = 3$, the MPS matrices $M^{[i]}$ used for the decoration have to be symmetric under the swapping of the two virtual indices (transpose). This ensures that there is no ambiguity in the direction of contracting the MPS along a loop within the TNS¹. While the original MPS matrices (7.3) are not symmetric under transpose, in Appendix D.5, we utilize the gauge redundancy in the MPS representation to obtain a set of equivalent MPS tensors M_A and M_B in a two-site unit cell, which have the desired property. Since the honeycomb lattice is a bipartite lattice, we use M_A and M_B to define two vertex tensors \tilde{V}_A and \tilde{V}_B for the two sublattices A and B of the honeycomb lattice, separately. In summary, the tensor $\tilde{V}_A(g)$ on the A sublattice is

$$\tilde{V}_{A,\alpha\beta\gamma}^{[i]}(g) = \begin{cases} 1, & \text{if } \alpha = \beta = \gamma = 0; \\ M_{A,\alpha\beta}^{[i]}(g), & \text{if } p(\alpha) = p(\beta) = 1, \gamma = 0; \\ M_{A,\alpha\gamma}^{[i]}(g), & \text{if } p(\alpha) = p(\gamma) = 1, \beta = 0; \\ M_{A,\beta\gamma}^{[i]}(g), & \text{if } p(\beta) = p(\gamma) = 1, \alpha = 0; \\ 0, & \text{otherwise,} \end{cases} \quad (7.11)$$

where $p(\alpha)$ denotes the parity of $|\alpha\rangle$. The construction works analogously for the tensor $\tilde{V}_B(g)$.

The edge tensor \tilde{E} of the decorated TNS is shown in Fig. 7.3a and it maps the parity of the virtual degree of freedom to the physical degree of freedom and implements the string

¹Alternatively, we could decorate the MPS onto the double-line TNS of toric code [246], which can keep track of the direction of tensor contraction along a loop in the cost of a larger bond dimension.

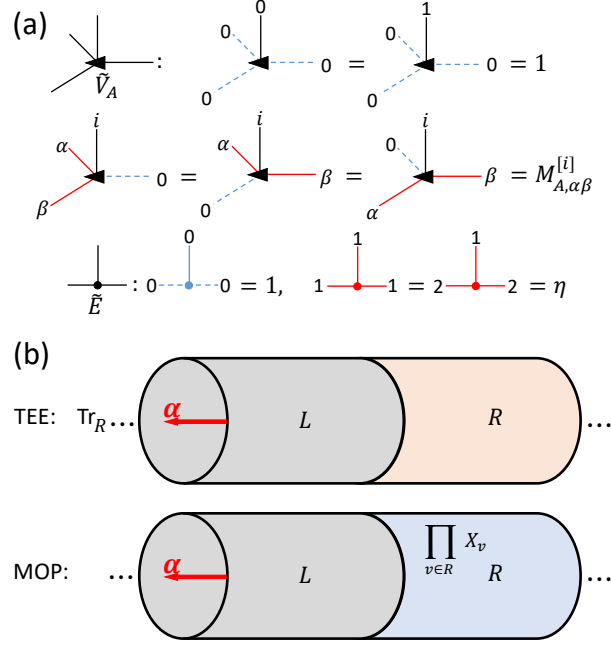


Figure 7.3.: (a) The local tensors \tilde{V}_A and \tilde{E} of the decorated TNS and their non-zero entries, \tilde{V}_B is obtained by replacing M_A in \tilde{V}_A with M_B . (b) The TEE and MOP on an infinitely long cylinder, where the anyon flux α penetrating inside the cylinder gives rise to the MES $|\Psi_\alpha\rangle$. The TEE comes from the reduced density matrix obtained by tracing out all physical qubits on half of the cylinder, and the MOP is obtained by applying the symmetry operator to the vertices on half of the cylinder and evaluating the expectation value.

tension:

$$\tilde{E}_{ij}^{[s]}(\eta) = \eta^s \delta_{ij} \delta_{p(i),s}. \quad (7.12)$$

With these local tensors, the decorated TNS can be constructed as

$$|\Psi(g, \eta)\rangle = \frac{1}{\sqrt{\mathcal{N}(g, \eta)}} \sum_{\{s_e, i_v\}} \text{tTr} \left(\bigotimes_v \tilde{V}^{[i_v]}(g) \bigotimes_e \tilde{E}^{[s_e]}(\eta) \right) |\{s_e, i_v\}\rangle, \quad (7.13)$$

where \tilde{V} can be \tilde{V}_A or \tilde{V}_B depending on which sublattice the vertex belongs to, and $\mathcal{N}(g, \eta)$ is the squared norm of the decorated TNS.

7.4. Parent Hamiltonian

So far, we have obtained a continuously parameterized family of TNS that interpolates between different fixed-point wavefunctions. We can also show that the states in Eq. (7.13) are indeed ground states of a local Hamiltonian, which depends smoothly on the same set of parameters. More precisely, there exists a frustration-free, \mathbb{Z}_2^T -symmetric parent Hamiltonian that is a sum of local projectors

$$H(g, \eta) = \sum_v A_v + \sum_p B_p(g, \eta) + \sum_v Q_v(g), \quad (7.14)$$

where $g \in [-1, 1]$ and $\eta > 0$. Each vertex projector A_v , analogous to those in Eq. (7.4), projects onto the +1 eigenspace of the product of Pauli Z around the vertex v . The plaquette projector $B_p(g, \eta)$ and the vertex projector $Q_v(g)$ act on the spins of a plaquette and

around a vertex, respectively (see Fig. 7.2). Let $v(e), v'(e)$ be the two vertices connected via the edge e , the projectors are explicitly given by

$$\begin{aligned} B_p(g, \eta) &= \frac{K_p}{2} \operatorname{sech} \left(\sum_{e \in p} [\tau(g) Z_e (1 - Z_{v(e)} Z_{v'(e)}) + \lambda(\eta) Z_e] \right), \\ Q_v(g) &= \frac{(1 - A_v) M_v}{2} \operatorname{sech} \left(\tau(g) \sum_{e \in v} (1 - Z_e) Z_{v(e)} Z_{v'(e)} \right), \end{aligned} \quad (7.15)$$

with

$$\begin{aligned} K_p &= - \prod_{e \in p} X_e + \prod_{e \in p} e^{-\tau(g) Z_e (1 - Z_{v(e)} Z_{v'(e)})} \eta^{-Z_e}, \\ M_v &= -X_v + \prod_{e \in v} e^{-\tau(g) (1 - Z_e) Z_{v(e)} Z_{v'(e)}}, \end{aligned} \quad (7.16)$$

where $\lambda(\eta) = \log(\eta)$ and $\tau(g) = -\log(g)/4$. Although for $g \leq 0$, the complex-valued logarithmic function $\tau(g)$ encounters a singularity and branch points, the plaquette and the vertex projectors in Eq. (7.15) remain analytic in g for $g \in (-1, 1)$, i.e. all the singularities are removable. We present the details of the derivation in Appendix D.1.

At $g = 1$ and $\eta = 1$, we recover $B_p(1, 1) = B_p$ as in Eq. (7.4). The vertex term $Q_v(1) = (1 - A_v)(1 - X_v)/2$ fixes the spin on the vertex v to be in the state $|+\rangle$ in the ground state. The Hamiltonian is thus the same as the toric code Hamiltonian Eq. (7.4) with the additional vertex terms. For $g = 1$ and $\eta > 0$, when removing the Q_v term, the Hamiltonian is a parent Hamiltonian for the toric code ground state with string tension shown in Eq. (7.5). An alternative parent Hamiltonian is given in Ref. [244]. At $g = -1$ and $\eta = 1$, we recover the fixed-point Hamiltonian for the SET-TC phase:

$$\begin{aligned} B_p(-1, 1) &= \frac{1}{2} \left(1 - \prod_{e \in p} X_e e^{-i\pi Z_e (1 - Z_{v(e)} Z_{v'(e)})/4} \right), \\ Q_v(-1) &= \frac{1 - A_v}{2} \left(1 - X_v \prod_{e \in v} e^{i\pi (1 - Z_e) Z_{v(e)} Z_{v'(e)}/4} \right). \end{aligned} \quad (7.17)$$

Note that the projector $(1 - A_v)$ in $Q_v(-1)$ is necessary for $Q_v(-1)$ being Hermitian.

The Hamiltonian also has the duality $H(-g, \eta) = UH(g, \eta)U^\dagger = e^{-i\pi H_{\text{pivot}}/8} H(g, \eta) e^{i\pi H_{\text{pivot}}/8}$, where U is a finite-depth local quantum circuit given in Eq. (7.9) and H_{pivot} is an example of a pivot Hamiltonian [232]

$$H_{\text{pivot}} = \sum_{e \in E} (1 - Z_e)(1 - Z_{v(e)} Z_{v'(e)}), \quad (7.18)$$

where E denotes the set of all the edges. The Hamiltonians at $g > 0$ and $g < 0$ thus share the same spectrum. At the line $g = 0$, the Hamiltonian has an enhanced $U(1)$ pivot symmetry generated by H_{pivot} , i.e. $[\exp(i\theta H_{\text{pivot}}), H(0, \eta)] = 0, \forall \theta \in \mathbb{R}$, see Appendix D.2 for the proof. The $U(1)$ symmetry manifests itself in the $O(2)$ criticality along the SET transition line, which we discuss in the next section (see Fig. 7.4).

By tuning the parameter g from -1 to $+1$, the system can change from one SET phase to another SET phase. However, an intermediate phase generically exists between the two SET phases. The parameter η can be tuned to avoid such an intermediate phase so that a direct transition between the two SET phases is possible.

7.5. Phase diagram and order parameters

To obtain the phase diagram of the system, we extract the correlation length of the ground state by the corner transfer matrix renormalization group algorithm [247, 248] (see Appendix D.6 for details), and the resulting phase diagram is shown in Fig 7.4a. The system hosts three distinct phases, the SET-TC phase with \mathbb{Z}_2 topological order and a non-trivial \mathbb{Z}_2^T symmetry fractionalization, the TC phase with \mathbb{Z}_2 topological order and trivial symmetry fractionalization, and a totally trivial phase without topological order. Note that the norm of each MPS loop inside the wavefunction $|\Psi(g, \eta)\rangle$ contributes weight to the amplitude of the configuration (an explicit expression for the amplitude is given in Appendix D.3).

The universality class of the phase boundaries can be determined by mapping the squared norm of the decorated TNS to the partition function of classical statistical models. As shown in Appendix D.3, along $g = \pm 1$, the decorated TNS can be mapped to the 2D classical Ising model, the two critical points are located at $(g, \eta) = (\pm 1, 3^{-1/4})$. For $g \neq 0$ and $g \neq \pm 1$, the model is mapped to an anisotropic Ashkin-Teller model (see Appendix D.4). The phase boundary between the TC (SET-TC) phase and the trivial phase is thus described by the $(2+0)$ D Ising CFT with a central charge $c = 1/2$. Along $g = 0$, the decorated TNS can be mapped to the classical $O(2)$ loop model, which has a high-temperature gapped phase and a low-temperature critical phase described by the compactified free boson CFT with central charge $c = 1$ [249–251]. The transition between low- and high-temperature phases at $\eta = 2^{1/4}$ is of the Kosterlitz-Thouless (KT) type. Therefore, the phase boundary between the SET-TC and the TC phase, including the tricritical point, has a central charge $c = 1$.

We further characterize these phases using non-local order parameters. The presence of an intrinsic topological order can be detected by the topological entanglement entropy (TEE) (see e.g. Section 2.1). The entanglement entropy of a topological state satisfies $S \sim aN - \gamma$, where γ is a universal correction called TEE, a is a non-universal coefficient from the area law, and N is the length of the entanglement bipartition. On a torus, the TEE has to be extracted from the minimally entangled states (MES) [134], which are topologically degenerate ground states in a special basis such that the entanglement entropy is minimal. There are four MES $|\Psi_{\alpha}\rangle$ labelled by the anyons $\alpha = \mathbf{1}, \mathbf{e}, \mathbf{m}, \mathbf{f}$.

Instead of the von Neumann entropy, we consider the Renyi entropy, which is easier to calculate using tensor-network methods. As shown in Fig. 7.3b, for a system on an infinitely long cylinder with circumference N , the n -Renyi entropy is

$$S_{\alpha}^{(n)} = \frac{1}{1-n} \log \text{Tr}(\rho_{\alpha}^n), \quad \rho_{\alpha} = \text{Tr}_R |\Psi_{\alpha}\rangle \langle \Psi_{\alpha}|, \quad (7.19)$$

where Tr_R is the partial trace over all physical degrees of freedom of the MES $|\Psi_{\alpha}\rangle$ on the right half of the infinite cylinder. The topological Renyi entropy is independent of n [104], we choose $n = 2$ for our calculation. In Appendix D.8, we exploit the tensor-network approach to calculate the TEE γ directly in the limit $N \rightarrow \infty$ without extrapolation. The TEE obtained from a boundary MPS with bond dimension $\chi = 20$ is shown in Fig 7.4b. In the SET-TC phase and the TC phase, the four MES $|\Psi_{\alpha}\rangle$ give the same TEE $\gamma = \log 2$ as expected from the \mathbb{Z}_2 topological order. In the trivial phase, the ground state of the system becomes unique on a torus and the MES states are no longer well-defined. In this unique ground state, we indeed obtain $\gamma = 0$, indicating the absence of topological order.

As the SET-TC phase and the TC phase share the same TEE, we can further distinguish the two using the membrane order parameter (MOP), which captures the symmetry fractionalization pattern of SET phases [229]. In our case, the system has an additional \mathbb{Z}_2 symmetry generated by a global spin flip on the vertices $\prod_v X_v$ (it follows from the

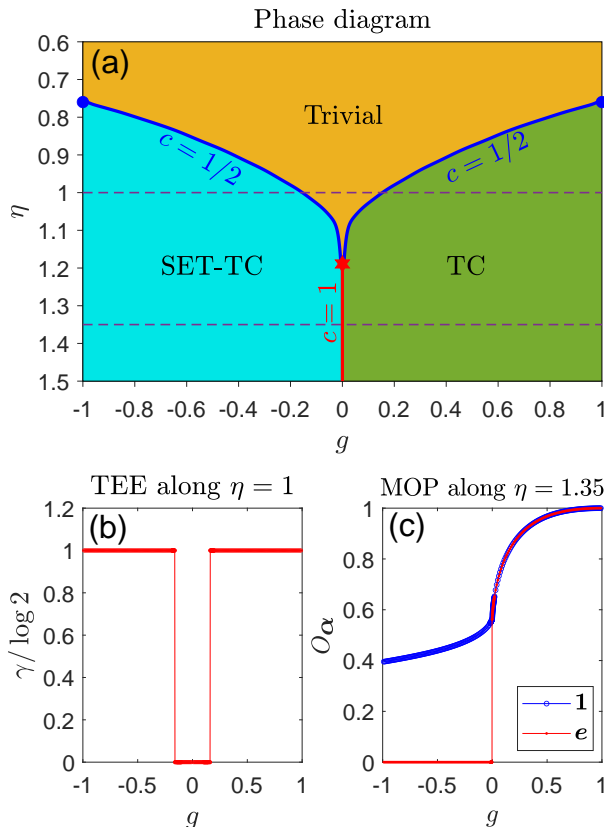


Figure 7.4.: (a) Phase diagram of the decorated TNS spanned by the string tension η and a tuning parameter g . The central charge is denoted by c . The phase transitions along vertical lines at $g = \pm 1$, highlighted by the blue dots, occur at $\eta = 3^{-1/4}$. The tricritical point is at $(g, \eta) = (0, 2^{1/4})$. (b) The topological entanglement entropy of a minimally entangled state along $\eta = 1$. (c) The membrane order parameters from the minimally entangled states $\mathbf{1}$ and \mathbf{e} .

additional global spin flip symmetry in the 1D model Eq. (7.1)). This allows us to define a MOP on an infinitely long cylinder as

$$O_{\alpha} = \lim_{N \rightarrow \infty} \left(\langle \Psi_{\alpha} | \prod_{v \in R} X_v | \Psi_{\alpha} \rangle \right)^{1/N}, \quad (7.20)$$

where $|\Psi_{\alpha}\rangle$ is an MES, N is the circumference of the cylinder, and R is the set of vertices of the right part of the cylinder. It can be shown that the MOP has a selection rule and dictates that $O_{\alpha} = 0$ if the symmetry fractionalizes non-trivially on the anyon α ². As shown in Appendix D.7, the calculation of the MOP is similar to that of the TEE, and we can use tensor-network methods to directly calculate O_{α} in the limit $N \rightarrow \infty$ without extrapolation. Fig. 7.4c shows the MOP obtained from a boundary MPS with $\chi = 20$. Since the symmetry fractionalization on $\mathbf{1}$ and \mathbf{e} is identical to that on \mathbf{m} and \mathbf{f} , we have $O_{\mathbf{1}} = O_{\mathbf{m}}$ and $O_{\mathbf{e}} = O_{\mathbf{f}}$. We only show $O_{\mathbf{1}}$ and $O_{\mathbf{e}}$ in Fig. 7.4c. In the TC phase, $O_{\mathbf{1}}$ and $O_{\mathbf{e}}$ are non-zero, implying no symmetry fractionalization on the anyons. In the SET-TC phase, $O_{\mathbf{e}}$ vanishes, indicating that the symmetry fractionalizes on the \mathbf{e} and \mathbf{f} anyons.

²More precisely, using the additional symmetry $\prod_v X_v$ and the technique from Ref. [172], one can show that the MOP will vanish if only one of the symmetries $K \prod_v X_v$ or K fractionalizes over the anyons. Our example belongs to the first case. The symmetry K is not fractionalized, similar to the 1D SPT chain used for the decoration.

An alternative way to distinguish the SET-TC phase from the TC phase is by examining the entanglement spectrum. In the SET-TC phase, the time-reversal symmetry represented by \mathcal{T} on $\rho_{\mathbf{1}}$ and $\rho_{\mathbf{m}}$ satisfies $\mathcal{T}^2 = 1$, whereas the time-reversal symmetry on $\rho_{\mathbf{e}}$ and $\rho_{\mathbf{f}}$ is represented projectively, i.e., $\mathcal{T}^2 = -1$, due to symmetry fractionalization, as shown in Appendix D.8. Therefore, from Kramers' theorem, each level of the entanglement spectra in the \mathbf{e} and \mathbf{f} sectors is even-fold degenerate in the SET-TC phase, which is an important feature inherited from 1D non-trivial SPT states [13].

7.6. Discussion and conclusion

In this chapter, we construct a family of 2D TNS that corresponds to the exact ground states of \mathbb{Z}_2^T -symmetric Hamiltonians. In particular, the system describes a direct continuous quantum phase transition between two distinct SET phases with \mathbb{Z}_2^T time-reversal symmetry. Although we expect that these constructed ground states require fine tuning to be reached, they serve as a useful starting point for a more general understanding of the SET phase transitions.

Along the phase boundary separating the two SET phases, we obtain a particularly interesting class of toy states which are ground states of local Hamiltonians. For example, one of these states is $|\Psi(0, \sqrt{2})\rangle \propto \sum_C 2^{N(C)/2} |C\rangle$, where C labels the configurations of closed loops decorated with GHZ states, and $N(C)$ denotes the total number of loops in C . The power-law decay of correlation functions is revealed by non-local operators [252]. Moreover, these states have an area-law entanglement entropy up to a subleading logarithmic correction [253]. They serve as interesting examples for studying topological critical phases [252, 254, 255], whose universality is characterized by non-local correlators.

The phase diagram of the system can be further extended. As we discuss in Appendix D.4, by introducing Ising couplings to vertex spins, it is possible to continuously tune the system along a tensor-network solvable path to ferromagnetic or antiferromagnetic phases, where the \mathbb{Z}_2^T symmetry is spontaneously broken. By the quantum-classical mapping mentioned in Section 7.5, the phase boundaries of these transitions can be shown to align with the critical regimes of an anisotropic Ashkin-Teller model.

The construction can be straightforwardly generalized to enrich the double-semion model [52, 123]. When restricted to the closed loop subspace, the toric code model and the double-semion model are related by a diagonal unitary transformation $U_{\text{TC-DS}} = \sum_C (-1)^{N(C)} |C\rangle \langle C|$, where C is a configuration of decorated loops. Because $U_{\text{TC-DS}}$ commutes with the decoration procedure (we state this more precisely in Appendix D.1), the phase diagram in Fig. 7.4a is preserved under the unitary transformation. In the non-trivial SET double-semion phase, the symmetry fractionalizes over the semions and the anti-semions. For the gauge group \mathbb{Z}_2 and the global symmetry \mathbb{Z}_2^T , the SET classification based on Abelian Chern-Simons theories is given by the third cohomology group $H^3(\mathbb{Z}_2 \times \mathbb{Z}_2^T, U(1)) = \mathbb{Z}_2 \times \mathbb{Z}_2$ [22, 25]. Here the first \mathbb{Z}_2 index originates from the Dijkgraaf-Witten classification and it labels two topological orders described by the toric code and double-semion theories. The second \mathbb{Z}_2 labels different symmetry fractionalization patterns over the anyons under time-reversal symmetry. Our construction thus generates direct phase transitions between all of those with the same topological order.

By a similar procedure, decorating the domain walls in 2D \mathbb{Z}_2 SPT phases gives rise to SPT phases protected by the symmetry $\mathbb{Z}_2 \times \mathbb{Z}_2^T$ [227]. By a duality transformation, the SET-TC and the TC phases can be mapped to the 2D $\mathbb{Z}_2 \times \mathbb{Z}_2^T$ SPT phases (see Ref. [226] and Appendix D.4), the tensor-network solvable phase diagram Fig. 7.4a is thus dual to a $\mathbb{Z}_2 \times \mathbb{Z}_2^T$ -protected phase diagram, where the two SET phases are replaced by two 2D $\mathbb{Z}_2 \times \mathbb{Z}_2^T$ SPT phases and the trivial phase is replaced by a ferromagnetic phase in which the \mathbb{Z}_2 symmetry is spontaneously broken.

A key ingredient for the construction is the existence of an MPS path that interpolates between the 1D SPT phases with a constant bond dimension. It will be interesting to apply the proposed construction to the generalization of such MPS paths, such as the MPS skeletons [243], to obtain a broader class of SET phases and their phase transitions. The simplicity of the TNS description of the ground states raises the question of whether these states admit an efficient quantum circuit representation and are easy to study on a quantum computer, similar to the 1D MPS path [143]. While the SET fixed points may be efficiently prepared [4, 5], the existence of an efficient state preparation near or at the critical points remains an intriguing open question. We address this open question in the next chapter using the subclass of 2D TNS, the isometric tensor-tensor states.

8. Efficient quantum circuits and holographic quantum algorithms for simulating topological quantum phase transitions from 2D isometric tensor networks

The search for exotic quantum phases of matter is a central theme in condensed matter physics. While the last decades have witnessed tremendous progress in our theoretical understanding of topologically ordered phases, physical realization of topological phases remains a significant challenge, with the fractional quantum Hall effect [48] representing one of the few unambiguous examples in the solid state. The advent of programmable quantum hardware has opened up unprecedented avenues for accessing novel quantum states. Recently, breakthroughs were made in the realization of topologically ordered states using Rydberg simulators [65, 255], superconducting qubits [4, 5] (see also Part I) and trapped ions [70, 256]. While these realizations focused on specific topological states, the important question of realizing the topological quantum phase transitions, i.e. transitions that cannot be detected by any local order parameters, is more challenging. Progress has been made in one-dimensional (1D) symmetry-protected topological (SPT) systems by exploiting the correspondence between sequential quantum circuits and matrix-product states (MPS) [220] (a brief review is given in Section 7.1). The exact ground states across SPT phase transitions can be represented by a parameterized MPS with a finite bond dimension and can be physically realized using its efficient quantum circuit representation [143, 242, 243]. General two-dimensional (2D) tensor-network states (TNS) with a finite bond dimension can describe exact ground states across various quantum phase transitions—including some critical states with a power-law correlation [3, 235–238, 240, 241]. However, general 2D TNS cannot be efficiently prepared on a quantum computer [221]. Recently, measurements are explored as a tool for generating such 2D TNS-solvable ground states [257, 258]. However, post-selection among exponentially many outcomes is required.

One can also consider realizing ground state away from the fixed point by deforming the local unitary gates within the quantum circuit of the fixed point. However, with this approach it is difficult to retain the global symmetry of the system when deforming the circuit. A more subtle issue appears if the state has intrinsic topological order: small deformation of the local gates can lead to non-local perturbation to the wavefunction and the topological order becomes unstable [217]. While these problems pose a significant challenge in working directly with quantum-circuit representation, they can be conveniently addressed in the tensor-network representation: A global on-site symmetry can be preserved by enforcing local conditions on the tensor [214]. The stability of the intrinsic topological order can be ensured by enforcing the correct virtual symmetries on the local tensors [215–217].

With the above motivation, we investigate topological quantum phase transitions between states *exactly* representable by 2D isometric tensor-network states (isoTNS) [128]. IsoTNS form a subclass of 2D TNS with an additional isometry condition and can represent a large class of gapped quantum phases [129]. The isometry condition establishes a 2D analogue of the canonical form in 1D MPS and directly leads to the correspondence

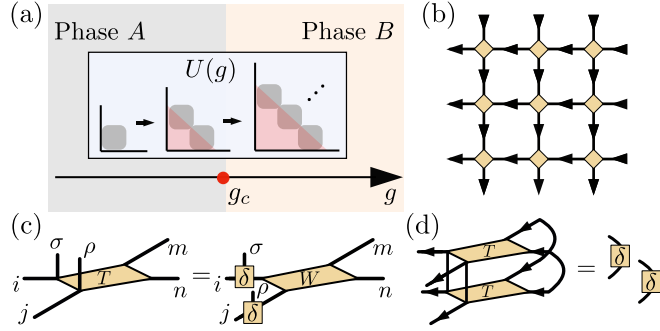


Figure 8.1.: (a) Designing parametrized sequential circuits for ground states crossing 2D quantum phase transitions. (b) Each yellow node labels a tensor. The isoTNS wavefunction is obtained by contracting the virtual legs of the tensors. The physical legs of the tensors, which encode the physical spins, are omitted. (c) Each tensor has two physical legs (σ and ρ) and four virtual legs i, j, m, n . The local tensor T is a product of some matrix W and two δ -tensors. The δ -tensor is 1 when all the legs are equal, and zero otherwise. (d) The isometry condition. The contraction of the tensor T with its complex conjugate (depicted with flipped physical legs) yields two two-leg δ -tensors. The arrows indicate the direction of the contraction.

between isoTNS and linear sequentially generated quantum circuits [128, 130] (see a brief review of this property in Chapter 6). The isoTNS have the advantages from both the tensor-network and efficient quantum-circuit presentation, they therefore constitute an ideal starting point for exploring efficient realization of ground states across 2D quantum phase transitions, going beyond realizing specific fixed points.

In this chapter, we show how to use isoTNS as a tool to design efficient quantum circuits across quantum phase transitions (see Fig. 8.1a). We propose a simple “plumbing” method to construct isoTNS such that the coefficients in the wavefunction can be associated with the Boltzmann weights of certain 2D classical partition functions. By introducing an internal parameter, the system can be deformed continuously from one phase to another phase via a quantum phase transition. We illustrate this method by constructing a quantum phase transition in the ground states between symmetry-enriched topological (SET) phases, where the system has an intrinsic \mathbb{Z}_2 topological order enriched by an anti-unitary \mathbb{Z}_2^T symmetry. We discuss the properties of the ground state both away from and at the transition point. At the end, we discuss a hardware-efficient experimental proposal to realize the isoTNS path and probe the SET phase transition based on the holographic duality of the isoTNS.

8.1. Isometric tensor networks and classical partition functions

We focus our discussion on the 2D systems, the generalization of the construction to arbitrary higher dimensions is straightforward. We begin by briefly reviewing the concept of 2D TNS (Fig. 8.1b). Consider a 2D spin system on a square lattice with local Hilbert space dimension d and each spin is located on the edges of the square lattice. A 2D TNS can be defined via a rank-6 local tensor $T_{ijmn}^{\sigma\rho}$ at each vertex, where σ (ρ) represents the spin degree of freedom on the left (bottom) edge connected to the vertex. The legs i, j, m, n label the virtual degrees of freedom (Fig. 8.1c). The dimension of the virtual legs is referred to as bond dimension. For a translationally invariant system with N spins, the

8.2. A continuous isoTNS path between symmetry-enriched topological phases crossing a quantum critical point

wavefunction is obtained by contracting the neighbouring virtual legs of all the tensors

$$|\psi\rangle = \sum_{\sigma_1, \dots, \sigma_N} \text{tTr}(\{T^{\sigma_1 \sigma_2}, \dots, T^{\sigma_{N-1} \sigma_N}\} |\sigma_1, \dots, \sigma_N\rangle), \quad (8.1)$$

where tTr denotes the tensor contraction.

Classical partition functions can be encoded in the TNS with a finite bond dimension [235], such that the squared norm of the coefficients in the wavefunction is equal to the Boltzmann weights in the classical partition function [50]. The thermal phase transition in the classical system is mapped to a quantum phase transition, where the classical criticality is mapped to criticality in the wavefunction. We consider the restriction of this class of tensor networks to isoTNS. To achieve this, we impose the following conditions on the local tensors: (i) The local tensor $T_{ijmn}^{\sigma\rho}$ can be decomposed as

$$T_{ijmn}^{\sigma\rho} = \sum_{i', j'} \delta_{ii'}^\sigma \delta_{jj'}^\rho W_{i'j'mn}, \quad (8.2)$$

where $W_{i'j'mn}$ is a $d^2 \times d^2$ matrix and δ_{ab}^σ denotes a ‘‘plumbing’’ δ -tensor such that $\delta_{ab}^\sigma = 1$ if $\sigma = a = b$, and zero otherwise. This relation is depicted in Fig. 8.1c. This condition relates the quantum wavefunction to a classical partition function in the following way: The tensor δ_{ab}^σ makes the virtual legs equivalent to the physical degrees of freedom in the quantum system. As a result, the probabilities for the spin configurations at each vertex in the tensor-network wavefunction are encoded in a local tensor $R_{ijmn} = |W_{ijmn}|^2$, where R is a weight matrix for spin states i, j, m, n around the vertex. The transfer matrix of the isoTNS is thus the same as the transfer matrix for a classical partition function contracted from the local weight matrix (see Appendix E for more details). (ii) We enforce an isometry condition on the local tensor $T_{ijmn}^{\sigma\rho}$. More precisely, we require

$$\sum_{\sigma, \rho, m, n} \left(T_{ijmn}^{\sigma\rho} \right)^* T_{i'j'mn}^{\sigma\rho} = \delta_{ii'} \delta_{jj'}. \quad (8.3)$$

This is pictorially shown in Fig. 8.1d. The set of TNS satisfying this condition is isoTNS. For the plumbed isoTNS satisfying Eq (8.2), the 2D isometry condition Eq. (8.3) is satisfied if and only if

$$\sum_{m, n} |W_{ijmn}|^2 = 1, \quad \forall i, j. \quad (8.4)$$

For a given bond dimension, the W -matrix representing the plumbed isoTNS forms a finite dimensional manifold. Our strategy is to search for continuous paths within this manifold that connect between ground states having different quantum phases. It is worth mentioning that in 1D the plumbed isoTNS is a subclass of the canonical form for 1D matrix-product states (MPS). Simple examples of quantum phase transitions previously known in MPS [242] can also be constructed using the plumbing construction (see Appendix E for an explicit discussion).

8.2. A continuous isoTNS path between symmetry-enriched topological phases crossing a quantum critical point

Let us consider a spin-1/2 system where each spin is encoded by a qubit with the Pauli basis such that $Z|0\rangle = |0\rangle$ and $Z|1\rangle = -|1\rangle$. The physical leg of the tensor has dimension $d = 2$, Eq. (8.2) implies that the plumbed isoTNS has bond dimension $D = d = 2$. The

toric code ground state with \mathbb{Z}_2 topological order [43] naturally falls into this family of isoTNS, with

$$W^{(\text{TC})} = \begin{pmatrix} |00\rangle & |01\rangle & |10\rangle & |11\rangle \\ \frac{1}{\sqrt{2}} & 0 & 0 & \frac{1}{\sqrt{2}} \\ 0 & \frac{1}{\sqrt{2}} & \frac{1}{\sqrt{2}} & 0 \\ 0 & \frac{1}{\sqrt{2}} & \frac{1}{\sqrt{2}} & 0 \\ \frac{1}{\sqrt{2}} & 0 & 0 & \frac{1}{\sqrt{2}} \end{pmatrix} \begin{matrix} |00\rangle \\ |01\rangle \\ |10\rangle \\ |11\rangle \end{matrix}, \quad (8.5)$$

where the indices label the legs i, j, m, n in W_{ijmn} . If we view $|1\rangle$ as occupied by a string and $|0\rangle$ as empty, the eight non-zero entries in W are exactly the eight vertex configurations with no broken strings. The resulting wavefunction is an equal-weight superposition of all the closed-loop configuration as we expect from the toric code ground state. Consider the following continuous path of W -matrix for $g \in [-1, 1]$

$$W(g) = \begin{pmatrix} \frac{1}{\sqrt{1+|g|}} & 0 & 0 & \text{sign}(g)\sqrt{\frac{|g|}{1+|g|}} \\ 0 & \frac{1}{\sqrt{2}} & \frac{1}{\sqrt{2}} & 0 \\ 0 & \frac{1}{\sqrt{2}} & \frac{1}{\sqrt{2}} & 0 \\ \sqrt{\frac{|g|}{1+|g|}} & 0 & 0 & \frac{1}{\sqrt{1+|g|}} \end{pmatrix}, \quad (8.6)$$

where the function $\text{sign}(g)$ picks up the sign of g . At $g = 1$, we recover the exact toric code. At $g = -1$, the W -matrix differs from the toric code $W^{(\text{TC})}$ by a minus sign for one of the vertex configurations. This implies that the wavefunction is related to the toric code ground state by a finite-depth local quantum circuit. However, as we will show below that, the two limits belong to distinct quantum phases due to the presence of physical symmetries.

The ground state along this path respects an anti-unitary \mathbb{Z}_2^T symmetry generated by the global spin flip composed with complex conjugation ($\prod_i X_i$) K . While at $g = 1$, the system is the usual toric code with only an intrinsic \mathbb{Z}_2 topological order, at $g = -1$ the TNS describes a ground state with a non-trivial symmetry-enriched topological (SET) order, where the \mathbb{Z}_2 topological order is enriched by \mathbb{Z}_2^T symmetry. Along the path, there exists a \mathbb{Z}_2^T -symmetric local parent Hamiltonian which remains frustration-free and continuous in g (see Appendix E).

Recall that a topologically ordered system has a non-trivial SET order when the anyonic excitations of the system transform non-trivially under the physical symmetries [22–24, 28]. The SET order in the ground state can be diagnosed by inspecting how the action of the physical symmetries on the bulk relates to a non-trivial action on the open boundary of the system; the boundary action carries labels that characterize the phases of the system [215, 216, 218]. To see this explicitly, we consider a cylindrical geometry with open ends. At the boundary, the uncontracted virtual bonds of the TNS form an effective 1D system (see Fig. 8.2a). Suppose a physical symmetry U is applied to the ground state in the bulk; this physical action is equivalent to a virtual action of a boundary operator V . Using the TNS defined by Eq. (8.6) on a cylinder with circumference $L \in 4\mathbb{N}$, we have

$$U = \left(\prod_i X_i \right) K \rightarrow V(g) = \left(\prod_b X_b \right) \text{sign}(g)^{\frac{n(n-1)}{2}}, \quad (8.7)$$

where b labels the virtual bonds forming the effective boundary spin-1/2 system and $n = \sum_b (1 - Z_b)/2$ is a sum of Pauli Z matrices at each virtual bond (n essentially counts the number of states $|1\rangle$ on the boundary). For \mathbb{Z}_2^T symmetry, a discrete label for the SET phase can be obtained from $V(g)^* V(g) = \text{sign}(g)^P$, where $*$ denotes the complex conjugation and P is the parity of the boundary spin system. Different parity P corresponds to

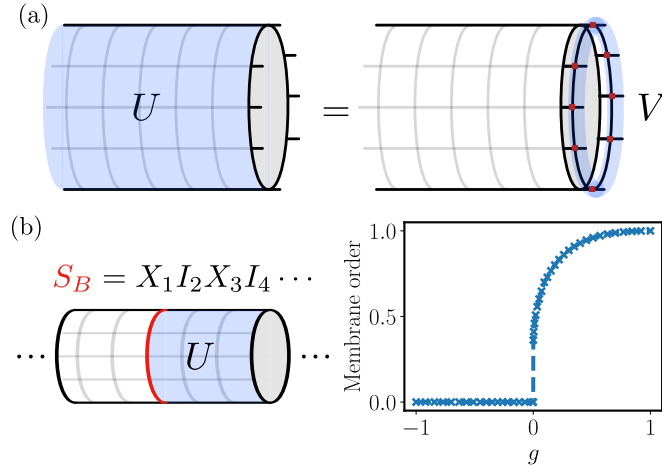


Figure 8.2.: Detecting SET order: (a) Physical symmetry U , consisting of Pauli X on all the qubits in the bulk, is mapped to a virtual matrix-product operator (MPO) V on the boundary formed by the uncontracted virtual legs of the tensors. (b) The membrane order \mathcal{M} computed on the minimally entangled ground state corresponding to the anyon \mathbf{e} at the thermodynamic limit. The numerical method for extracting the membrane order is described in Appendix D.7. Here S_B is the appropriated string operator inserted at the boundary of the partial action of the physical symmetry.

distinct anyon labels carried by the minimally entangled states [134]. In our convention, $P = 0$ labels the trivial quasiparticle while $P = 1$ labels the vertex excitation (i.e. the \mathbf{e} anyon) in the toric code. For a given parity, the quantity $V(g)^*V(g)$ is a discrete invariant that labels the elements in the second cohomology group $H^{(2)}(\mathbb{Z}_2^T, \mathbb{Z}_2) = \mathbb{Z}_2$, which classifies the symmetry fractionalization patterns on the anyons in \mathbb{Z}_2 topological order under \mathbb{Z}_2^T symmetry (without permutation of anyons) [22, 25]. Therefore, the symmetry fractionalization patterns on the \mathbf{e} anyon are distinct for $g > 0$ and $g < 0$, the system belongs to different SET phases, with the phase transition occurring at $g = 0$.

Distinct SET orders cannot be measured via any local order parameters, but they can be distinguished via a non-local membrane order parameter [194, 229], which generalizes the usual string order parameters for 1D symmetry-protected topological (SPT) phases [168, 169]. Consider the system on an infinite cylinder and let L be the circumference, a suitable membrane order parameter in this case is given by $\mathcal{M} = \lim_{L \rightarrow \infty} |\langle \psi | S_B U_{\text{subsys}} S_B | \psi \rangle|^{1/L}$, where $U_{\text{subsys}} = \prod_{i \in \text{subsys}} X_i$ acts only partially on the bulk and the closed string operator $S_B = X_1 I_2 X_3 I_4 \dots X_{L-1} I_L$ around the cylinder is the operator on the boundary of U_{subsys} . In Fig. 8.2b, we show the membrane order for the minimally entangled state labeling the \mathbf{e} anyon. At $g < 0$, a non-trivial symmetry fractionalization over the anyon leads to $\mathcal{M} = 0$ due to a superselection rule [172], while $\mathcal{M} \neq 0$ for $g > 0$ corroborates the absence of non-trivial symmetry fractionalization ¹.

8.3. Power-law correlation at the critical isoTNS

Along the entire isoTNS path, the classical weight matrix associated with the isoTNS from Eq. (8.6) is the same as the weight matrix of the classical eight-vertex model which is exactly solvable [259]. At the SET transition point $g = 0$, the classical eight-vertex

¹Since the wavefunction is real, one can use the argument presented in Ref. [172] and show that this additional symmetry implies that the membrane order parameter \mathcal{M} vanishes in a non-trivial SET phase protected by $(\prod_i X_i) K$.

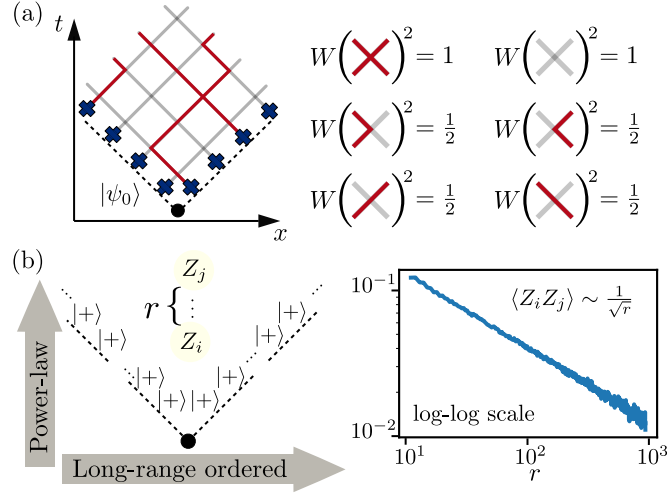


Figure 8.3.: Quantum critical point at $g = 0$: (a) The system in Fig. 8.1c is rotated 45 degrees anticlockwise. The isoTNS is contracted from some boundary state $|\psi_0\rangle$ formed by the boundary qubits (dark blue crosses). An example configuration in the wavefunction is shown. The red line denotes $|1\rangle$ and the grey line denotes $|0\rangle$. The particles are located at the endpoints of the red lines and emanate from the boundary (dashed line). They move according to stochastic jumps determined by the W -matrix. (b) The correlation along the t -direction averaging over 2×10^6 classical trajectories. Here $|+\rangle = (|0\rangle + |1\rangle)/\sqrt{2}$. The correlator shows a power law decay with an exponent $1/2$.

model reduces to a gapless point of the six-vertex model. Interestingly, the corresponding transfer matrix of the six-vertex model has the same spectrum as the Hamiltonian of the 1D ferromagnetic Heisenberg XXX chain (they are solved by the same Bethe Ansatz [259]), exhibiting a spectral gap closing of $O(1/L^2)$. The Heisenberg chain has a long-range order in space and it can support power-law temporal correlation. By analogy, we expect the 2D critical wavefunction to exhibit a similar anisotropy in the correlation functions along the two spatial directions.

In the gapped phases (i.e. $g \neq 0$), the boundary conditions are irrelevant for the bulk properties. However, they become important at the transition point $g = 0$. It is convenient to rotate the lattice in Fig. 8.1b anticlockwise by 45 degrees and consider the system on a planar geometry with open boundaries. The isoTNS is then obtained by initializing the tensor network contraction from an arbitrary 1D boundary state $|\psi_0\rangle$ formed by the qubits at the bottom boundary (see Fig. 8.3a). The resulting critical wavefunction respects a conservation law: The number of lines formed by states $|1\rangle$ is conserved across any horizontal slice, unless they terminate on the boundary. A snapshot of the wavefunction is given in Fig. 8.3a. This conservation law reveals a direct relation between the quantum critical ground state and the dynamics of an 1D classical system. Suppose the boundary state $|\psi_0\rangle$ is a product state in the Pauli- Z basis and we interpret the endpoint vertex of a string of state $|1\rangle$ as being occupied by a particle. In this picture, the conservation law is simply that of the particle number. As the tensor network is sequentially contracted from the bottom to the top, the particles are moving forward in time and tracing out their worldlines (the x - and t -direction in Fig. 8.3a). The Floquet-type dynamics are generated by stochastic jumps with probability given by the matrix elements $|W_{ijmn}|^2$. At a given time t , a single particle either moves to the left or to the right along the x -direction with an equal probability. If two particles meet at the same vertex, they bounce away from each other. The classical picture suggests that the critical wavefunction is a superposition of all

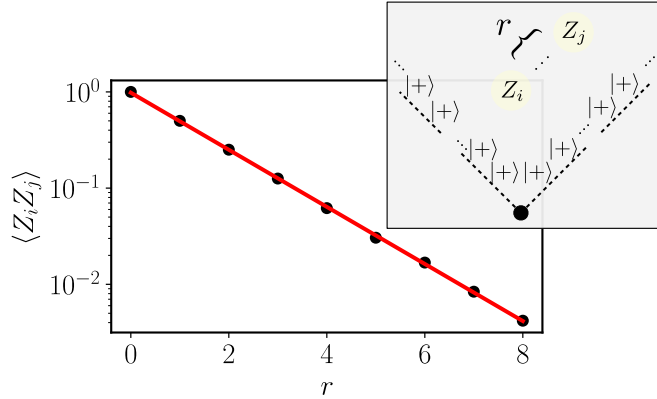


Figure 8.4.: The two-point correlation along the 45-degree direction exhibits an exponential decay. The plot is displayed with log scale in the y -axis. The black dots are the results from Monte Carlo sampling over 1.5×10^6 samples on a system of 21×21 plaquettes. The red line is a linear fit with a gradient around -0.68 .

the worldlines of the particles emanating from the boundary.

A few properties of the critical wavefunction follow directly from the classical picture. (i) The critical wavefunction can have a long-range order along the x -direction. This long-range order comes from the long-range order at the boundary state $|\psi_0\rangle$ due to the particle-number conservation: The number of states $|1\rangle$ at any row along the x -direction is determined by the number of states $|1\rangle$ in $|\psi_0\rangle$. (ii) The critical wavefunction can support correlation with a power-law decay along the t -direction. To see this, suppose the boundary state $|\psi_0\rangle$ only contains few particles. The moving particles have a small chance of interacting with each other and the process thus behaves similarly to an independent random walk with diffusive dynamics. More generally, the process is an example of the nonunitary Floquet XXX model [260–262]. We verify the power-law correlation by computing the spin-spin correlation $\langle Z_i Z_j \rangle$ between sites i, j in the bulk along the t -direction for the boundary condition $|\psi_0\rangle = |++\dots+\rangle$, where $|+\rangle = (|0\rangle + |1\rangle)\sqrt{2}$. This boundary condition is an equal-weight superposition of all the possible classical initial conditions. The resulting correlation corresponds to the typical correlation function over this ensemble. The result is shown in Fig. 8.3b, a clear power-law decay as $1/\sqrt{r}$ can be seen, which is consistent with a diffusive behaviour.

8.4. Anisotropic correlation at the quantum critical point

In the previous section, we show that at the critical point with a boundary state $|\psi_0\rangle = |++\dots+\rangle$, the two-point correlation along a particular spatial dimension decays algebraically. Along other spatial directions, we expect that the correlation decays exponentially, similarly to the spatial-temporal correlation for a single random walker in the 1D classical dynamics.

We note that along the x -direction in Fig. 8.3a, the spin-spin correlation $\langle Z_i Z_j \rangle$ vanishes due to the disordered boundary state. To further verify the correlation, suppose now we measure the correlation along the 45-degree angle (see Fig. 8.4), a clear exponential decay is observed. More generally, when $\langle Z_i Z_j \rangle$ is measured along a direction different from the t -direction in Fig. 8.3a, we expect that the correlation decays exponentially with an angle-dependent correlation length.

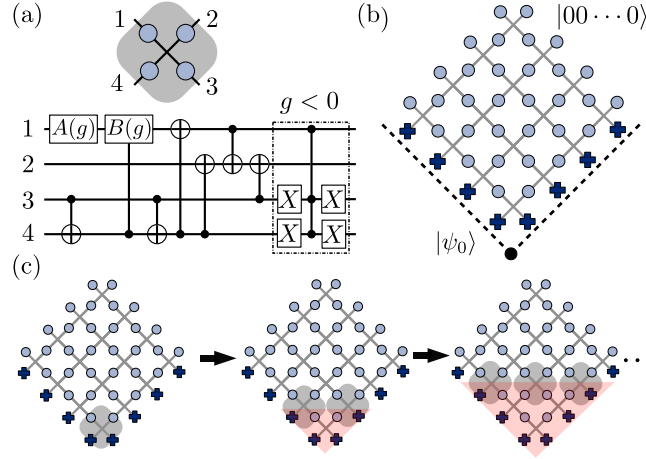


Figure 8.5.: Quantum circuit: (a) A parametrized 4-qubit gate generating the isoTNS. The gate is decomposed into a single-qubit gate, two-qubit CNOT gates and a control-rotation gate. An additional three-qubit gate is included for $g < 0$. Here, $A(g)$ and $B(g)$ are single-qubit gates such that $A(g)|0\rangle = \sqrt{1/(1+|g|)}|0\rangle + \sqrt{|g|/(1+|g|)}|1\rangle$ and $B(g) = HA(g)^\dagger$, where H is the Hadamard gate. The three-qubit gate is a CCZ gate such that $\text{CCZ}|111\rangle = -|111\rangle$ and it acts trivially otherwise. (b) Initialization. The physical qubits (blue circles) are located at the edges of a square lattice. The system is initialized as $|\psi_0\rangle \otimes |00\dots 0\rangle$, where $|\psi_0\rangle$ is the boundary state. (c) Generating the isoTNS. The gate in (a) is applied diagonally in parallel. The red shade marks the spread of the entanglement.

8.5. Realizing 2D quantum phase transition based on holographic duality of isoTNS

The isoTNS path above can be realized experimentally on a 2D array of qubits using an efficient quantum circuit (see Chapter 6). In this section, we present the explicit quantum circuit for the path. Furthermore, we show that the isoTNS path can also be realized in a hardware-efficient way via the holographic duality of isoTNS. We further show how to characterize the SET phase transition experimentally. This provides a minimal proposal for proof-of-principle experiments for the realization of a 2D quantum phase transition on programmable quantum hardware.

8.5.1. Quantum circuit representation

The quantum circuit representation for the isoTNS path can be easily found when the system is defined with open boundaries². The isoTNS tensor is mapped to a 4-qubit quantum gate acting on each vertex, as shown in Fig. 8.5a. The system is initialized as $|\psi_0\rangle \otimes |00\dots 0\rangle$, where $|\psi_0\rangle$ is any 1D quantum state formed by the boundary qubits (see Fig. 8.5b). The state is generated by sequentially applying the 4-qubit gate to each vertex along the diagonal direction, as depicted in Fig. 8.5c. The depth of the circuit thus scales as $O(L)$ as long as the boundary state $|\psi_0\rangle$ can be prepared with an $O(L)$ -depth circuit. Using the exact quantum circuit, the ground states along the entire path can be realized without any post-selection.

²For systems with a periodic boundary condition, there is no clear way to initialize the contraction of the isoTNS.

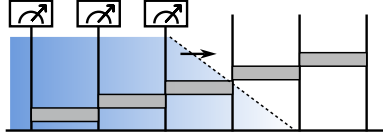


Figure 8.6.: A side view of the sequential circuit for the isoTNS. A lightcone for the isoTNS can be clearly seen (denoted by the dashed line). The measurement outcomes are uncorrelated with the qubits at the far side (right) along which the sequential circuit is applied. This implies that measurements of a tensor product of single-site operators can be sampled sequentially as we sequentially apply the circuit.

8.5.2. Simulating the isoTNS via holographic duality

An 1D matrix-product state (MPS) can be implemented on a quantum simulator with a constant number of qubits by performing the contraction of the MPS temporally. This provides a hardware-efficient way to realize MPS on quantum computers (see e.g. Ref. [263]). Here we show that the same idea can be used to simulate the isoTNS with only an one-dimensional array of qubits. The approach provides a hardware-efficient protocol for simulating the 2D topological quantum phase transition described by isoTNS on a programmable quantum processor.

The sequential quantum circuit for preparing the isoTNS (Fig. 8.5c) has a simple causal structure. Following the direction of the sequential circuit, the measurements of any local operators supported at the bulk of the wavefunction are unaffected by the qubits at the far side along the direction of the sequential circuit (see Fig. 8.6). Consequently, the measurement of a tensor product of single-site Hermitian operators $\langle O_1 O_2 \cdots O_N \rangle$ is equivalent to a sequential measurement as follows:

1. Following the orientation in Fig. 8.5c, we apply the first step of the sequential circuit and measure the single-site observable O_k at the first row of qubits. Each measurement is performed in the basis of O_k for each site k .
2. Proceed to the next step of the sequential circuit and increment to the next row of qubits for measurement, repeat 1.

Note that a key feature of the sequential measurement is that at each step, the measurements are not performed on the full isoTNS, but on the boundary of a partially prepared isoTNS. Due to the causal structure of the isoTNS and commutativity of the measurements on each row, the sampling based on the sequential algorithm is the same as directly sampling $\langle O_1 O_2 \cdots O_N \rangle$ on the full isoTNS wavefunction.

After each step of the sequential measurement, the post-measurement qubit at site k collapses into some eigenstate of O_k and becomes completely disentangled from the system. An immediate simplification is to re-initialize the disentangled qubits back to states $|0\rangle$ and reuse them for the next step of the sequential measurement, as depicted in Fig. 8.7. Then the whole measurement process can be performed with two 1D arrays of qubits (which can be implemented by the even and odd sites of an 1D array of qubits). Since at each step, the quantum system stores the 1D boundary state of the partially prepared isoTNS conditioned on the measurement outcomes, this is a generalization of the holographic realization of 1D MPS to 2D isoTNS.

As a side comment, the sequential measurement also provides a classical numerical method for sampling isoTNS. Since an MPS with a finite-bond dimension can be efficiently sampled, the sequential measurement can be simulated by representing the 1D boundary state as an MPS (conditioned on the sequential measurement outcomes from

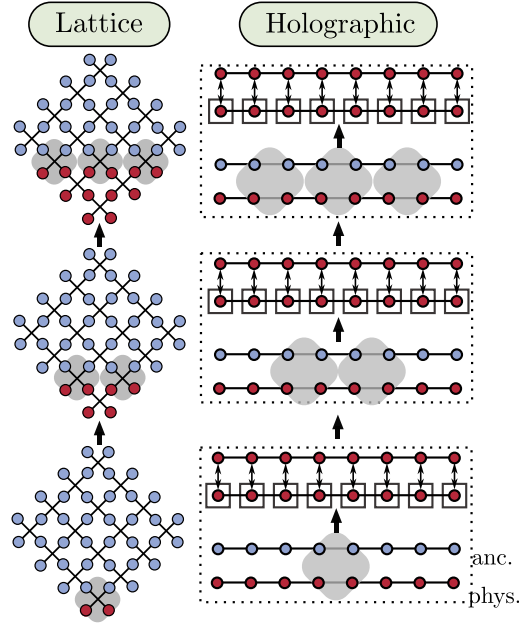


Figure 8.7.: Schematics for the holographic realization of the 2D isoTNS. On the left, the steps of sequential circuit preparation on a 2D lattice are shown. The grey four-qubit gate is given in Fig. 8.5a. On the right, the corresponding step (dashed box) in the holographic realization is shown. At each step, we implement the sequential circuit on both the entangled physical qubit array (red) and the ancillary qubit array (blue), then we measure and collect the outcomes from the output of the physical qubit array and reset the post-measurement qubits to $|0\rangle$ (solid black box). The reseted qubits are swapped and reused as the ancillary qubit array in the next step (double arrow). Iterating the steps is equivalent to sequentially sampling the ground state generated by the sequential circuit. The swap operations can be performed classically by a relabeling of the qubits.

the previous steps). If the 1D boundary state can be efficiently approximated by an MPS, then we expect that the sampling of the isoTNS is classically simulable, otherwise (i.e. when the MPS has an volume-law entanglement) the classical simulation is hard. This is in spirit similar to the numerical method proposed for simulating 2D shallow quantum circuits [264].

With this realization, it becomes easy to measure general observables. Entanglement entropy can also be accessed via the technique of randomized measurements (which is based on sampling bitstrings on random basis) [5, 149, 157]. A signature of phase transition can in principle be captured by observing a diverging correlation length extracted from the measurement of the correlators. However, the measurement of the membrane order parameter used in Section 8.2, which distinguishes the SET phases, relies on the preparation of minimally entangled states on a cylindrical geometry and is therefore experimentally challenging to achieve. In the next section, we discuss how the issue of preparing minimally entangled states can be circumvented and a similar SET membrane order parameter can be measured using the holographic quantum algorithm for the isoTNS.

8.5.3. Probing the SET transition

A defining feature of the non-trivial SET phase is that the symmetry action fractionalizes non-trivially around the anyon. A straightforward order parameter for the SET phases

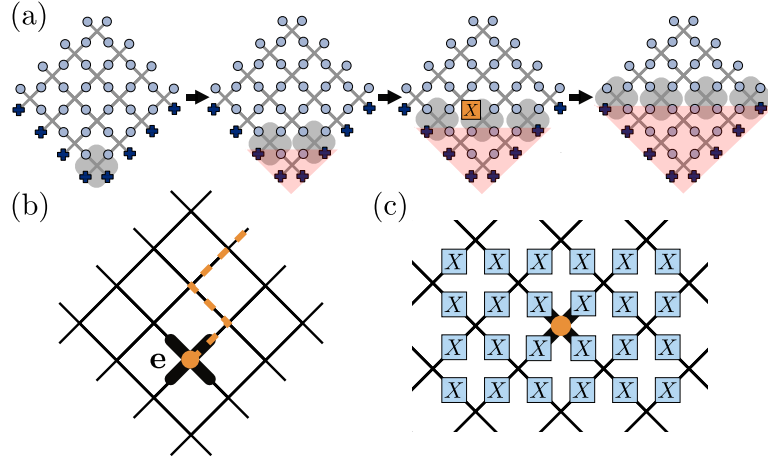


Figure 8.8.: An illustration of a defect (\mathbf{e} anyon) insertion into the isoTNS wavefunction. (a) A defect can be inserted by applying an additional Pauli X flip to an output qubit after a step of the sequential circuit. (b) The resulting wavefunction corresponds to the ground state with an \mathbf{e} anyon at the defected vertex. This is equivalent to generating an \mathbf{e} anyon by applying some dressed string operator connecting the defect and the open boundary. (c) The membrane order parameter consists of a product of Pauli X on adjacent non-overlapping plaquettes surrounding the defect.

is obtained by measuring the membrane order parameter in Section 8.2 around a single anyon in the bulk. The membrane order parameter, which consists of partial symmetry action, will vanish if there is a non-trivial symmetry fractionalization and remain non-zero otherwise.

The difficulty of this approach lies on the creation of a single anyon in the bulk. While this is easy at the two fixed points of the toric code ($g = \pm 1$), where the creation operators for the anyons are some string-like operators that are exactly known and are simple to realize, efficient ways to create and manipulate the anyons are not a priori known away from the fixed-point limits.

The use of isoTNS provides a solution to the problem. To create an anyon, we simply need to replace one of the local tensors in the isoTNS by a single “defect” tensor. The defect tensor is still required to satisfy the isometry condition in Eq. (8.3) but unlike the local tensor formed by the states summed to an even parity at each vertex (see Eq. (8.6)), the defect tensor only allows for states that are summed to odd parity to meet at the vertex. The rest of the tensors in the isoTNS stay the same. As a result, the isoTNS wavefunction with a single defect local tensor is orthogonal to the ground state isoTNS. Physically, the defected isoTNS corresponds to the ground state with a single vertex (or \mathbf{e} anyon in the toric code) excitation (potentially dressed by some local pairs of plaquette excitations, or \mathbf{m} anyons) at the defect vertex³. Since the defected isoTNS is still an isoTNS, it can be efficiently generated and simulated via the sequential protocol. An excitation is inserted without the use of explicit particle-creation operators.

On a quantum circuit level, inserting a defect tensor is easy to achieve. In Fig. 8.8a, we show one way of inserting defect by simply flipping an output qubit after one of the sequential steps. The sequential steps afterwards stay the same as before.

³Note that on a closed manifold, we expect that all the anyons above \mathbb{Z}_2 topologically ordered ground state to come in pairs. Here a single anyon is possible due to the open boundary condition, where one anyon is in the bulk, the other anyon condenses on the boundary of the system (see Fig. 8.8b).

Once we insert an \mathbf{e} anyon, we can measure a membrane order parameter \mathcal{M} , where

$$\mathcal{M} = \lim_{L \rightarrow \infty} |\langle \psi | \prod_{i \in P_e} X_i | \psi \rangle|^{1/L}, \quad (8.8)$$

where $|\psi\rangle$ is the wavefunction with inserted excitation and P_e denotes a set of sites on adjacent non-overlapping plaquettes around the anyon (as shown in Fig. 8.8c), and L is the perimeter of the supported region of this membrane. Similar to the membrane order on the minimally entangled states in Section 8.2, for a real wavefunction, we expect this membrane order to vanish at the non-trivial SET protected by $(\prod_i X_i)K$, where K is complex conjugation. In a trivial SET, \mathcal{M} is generically non-zero. Now since \mathcal{M} can be measured by a product of Pauli X , this can be easily measured from the holographic realization of the isoTNS path.

8.6. Discussion and conclusion

In this chapter, we proposed to design efficient quantum circuits for the realization of 2D topological quantum phase transitions using the tool of isoTNS. We achieved this by restricting to a subclass of isoTNS via the plumbing construction, which connects the resulting isoTNS wavefunctions to classical partition foundations. We illustrated the method by constructing a minimal example of an $D = 2$ isoTNS path between distinct SET phases and discussed the experimental protocols for physical realization on a digital quantum computer via the holographic duality of isoTNS.

While we have illustrated the design of an efficient circuit based on a specific isoTNS path interpolating between distinct SET phases, the method can be applied more generally. A large class of topologically ordered states admits exact isoTNS representation where the virtual legs and the physical legs can be related by the plumbing tensor (e.g. string-net states [129]). One can start from these fixed-point isoTNS and apply the plumbing method to prepare other ground states away from the fixed points and potentially cross a quantum phase transition to reach a distinct phase of matter. For example, by adapting the plumbing method to the domain walls of tensor-network virtual legs (the double-line TNS [246]), we expect that an isoTNS path with bond dimension $D = 4$ can be constructed between the toric code and the double-semion ground state with distinct \mathbb{Z}_2 topological order [52, 123], crossing the same critical point as the SET case. The isoTNS path will be analogous to the $D = 4$ non-isometric TNS path studied in Ref. [236], which crosses a critical point with a different six-vertex criticality. Another example is the tensor-network solvable path noted in Ref. [232]. It can be verified that the path is in fact an isoTNS path that can be constructed with the plumbing method. This path interpolates between two 1-form SPT phases with the exact toric code ground state being the critical wavefunction. Another interesting example is to consider a path between two intrinsically topological phases. An exciting direction is to explore the possibility of connecting generic gapped quantum phases via continuous isoTNS paths.

It has been known that the typical correlation in isoTNS follows an exponential decay [265]. An open question remained whether isoTNS can support power-law correlation. In our work, by giving a concrete example, we show that this is indeed possible. More intriguingly, we find that the power-law decay in the example originates from a direct connection between the worldlines of 1D stochastic dynamics and 2D isoTNS ground states. Whether this connection leads to more interesting isoTNS is an open question. The efficient physical realization of 2D topological quantum phase transitions is also a valuable resource for performing and benchmarking algorithms for quantum phase recognition in higher than 1D [2, 180].

9. Summary and outlook

To conclude, let us summarize the main findings of this thesis. We started out by giving a general overview and highlighted the importance of quantum simulation of topologically ordered systems in Chapter 1. With the rapid advances in synthetic quantum systems, the unprecedented degree of control over interacting quantum systems allows for evermore direct access to exotic properties of topologically ordered systems. The thesis aimed to address three core questions:

- (i) How do we realize topologically ordered systems on currently available quantum computers?
- (ii) Once we have realized a topologically ordered system, how do we distinguish these exotic quantum phases of matter?
- (iii) Can we go beyond the realization of specific topologically ordered systems, and realize quantum phase transitions between topologically ordered systems?

Indeed, the questions are too broad to be fully answered and are still under intense active investigation by the broader community. In this thesis, we have shown our contribution to each of these questions.

In Part I, we first briefly reviewed the concept of topologically ordered phases of matter and their characteristic features. We addressed question (i) by describing in Chapter 3 a general algorithm for constructing efficient quantum circuits for the string-net states—a class of exactly solvable models realizing non-chiral topologically ordered systems. In particular, our algorithm yields the theoretically optimal circuit complexity when the system size is increased. We also provided efficient quantum circuits, again with an optimal resource scaling, for creation and manipulation of anyonic excitations above the string-net states. These together form a complete toolkit for the realization of topological ground states on near-term quantum devices. In the following Chapter 4, we presented the successful experimental realization of a 31-qubit \mathbb{Z}_2 topologically ordered state on the Google Sycamore quantum processor using the method in Chapter 3. In particular, we measured various quantities, including the stabilizer values, the topological entanglement entropy (up to 9-qubit subsystems) and the anyonic statistics to establish the high quality of the realization and to provide strong experimental evidence for the topological nature of the wavefunction. The topological states were then used to demonstrate certain aspects of quantum error correction, including logical state injection and logical state readout. The experimental realization marked a milestone in the realization of topologically ordered states on synthetic quantum systems and paved the way to larger-scale quantum simulation of strongly correlated systems. More recently, our methods have been used to successfully demonstrate the non-abelian anyonic braiding [68] and non-abelian ground states of the double Fibonacci model [69].

In Part II, we addressed question (ii) by proposing a simple method to generate a large amount of quantum states as training data for training a quantum convolutional neural network (QCNN) to discover order parameters for quantum phases of matter (Chapter 5). We showed that this method discovers efficiently measurable observables that accurately identify distinct 1D quantum phases protected by time-reversal symmetry. The proposed method can be easily generalized to higher-dimensional systems, including systems with

intrinsic topological order. Although in this case, classical simulation will be severely limited, quantum simulation can be used to perform the training task and discover suitable order parameters for topologically ordered states. At the end of the chapter, we outline another idea to efficiently characterize the topologically ordered phases and the quantum phase transitions between them based on the framework of active quantum error correction. In particular, the recoverability of active quantum error correction naturally leads to an order parameter for emergent 1-form symmetries, which in turn can be used to determine the topological order of the systems. While there are known quantities, such as the entanglement measure, that can be used to detect the topological order from the wavefunction, to our knowledge none of the methods are scalable. Our results in this chapter pointed out novel approaches that could achieve efficient characterization of topological order in synthetic quantum systems.

In Part III, we addressed question (iii) by drawing inspiration from the method of tensor networks. In Chapter 6, we reviewed the basic concepts of tensor networks in 1D and 2D, and the efficient preparation of tensor-network states. In Chapter 7, we constructed simple exact tensor-network states with a finite bond dimension describing a quantum phase transition between symmetry-enriched topological (SET) phases. These states demonstrate that the 2D tensor-network states with a finite bond dimension are sufficiently expressive to represent topological quantum phase transitions. However, there are no generic methods to efficiently generate the states on a quantum computer. To achieve efficient generation, in Chapter 8, we used the new concept of 2D isometric tensor networks (isoTNS), which can be efficiently prepared by a sequential linear quantum circuit, as a tool to design efficient protocols to realize topological quantum phase transitions on a quantum computer. We proposed a plumbing protocol which allows for the construction of isoTNS that are closely related to classical partition functions. As an illustration, we constructed the similar isoTNS-solvable SET phase transition as in Chapter 7. The construction led to two efficient experimental proposals for the realization and detection of the topological phase transition on near-term quantum computers: one approach is based on the lattice realization of the states with efficient quantum circuits, the other approach is more hardware-efficient and is based on the holographic realization of the isoTNS. In the holographic realization, only the boundary of the isoTNS is realized rather than the full wavefunction, but observables on the full isoTNS can be efficiently measured. The realization considered in this chapter focused on the level of the ground states across a quantum critical point. They will serve as an important first step towards simulation of quantum phase transitions on synthetic quantum systems beyond any classical simulation.

To summarize, we presented our findings in the realization and characterization of topologically ordered systems on gate-based quantum computers by addressing questions (i)-(iii). Our findings serve as valuable resources for the broader community of quantum simulation, quantum information and quantum many-body physics. We also expect that our findings are easily generalizable to the simulation of more general quantum phases of matter on gate-based quantum computers. Furthermore, they open up a few novel and important directions to be explored in the near future:

1. **Realization of specific topologically ordered states/systems.** Can we go beyond the realization of systems with abelian topological order, and realize ground states with non-abelian topological order and braid non-abelian anyons, as done in Chapter 4. E.g., following a similar method, the recent experiment in Ref. [69] realized the ground state of the double Fibonacci string-net model with a non-abelian topological order, but a general braiding is lacking. Can we utilize the ground states with non-abelian topological order to achieve and stabilize (perhaps combined with mid-circuit measurements) universal quantum computation via braiding of the non-abelian anyons [113]?

2. **Characterization of topological order.** Can we gain a better understanding of the learned order parameters from the quantum machine learning approach? E.g. progress has been made recently by the work in Ref. [198], where analytical solutions of QCNN are constructed for a wide class of 1D quantum phases of matter. How about higher-dimensional systems? Can we design an experimental protocol to perform the training assisted by actual quantum hardware? What is the general connection between quantum error correction and quantum phases of matter? Is there a fundamental limit on the resource required to detect a quantum phase transition based on this connection?
3. **Realization of topological quantum phase transitions.** An immediate next step is the experimental realization of the proposals in Chapter 8. It would be very interesting to explore the realized states, e.g. by measuring their topological order and detecting their critical point via experimental probes. An important open question is whether there are other minimal examples constructed from isoTNS paths that can be achieved on near-term quantum devices, and to what extent the proposed construction is general. For example, can we apply the construction to higher dimensional systems such as those with fracton order [266]?

The field of quantum simulation is rapidly evolving. The collision of quantum simulation, quantum information and quantum many-body physics has sparked a fascinating line of research in the physics community. Can we eventually use quantum computers to tackle questions that are beyond the capabilities of any classical computers? Do quantum computers really provide a key to unlock some of the unsolved mysteries in quantum many-body systems? Does this mean that we have a solution for everything? I don't know, but I am very much looking forward to the journey ahead and whatever may be at the other end of the quest.

A. Appendix: Theoretical proposals for simulating string-net states and anyons on gate-based quantum computers

A.1. Isometry Property of Plaquette Operator \hat{B}_p^s and the Open String Operator

Here we prove that \hat{B}_p^s is an isometry on the given subspace as in Fig. 3.3a, when the representative qudit is in the null state initially. This follows directly from the algebraic definition of \hat{B}_p^s in Eq. (2.17). We show this isometry property for the case when $h = 0$ (by continuity of the strings $b = g$ and $c = i^*$), i.e. we compute the overlap

$$\left\langle \begin{array}{c} b \\ \swarrow \quad \searrow \\ a \quad \quad c \\ \swarrow \quad \searrow \\ l_1 \quad \quad j_1 \\ \swarrow \quad \searrow \\ f \quad \quad k_1 \quad \quad e \end{array} \middle| \left(\hat{B}_p^s \right)^\dagger \hat{B}_p^s \middle| \begin{array}{c} b \\ \swarrow \quad \searrow \\ a \quad \quad c \\ \swarrow \quad \searrow \\ l_2 \quad \quad j_2 \\ \swarrow \quad \searrow \\ f \quad \quad k_2 \quad \quad e \end{array} \right\rangle. \quad (\text{A.1})$$

Taking the algebraic definition of \hat{B}_p^s

$$\begin{aligned} & \sum_{g' i' j' k' l'} F_{s^* s g'^*}^{bb^* 0} \left(F_{s^* s g'^*}^{bb^* 0} \right)^* F_{s^* i' s^*}^{c 0 c^*} \left(F_{s^* i' s^*}^{c 0 c^*} \right)^* F_{s^* j' i'^*}^{d c j_1} \left(F_{s^* j' i'^*}^{d c j_2} \right)^* \\ & \quad F_{s^* k' j'^*}^{e j_1^* k_1} \left(F_{s^* k' j'^*}^{e j_2^* k_2} \right)^* F_{s^* l' k'^*}^{f k_1^* l_1} \left(F_{s^* l' k'^*}^{f k_2^* l_2} \right)^* F_{s^* g' l'^*}^{a l^* b} \left(F_{s^* g' l'^*}^{a l^* b} \right)^* \\ = & \sum_{g' i' j' k' l'} \delta_{s^* i' c} F_{s^* s g'^*}^{bb^* 0} \left(F_{s^* s g'^*}^{bb^* 0} \right)^* F_{s^* j' i'^*}^{d c j_1} \left(F_{s^* j' i'^*}^{d c j_2} \right)^* \\ & \quad F_{s^* k' j'^*}^{e j_1^* k_1} \left(F_{s^* k' j'^*}^{e j_2^* k_2} \right)^* F_{s^* l' k'^*}^{f k_1^* l_1} \left(F_{s^* l' k'^*}^{f k_2^* l_2} \right)^* F_{s^* g' l'^*}^{a l^* b} \left(F_{s^* g' l'^*}^{a l^* b} \right)^* \\ = & \delta_{j_1 j_2} \delta_{k_1 k_2} \delta_{l_1 l_2} \sum_{g'} \delta_{s^* g' b^*} F_{s^* s g'^*}^{bb^* 0} \left(F_{s^* s g'^*}^{bb^* 0} \right)^* = \delta_{j_1 j_2} \delta_{k_1 k_2} \delta_{l_1 l_2}, \end{aligned} \quad (\text{A.2})$$

where we repeatedly used the unitarity of the F -symbol in Eq. (2.14). The isometry property required in Eq. (3.6) for $C\text{-}\hat{B}_p$ to be well-defined follows by setting $b = c = 0$. However, the isometry property holds even for $b, c \neq 0$, this allows us to define $C\text{-}\hat{B}_p$ on a more general subspace, it follows that any permissible order, other than the row-wise algorithm presented in the main texts, can be used for the string-net state construction.

In Section 3.5.1, we claim there exist unitary operators that can be used to prepare and move the anyons on the string-net ground state. To see the conditions are compatible with unitarity, it suffices to consider the non-abelian case of the operators, the form of the abelian open string operator is a special case of the non-abelian string operator (see Section 3.5.1). The isometry property of the operator for moving directly comes from the unitarity (2.14) of F -symbol and ω being a phase. The isometry condition on the

preparation operator in Eq. (3.10) can be computed as

$$\begin{aligned}
& \langle mp_1p_2p_2 | \left(\hat{U}_{\text{prep}}^s \right)^\dagger \hat{U}_{\text{prep}}^s | eq_1q_2q_2 \rangle \\
&= \sum_{q'_1, q'_2, p'_1, p'_2} \frac{d_{q'_1}}{d_{q_1} d_s} \left(F_{s^* q'_1 q'_2}^{mp_2^* p_1} \right)^* F_{s^* q'_1 q'_2}^{eq_2^* q_1} \delta_{me} \delta_{p_2 q_2} \delta_{p'_1 q'_1} \delta_{p'_2 q'_2} \\
&= \delta_{me} \delta_{p_2 q_2} \delta_{q_1 p_1} \sum_{q'_1} \frac{d_{q'_1}}{d_{q_1} d_s} \delta_{s q'_1^* q_1} \\
&= \delta_{me} \delta_{p_2 q_2} \delta_{q_1 p_1}, \tag{A.3}
\end{aligned}$$

where the labels m, p_1, p_2 correspond to a qudit configuration matching e, q_1, q_2 in Eq. (3.10). In the second line of the calculation, we used Eq. (2.14) and the definition $d = |v|^2$. The last equality follows from Eq. (2.15).

Note that in Eq. (A.3) it is important to have an ancillary qudit at the endpoint to orthogonalize the states. We expect that a similar construction using ancillary qudits can be used to realize non-simple open string operators. However, non-simple string operators will no longer correspond to a single string type, instead it is a mixture of several string types. Correspondingly, the phase factors ω_k in Eq. (2.19) associated with the strings are replaced with tensors [52]. The construction will likely have to be modified.

A.2. Determine the S -matrix from Measurement

The measurement of S -matrix relies on measuring the expectation of the unitary paths by an interferometry-like experiment (see Section 2.2). The S -matrix is obtained by $S_{ab} = d_a d_b M_{ab} / \mathcal{D}$, where M_{ab} is called the monodromy and is measured by braiding anyons a and b , as shown in Eq. (2.2). Sometimes we know the quantum dimension d of the quasiparticles beforehand and sometimes we do not. However, it turns out we can directly obtain the S -matrix just from the monodromy M_{ab} without knowing the quantum dimensions. This is because we restrict ourselves to anyon models that are described by a unitary modular tensor category, where the S -matrix is unitary. The constraint of unitarity implies $S^\dagger = S^{-1}$, it follows that

$$\left(\frac{d_a d_b}{\mathcal{D}} \right)^2 = \frac{(M^{-1})_{ba}^*}{M_{ab}}, \tag{A.4}$$

where M^{-1} is the inverse of the matrix M_{ab} . We can substitute this relation into Eq. (2.2), S -matrix is directly given by

$$S_{ab} = \sqrt{\frac{(M^{-1})_{ba}^*}{M_{ab}}} M_{ab}, \tag{A.5}$$

solely in terms of the measurement outcomes. Due to the structure of the S -matrix, the monodromy M_{ab} should also satisfy a set of constraints in order to yield a physical S -matrix. For example, from Eq. (A.4) we can immediately conclude that $(M^{-1})_{ba}^* / M_{ab} > 0$. By definition we have $S_{ab} = S_{ba}$, this suggests $M_{ab} = M_{ba}$. The list of constraints is not exhausted. Other constraints can come from, e.g. the Verlinde formula [112] or being (together with the twist factors) the generator for the modular group [109]. In practice, these stringent constraints and Eq. (A.5) will be very helpful in benchmarking the experimental data and identify the correct S -matrix for the underlying modular tensor category from the noisy data.

B. Appendix: Experimental realization of topologically ordered states on a programmable quantum processor

B.1. Linear quantum circuit for the toric code

We provide a general circuit design principle for the toric code on a square lattice. The construction can be implemented on Sycamore to (i) realize toric code with $3+2\lfloor(N-1)/2\rfloor$ nearest-neighbor (NN) CNOT layers for a lattice with $N \times M$ plaquettes, where $N \leq M$, and (ii) encode arbitrary distance- d logical qubit with $d+1$ layers of nearest-neighbour CNOT (however, in some instances this reduces to $(d+3)/2$ layers). Such construction is generalizable to a wide range of Abelian and non-Abelian quantum codes [4]. The linear scaling of the circuit is essentially optimal for topologically ordered states [125].

As mentioned in the main text, a toric code ground state takes the form of a product of commuting projectors

$$|G\rangle = \frac{1}{\sqrt{2^{NM}}} \prod_p (\mathbb{1} + B_p) |00\dots 0\rangle, \quad (\text{B.1})$$

where $N \times M$ is the total number of plaquettes. We note that the choice of A_s and B_p is dual to that originally used by Kitaev; both conventions are widely used in literature and can be related by a single layer of Hadamards. An expansion of the product suggests $|G\rangle$ is an equal-weight linear combination of configurations with each plaquette p acted on by $\mathbb{1}$ or B_p with equal probability. This resembles an equal-weight superposition of all the binary digits with each binary representing the action of operators at p , with the relations $0 \rightarrow \mathbb{1}$ and $1 \rightarrow B_p = \prod_{i \in p} X_i$ (see Fig. B.1). This motivates the following construction of toric code

1. Initialize the product state $|00\dots 0\rangle$ on all the qubits.
2. Identify a representative qubit for each plaquette.
3. Apply Hadamard gate H on each representative qubit.
4. Within each plaquette, apply CNOTs controlled by the representative qubit and targeting the other qubits in the plaquette. Perform the control operation over all plaquettes in an order such that the state stored in the representative qubits are not changed until the CNOT operations in their plaquette have been applied.

Steps 1-3 initialize an equal weight superposition of all the binary strings of representative qubits, in Step 4 we apply the plaquette operator B_p on each plaquette depending on the representative qubit state, which turns a qubit binary string into a plaquette configuration. We illustrate this in further detail in Fig. B.2.

To specify the state on a finite system, we need to impose boundary conditions. These can either be "matching" or "mixed," corresponding to whether the boundary plaquettes are of the same type or not, respectively. For the former, there is a unique ground state—we call this the toric code ground state in the main text. For the latter, the ground state subspace is two-dimensional and can thus encode a logical qubit—we refer to these states as

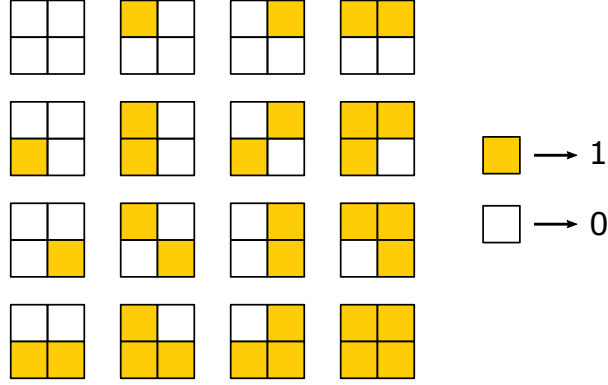


Figure B.1.: The binary correspondence of the configurations (toric code on 2×2 plaquette system). The yellow plaquettes are acted by B_p , the white plaquettes are acted by $\mathbb{1}$. This can be viewed as an equal-weight superposition of binary strings where the binary digit corresponds to the two operators.

logical states of the surface code in the main text. Other boundary conditions are possible, though we do not explore them here, such as periodic boundary conditions placing the code on a torus, or inserting defects inside the lattice.

B.1.1. Matching boundary conditions

In the case of matching boundary conditions, the lattice consists of a rectangular array of complete plaquettes (see Figs. 4.1A and B.2). Following the design principle, all the qubits are initialized with state $|0\rangle$. We choose the top qubit on each plaquette to be the representative qubit.

To proceed, let us consider a system of two plaquette columns, shown in Fig B.2. In panel B, we initialize the qubits, apply Hadamards on the representative qubits, and apply CNOTs from the representative qubits to the other qubits. Note that after B(1-3), the states of representative qubits are stored in the boundary qubits on the sides, so in panel B(4) the side qubits control the CNOTs, reducing the circuit depth. Fig. B.2C shows the wavefunction after the Hadamards. The CNOTs act to “spread out” the 1’s to form loops around the plaquettes, effectively realizing $(\mathbb{1} + B_p)$. As discussed in the main text, each bitstring is an eigenstate of all the stars A_s (blue), and the superposition of all 16 is an eigenstate of all the plaquettes B_p (purple): $B_p |G\rangle$ maintains the same superposition. The situation for the 31-qubit system in Fig. 4.1A is analogous but intractable to draw, involving superpositions of $2^{12} = 4096$ bitstrings.

For systems with more columns, we can grow the toric code starting from the middle out, following a similar strategy. This is shown in Fig. 4.1B. This larger circuit begins similarly to Fig. B.2B, for the central two columns, and then extends outward (overlapping CNOT layers where possible to reduce depth). This procedure generalizes easily to wider systems with linear depth scaling, independent of the height.

B.1.2. Mixed boundary conditions (logical states)

Mixed boundary conditions result in a two-dimensional ground state subspace that can encode a logical qubit. The distance-3 and 5 surface code can be encoded on the lattice shown in Fig. 4.6A, where the plaquette (purple) and the star (blue) stabilizers correspond to $\prod_{i \in p} X_i$ and $\prod_{i \in s} Z_i$. On the boundary, some stars and plaquettes are incomplete, the stabilizers there are taken to be the product of Pauli operators on the two remaining bonds.

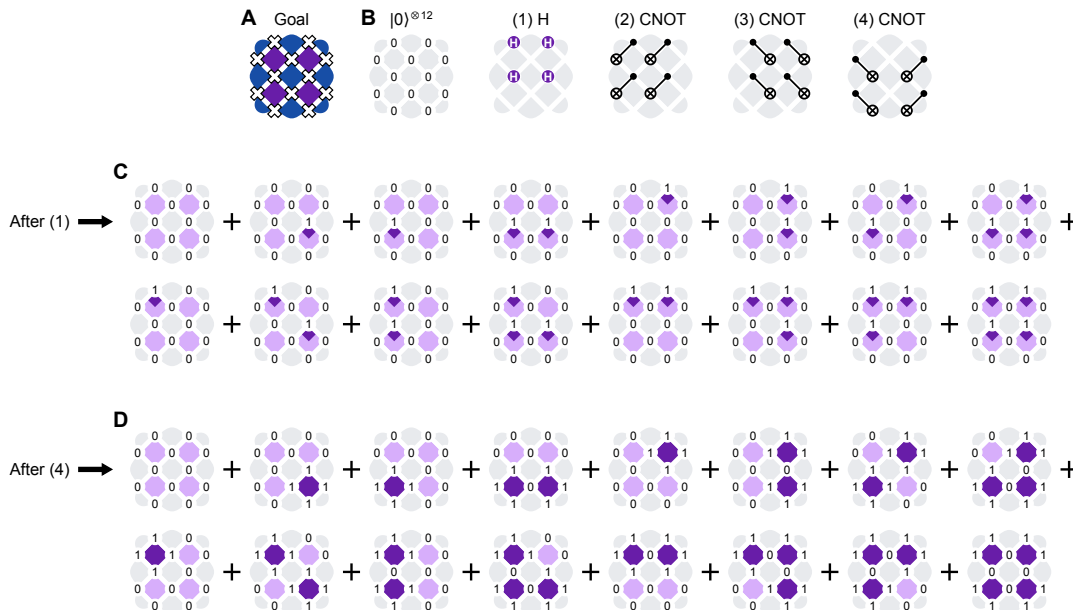


Figure B.2.: **State preparation illustration for 12 qubits, matching boundary.** (A) Schematic showing the 12-qubit system with four plaquettes (purple), similar to Fig. 4.1A. (B) Quantum circuit to transform $|0\rangle^{\otimes 12} \rightarrow |G\rangle$, similar to Fig. 4.1B. (C) Wavefunction after the four Hadamard gates, a uniform superposition of $2^4 = 16$ bitstrings. Each Hadamard is associated with the plaquette (purple) below. We darken a portion of each plaquette underneath the 1's that came from its associated Hadamard. Each plaquette has a darkened portion in exactly half the bitstrings. (D) Wavefunction $|G\rangle$ after the complete circuit.

To construct the circuit for the distance-3 and 5 codes, we again follow the design principle above. The representative qubit is chosen as the outer-top qubit referenced to the center of the system. In the case of the incomplete plaquettes on the top boundary, we choose the outer qubit to be representative (see Fig. B.3 and Fig. B.5).

Fig. B.3 shows the circuit construction to encode the logical state $|0_L\rangle$ for a distance-3 code, with many parallels to Fig. B.2 to help visualize the state. Here again, the CNOTs act to “spread out” the 1’s to form loops around the plaquettes, effectively realizing $(\mathbb{1} + B_p)$. This state is a +1 eigenstate of Z_L (see Fig. 4.6A). The situation for the 5×5 system in Fig. 4.6A is analogous but intractable to draw, involving superpositions of $2^{12} = 4096$ bitstrings. We can readily create $|1_L\rangle$ using $X_L|0_L\rangle$, where X_L is simply a product of single-qubit X gates.

To create X_L eigenstates, we take advantage of the transversal logical Hadamard, where applying H to all the qubits performs a logical H and, as a side effect, also rotates the code 90° [267]. To compensate, we simply rotate the $|0_L\rangle$ circuit 90° and add the transversal Hadamard, as shown in Fig. B.4. This creates $|+_L\rangle$, and we can also readily create $|-_L\rangle = Z_L|+_L\rangle$.

These circuits generalize readily to larger circuits, such as the distance-5 case shown in Fig. B.5A. Distance- d requires only $(d + 3)/2$ CNOT layers (for odd d).

By altering the beginning of the circuit, we can inject an arbitrary logical state. This is shown in Fig. B.5B for the distance-5 case (it generalizes easily with depth linear in distance). The center qubit (red) is prepared in arbitrary single-qubit state $\alpha|0\rangle + \beta|1\rangle$.

Appendix B. Appendix: Experimental realization of topologically ordered states on a programmable quantum processor

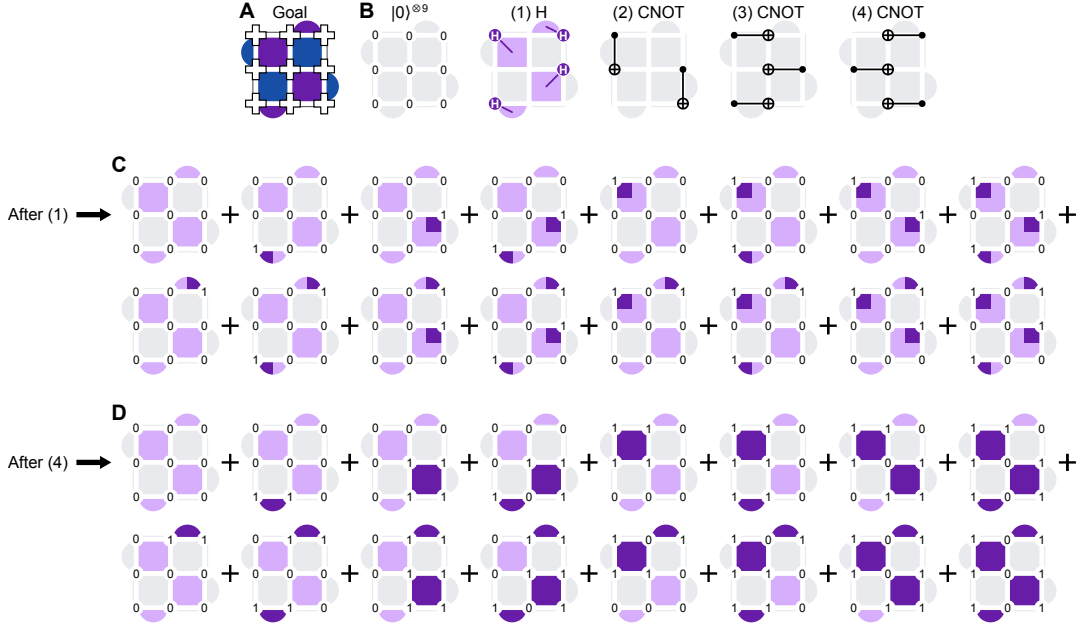


Figure B.3.: **State preparation illustration for 9 qubits, mixed boundary, $|0_L\rangle$.** (A) Schematic showing a 3×3 logical qubit with four plaquettes (purple), similar to Fig. 4.6A. (B) Quantum circuit to transform $|0\rangle^{\otimes 9} \rightarrow |0_L\rangle$. This maintains $Z_L = +1$. (C) Wavefunction after the four Hadamard gates, a uniform superposition of $2^4 = 16$ bitstrings. Each Hadamard is associated with a plaquette (purple). We darken a portion of each plaquette by the 1's that came from its associated Hadamard. Each plaquette has a darkened portion in exactly half the bitstrings. (D) Wavefunction $|0_L\rangle$ after the complete circuit.

In (1a), we initialize the center qubit in $|\psi\rangle = \alpha|0\rangle + \beta|1\rangle$ along with the Hadamards. In (2a-c), we “spread” this state along the qubits of X_L (the five qubits in the center column; see Fig. 4.6A) using the CNOTs highlighted in red. This creates a GHZ-like state on those five qubits, $(\alpha\mathbb{1} + \beta X_L)|00000\rangle = \alpha|00000\rangle + \beta|11111\rangle$. Step (2c) includes the final layer of red CNOTs as well as step (2) from Fig. B.5A to minimize circuit depth. We then proceed with steps (3-5) from Fig. B.5A.

B.1.3. Circuit compilation and optimization

In Fig. B.6, we walk through our circuit optimization techniques for an example state preparation circuit. We use these optimization steps on all of the circuits run in the main text except for the randomized compiling case (see Sec. B.4.2).

B.1. Linear quantum circuit for the toric code

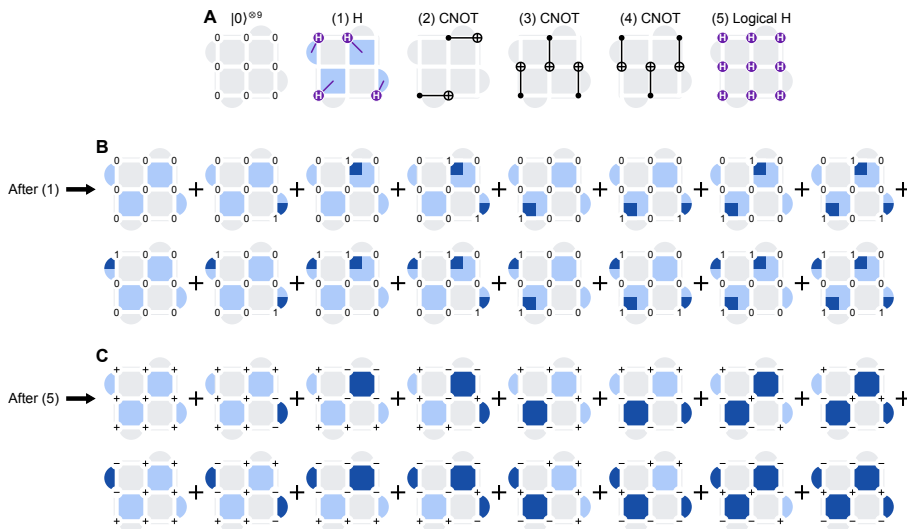


Figure B.4.: **State preparation illustration for 9 qubits, mixed boundary, $|+L\rangle$.** (A) Quantum circuit to transform $|0\rangle^{\otimes 9} \rightarrow |+L\rangle$. Steps (1-4) are the same as Fig. B.3B but rotated 90° . The final step is a transversal logical Hadamard [267], which transforms $|0_L\rangle \rightarrow |+L\rangle$ and effectively rotates the code 90° . (B) Wavefunction after the four Hadamard gates, a uniform superposition of $2^4 = 16$ bitstrings. Each Hadamard is associated with a star (blue). We darken a portion of each star by the 1's that came from its associated Hadamard. Each star has a darkened portion in exactly half the bitstrings. (C) Wavefunction $|+L\rangle$ after the complete circuit. This is similar to $|0_L\rangle$ in Fig. B.3D, but in X basis and rotated by 90° . Each element in the sum is an eigenstate of all the plaquettes B_p , and the superposition of all 16 is an eigenstate of all the stars A_s (blue). The state can also be written in Z basis as $(|0_L\rangle + |1_L\rangle)/\sqrt{2} = (|0_L\rangle + X_L|0_L\rangle)/\sqrt{2}$. The situation for the 5×5 system in Fig. 4.6A is analogous. To prepare $|+L\rangle$ in the 5×5 system, we rotate the circuit in Fig. B.5A by 90° and end with a transversal logical Hadamard.

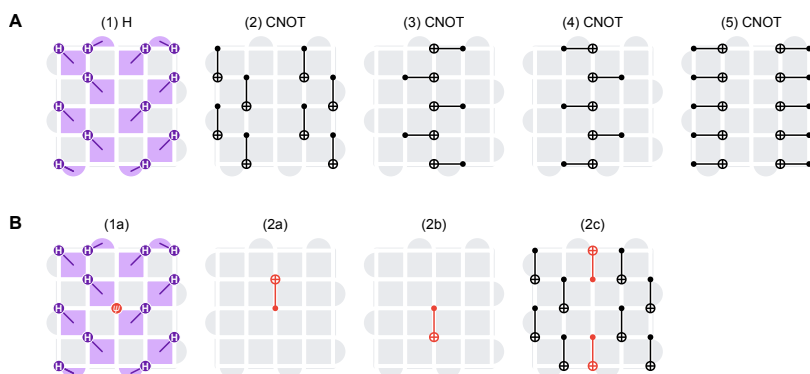


Figure B.5.: **(Repeated Fig. 4.5 from the main text for convenience) State preparation and injection circuits for 5×5 logical qubit states (mixed boundary).** (A) Quantum circuit to transform $|0\rangle^{\otimes 25} \rightarrow |0_L\rangle$, similar to Fig. B.3A. This maintains $Z_L = +1$ (see Fig. 4.6A). To prepare $|+L\rangle$, we rotate the circuit 90° and perform a transversal logical Hadamard at the end, as in Fig. B.4. (B) To inject an arbitrary logical state $\alpha|0_L\rangle + \beta|1_L\rangle$, we replace steps (1) and (2) from A, initializing the center qubit to the desired $|\psi\rangle = \alpha|0\rangle + \beta|1\rangle$.

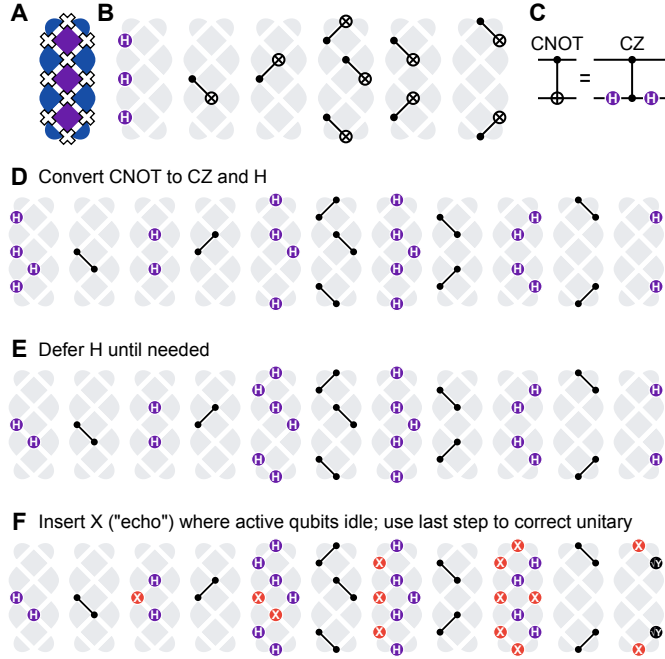


Figure B.6.: **Circuit compilation example.** (A) Example 10-qubit system with matching boundaries, similar to Fig. B.2A. (B) Circuit to prepare $|G\rangle$, similar to Fig. 4.1B but rotated 90° . We intentionally use this orientation with 5 CNOT layers to illustrate the optimization steps. (C) Decomposition of CNOT into CZ and Hadamard. (D) Using C, convert B into CZ and H, preserving the CNOT layer structure. (E) Defer H gates to keep qubits longer in $|0\rangle$. (F) Insert X gates to echo low-frequency noise. Once a qubit leaves $|0\rangle$, we do not let it idle between CZ layers. In the final step, we transform the single qubit gates to cancel out the effects of the inserted X gates, in this case using X, \sqrt{Y} , and identity.

B.2. Readout error mitigation

Measuring superconducting qubits is vulnerable to various errors, such as qubit decay, other unwanted qubit transitions, and separation error. Without full error correction, these readout errors impose severe limitations on the computational fidelity of quantum processors. It is therefore important to mitigate the readout errors strategically when using NISQ devices.

Note we discuss and benchmark readout performance in Sec. B.5.3, including discussion of related errors as state preparation and gate error, which we neglect here, since measurement error is dominant on this device.

One way to mitigate readout errors is using the response matrix [155]. Suppose, for bitstrings s, s' , the observed probabilities are $P_o(s)$ and the actual error-free probabilities are $P_a(s')$. This method assumes the two probability distributions are related by a response matrix $P(s|s')$ via $P_o(s) = \sum_{s'} P(s|s')P_a(s')$. In the experiment, the response matrix is obtained by a set of calibration experiments over computational basis states [155]. This is done by preparing the product state $|s\rangle$ for some bitstring s , then measuring the probability distribution by repeated bitstring readouts. Such measurements are carried out for all the possible bitstring s . The measured probabilities are then used to approximate the response matrix. In this work, the number of repetitions used in each bitstring basis is 10000, 64000 and 64000 for 4-, 6- and 9-qubit error-mitigation, respectively.

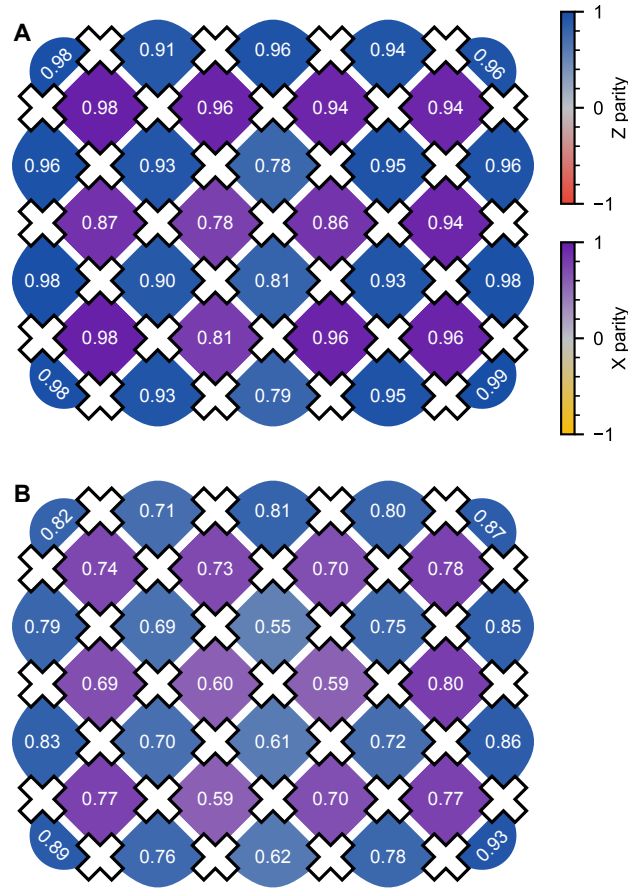


Figure B.7.: **Parity data with and without readout correction.** (A) Same as Fig. 4.1A. Before evaluating the parities, we correct each probability distribution using iterative Bayesian unfolding (see text). (B) Evaluating the parities directly from the measured probability distributions (no iterative Bayesian unfolding or other correction).

The task of error-mitigation becomes a matter of inverting the response matrix to infer the actual distribution from the observed distribution; this procedure is known as “unfolding” in high energy physics. The unfolding of the response matrix can be performed with different methods. Here we employ iterative Bayesian unfolding (IBU) [155], where the unfolded distribution is inferred by recursively calling Bayes’ theorem. This error-mitigation scheme is used to mitigate the readout errors in the parity measurements (see Fig. B.7) and the entropy measurements (see Sec. B.3). The regularization parameter for IBU is the number of iteration steps, which can be chosen in advance, seeking optimal convergence.

The full response matrix is known to capture typical uncorrelated and correlated noise. However, obtaining and unfolding the full response matrix is in general exponentially costly for large systems. This limits the scalability of such error-mitigation techniques. For certain types of error models that are typical in the current superconducting qubits device (such as the uncorrelated errors), the cost of the calibration and the classical processing can be greatly reduced. This allows a possible scalable protocol for mitigating readout errors [268].

In our experiment, the structures of the response matrices were consistent with uncorrelated errors (see Fig. B.8 for typical response matrices measured in the experiments). This allows us to understand the error effects by Monte Carlo simulation.

Appendix B. Appendix: Experimental realization of topologically ordered states on a programmable quantum processor

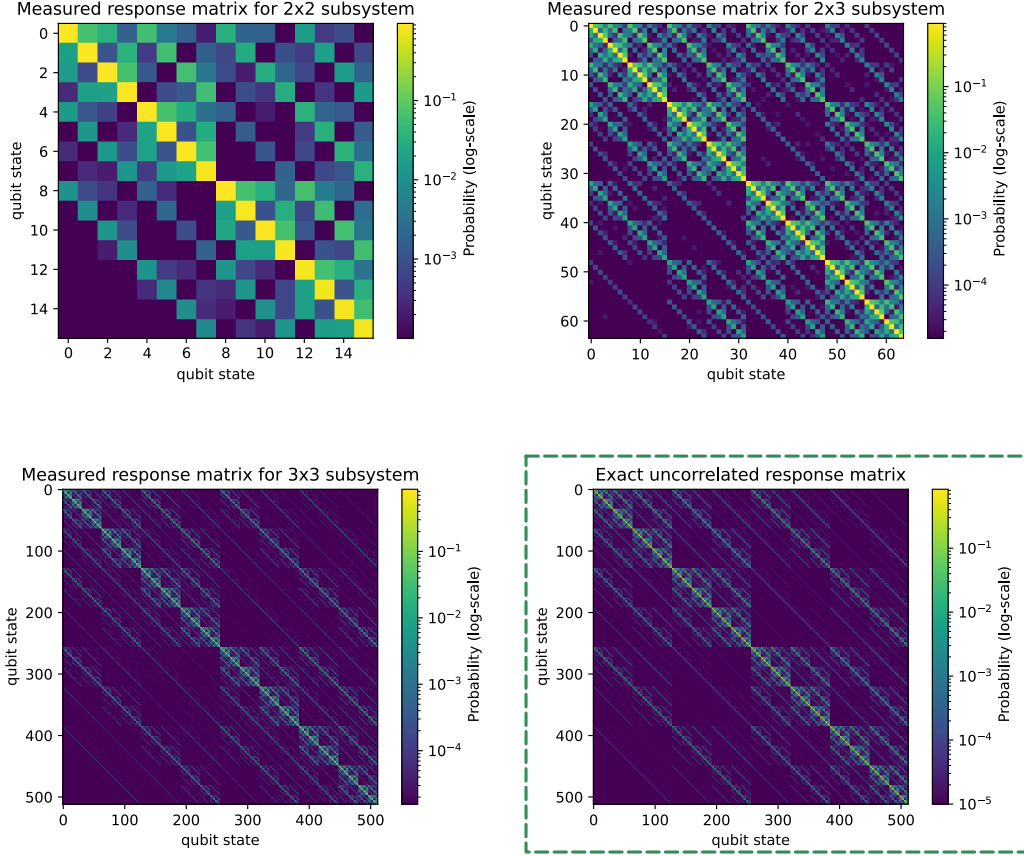


Figure B.8.: **Selected response matrices displayed in log-scale to highlight uncorrelated pattern.** Visualization of typical response matrices obtained in the error-mitigation calibration experiments. The colors are displayed in log-scale to highlight the uncorrelated noise pattern in the response matrices. We extract effective uncorrelated error rates from the matrices given respectively by (2×2) $e_0 = 0.016$ and $e_1 = 0.056$, (2×3) $e_0 = 0.019$ and $e_1 = 0.050$, (3×3) $e_0 = 0.018$ and $e_1 = 0.048$. For comparison we show the image for an exact response matrix of a 3×3 subsystem for uncorrelated noise with error rates $e_0 = 0.02$ and $e_1 = 0.05$ (green dashed box).

B.3. Measuring topological entanglement entropy

Measuring the entropy of a system is experimentally challenging: one often needs the density matrix ρ , from which one can extract the von Neumann entropy

$$S = -\text{Tr}[\rho \ln \rho], \quad (\text{B.2})$$

or n -th order Rényi entropy

$$S^{(n)} = \frac{1}{1-n} \ln(\text{Tr} \rho^n). \quad (\text{B.3})$$

The entropy cannot be measured directly, but can be accessed through quantum state tomography of the density matrix. Full quantum state tomography is resource intensive, with cost typically scaling exponentially with the subsystem size. Moreover, tomography produces a biased estimator [158], which can sometimes be tricky to account for.

B.3.1. Randomized measurement of second Rényi entropy

In this work, we focus on the randomized measurement (RM) protocol that measures the second Rényi entropy using single-qubit random unitary. Consider a subsystem A , whose purity is given by

$$\text{Tr}(\rho_A^2) = 2^{N_A} \sum_{s,s'} (-2)^{-H(s,s')} \overline{P(s)P(s')}, \quad (\text{B.4})$$

where N_A, ρ_A is the number of qubits and the density matrix of A . The average is over the tensor product of single-qubit random unitaries which act on the qubits in A and are independently drawn from the circular unitary ensemble (CUE). s, s' are the binary strings in the computational basis with $H(s, s')$ outputting the hamming distance between them, and $P(s)$ denotes the probability of observing s . The second Rényi entropy is given by $S^{(2)}(\rho_A) = -\ln(\text{Tr}(\rho_A^2))$. A nice feature of the randomized method is that the same set of measurement data can be used to compute the entropies for multiple subsystems at the same time. This renders particular convenience in measuring the S_{topo} , which is inferred from a linear combination of the entropies from different partitions. In the experiment, we only have to measure the entropy of the subsystems themselves, from which S_{topo} can be obtained by calculating all the entropies for different partitions using the same data. This avoids having several randomized measurements on the subsystem partitions and the large statistical errors built up from adding and subtracting these independently-measured entropies.

In practice, $P(s)^2$ is a biased estimator for $\mathbb{E}(P(s))^2$ and needs to be replaced with an unbiased estimator

$$P \rightarrow P \times \frac{nP - 1}{n - 1}, \quad (\text{B.5})$$

where n is the number of measurements used to determine $P(s)$ [159]. The random unitaries can be drawn from the continuous (Haar) measure. However, on many current devices it is more desirable to use a given finite set of pre-calibrated quantum gates. This is made possible by approximating the ensemble (up to certain statistical moment) using a unitary 3-design, e.g. the Clifford group [160, 161]. The single-qubit random unitary can be implemented as random single-qubit Clifford gates.

In the setting of RM, averaging over the tensor product of single-qubit Clifford gates is equivalent to averaging over all the Pauli basis measurement [106]. This can be seen by noting the qubit measurement projects the state onto Pauli Z basis, i.e. $|0\rangle\langle 0| = (1 + Z)/2$ and $|1\rangle\langle 1| = (1 - Z)/2$. The single-qubit Clifford gates send the Pauli Z to any other non-identity Pauli gates with equal frequency, $U^\dagger Z U = \pm P$, where $U \in \text{Cliff}(2)$ and $P \in \{X, Y, Z\}$. One can then go back to the Pauli Z basis as in the usual Pauli measurements. The mapping with phase -1 corresponds to a bit-flip when transforming back to the Pauli Z basis. The Hamming prefactor in Eq. (B.4) is preserved under bit-flip on s, s' , hence the equivalence follows.

Despite the properties of unitary 3-design, discretizing the random unitary measure with the Clifford group can give rise to different behaviour in the statistical fluctuations of the entropy measurement. In the example of toric code subsystems, the statistical errors are observed to be much larger in the random Clifford/Pauli case than in the Haar-random case. We illustrate this with the Monte Carlo simulation in Figure. B.9. In the simulation, we estimate the second Rényi entropy of the 2×3 (6-qubit) subsystem within the toric code assuming the bitstring probabilities can be measured perfectly, and compare the results of using random Pauli basis rotations and using Haar-random unitaries. To draw the random Pauli rotations from a finite set of $3^6 = 729$ elements, we can either sample with or without replacement. For the entropy estimation, the random Pauli protocol is observed to be biased upward. In the case when the samples are statistically independent (sampling

Appendix B. Appendix: Experimental realization of topologically ordered states on a programmable quantum processor

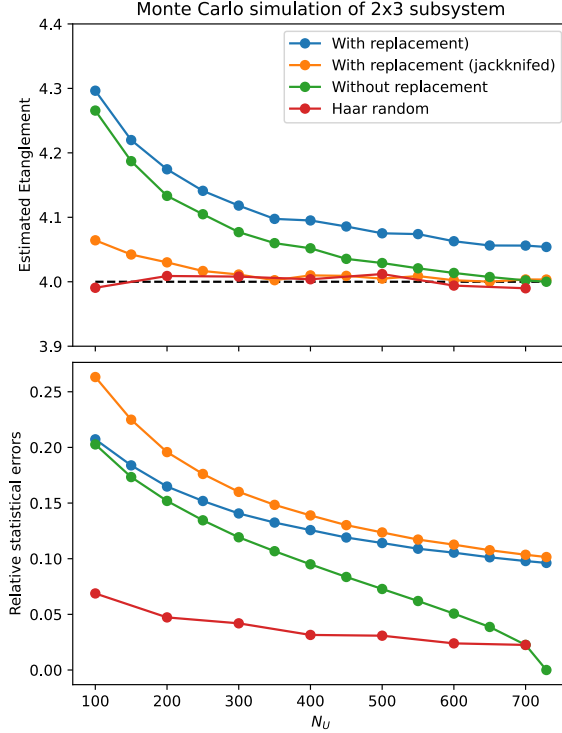


Figure B.9.: **Monte Carlo simulation of entropy estimation.** We show the difference of using the discrete random Pauli rotations and using Haar-random unitary for estimating the second Rényi entropy of a 6-qubit subsystem (2×3 qubit array) in toric code. In the simulation, the bitstring probability distributions are measured perfectly in each random unitary instance. We use 200 Monte Carlo experiments for the Haar-random case and $> 10^4$ experiments for the discrete Pauli rotation case. The Haar-random unitary protocol shows much smaller statistical errors and bias in the estimation.

with replacement), the bias can be mitigated by a jackknife resampling technique [269]. The Haar-random case, however, produces nice estimation with minimal bias. The relative statistical errors reveal the advantage of the Haar-random protocol when the number of random unitaries drawn N_U are fewer than the full set of Pauli rotations, with much smaller statistical errors than the other protocols. When $N_U \geq 3^6$, random sampling becomes unnecessary, as we can simply sum over all the possible Pauli rotations to obtain the exact average over the ensemble, resulting in zero statistical errors.

This motivates the RM experiments to use the random Pauli rotations in 4- and 6-qubit systems where the measurements over the full Pauli basis are feasible ($3^4 = 81$ for 4-qubit and $3^6 = 729$ for 6-qubit, equivalent to full tomography), and use 1000 instances of Haar-random single-qubit unitaries in the 9-qubit system where a scan of the full Pauli basis is not feasible ($3^9 = 19683$ basis states). For each instance of the single-qubit unitaries, we repeat the bitstring measurement 10000 times, and then we attempt to correct the measured probability distribution for readout error (see Sec. B.2).

B.3.2. Extended experimental details

As a check for the state quality and the success of the entropy measurement protocol, we probed the (second Rényi) entropy for the 4-qubit subsystems by taking snapshots of the entropy values after each step of the state preparation in Fig. 4.1B. The entropies of all the 4-qubit subsystems at the stars and plaquettes are measured following the protocol de-

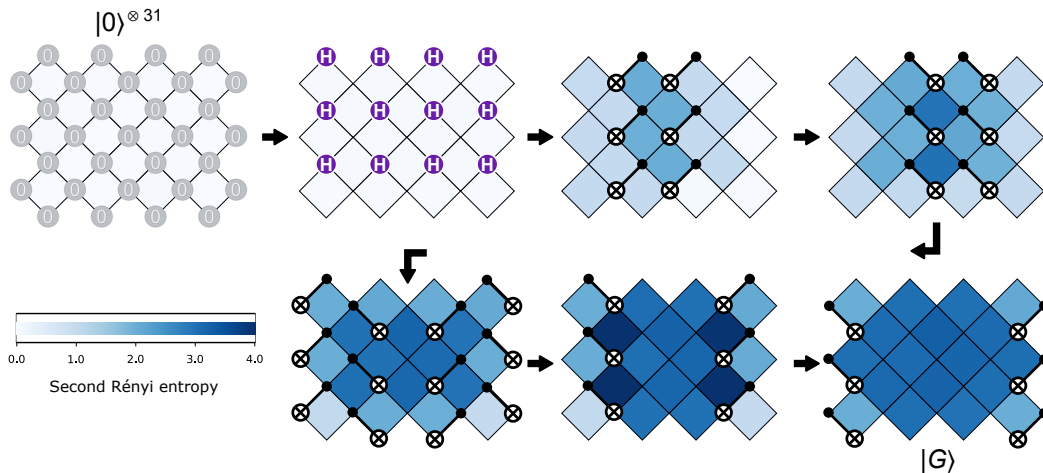


Figure B.10.: **Experimental snapshots of the second Rényi entropies during the ground state preparation steps.** We probed the second Rényi entropy of all the 2×2 subsystems during the state preparation steps using randomized measurement, measuring over all $3^4 = 81$ Pauli basis combinations (10000 repetitions per basis). The values are shown in units of $\ln 2$ and are consistent with the predicted values. Note that the corner plaquettes end with an entropy of 2, as expected due to the boundary conditions.

scribed above, giving a sequence of the 4-qubit subsystem entropies at each step as shown in Figure. B.10. The measured entropies closely match the ideal values (by carefully following the CNOT gates), demonstrating the quality of the state and entropy measurements.

As mentioned earlier, the topological entanglement entropy (S_{topo}) can be computed using a single set of randomized measurements data for a given subsystem. In our experiments, we perform the S_{topo} measurements on 14 4-qubit subsystems, 20 6-qubit subsystems and 3 9-qubit subsystems across the device (see Figure. B.11). For each subsystem, we extracted multiple S_{topo} values based on different partitions. By rotation and reflection, we can have 4, 2 and 8 ways to partition the 4-, 6- and 9-qubit subsystems. The S_{topo} distributions for all these values are summarized in Fig. 4.2. In Fig. B.12, we present the individual S_{topo} values with estimated error bars of one standard deviation. We estimate the statistical errors with bootstrapping [270]. Despite the much larger Hilbert space, the 9-qubit subsystems show small uncertainty with an average relative statistical errors of 12%. This compares favorably against the uncorrelated error modelling on a 9-qubit subsystem with asymmetric error rates $e(0 \rightarrow 1) = 0.01$ and $e(1 \rightarrow 0) = 0.05$, estimating a relative statistical errors of 13%.

The data for the 4- and 6-qubit randomized measurements were taken by measuring the bitstring probability distributions over all the Pauli bases, which is equivalent to a full quantum state tomography. We can therefore analyze the same set of data with standard quantum state tomography techniques. We find the reduced density matrices using maximum likelihood estimation through convex optimization. In Figure. B.13, we show the comparison of the estimated S_{topo} between the tomographic analysis and the randomized analysis on the same sets of data. The direct access to the density matrices also allows the computation of the corresponding von Neumann entropy for the subsystem, which is the usual entropy measure used to define S_{topo} , as opposed to the second Rényi entropy. The consistency between the S_{topo} values obtained through different analysis of the same data again supports the reliability of the experiments.

In Figure. B.14, we show the examples of reduced density matrices for 4- and 6-qubit

Appendix B. Appendix: Experimental realization of topologically ordered states on a programmable quantum processor

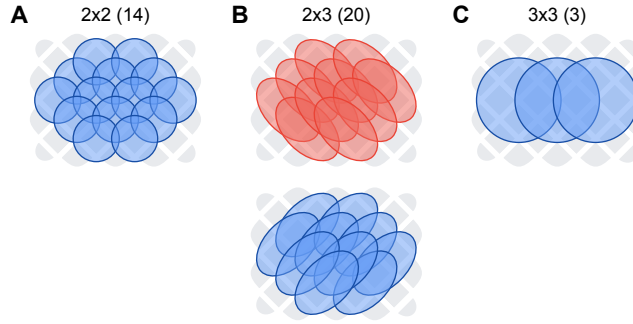


Figure B.11.: **Systems used for S_{topo} measurements.** Refer to the 2×2 , 2×3 , and 3×3 systems in Fig. 4.2A. As discussed in the main text, for the entropy data in Fig. 4.2C-D, we measure several of each system shape across the 31-qubit toric code ground state (see Fig. 4.1A). (A) 2×2 systems (14). Note we exclude the corners which have different entropy; see Fig. B.10. (B) 2×3 systems (20). For clarity, we split into two groups with different orientations. (C) 3×3 systems (3).

subsystems obtained by tomographic analysis. The non-trivial entanglement pattern of the states are manifested by the rank deficiencies in the matrices. We can further extract the state fidelity of the subsystems against the exact toric code, which is summarized in the histograms in Figure. B.14. The average fidelity of the 4- and 6-qubit subsystems have reached 94% and 88% respectively.

B.3. Measuring topological entanglement entropy

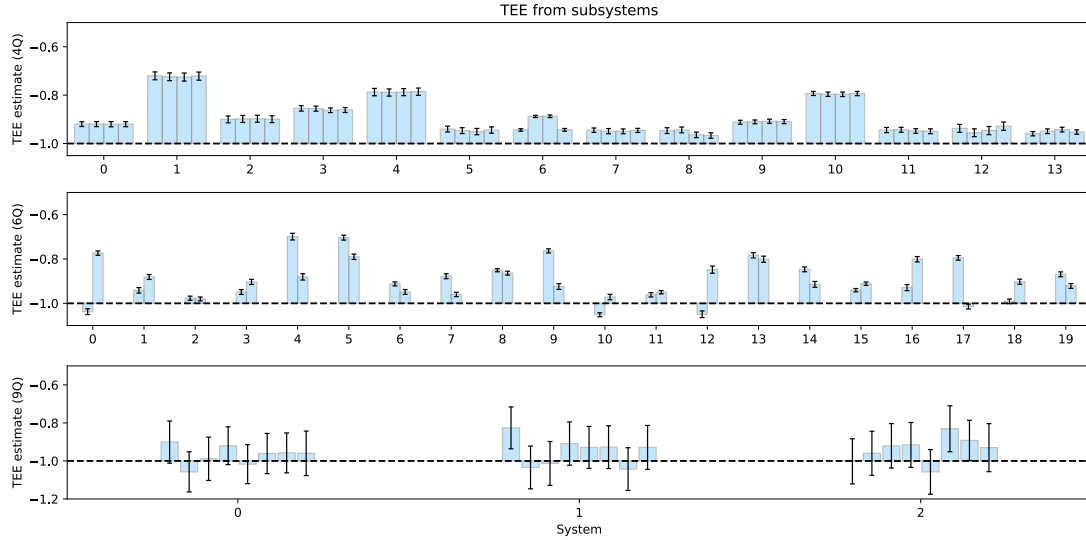


Figure B.12.: **The individual values of S_{topo} of each subsystem for different partitions into subregions.** Here we present details for the histograms shown in Figure. 4.2D. In units of $\ln 2$, the expected topological entanglement entropy for the toric code is -1. The average relative statistical errors are 1.3%, 1.2% and 12% for the 4-, 6- and 9-qubit subsystems, respectively.

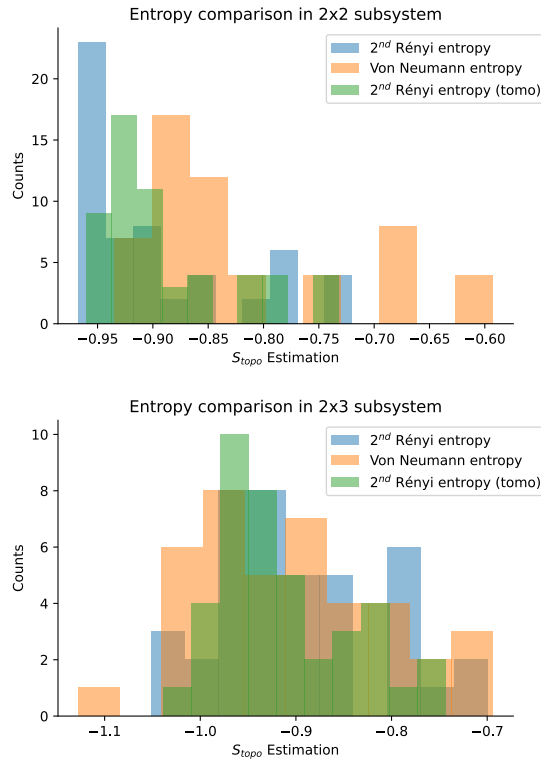


Figure B.13.: **Comparison between the topological entanglement entropy estimation obtained with randomized measurements and quantum state tomography.** The full Pauli basis rotation data can be analyzed using randomized measurements and also quantum state tomography. We compare both cases to check consistency. Top: 2×2 subsystems. Distribution mean and standard deviation: $S_{\text{rand}}^{(2)} = -0.89 \pm 0.07$, $S_{\text{tomo}} = -0.82 \pm 0.1$ and $S_{\text{tomo}}^{(2)} = -0.89 \pm 0.06$. Bottom: 2×3 subsystems, $S_{\text{rand}}^{(2)} = -0.90 \pm 0.09$, $S_{\text{tomo}} = -0.91 \pm 0.1$ and $S_{\text{tomo}}^{(2)} = -0.91 \pm 0.07$.

Appendix B. Appendix: Experimental realization of topologically ordered states on a programmable quantum processor

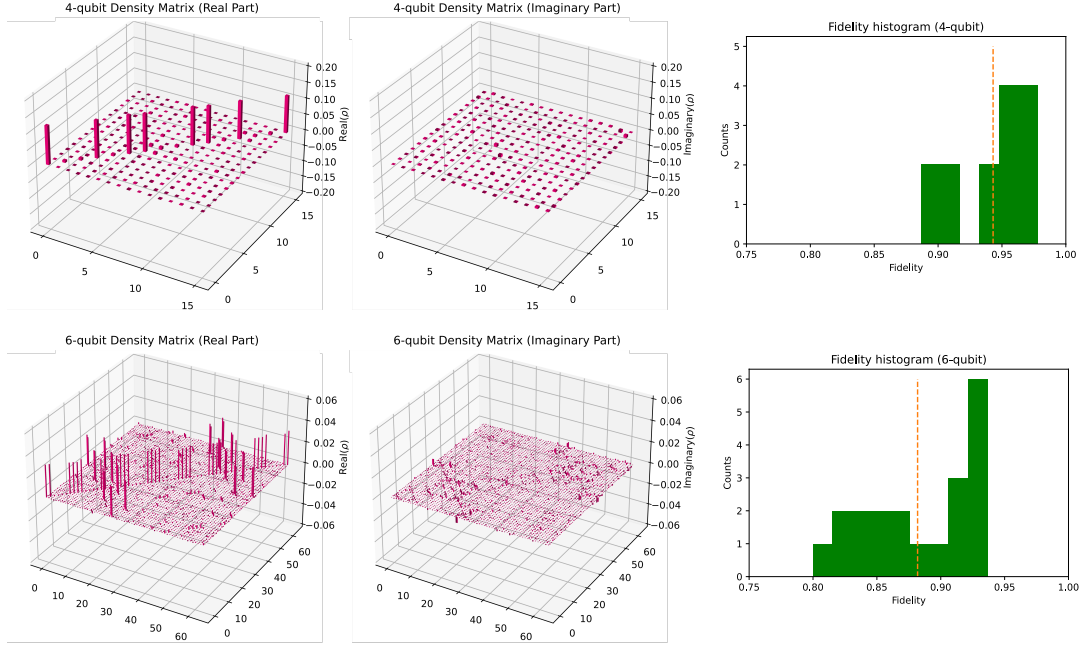


Figure B.14.: **Example density matrices and fidelity histogram.** The left panels show examples of 4- and 6-qubit measured density matrices. The density matrices are obtained using maximum likelihood estimation based on full quantum state tomography (with 10000 repeated measurements in each basis). The right panels show the histograms of fidelity for all the measured density matrices against the corresponding toric code subsystems. The average fidelity reaches 94% and 88% for 4- and 6-qubit states, respectively. On average, we estimate the uncertainty of the fidelity to be 0.004 and 0.002 for 4- and 6-qubit subsystems, respectively. The shown examples are chosen to be near the average, having fidelity 94% (4-qubit) and 91% (6-qubit).

B.4. Simulating braiding

In this Appendix, we elaborate on the protocol for simulating braiding in Fig. 4.4 of the main text, *cf.* Fig. B.15. Exchange statistics refers to interchanging the position of a pair of identical anyons, while mutual statistics refers to exchanging the positions of two (possibly distinct) anyons twice. Equivalently, mutual statistics arise when circling one anyon around another (the two pictures are related by switching to the reference frame of one of the anyons). While fundamental particles have trivial mutual statistics (all +1) and exchange statistics (+1 for bosons and -1 for fermions), braiding Abelian anyons can result in more general phases.

B.4.1. Interferometry

The interferometric protocol is motivated by the simple quantum optics picture in which a single light source is split into two paths that interfere when recombined. In our digital quantum processor, we use an auxiliary qubit a which is initially prepared as $(|0\rangle + |1\rangle)/\sqrt{2}$ to “split” the target state $|\varphi\rangle$ into a superposition

$$|\Psi\rangle = |0\rangle \otimes |\varphi\rangle + |1\rangle \otimes U|\varphi\rangle \quad (\text{B.6})$$

by an controlled- U operation using the auxiliary a . Then

$$\langle\varphi|U|\varphi\rangle = \langle\Psi|X_a|\Psi\rangle + i\langle\Psi|Y_a|\Psi\rangle, \quad (\text{B.7})$$

where X_a, Y_a are single-qubit Pauli operators that act on a . This procedure thus allows an experimental measurement of the overlap $\langle \varphi | U | \varphi \rangle$ for some state $|\varphi\rangle$ and local unitary U . The final overlap can be measured by single-qubit tomography of the auxiliary qubit a .

In our case, the unitary U is a Pauli string simulating moving the anyons of the toric code. In Fig. B.16, we show the set of minimal experiments to measure all the braiding statistics between the anyons. Most of these paths can be understood based on the ψ (fermion) exchange as shown in Fig. B.15E. To exchange ψ , we first create two pairs of ψ near the corner of the device. Each movement of ψ consists of a single Pauli X and Pauli Z that move the constituent e and m respectively. The resulting total path simplifies to a Pauli string $XXYYZZ$ (see Figure. B.15F). Other minimal braiding paths can be deduced from the ψ -exchange case by only keeping the anyon of interest. The exception is the $e - m$ mutual statistics. If we perform two exchanges between the m near the corner and e away from the corner, we can extract the $e - m$ mutual statistics with a Pauli string of 6 Pauli operators. However, a simpler path is to move e around m (topologically equivalent to exchanging e and m twice). This path only consists of a Pauli string $XXXX$ (4 operators) as shown in Figure. B.16A.

The major cost of the procedure comes from the implementation of the controlled- U that controls the auxiliary qubit and targets the support of U , which in general will involve multiple swap gates when decomposed into nearest-neighbor CNOTs. In order to reduce the depth of the circuit, we made use of a second auxiliary qubit (gray). The two auxiliary qubits are initially entangled in a Bell pair $(|00\rangle + |11\rangle)\sqrt{2}$. Then we can parallelize the decomposition of the controlled- U by using both auxiliary qubits as control qubits (see Figure. B.15A-D). At the end of the circuit, we disentangle the second auxiliary qubit from the system by a single CNOT. This trick roughly halves the depth of the circuit in terms of nearest-neighbour gates. Rather than disentangling, it is also possible to directly measure a Pauli string $\langle \varphi | U | \varphi \rangle = \langle \Psi | X_a X_b | \Psi \rangle + i \langle \Psi | X_a Y_b | \Psi \rangle$, where a, b are the two auxiliary qubits. In our case, disentangling is advantageous because our CZ error (≈ 0.005) is much lower than our measurement error (≈ 0.04); see Sec. B.5.3.

This interferometric protocol can be generalized beyond the Abelian braiding statistics of the toric code to measure the braiding statistics of other models, including some with non-Abelian braiding statistics supporting universal quantum computation [4].

B.4.2. Randomized compiling

For the phase measurements in Fig. 4.4F, we utilize randomized compiling [163, 271]. This is a more sophisticated technique than the circuit optimizations described above (primarily inserting many X gates) used for all the other experiments. Essentially, the layers of single-qubit gates (between layers of CZs) are transformed by random single-qubit Paulis in such a way that the overall circuit unitary is unchanged. We use 30 different randomly-compiled instances for each experiment. Each individual instance has a different perspective on the various coherent and non-Markovian errors that we wish to mitigate.

For example, in Fig. B.17, we plot the scatter in the measured Bloch vector for the em mutual measurement from Fig. 4.4F, as well as two control experiments. The key result of Ref. [163] is that by averaging over randomly-compiled instances, we tailor these coherent and non-Markovian errors into a depolarizing channel, which is suitable since here our focus is on extracting the *phase* of a qubit after a sophisticated and deep 33-qubit circuit. The price is that all the errors now manifest incoherently, so the Bloch vector length is decreased.

There is not a well-established method of estimating the uncertainty in the phase, so we employ a simple technique, jackknife resampling [269]. Resampling techniques are appealing here because each individual instance is subject to significant coherent and non-

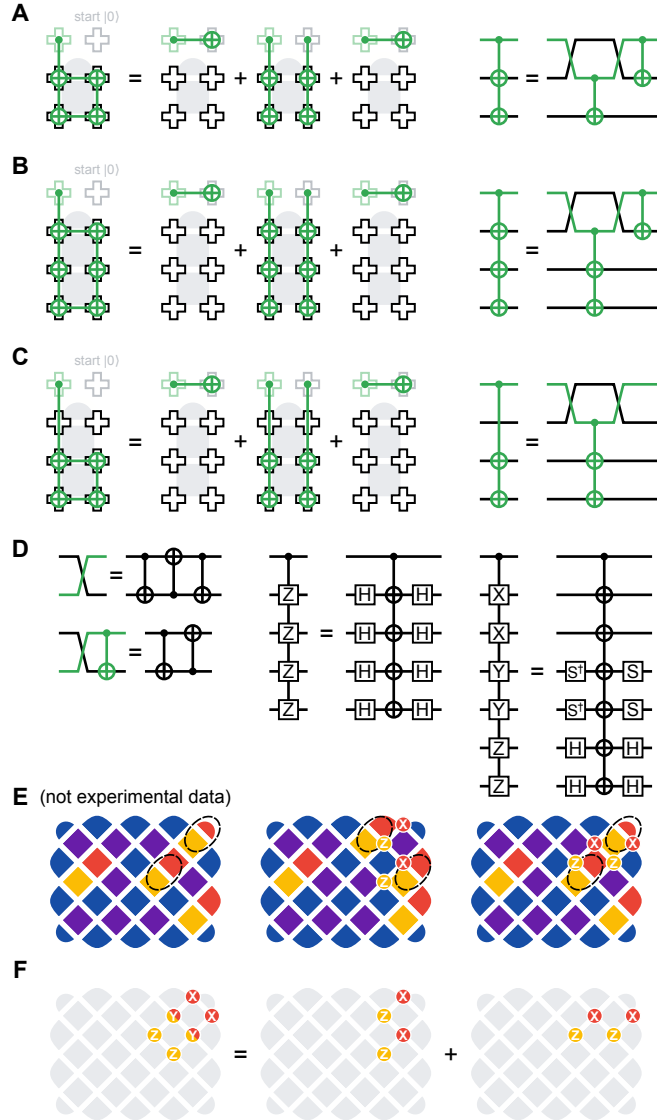


Figure B.15.: **Circuit decompositions for Fig. 4.4.** (A) Circuit decomposition of controlled-XXXX for Fig. 4.4D. We use a second auxiliary qubit, initially in $|0\rangle$, to decrease the circuit depth. We decompose into swap and CNOT (see D for further decomposition). (B) Circuit decomposition of controlled-XXXXXX, which is used for Fig. 4.4E. (C) Circuit decomposition of controlled-XXXX targeting qubits deeper in the array, which is used for other interferometry experiments. (D) Additional circuit decomposition details. Left: Conversions between swap and CNOT. Middle and right: example conversions between controlled operators using single-qubit rotations (S is $Z^{1/2}$). Ultimately, everything is compiled into CZ gates, and we use randomized compiling on these circuits when we extract the phases (see Sec. B.4.2). (E) Schematic showing the idea behind the controlled-XXYYZZ used in Fig. 4.4E. In two steps, we exchange the location of two ψ 's. Unlike the similar plots in the main text, these are not experimentally-measured parities. (F) Simplification of the two-step sequence in E to a single step XXYYZZ, as used in Fig. 4.4E.

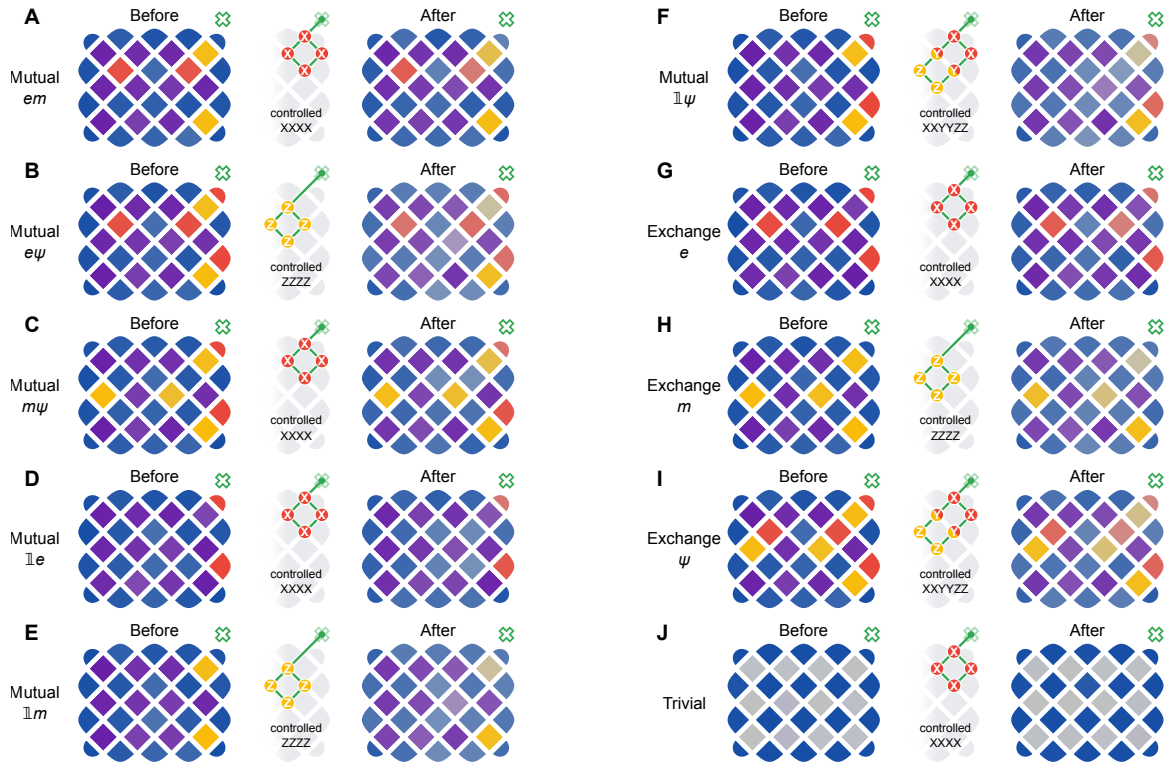


Figure B.16.: **Extended version of Fig. 4.4D-E.** (A-I) Measured parity values for toric code eigenstates before and after the indicated controlled operation (green auxiliary qubit starts in $|+\rangle$), in the same order as the measured phases in Fig. 4.4F. (A) Same as Fig. 4.4D. (B) Note the simplification where two sets of $XXXX$ cancel, similar to the simplification in Fig. B.15F. (C) Similar $ZZZZ$ cancellation. (I) Same as Fig. 4.4E. (J) Trivial case, effectively measuring $\langle 0000 | XXXX | 0000 \rangle = 0$ (also see Fig. B.17C).

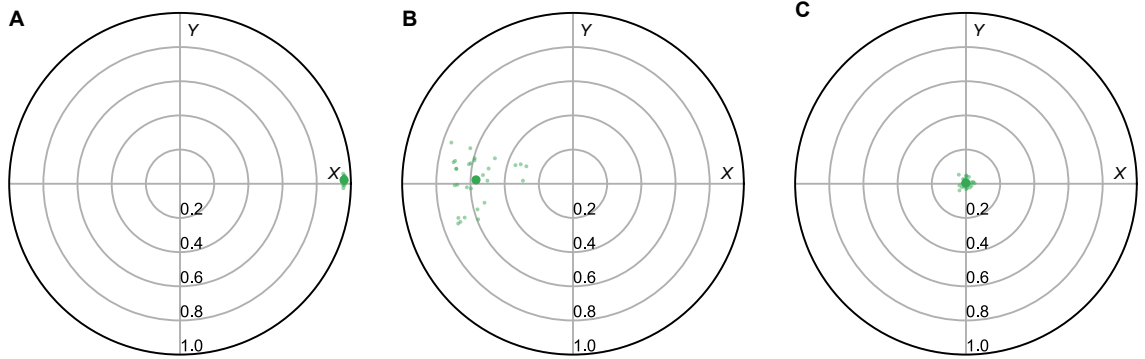


Figure B.17.: **Example scatter over randomized compiling instances.** For each randomized compiling instance, we perform single-qubit tomography on the auxiliary qubit to obtain its Bloch vector. This single-qubit tomography consists of six sequences, effectively measuring along $\pm X$, $\pm Y$, and $\pm Z$, which averages out readout bias. We do not use any readout correction such as unfolding here. We plot the projection of the Bloch vector in the XY plane, which determines the phase of the qubit state. The Bloch vector for each instance is shown in a smaller light green point (30 total), while the average Bloch vector over all the instances is a larger dark green point. **(A)** Control experiment where we prepare $|+\rangle$ and immediately perform tomography. The measured phase is $(0.007 \pm 0.001)\pi$ (see text for discussion of estimating the phase uncertainty). The mean Bloch vector length is 0.96, where the discrepancy from 1.0 is dominated by measurement error. **(B)** Data used for the *em* mutual datapoint in Fig. 4.4F, also connected to Fig. 4.4D and Fig. B.16A. Note the scatter in the data from individual instances, which we attribute to coherent and non-Markovian errors manifesting differently in different compiled instances. **(C)** Control experiment measuring $XXXX$ on the trivial state $|0\rangle^{\otimes 31}$, as shown in Fig. B.16J. We measure a Bloch vector close to $(0, 0, 0)$ without any well-defined phase, as expected, since $|0\rangle^{\otimes 31}$ is not an eigenstate of $XXXX$: $\langle 0000 | XXXX | 0000 \rangle = 0$.

Markovian error, while averaging over many instances should be less sensitive. For each instance i (of $n = 30$ total), we compute the phase $\bar{\theta}_i$ averaging the Bloch vector over the $n - 1$ other instances. The average over all n instances is $\bar{\theta}$. Then we estimate the standard error of the mean value of $\bar{\theta}$,

$$\sigma = \left[\frac{n-1}{n} \sum_{i=1}^n (\bar{\theta}_i - \bar{\theta})^2 \right]^{1/2}.$$

This is how we compute the error bars in Fig. 4.4F.

B.5. Logical qubit states

B.5.1. Logical state measurement

Now we expand on the logical state measurement and error correction illustrated in Fig. 4.6B. The logical measurement proceeds as follows. We fix a basis, Z or X , and measure all qubits in that basis. We use the resulting bitstring to evaluate the logical operator, Z_L or X_L , respectively. At this stage, we work with individual measured bitstrings, rather than probability distributions. The bitstring can be used to evaluate the local parities, A_s or B_p , respectively, equal to ± 1 . We perform error correction on the logical measurement by finding the minimal set of qubits to flip such that all local parities are $+1$.

There are various ways to choose which qubit measurements to flip. Here, we use a brute force approach. Consider Z basis. For the distance-3 surface code, the logical Z states $|0_L\rangle$ and $|1_L\rangle = X_L|0_L\rangle$ are superpositions of $2^4 = 16$ bitstrings. For the distance-5 surface code, the logical Z states are superpositions of $2^{12} = 4096$ bitstrings. Each bitstring satisfies $A_s = +1$ for all s . By taking the Hamming distance (number of differing bits) between the measured bitstring and all the constituent bitstrings of the logical Z states, we can find which constituent bitstring is closest to the measured bitstring. The correct logical measurement outcome is then simply whether that closest bitstring is associated with $|0_L\rangle$ or $|1_L\rangle$. The logical X measurement proceeds similarly with all measurements in the X basis.

As discussed in the main text, we use a logical operation $X_L^{1/2}$ for logical tomography. This rotates the Y_L axis onto Z_L , so that measuring Y_L on $|\psi_L\rangle$ is nominally equivalent to measuring Z_L on $X_L^{1/2}|\psi_L\rangle$. Unfortunately, this is a nontrivial entangling operation that essentially involves shrinking the X_L observable to two qubits, performing the desired rotation, and expanding the X_L observable back across the array. This makes it especially vulnerable to errors, similar to the state injection protocol. This can be generalized for other powers X_L^α (and also Z_L^α) using a complementary circuit. The ladder structure also generalizes to larger code distances. We show the specific CZ circuits used for $X_L^{1/2}$ in Fig. B.18.

B.5.2. Dynamical decoupling

Studying the onset of logical errors over time in Fig. 4.6D, we observe a significant basis dependence where $|+_L\rangle$ decays much more rapidly than $|1_L\rangle$. This is expected due to qubit frequency drift and low-frequency noise, which manifest as Z errors. For example, if a qubit has a constant 500 kHz frequency offset, it will precess a π rotation (Z error) in 1 μ s. These issues can be studied and mitigated using dynamical decoupling, techniques developed for nuclear magnetic resonance [272–275] that have been adopted successfully for superconducting qubits [276].

The dynamical decoupling we test in Fig. 4.6D is extremely simple. Given a particular wait time t , we apply an X gate on each qubit at $t/4$ and again at $3t/4$, very similar to a

Appendix B. Appendix: Experimental realization of topologically ordered states on a programmable quantum processor

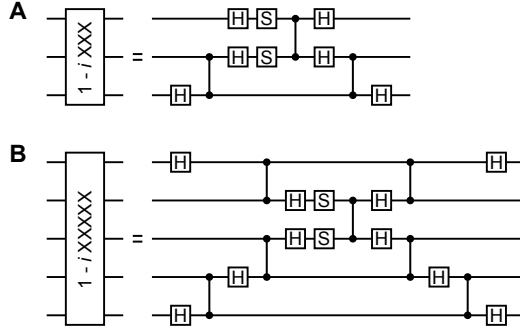


Figure B.18.: **CZ decomposition for $X_L^{1/2}$.** The operator $X_L^{1/2} = (\mathbb{1} - iX_L)/\sqrt{2}$ is useful for logical tomography as it maps $|+i_L\rangle = (|0_L\rangle + i|1_L\rangle)/\sqrt{2} \rightarrow |0_L\rangle$. We operate on the qubits that appear in X_L . The circuit decomposes the operator $(\mathbb{1} - iX_L)/\sqrt{2}$ into CZ, H, and S ($Z^{1/2}$) for the (A) 3×3 and (B) 5×5 qubit arrays. The S and H gates are compiled into one step, and we use the optimizations discussed in Fig. B.6.

“spin echo” sequence. These X gates nominally cancel out each other, but they also cancel out quasi-static Z rotations over the course of the wait time. As shown in Figs. B.19-B.20, using dynamical decoupling dramatically improves the performance for $|+L\rangle$ and $|-L\rangle$ (X_L eigenstates sensitive to Z errors), while it does not make a significant difference for $|0_L\rangle$ or $|1_L\rangle$, as expected.

Minimizing idle error in these states is important for the surface code, where an appreciable amount of time is spent idling while stabilizers are measured [166]. One direction to explore in future work is to look at other states, notably Y_L eigenstates. Developing protocols that work well for all logical states, such as alternating X and Y pulses (see Ref. [275]) are highly desirable. Another direction is to study the noise frequency spectrum by using different numbers of decoupling pulses, as demonstrated for a single physical qubit in Ref. [276].

B.5.3. Extended experimental results

In Figs. B.19-B.20, we present the data from Fig. 4.6D with extended context. We examine all four Z_L and X_L eigenstates for both 5×5 and 3×3 , for raw measurement, corrected measurement, and corrected measurement with dynamical decoupling. Primarily, this supports the claim in the main text that dynamical decoupling does not substantially affect the Z_L eigenstates $|0_L\rangle$ and $|1_L\rangle$. We observe that generally $|0_L\rangle$ and $|1_L\rangle$ (Z_L eigenstates) behave similarly, as do $|+L\rangle$ and $|-L\rangle$ (X_L eigenstates). Note the interesting oscillations for $|+L\rangle$ and $|-L\rangle$ without dynamical decoupling with microsecond timescale, only visible in Fig. B.20. The oscillations are most pronounced for the 3×3 data and may come from individual qubits’ static frequency offsets. The sharp dips in the corrected data suggest brief windows when the Z errors coherently cancel enough that error correction can still succeed.

In Fig. 4.6A, we display local parity measurements for a particular logical state to illustrate we are in a toric code ground state (all local parities close to +1). In Fig. B.21, we plot similar data for seven different logical states, both for 5×5 and 3×3 . Although the logical states can be distinguished by *global* observables (Z_L and X_L), they all look the same to the local parity operators A_s and B_p . We also show logical tomography data for both 5×5 (same as Fig. 4.6C) and 3×3 state injection in Fig. B.22. Note the longer Bloch vectors for the 3×3 case: the state injection, state preparation, and Y_L tomography circuits are all lower depth for the 3×3 case (each one has linear depth in code distance).

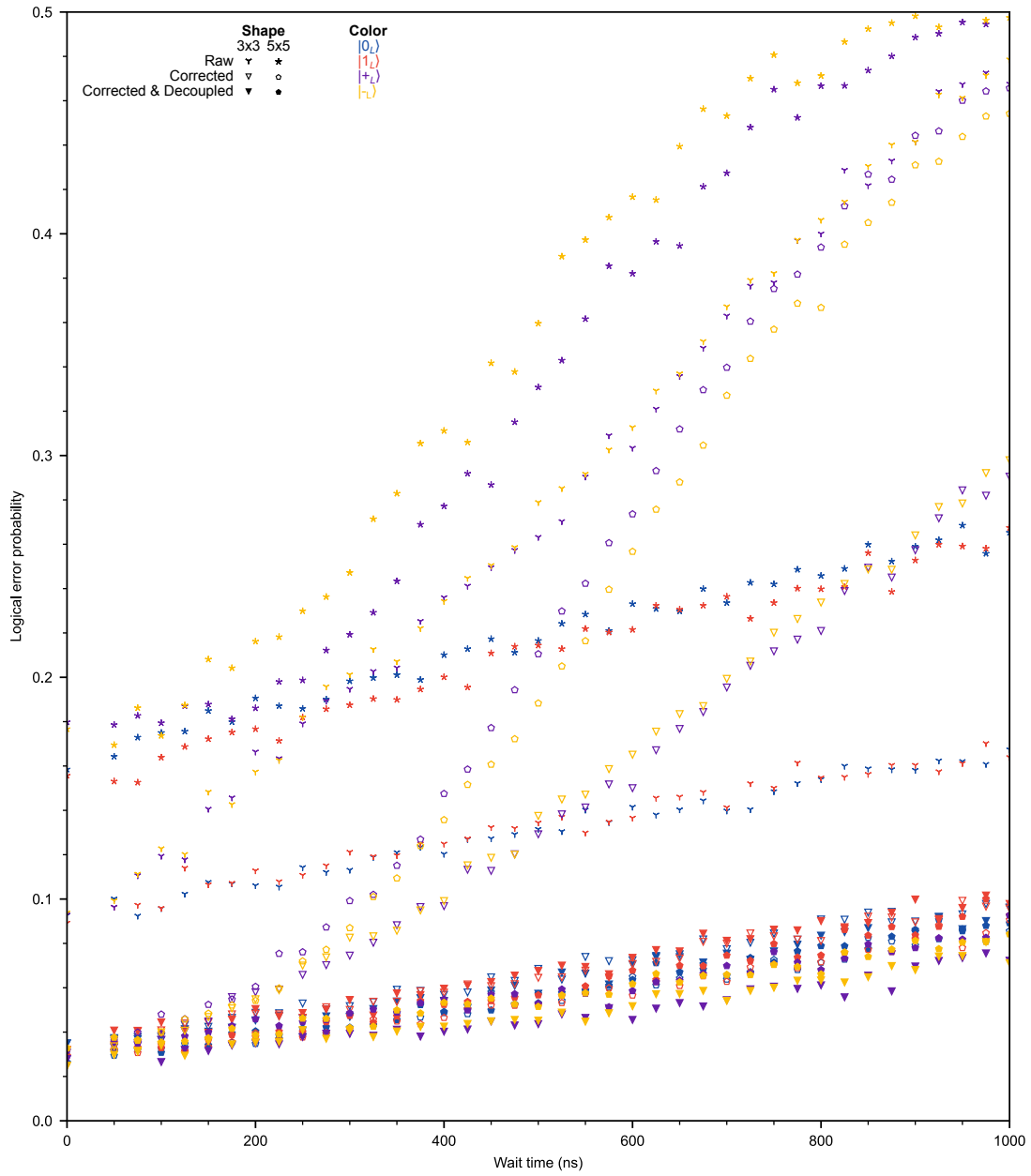


Figure B.19.: Logical error versus wait time ($1 \mu\text{s}$). Extended version of Fig. 4.6D.

Appendix B. Appendix: Experimental realization of topologically ordered states on a programmable quantum processor

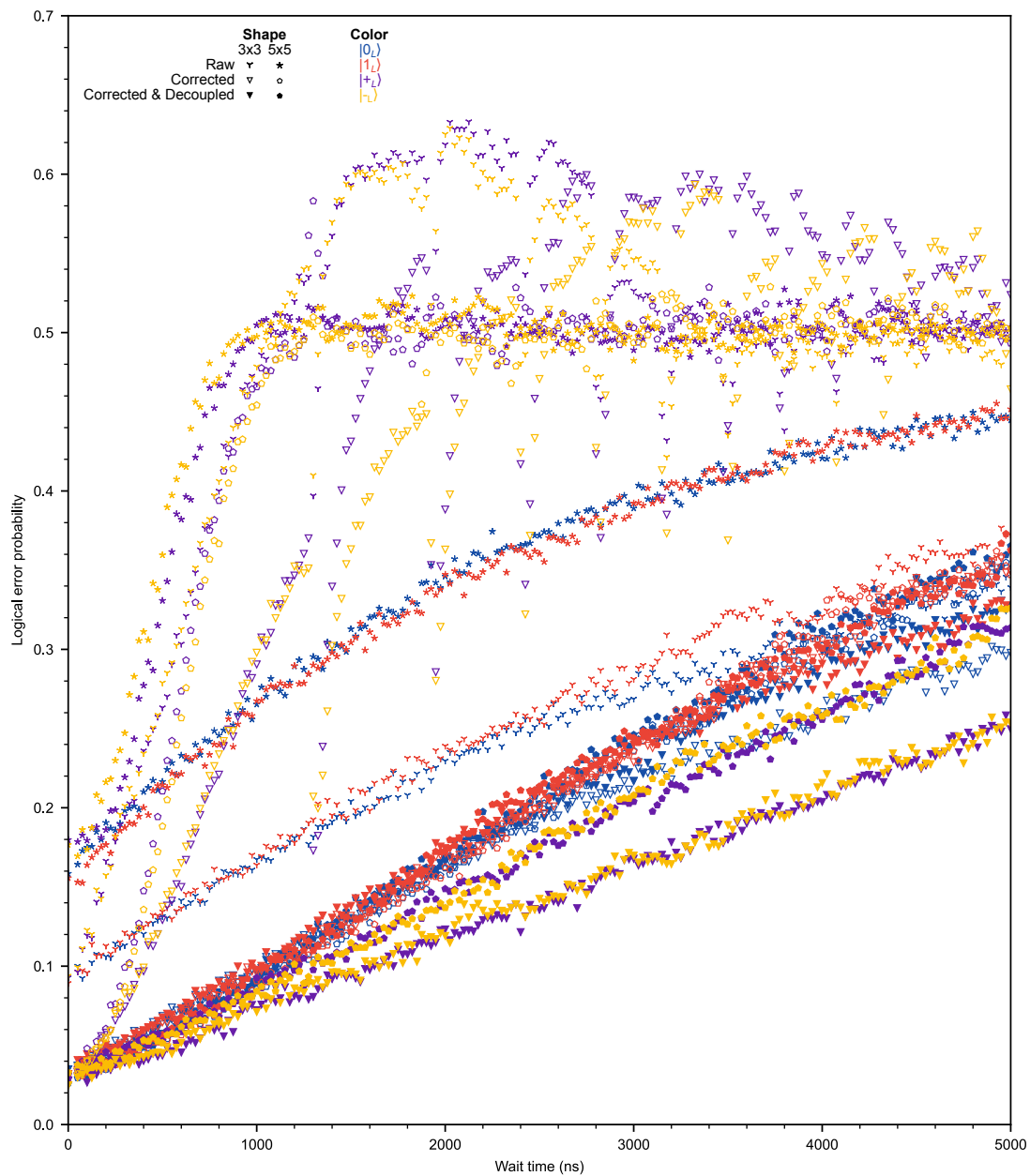


Figure B.20.: Logical error versus wait time ($5 \mu\text{s}$). Extended version of Fig. 4.6D.

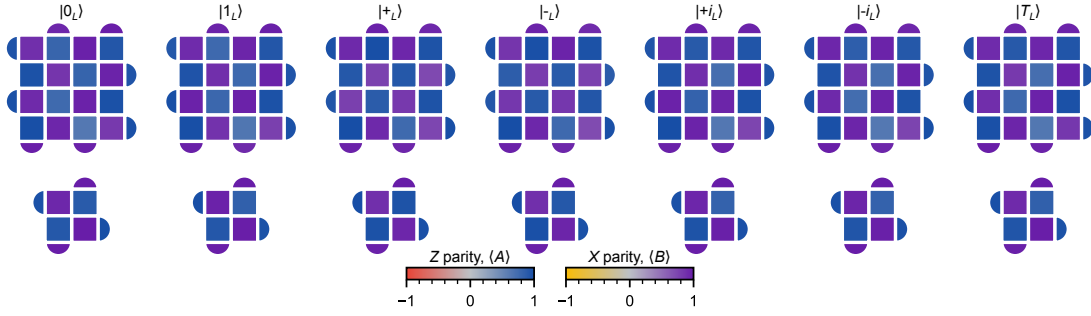


Figure B.21.: **Local parity measurements for various logical states.** Extended version of Fig. 4.6A. Experimental parity measurements $\langle A_s \rangle$ and $\langle B_p \rangle$. For each column, we prepare a different logical state. We prepare Z_L eigenstates ($|0_L\rangle$ and $|1_L\rangle$) and X_L eigenstates ($|+_L\rangle$ and $|-_L\rangle$) directly. We prepare Y_L eigenstates ($|+_iL\rangle$ and $|-_iL\rangle$) and $|T_L\rangle = (|0\rangle + e^{i\pi/4}|1\rangle)/\sqrt{2}$ using state injection. Top row: 5×5 , bottom row: 3×3 . The rightmost column is the same data as Fig. 4.6A.

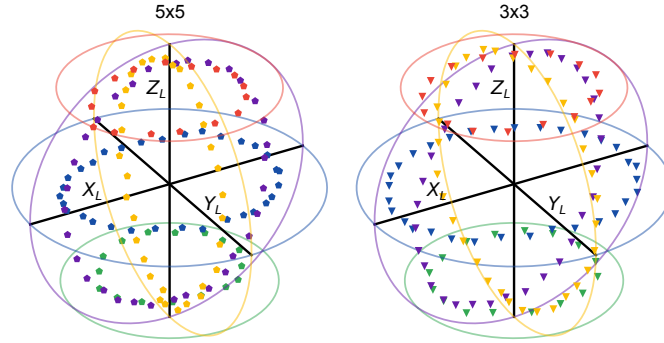


Figure B.22.: **Logical tomography of injected states.** Extended version of Fig. 4.6C. Left: Logical tomography of injected states for the 5×5 logical qubit, same as Fig. 4.6C. Right: 3×3 version.

B.6. Experimental details

We use precisely the same Sycamore processor and experimental setup as in Ref. [37]. We use CZ gates, resonantly swapping $|11\rangle$ with $|02\rangle$ and back; see Refs. [166, 277]. We optimize a frequency configuration for CZ gates with 35 active qubits and the others biased to low frequency, similar to Ref. [166].

In Fig. B.23-B.24, we map experimental benchmarks across our qubit configuration. The center qubit, both in Fig. 4.1A and Fig. 4.6A, is (row, column) = (5, 4). The toric code rectangle (Fig. 4.1A) is rotated 45° with respect to these plots. The auxiliary qubits used in Fig. 4.4 are (1, 4) and (1, 5). Qubits (3, 2) and (7, 6) are only used in the 5×5 logical qubit experiments, Fig. 4.6.

In Fig. B.23, we present typical readout error benchmark results. Each experiment involves readout assignment error and also state preparation error. Readout assignment error is dominant, for example from unwanted transmon transitions and separation error. State preparation error includes stray $|1\rangle$ population, typically < 0.01 , and π pulse error, typically ≈ 0.001 . The single-qubit measurements (left panel) are representative of the errors we experience in multi-qubit experiments. In the center and right panels, we show the specific errors we observed for simultaneous 25-qubit and 9-qubit readout used for logical

Appendix B. Appendix: Experimental realization of topologically ordered states on a programmable quantum processor

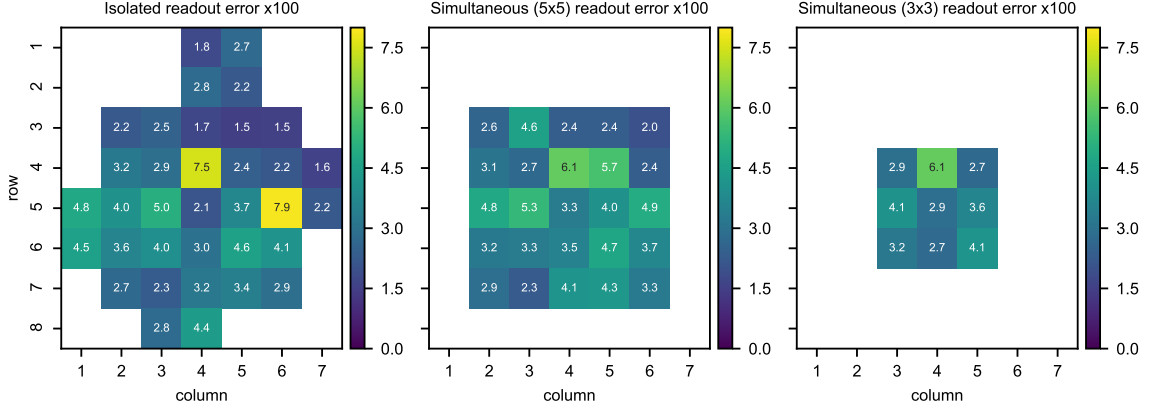


Figure B.23.: **Typical readout error.** State preparation and measurement error on each qubit, averaging over $|0\rangle$ and $|1\rangle$ error. Left: “Isolated” error measuring one qubit at a time. Center: Simultaneous 25-qubit error for the 5×5 system used in Fig. 4.6. Right: Simultaneous 9-qubit error for the 3×3 system used in Fig. 4.6.

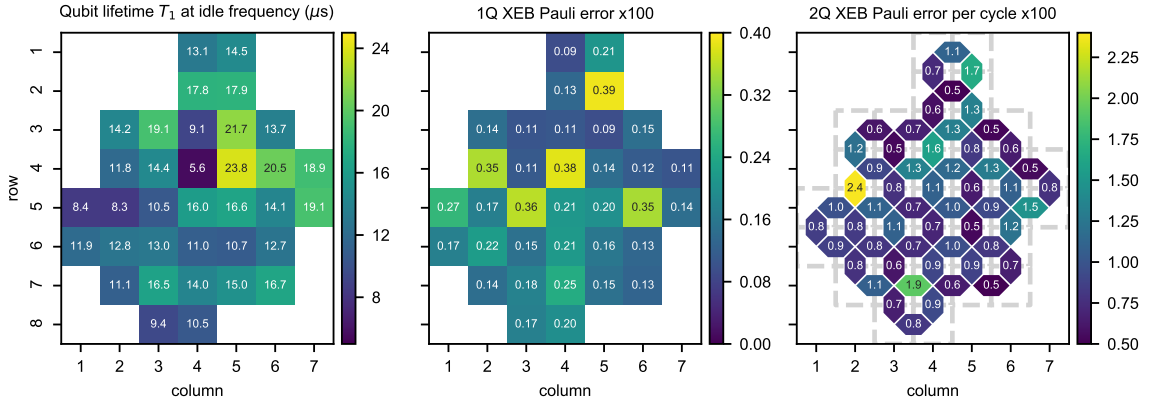


Figure B.24.: **Typical lifetime and gate error.** Left: Qubit lifetime T_1 for each qubit, measured at its idle frequency in our configuration. Center: Single-qubit $\pi/2$ pulse cross-entropy benchmarking results, in Pauli error. Median: 0.0016. Right: Two-qubit CZ cross-entropy benchmarking results, in Pauli error per cycle. Each cycle contains one CZ and two single-qubit $\pi/2$ pulses. Median: 0.0084.

measurements in Fig. 4.6. We benchmark 200 random bitstrings and 2000 repetitions each, then plot the fraction of runs where each qubit had an error. For more details about the readout setup, calibration, and benchmarking, see Ref. [37].

In Fig. B.24, we present typical qubit lifetime and gate error. We benchmark gate error (single-qubit $\pi/2$ pulses and two-qubit CZ gates) using cross-entropy benchmarking (XEB). Note we present Pauli error, and the CZ benchmarks (right panel) are error per cycle, where a cycle includes a CZ and two single-qubit $\pi/2$ pulses. Taking into account the single-qubit gate errors, the typical CZ Pauli error is about 0.005. In these benchmarks, we only examine one qubit or pair at a time, while we use many different gate patterns throughout the experiments in the main text. For more details, see Ref. [37].

C. Appendix: QCNN and quantum phase classifications

The appendix provides further details for the chapters on quantum convolutional neural networks (QCNN) and quantum phase classification.

C.1. QCNN prediction with modified training setup

As we remark in the main text, the QCNN trained by the perturbed fixed-point wavefunction can pick up the long-range order of the system. We therefore expect that the fixed-point wavefunctions can be replaced by any wavefunctions that share the same long-range order of the phase. For example, we can simplify the training procedure by replacing the symmetric SB state $(|\cdots 000 \cdots\rangle + |\cdots 111 \cdots\rangle)/\sqrt{2}$ by the asymmetric product state $|\cdots 000 \cdots\rangle$ or $|\cdots 111 \cdots\rangle$ which are much easier to prepare on a quantum hardware.

We test this thought by performing the training of an 8-qubit QCNN for the time-reversal symmetry using the SB state $|\cdots 000 \cdots\rangle$. Again, for each training session we use 60000 training samples and 1000 testing samples. We run the training with a batch size of 50 and 1000 epochs in total. At the end, we test the performance on 10000 data generated by the set of fixed-points involving the symmetric state, namely, the same test set for the QCNN in the previous section. For $L_{\text{noise}} = 1$, we achieve a test accuracy of 100% and for $L_{\text{noise}} = 2$ we achieve a test accuracy of 96.4%. We see the performance is comparable to the QCNN trained with the symmetric fixed-point.

C.2. Training with $\mathbb{Z}_2 \times \mathbb{Z}_2^T$ symmetry

In this section, we apply the protocol to training the QCNN based on $\mathbb{Z}_2 \times \mathbb{Z}_2^T$ generated by global spin flip and complex conjugation. We use the three fixed points provided in the main text. Note that, by using only three fixed points, we restrict to the phases that contain the fixed points, which only cover a subset of all the phases protected by the symmetry (with TI). Unlike the time-reversal case, we found the training in this case converges much quicker. We do not need to split the entire training into sessions with different L_{noise} . Instead, we directly train on the data with the prescribed L_{noise} . We used a training sample size of 30000 and a batch size of 30.

In this case, the symmetric local unitary is generated by the Pauli strings iZ_1Y_2 and iY_1Z_2 . We first train a 4-qubit QCNN. The 4-qubit QCNN reaches a test accuracy of 99.98% for $L_{\text{noise}} = 1$. In Fig. C.1, we show the phase diagram prediction similar to Fig. 5.4a and 2b using the 4-qubit QCNN. We see the QCNN does a nice job away from the phase boundary. Near the phase boundary, the QCNN again suffers from the large correlation length of the system and is less accurate.

Next, we train an 8-qubit QCNN and the QCNN reaches a test accuracy of 100% for both $L_{\text{noise}} = 1$ and 2. For $L_{\text{noise}} = 3$, the QCNN is not perfect and achieves 99.93% test accuracy. The phase diagram prediction is shown in Fig. C.2. Compared to the 4-qubit case, we see that the 8-qubit QCNN indeed improves significantly. Near the phase boundary, the 8-qubit QCNN is able to distinguish the phases accurately.

Appendix C. Appendix: QCNN and quantum phase classifications

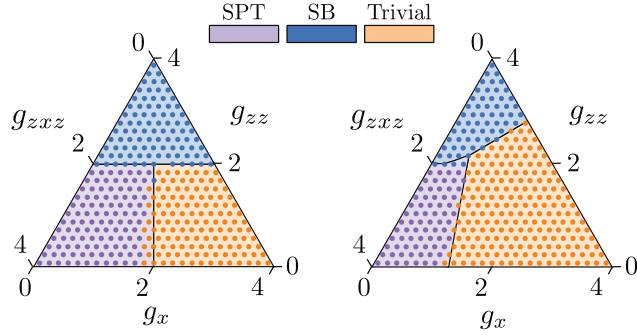


Figure C.1.: Comparing the theoretical phase diagram and the phase diagram predicted by the 4-qubit QCNN trained based on $\mathbb{Z}_2 \times \mathbb{Z}_2^T$ symmetry.

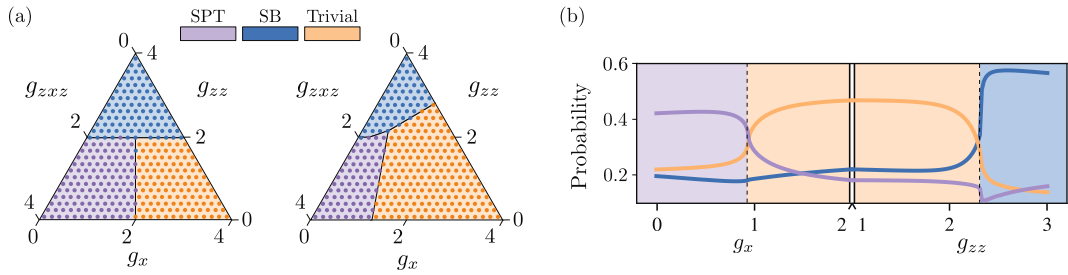


Figure C.2.: The 8-qubit QCNN trained based on $\mathbb{Z}_2 \times \mathbb{Z}_2^T$ symmetry. Panel (a) and (b) are similar to Fig. 5.4 in the main text.

We summarize the test accuracy of the trained QCNN for different symmetries and number of qubits in Table C.1 and C.2 with the values of L_{noise} , which we selected for the training of the QCNN in this section and Section 5.3.1 marked in blue.

As we mentioned in the beginning of the section, the training is performed only with three fixed points under $\mathbb{Z}_2 \times \mathbb{Z}_2^T$ symmetry. What happens if we apply the trained QCNN to predict an unknown phase? To experiment with this, we consider the following Hamiltonian with $\mathbb{Z}_2 \times \mathbb{Z}_2^T$ symmetry

$$H = (1 - \lambda) \sum_i Z_{i-1} X_i Z_{i+1} - \lambda \sum_i Y_{i-1} X_i Y_{i+1}, \quad (\text{C.1})$$

where $\lambda \in [0, 1]$. At $\lambda = 0$, we recover the fixed point we used in the main text and the training. At $\lambda = 1$, the system in fact has a non-trivial SPT order where the symmetry of complex conjugation K acquires a non-trivial fractionalization, but $K \prod_i X_i$ fractionalizes trivially. This phase is an unknown phase for the trained QCNN. Applying the trained QCNN to this model with different λ yields the prediction as shown in Fig. C.3. We see that after a phase transition at $\lambda = 1/2$, the QCNN starts to get confused by multiple phases with a similar probability for $\lambda > 1/2$. Whether this behavior is generic for other unknown phases using a larger QCNN is an interesting question to be investigated in the future.

C.2. Training with $\mathbb{Z}_2 \times \mathbb{Z}_2^T$ symmetry

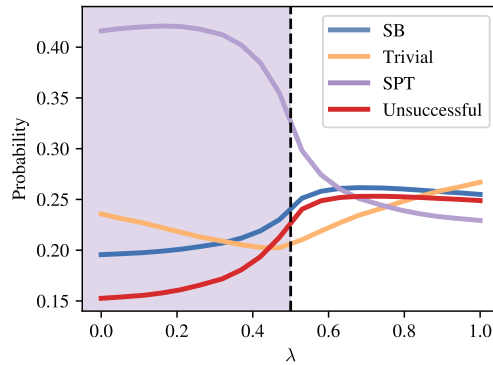


Figure C.3.: The 8-qubit QCNN trained with $\mathbb{Z}_2 \times \mathbb{Z}_2^T$ symmetric samples gets confused by multiple phases with matching probability when applied to an unknown phase.

Time-reversal		$L_{\text{noise}} = 1$	$L_{\text{noise}} = 2$	$L_{\text{noise}} = 3$
4-qubit (90 parameters)	$L_{\text{noise}} = 1$	87.21%	68.69%	60.18%
	$L_{\text{noise}} = 2$	84.66%	71.33%	64.44%
	$L_{\text{noise}} = 3$	79.02%	69.44%	63.99%
8-qubit (255 parameters)	$L_{\text{noise}} = 1$	100%	94.71%	89.88%
	$L_{\text{noise}} = 2$	100%	97.37%	93.46%
	$L_{\text{noise}} = 3$	100%	97.09%	93.62%
Uniform 8-qubit (165 parameters)	$L_{\text{noise}} = 1$	100%	93.64%	87.61%
	$L_{\text{noise}} = 2$	100%	96.76%	92.46%
	$L_{\text{noise}} = 3$	100%	97.19%	93.37%

Table C.1.: The extended table for time-reversal symmetry. Different rows in the table correspond to different L_{noise} used for the training. Different columns show the test accuracy on data with different L_{noise} using the trained QCNN. The blue L_{noise} are the ones we selected for the training in the main text and in Section 5.3.1 and C.3. They are chosen based on the stopping criterion we propose.

$\mathbb{Z}_2 \times \mathbb{Z}_2^T$		$L_{\text{noise}} = 1$	$L_{\text{noise}} = 2$	$L_{\text{noise}} = 3$
4-qubit (90 parameters)	$L_{\text{noise}} = 1$	99.98%	86.88%	83.17%
	$L_{\text{noise}} = 2$	99.72%	98.08%	95.41%
	$L_{\text{noise}} = 3$	99.62%	98.08%	95.94%
8-qubit (255 parameters)	$L_{\text{noise}} = 1$	100%	97.67%	94.41%
	$L_{\text{noise}} = 2$	100%	100%	99.53%
	$L_{\text{noise}} = 3$	100%	100%	99.93%
Uniform 8-qubit (165 parameters)	$L_{\text{noise}} = 1$	100%	91.97%	89.07%
	$L_{\text{noise}} = 2$	100%	100%	99.21%
	$L_{\text{noise}} = 3$	100%	100%	99.76%

Table C.2.: The extended table for $\mathbb{Z}_2 \times \mathbb{Z}_2^T$ symmetry. The blue L_{noise} are the ones we selected for the training in Section C.2 and C.3. They are chosen based on the stopping criterion we propose.

C.3. Results for uniform QCNN

In this section, we show results for training the uniform ansatz of the QCNN based on both the time-reversal symmetry and $\mathbb{Z}_2 \times \mathbb{Z}_2^T$. The uniform ansatz has the same structure as the non-uniform case depicted in Fig. 5.1a in the main text, but with all unitaries at the same circuit layer being identical now. We compare the uniform ansatz to the non-uniform ansatz and observe that the performance is worse for the uniform ansatz when the depth of the convolutional layer is 3 as in Fig. 5.1a. To achieve a similar performance, we increase the depth of the convolutional layer from 3 to 5. For illustration, we will focus on the QCNN that acts on 8 qubits. The optimization is similar to the training of the time-reversal case. For each training session, we generate 30000 training samples and 1000 test samples. At the very end, we obtain a final test accuracy of the already-trained QCNN on 10000 engineered data with different L_{noise} .

For time-reversal symmetric systems, we obtain a QCNN that achieves 100% on $L_{\text{noise}} = 1$ data and 96.76% on $L_{\text{noise}} = 2$ data when training with $L_{\text{noise}} = 2$. For the symmetry $\mathbb{Z}_2 \times \mathbb{Z}_2^T$, we obtain a QCNN that achieves 100% for both $L_{\text{noise}} = 1$ and 2 data. For $L_{\text{noise}} = 3$ it achieves an accuracy of 99.76% when training with $L_{\text{noise}} = 3$. Both ansatzs are therefore comparable, see Table. C.1 and C.2,

C.4. Extended numerical results

In the previous sections, we show the testing results of the trained QCNN for the time-reversal case. The QCNN is trained on a prescribed L_{noise} picked by the stopping criterion we adopt. Namely, we increase L_{noise} used in the training, until the test accuracy for the current L_{noise} drops below certain threshold, which we choose to be 100%. It is important that we do not over train the classifier with L_{noise} that is too large, since this can potentially lead to over-fitting. The criterion aims to provide a stopping point where the classifier is reasonably converged and not over-fitted. We show the extended Table C.1 for time-reversal symmetry. In the extended table, we train and test the QCNN with $L_{\text{noise}} = 1, 2$ and 3. The training is performed sequentially: we start the training with data generated by $L_{\text{noise}} = 1$ layer of noise. Once a convergence is reached we continue the training with $L_{\text{noise}} = 2$ and so on until we reach the prescribed L_{noise} . The color blue marks the L_{noise} we use for the training based on the stopping criterion. We see that at the stopping points, the QCNNs have reasonably converged.

In contrast to the time-reversal case, we do not use the sequential training for obtaining the $\mathbb{Z}_2 \times \mathbb{Z}_2^T$ results. Instead, we directly train on the data with a prescribed L_{noise} . We also picked a suitable L_{noise} used in the training based on the same stopping criterion, which correspond to the L_{noise} marked blue in the extended Table C.2. For the 4-qubit case, we see that the performance of the QCNN can be further improved. This can be taken into account if we were to modify the threshold for the test accuracy from 100% to 99%.

C.5. Making predictions with weak disorder

The non-existence results in Section 5.5 suggest that if the system is perturbed with noise that is not translationally invariant, the trained QCNNs in Section 5.3.1 and C.2 will not be able to retain their high prediction accuracy even when the system only has a very short correlation length. However, when the breaking of the translation symmetry is weak, namely the perturbation is close to a symmetric operator, we still expect certain level of robustness. In particular, the robustness is characterized by a finite difference between the probability of the predicted phase and the other probabilities in the output distribution, i.e., by a finite probability gap.

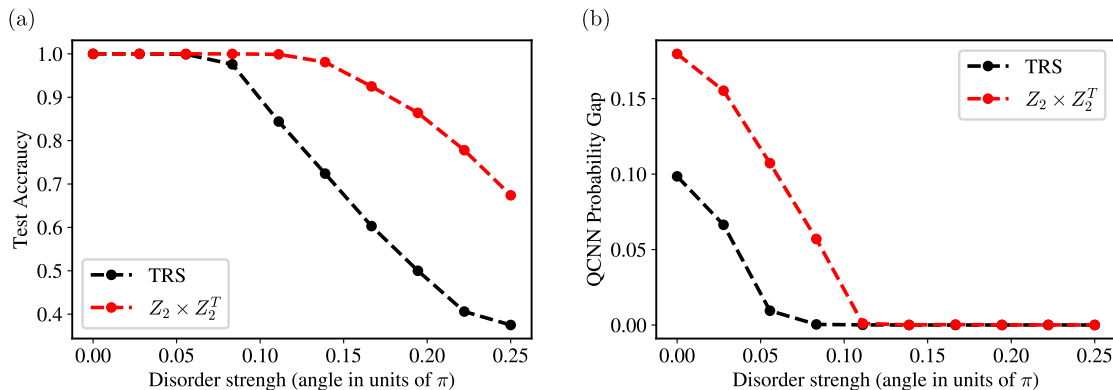


Figure C.4.: Predictions of the pre-trained 8-qubit QCNNS states generated with spatially disordered perturbation. (a) The test accuracy over 1000 test states generated by perturbing the fixed-points with one layer of independent two-qubit symmetric noise. Each noisy unitary is parametrized as described in Section 5.3.1, with each angle parameter uniformly sampled from $[-\theta, \theta]$, where $\theta \geq 0$ characterizes the disorder strength (the x -axis). TRS stands for time-reversal symmetry. (b) Smallest difference between the probability of the predicted phase and the rest of the probabilities. A finite probability gap ensures some stability of the prediction against weak disorder.

In Fig. C.4, we study this using the already-trained QCNNS from Section 5.3.1 and C.2 to make prediction on the fixed-points perturbed by disordered noise. When the probability gap (Fig. C.4(b)) is finite we obtain a perfect test accuracy (Fig. C.4(a)). When the probability gap closes (Fig. C.4(b) gets close to zero), the prediction no longer guaranteed to be stable against disordered perturbation and the test accuracy in Fig. C.4(a) deviates from the perfect 100%.

C.6. Alternating-bond Heisenberg model

In this section, we show the two dimerized limits in the alternating Heisenberg model belong to the same trivial phase under the time-reversal symmetry $T = (\prod_i X_i) K$. In the dimerized limits, the ground state of the system is a product of local singlets. Since the wavefunctions are now real product states (K acts trivially), we can examine how T fractionalizes in the ground states by looking at how $\prod_i X_i$ fractionalizes. If we apply $\prod_i^L X_i$ to part of the system, we see that the operator acts as either X or I depending on whether the singlets are formed in the even or odd bonds. In both cases, the time-reversal SPT invariant is $X^2 = I^2 = +1$ [15, 171]. So they belong to the same trivial phase under T .

Next, we discuss how to connect the two dimerized limits by a gapped symmetric Hamiltonian path. Consider the Hamiltonian

$$H = (1 - \lambda) \sum_i \mathbf{S}_{2i+1} \mathbf{S}_{2i+2} + \lambda \sum_i \mathbf{S}_{2i} \mathbf{S}_{2i+1}, \quad (\text{C.2})$$

which corresponds to the case of $\Delta = 1$ in H_4 in the main text. The Hamiltonian has the same dimerized ground states at the limits $\lambda = 0, 1$. A transition exists at $\lambda = 1/2$. As we mention in the main text, this transition is protected by an π -rotation of the effective spin-1 (2-site unit cell) in the bulk followed by a complex conjugation. The transition can never be avoided if we keep this symmetry.

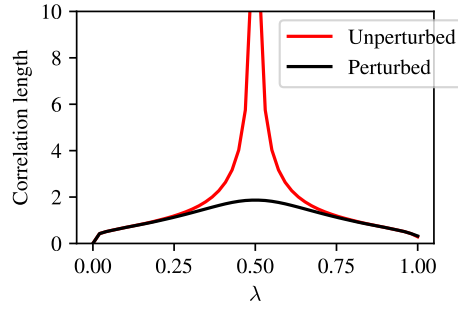


Figure C.5.: We verify the absence of transition in the bond-alternating Heisenberg model under time-reversal (T) symmetry, by examining the correlation length of the system. In the unperturbed case Eq. (C.2), the ground state has a diverging correlation length at $\lambda = 1/2$ (red solid line). This singular point can be avoided by adding a T -symmetric perturbation $\lambda(1 - \lambda) \sum_i (-1)^i X_i$. The perturbed ground state continuously interpolates between the two dimerized limits without a diverging correlation length (black solid line).

However, we can avoid this gap-closing point by adding T -symmetric perturbation. A continuous path can be found by considering, e.g. $(1 - \lambda) \sum_i \mathbf{S}_{2i+1} \mathbf{S}_{2i+2} + \lambda \sum_i \mathbf{S}_{2i} \mathbf{S}_{2i+1} + \lambda(1 - \lambda) \sum_i (-1)^i h_i$, where $h_i = X_i$ respects the symmetry T . The added perturbation allows interpolation between the dimerized ground states without gap-closing and therefore the two dimerized states can be continuously connected. The absence of a transition is verified numerically by DMRG, as shown in Fig. C.5.

C.7. Symmetrization of local quantum gates for generic symmetry groups

Suppose we are given an on-site symmetry of the form $U(g) = u(g) \otimes u(g) \otimes \cdots \otimes u(g)$ for $g \in G$, where G is a finite group and $u(g)$ is a linear representation of G . An important question related to the proposed method is, how to find symmetric local quantum gates under a given (representation of the) symmetry group? A direct way for achieving this is by solving a set of linear equations (assuming the local gates have the same support as $u(g)$):

$$[u(g), \sum_m c_m \hat{\sigma}_m] = 0, \quad g \in G, \quad c_m \in \mathbb{R}, \quad (\text{C.3})$$

where $\hat{\sigma}_m$ are the generators of the local unitary (usually anti-Hermitian Pauli strings). For time-reversal symmetry of the form $T = u(g)K$ with some $g \in G$ and $T^2 = 1$, we can enforce the symmetry locally and modify Eq. (C.3) to be

$$u(g) \left(\sum_m c_m \hat{\sigma}_m \right)^* - \left(\sum_m c_m \hat{\sigma}_m \right) u(g) = 0, \quad c_m \in \mathbb{R}, \quad (\text{C.4})$$

A convenient way to find the symmetric generators for on-site symmetry is by a twirling of the generators $\hat{\sigma}_m$.

$$\hat{\sigma}'_m = \mathcal{T}[\hat{\sigma}_m]_G = \frac{1}{|G|} \sum_{g \in G} u(g) \hat{\sigma}_m u(g)^\dagger, \quad (\text{C.5})$$

which automatically ensures that $[\hat{\sigma}'_m, u(g)] = 0$ for all m and $g \in G$. This symmetrization procedure is used in Ref. [199] to construct symmetric quantum circuit architectures. For

a time-reversal symmetry of the form $T = u(g)K$ with some $g \in G$ and $T^2 = 1$, we can define

$$\hat{o}'_m = \hat{o}_m + u(g)(\hat{o}_m)^*u(g)^\dagger, \quad (\text{C.6})$$

which ensures $[\hat{o}'_m, u(g)K] = 0$ for all m .

The two procedures mentioned can be easily extended to symmetries described by compact Lie groups as well.

C.8. The error probability for a majority vote

In this section, we derive an upper bound for prediction made by a majority vote process. This provides an estimate for the sample size we need in order to make a reliable prediction in practice.

Suppose we have a discrete probability distribution with M outcomes and the probabilities (p_1, p_2, \dots, p_M) , such that $\sum_{i=1}^M p_i = 1$ and $p_i \geq 0$. The task is to find the label with the largest probability based on a majority vote among $2N + 1$ independent samples from the distribution. We say a mistake is made if either (i) the majority vote cannot decide or (ii) the majority vote yields a wrong guess for the most probable label.

Without loss of generality, we sort the probability in descending order such that $p_1 > p_2 \geq p_3 \geq \dots \geq p_M$. The sampling process is multinomial and therefore we can write the error probability for the majority vote as

$$\begin{aligned} P &= \sum_{\substack{n_1 + \dots + n_M = 2N+1 \\ n_1 \leq n_i, \text{ for at least one } i \in [2, M]}} \binom{2N+1}{n_1, n_2, \dots, n_M} p_1^{n_1} p_2^{n_2} \dots p_M^{n_M} \\ &\leq \sum_{\substack{n_1 + \dots + n_M = 2N+1 \\ n_1 \leq n_i, \text{ for at least one } i \in [2, M]}} \binom{2N+1}{n_1, n_2, \dots, n_M} p_1^{n_1} p_2^{n_2 + \dots + n_M} \\ &\leq \sum_{\substack{n_1 + \dots + n_M = 2N+1 \\ n_1 \leq n_2 + \dots + n_M}} \binom{2N+1}{n_1, n_2, \dots, n_M} p_1^{n_1} p_2^{n_2 + \dots + n_M} \stackrel{k=n_2+\dots+n_M}{=} \sum_{k=N+1}^{2N+1} \binom{2N+1}{k} p_1^{2N+1-k} p_2^k \\ &= \sum_{q=0}^N \binom{2N+1}{N+1+q} p_1^{N-q} p_2^{N+1+q} \\ &\leq p_1^N p_2^{N+1} \sum_{q=0}^N \binom{2N+1}{N+1+q} = p_1^N p_2^{N+1} 2^{2N} \leq (4p_1 p_2)^N. \end{aligned} \quad (\text{C.7})$$

In the third line above, we summed over the free multinomial indices to obtain a binomial coefficient. If we denote the probability gap by $\delta = p_1 - p_2$, then we arrive at the bound

$$P \leq (4p_1 p_2)^N = ((p_1 + p_2)^2 - \delta^2)^N \leq (1 - \delta^2)^N. \quad (\text{C.8})$$

Suppose we want to ensure the error probability satisfies $P < \varepsilon$ for some positive $\varepsilon < 1$, the sample size should at least be

$$2N + 1 \geq \frac{2 \log \varepsilon}{\log(1 - \delta^2)} + 1, \quad (\text{C.9})$$

as claimed in the main text.

D. Appendix: Symmetry-enriched topological phase transitions in 2D tensor-network states

D.1. Parent Hamiltonians away from the fixed points

In this section, we construct a frustration-free parent Hamiltonian, whose ground states are exactly the decorated TNS. The parent Hamiltonian depends smoothly on the TNS parameters.

D.1.1. Warm-up: 1D case

Let us illustrate the idea of the parent Hamiltonian construction with a 1D example, which will later be generalized to the 2D case. One can verify that the MPS $|\psi(g)\rangle$ in Eq. (7.2) that smoothly depends on some parameter $g \in [-1, 1]$ can be re-parameterized as an imaginary-time evolved state. More precisely, when $g \in (0, 1]$ it satisfies that $|\psi(g)\rangle = |\phi(\tau(g))\rangle$, where $\tau(g) = -\log(g)/4$ and the 1D imaginary-time evolved state is given by

$$|\phi(\tau)\rangle \propto e^{\tau \sum_i Z_i Z_{i+1}} |+\dots+\rangle, \quad (\text{D.1})$$

By a direct substitution, we find the relation

$$K_i |\phi(\tau)\rangle = 0, \quad \forall i; \quad K_i = -X_i + e^{-2\tau Z_{i-1} Z_i - 2\tau Z_i Z_{i+1}}. \quad (\text{D.2})$$

Notice that K_i satisfies

$$K_i^2 = 2 \cosh(2\tau Z_{i-1} Z_i + 2\tau Z_i Z_{i+1}) K_i, \quad (\text{D.3})$$

and

$$[\cosh(2\tau Z_{i-1} Z_i + 2\tau Z_i Z_{i+1}), K_i] = 0. \quad (\text{D.4})$$

This suggests that we can define a projector

$$P_i = \frac{1}{2} \operatorname{sech}(2\tau Z_{i-1} Z_i + 2\tau Z_i Z_{i+1}) K_i, \quad (\text{D.5})$$

such that $P_i^2 = P_i$ and $P_i |\phi(\tau)\rangle = 0$. One choice of a local parent Hamiltonian for $\tau \geq 0$ is, therefore, $h = \sum_i P_i$ with a ground state energy of zero.

To obtain a Hamiltonian smooth in $g \in [-1, 1]$, we evaluate P_i in Eq. (D.5) in terms of g , this yields

$$\begin{aligned} & 2(1+g^2)P_i - 2(1+g^2) \\ &= -g_x X_i - \frac{g_{zz}}{2} (Z_{i-1} Z_i + Z_i Z_{i+1}) + g_{zxz} Z_{i-1} X_i Z_{i+1}, \end{aligned} \quad (\text{D.6})$$

where $g_x = (1+g)^2$, $g_{zz} = 2(1-g^2)$ and $g_{zxz} = (1-g)^2$. A parent Hamiltonian analytic in g is therefore given by

$$\begin{aligned} H(g) &= 2(1+g^2) \sum_i (P_i - 1) \\ &= -g_x \sum_i X_i - g_{zz} \sum_i Z_i Z_{i+1} + g_{zxz} \sum_i Z_{i-1} X_i Z_{i+1}, \end{aligned} \quad (\text{D.7})$$

with a ground state energy density of $-2(1+g^2)$. This Hamiltonian is exactly Eq. (7.1) found in Ref. [242]. While in the derivation we assume $g \in (0, 1]$, since all the functions depend analytically on g for $g \in \{a+i\varepsilon | a \in \mathbb{R}, \varepsilon \in (-1, 1)\}$, by analytic continuation $H(g)$ remains to be a valid parent Hamiltonian for $g \in [-1, 1]$.

D.1.2. 2D parent Hamiltonian

Since each configuration in the 2D wavefunction consists of loops of 1D chains (D.1), the 2D ground state also admits a representation in terms of imaginary time evolution starting from the fixed point of the TC phase

$$|\Psi(g, \eta)\rangle \propto \left(\prod_{e \in E} e^{\tau(g)[(1-Z_e)Z_{v(e)}Z_{v'(e)}+Z_e]/2} \eta^{Z_e/2} \right) |\Psi(1, 1)\rangle, \quad (\text{D.8})$$

where $\tau(g) = -\log(g)/4 \geq 0$ and $g \in (0, 1]$. Note that the alternative interpretation implies that the decoration (imaginary time evolution) commutes with any operators diagonal in the computational basis, including the unitary transformation $U_{\text{TC-DS}}$ discussed in Section 7.6 that maps between the toric code ground state and the double-semion ground state. A phase diagram of the same structure as Fig. 7.4a can, therefore, also be obtained by enriching the double-semion model.

Analogously to the 1D case shown in Eq. (D.2), it can be verified that

$$\begin{aligned} K_p |\Psi(g, \eta)\rangle &= 0, \quad \forall p; \\ K_p &= - \prod_{e \in p} X_e + \prod_{e \in p} e^{-\tau(g)Z_e(1-Z_{v(e)}Z_{v'(e)})} \eta^{-Z_e}. \end{aligned} \quad (\text{D.9})$$

Similar to Eq. (D.3) and (D.4), we can obtain a local plaquette projector for each plaquette p

$$B_p(g, \eta) = \frac{1}{2} \operatorname{sech} \left(\sum_{e \in p} [\tau(g)Z_e(1 - Z_{v(e)}Z_{v'(e)}) + \lambda(\eta)Z_e] \right) K_p, \quad (\text{D.10})$$

where $\lambda(\eta) = \log(\eta)$. The ground state $|\Psi(g, \eta)\rangle$ satisfies $B_p(g, \eta) |\Psi(g, \eta)\rangle = 0$ for all p . Recall that $|\Psi(g, \eta)\rangle$ can be understood as a linear combination of closed-loop configurations weighted by some loop tension, where each loop is the 1D MPS state that depends smoothly on a parameter for $g \in [-1, 1]$.

The operators

$$\operatorname{sech} \left(\tau \sum_{e \in p} Z_e(1 - Z_{v(e)}Z_{v'(e)}) + \lambda Z_e \right),$$

and

$$\operatorname{sech} \left(\sum_{e \in p} [\tau Z_e(1 - Z_{v(e)}Z_{v'(e)}) + \lambda Z_e] \right) \prod_{e \in p} e^{-\tau Z_e(1-Z_{v(e)}Z_{v'(e)})-\lambda Z_e},$$

are both diagonal in the computational basis with diagonal elements of the form $1/\cosh(4n_1\tau + 2n_2\lambda)$ and $e^{-4n_1\tau-2n_2\lambda}/\cosh(4n_1\tau + 2n_2\lambda)$ for some integers $n_1, n_2 \in [-3, 3]$. Inserting the reparameterization $\tau(g) = -\log(g)/4$, the matrix elements can be written as

$$\begin{aligned} \frac{1}{\cosh(4n_2\tau + 2n_2\lambda)} &= \frac{2g^{n_1}}{\eta^{2n_2} + g^{2n_1}\eta^{-2n_2}}, \\ \frac{e^{-4n_1\tau-2n_2\lambda}}{\cosh(4n_2\tau + 2n_2\lambda)} &= \frac{2g^{2n_1}\eta^{-2n_2}}{\eta^{2n_2} + g^{2n_1}\eta^{-2n_2}}, \end{aligned} \quad (\text{D.11})$$

D.2. $U(1)$ pivot symmetry at $g = 0$

which are analytic functions of g for all $\eta > 0$ and $g = a + i\varepsilon$, where $a, \varepsilon \in \mathbb{R}$ and $|\varepsilon| < \delta(\lambda)$. Here $\delta(\lambda)$ is the positive real number that corresponds to the smallest distance between the real line and the zeros of $\cosh(4n_1\tau + 2n_2\lambda)$ in the complex plane. Therefore, the projector Eq. (D.10) can be analytically continued to $\eta > 0$ and $g \in [-1, 1]$. For $g < 0$, the logarithmic function $\tau(g)$ will encounter a branch cut. As we have shown, all the singularities are removable regardless of how the function is defined across the branch cut.

A similar analysis can be performed for the vertex operators. We have the relation

$$(1 - A_v)M_v |\Psi(g, \eta)\rangle = 0, \quad \forall v; \quad (\text{D.12})$$

$$M_v = -X_v + \prod_{e \in v} e^{-\tau(g)(1 - Z_e)Z_{v(e)}Z_{v'(e)}}. \quad (\text{D.13})$$

Note that we include an additional projector $(1 - A_v)$ to project out the terms that violate the closed-loop constraint. The vertex projector at vertex v is given by

$$Q_v(g) = \frac{(1 - A_v)}{2} \operatorname{sech} \left(\tau(g) \sum_{e \in v} (1 - Z_e)Z_{v(e)}Z_{v'(e)} \right) M_v. \quad (\text{D.14})$$

Similar to the plaquette projectors, inserting $\tau(g) = -\log(g)/4$ in Eq. (D.14) results in a form analytic for g close to the real axis, allowing us to analytically continue the function to $g \in [-1, 1]$. We can define the analytically continued projector for $g \in [-1, 1]$.

Therefore, a parent Hamiltonian for $\eta \geq 0$ and $g \in [-1, 1]$ is, as claimed in the main text,

$$H(g, \eta) = \sum_v A_v + \sum_p B_p(g, \eta) + \sum_v Q_v(g), \quad (\text{D.15})$$

with a ground state energy of zero. At the fixed points $(g, \eta) = (\pm 1, 1)$, we recover the fixed-point Hamiltonians as given in the main text. As a consistency check of the analytic continuation, using the relation Eq. (D.29), it can be shown that the imaginary time-evolved state Eq. (D.8) satisfies the relation $|\Psi(-g, \eta)\rangle = U |\Psi(g, \eta)\rangle$, where $g \in [-1, 1]$ and U is the quantum circuit defined in Eq. (7.9). It follows that the analytically continued state (D.8) is proportional to the TNS defined in the main text when $g < 0$.

Indeed, the parent Hamiltonian is not unique. For example, Eq. (D.9) and (D.12) suggest that we may use $(g^3 K_p)^2$ and $(1 - A_v)(gM_v)^2$ to construct another parent Hamiltonian that depends smoothly on g and has a ground state energy of zero. Nonetheless, the parent Hamiltonians will share the same low-energy physics.

D.2. $U(1)$ pivot symmetry at $g = 0$

In Ref. [232], it is found that the 1D Ising-cluster model shown in Eq. (7.1) has a $U(1)$ pivot symmetry at $g = 0$. In this subsection, we show that the 2D Hamiltonian in Eq. (7.14) also has a $U(1)$ pivot symmetry at $g = 0$. We first derive the $U(1)$ pivot symmetry for the 1D case as a warm-up.

D.2.1. $U(1)$ pivot symmetry for 1D Hamiltonian

We start from a local term $P_i(g = 0)$ for the 1D parent Hamiltonian shown in Eq. (D.5). At $g = 0$, $\tau \rightarrow \infty$, it can be derived that

$$P_i \equiv \lim_{\tau \rightarrow \infty} \operatorname{sech}(2\tau Z_{i-1}Z_i + 2\tau Z_i Z_{i+1}) = \frac{1 - Z_{i-1}Z_{i+1}}{2}, \quad (\text{D.16})$$

Appendix D. Appendix: Symmetry-enriched topological phase transitions in 2D tensor-network states

and $P_i(g=0) = \mathcal{P}_i K_i/2$, $[\mathcal{P}_i, K_i] = 0$. Moreover, notice that $\mathcal{P}_i(Z_{i-1}Z_i + Z_iZ_{i+1}) = 0$ and P_i only acts on three sites, we have

$$\left[P_j(g=0), \sum_i Z_i Z_{i+1} \right] = 0, \quad \forall j. \quad (\text{D.17})$$

Above equation implies that the generator of the $U(1)$ pivot symmetry can be defined as $H_{\text{Ising}} = \sum_i Z_i Z_{i+1}$, such that

$$[H_{\text{Ising}}, H(g=0)] = 0, \quad H(g=0) = \sum_i P_i(g=0). \quad (\text{D.18})$$

The $U(1)$ pivot symmetry is $U_{\text{pivot}}(\theta) = e^{i\theta H_{\text{Ising}}}$, $\theta \in \mathbb{R}$. The Hamiltonian at $g=0$ is invariant under $U_{\text{pivot}}(\theta)$:

$$U_{\text{pivot}}(\theta) H(g=0) U_{\text{pivot}}^\dagger(\theta) = H(g=0), \quad \forall \theta. \quad (\text{D.19})$$

When $\theta = \pi/4$, one can check that

$$\begin{aligned} U_{\text{pivot}}\left(\frac{\pi}{4}\right) &= e^{\frac{\pi i}{4} \sum_n Z_n Z_{n+1}} = e^{\frac{\pi i}{4} \sum_n (1-2s_n)(1-2s_{n+1})} \\ &= e^{\frac{\pi i N}{4}} e^{-\pi i \sum_n s_n} e^{\pi i \sum_n s_n s_{n+1}} = e^{\frac{\pi i N}{4}} \prod_n Z_n \prod_n CZ_{n,n+1}, \end{aligned}$$

where N is the length of the 1D chain and $s_i = (1 - Z_i)/2$ is the transformation from Ising spins $Z_i = \pm 1$ to qubits $s_i = 0, 1$. Therefore the pivot symmetry at $\theta = \pi/4$ transforms between the trivial and non-trivial SPT state:

$$U_{\text{pivot}}\left(\frac{\pi}{4}\right) H(g) U_{\text{pivot}}^\dagger\left(\frac{\pi}{4}\right) = H(-g). \quad (\text{D.20})$$

D.2.2. $U(1)$ pivot symmetry for 2D parent Hamiltonian

For the 2D case, the $U(1)$ pivot symmetry can be derived similarly. We begin from $B_p(g, \eta)$ shown in Eq. (D.10). At $g=0$, $\tau \rightarrow \infty$, we have

$$\mathcal{P}_p \equiv \lim_{\tau \rightarrow \infty} \text{sech} \left(\tau G_p + \lambda(\eta) \sum_{e \in p} Z_e \right) = \text{sech} \left(\sum_{e \in p} \lambda(\eta) Z_e \right) \delta_{G_p, 0},$$

where

$$G_p = \sum_{e \in p} Z_e (1 - Z_{v(e)} Z_{v'(e)}). \quad (\text{D.21})$$

Therefore, $B_p(g=0, \eta) = \mathcal{P}_p K_p/2$, $[\mathcal{P}_p, K_p] = 0$. Moreover, using $\mathcal{P}_p G_p = 0$, it follows that

$$\left[B_p(g=0, \eta), \sum_{e \in E} Z_e (1 - Z_{v(e)} Z_{v'(e)}) \right] = 0, \quad \forall p. \quad (\text{D.22})$$

We can deal with the vertex terms $Q_v(g)$ shown in Eq. (D.14) similarly. At $g=0$, $\tau \rightarrow \infty$, another projector can be derived:

$$\mathcal{P}_v \equiv \lim_{\tau \rightarrow \infty} \text{sech}(\tau G_v) = \delta_{G_v, 0}, \quad G_v = \sum_{e \in v} (1 - Z_e) Z_{v(e)} Z_{v'(e)}. \quad (\text{D.23})$$

Analogous to the derivation of Eq. (D.22), we find

$$\left[Q_v(g=0), \sum_{e \in E} (1 - Z_e) Z_{v(e)} Z_{v'(e)} \right] = 0. \quad (\text{D.24})$$

D.3. Mapping the SET TNS norm to a partition function

To construct the $U(1)$ symmetry generator, we make use of the additional observation that

$$\left[B_p(g, \eta), \sum_{e \in E} (1 - Z_{v(e)} Z_{v'(e)}) \right] = \left[Q_v(g), \sum_{e \in E} (1 - Z_e) \right] = 0. \quad (\text{D.25})$$

Therefore, the generator $H_{\text{pivot}}^{(2D)}$ of the $U(1)$ pivot symmetry can be constructed as:

$$H_{\text{pivot}}^{(2D)} = \sum_e (1 - Z_e)(1 - Z_{v(e)} Z_{v'(e)}), \quad [H_{\text{pivot}}^{(2D)}, H(g=0, \eta)] = 0. \quad (\text{D.26})$$

The 2D parent Hamiltonian $H(g=0, \eta)$ is invariant under the transformation $U_{\text{pivot}}^{(2D)}(\theta) = \exp(i\theta H_{\text{pivot}}^{(2D)})$:

$$U_{\text{pivot}}^{(2D)}(\theta) H(g=0, \eta) U_{\text{pivot}}^{(2D)\dagger}(\theta) = H(g=0, \eta), \quad \theta \in \mathbb{R}. \quad (\text{D.27})$$

Analogous to the 1D case, at $\theta = \pi/8$, the $U(1)$ pivot symmetry realizes a unitary transformation:

$$U_{\text{pivot}}^{(2D)}\left(\frac{\pi}{8}\right) H(g, \eta) U_{\text{pivot}}^{(2D)\dagger}\left(\frac{\pi}{8}\right) = H(-g, \eta). \quad (\text{D.28})$$

Via the transformation from Ising spins to qubits $s_e = (1 - Z_e)/2$ and $s_v = (1 - Z_v)/2$, $U_{\text{pivot}}^{(2D)}(\pi/8)$ can be expressed in terms of CCZ gates:

$$\begin{aligned} U_{\text{pivot}}^{(2D)}\left(\frac{\pi}{8}\right) &= \exp\left[\frac{\pi i}{8} \sum_e (1 - Z_e)(1 - Z_{v(e)} Z_{v'(e)})\right] \\ &= \exp\left[\frac{\pi i}{2} \sum_e s_e (s_{v(e)} + s_{v'(e)} - 2s_{v(e)} s_{v'(e)})\right] \\ &= \exp\left[\frac{\pi i}{2} \sum_e s_e (s_{v(e)} + s_{v'(e)})\right] \prod_e CCZ_{v(e)v'(e)e} \\ &= \prod_v \exp\left(\frac{i\pi}{2} s_v \sum_{e \in v} s_e\right) \prod_e CCZ_{v(e)v'(e)e} \\ &= \prod_{\langle ee' \rangle} \exp(i\pi s_{v(e,e')} s_e s_{e'}) \prod_e CCZ_{v(e)v'(e)e} \\ &= \prod_{\langle ee' \rangle} CCZ_{v(e,e')ee'} \prod_{\langle vv' \rangle} CCZ_{vv'e(v,v')}. \end{aligned} \quad (\text{D.29})$$

The second to last line is obtained by substituting the relation $\sum_{e \in v} s_e = 2 \sum_{\langle ee' \rangle \in v} s_e s_{e'}$, which is only valid in the closed-loop subspace, into the third last line. We prove that $U_{\text{pivot}}^{(2D)}(\pi/8)$ is equivalent to the unitary transformation (7.9) in the main text.

D.3. Mapping the SET TNS norm to a partition function

In this Appendix, we show that along $g = \pm 1$, the decorated TNS can be mapped to the 2D classical Ising model, and along $g = 0$ they can be mapped to the 2D classical $O(2)$ loop model. The essence of the quantum-classical mapping is identifying the squared norm of the decorated TNS with the partition function of an exactly solved 2D classical statistical model.

When decorating the MPS onto the loops of the toric code, the norm of the MPS, which depends on the length of the MPS, will affect the coefficients in the 2D decorated

Appendix D. Appendix: Symmetry-enriched topological phase transitions in 2D tensor-network states

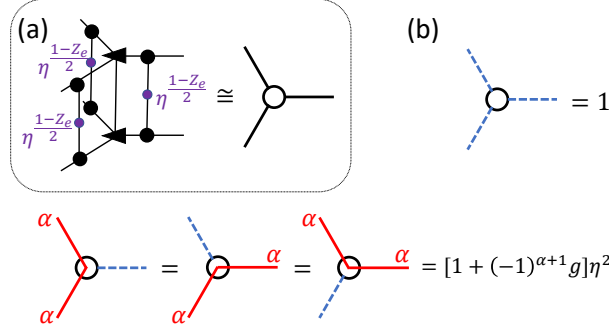


Figure D.1.: (a) Reduction of the double tensor bond dimension from $D^2 = 9$ to 3. (b) The non-zero entries of the reduced double tensor, where blue dashed lines represent the one-dimensional odd bond and red solid lines represent the two-dimensional even bond.

wavefunction. We first derive the norm of the MPS defined in Eqs. (7.2) and (7.3). The transfer operator can be defined from the MPS tensor

$$T = \sum_i M^{[i]} \otimes \bar{M}^{[i]}, \quad (\text{D.30})$$

whose eigenvalues are $(1+g, 1-g, 0, 0)$. The squared norm of the periodic MPS (7.2) with a length L is $\mathcal{N}(g) = (1+g)^L + (1-g)^L$.

Then, let us consider the norm of the decorated TNS, which is a tensor network generated by the double tensor in Fig. D.1a. We duplicate the physical degrees of freedom at the edges so that the tensor looks more symmetric. Because the virtual degrees of freedom in the bra and ket layers have the same parity, we can reduce the bond dimension of the double tensor from $D^2 = 9$ to 5. The bond dimension 5 is a direct sum of a 1-dimensional even bond and a 4-dimensional odd bond. The 4-dimensional odd bonds support the MPS transfer operator (D.30). However, since the MPS transfer operator has two zero eigenvalues, we can further reduce the dimension of an even bond from 4 to 2 by diagonalizing the MPS transfer operator. Finally, the bond dimension of the double tensor is reduced to 3 and its non-zero entries are given in Fig. D.1b.

From the reduced double tensor shown in Fig. D.1, there are two kinds of loops with labels $\alpha = 1, 2$ and loop tension $(1 \pm g)\eta^2$, respectively. Therefore, the squared norm of the decorated TNS (7.13) is given by

$$\mathcal{N}(g, \eta) = 2^{N_v} \sum_C \prod_{c \in C} \left[\left(\frac{\eta^2 + g\eta^2}{2} \right)^{l_c} + \left(\frac{\eta^2 - g\eta^2}{2} \right)^{l_c} \right], \quad (\text{D.31})$$

where N_v is total number of vertices, C is a given closed loop configuration, and $c \in C$ is a closed loop in C , and l_c is the length of a given loop c .

When $g = 0, \pm 1$, the squared norm of the decorated TNS becomes the partition function of the classical $O(n)$ loop models [249, 251]

$$\mathcal{Z}(n, K) = \sum_C n^{N(C)} K^{L(C)}, \quad (\text{D.32})$$

where $N(C)$ is the total number of loops in C , $L(C)$ is the total length of all loops in C , n is called the loop fugacity and K is the loop tension. The position of the critical point

D.4. 2D $\mathbb{Z}_2 \times \mathbb{Z}_2^T$ SPT states and corresponding partition function

K_c and the central charge c at the critical point are [250]

$$\begin{aligned} K_c &= (2 + \sqrt{2-n})^{-1/2}, \quad c = 1 - \frac{6(h-1)^2}{h}, \\ h &= -\frac{1}{\pi} \arccos\left(-\frac{n}{2}\right) + 1. \end{aligned} \quad (\text{D.33})$$

When $g = \pm 1$, the squared norm (D.31) of the decorated TNS is equivalent to the partition function of the $O(1)$ loop model

$$\mathcal{N}(g = \pm 1, \eta) \propto \sum_C \eta^{2L(C)} = \mathcal{Z}(1, \eta^2), \quad (\text{D.34})$$

which is also equivalent to the Ising model on a triangular lattice. The critical point is at $\eta_c = 3^{-1/4} \approx 0.7598$ and $c = 1/2$. When $g = 0$, the squared norm (D.31) of the decorated TNS is equivalent to the partition function of the $O(2)$ loop model:

$$\mathcal{N}(g = 0, \eta) \propto \sum_C 2^{N(C)} (\eta^2/2)^{L(C)} = \mathcal{Z}(2, \eta^2/2). \quad (\text{D.35})$$

It is well known that the $O(2)$ loop model is qualitatively equivalent to the classical XY model. The critical point $\eta_c = 2^{1/4} \approx 1.189$ is a Kosterlitz-Thouless phase transition point with central charge $c = 1$. When $\eta < \eta_c$, it is the gapped dilute loop phase. When $\eta > \eta_c$, it is the gapless dense loop phase described by a compactified free boson CFT with $c = 1$. The $O(2)$ symmetry of the loop model is consistent with the $U(1)$ pivot symmetry of the parent Hamiltonian shown in Appendix D.2.

D.4. 2D $\mathbb{Z}_2 \times \mathbb{Z}_2^T$ SPT states and corresponding partition function

A duality transformation exists between the 2D trivial (non-trivial) \mathbb{Z}_2 SPT model and the toric code (double-semion) model [226], which is given by

$$Z_e = Z_{p(e)} Z_{p'(e)}, \quad \prod_{e \in p} X_e = X_p, \quad (\text{D.36})$$

where the Z_p, X_p are Pauli operators located at plaquettes and $p(e), p'(e)$ are two plaquettes adjacent to edge e . Applying the duality transformation to the imaginary time evolved wavefunction (D.8) describing \mathbb{Z}_2^T SET phase transitions gives rise to the following wavefunction describing $\mathbb{Z}_2 \times \mathbb{Z}_2^T$ SPT phase transitions:

$$|\Psi_{\text{SPT}}\rangle \propto \prod_{e \in E} e^{\frac{\tau}{2} Z_{v(e)} Z_{v'(e)} + (\frac{\tau}{2} - \lambda) Z_{p(e)} Z_{p'(e)} - \frac{\tau}{2} Z_{v(e)} Z_{v'(e)} Z_{p(e)} Z_{p'(e)}} |+\rangle_v |+\rangle_p, \quad (\text{D.37})$$

where $|+\rangle_v$ ($|+\rangle_p$) is a product state $|+\dots+\rangle$ of all vertex (plaquette) qubits. The duality transformation preserves the structure of the phase diagram, as shown in Ref. [236]. The TC phase is mapped to the trivial $\mathbb{Z}_2 \times \mathbb{Z}_2^T$ SPT phase and the SET-TC phase is mapped to a non-trivial $\mathbb{Z}_2 \times \mathbb{Z}_2^T$ SPT phase. The trivial phase of the phase diagram shown in Fig. 7.4a is mapped to the symmetry broken phase, in which the \mathbb{Z}_2 spin flip symmetry of plaquette spins is spontaneously broken.

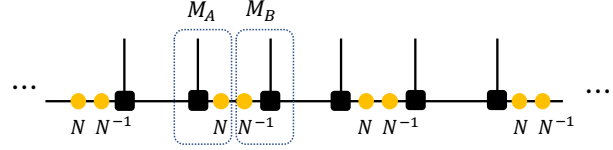
The squared norm of the wavefunction (D.37) can be expressed as

$$\| |\Psi_{\text{SPT}}\rangle \|^2 \propto \sum_{\{Z_p, Z_v\}} \prod_{e \in E} e^{\tau Z_{v(e)} Z_{v'(e)} + (\tau - 2\lambda) Z_{p(e)} Z_{p'(e)} - \tau Z_{v(e)} Z_{v'(e)} Z_{p(e)} Z_{p'(e)}}. \quad (\text{D.38})$$

It can be interpreted as the partition function of the Ashkin-Teller model, which consists of two coupled Ising models, one has Ising spins $\{Z_v\}$ on the honeycomb lattice and the other has Ising spins $\{Z_p\}$ on the triangular lattice. This partition function is equivalent to the partition function (D.31). This suggests that we can also add the additional deformation $\prod_e e^{\beta Z_v(e) Z_{v'(e)}}$ to the original SET model and obtain a ferromagnetic phase or antiferromagnetic phase in which the \mathbb{Z}_2^T symmetry is broken spontaneously.

D.5. Real symmetric tensors and symmetry fractionalization

Here, we show that the MPS tensors have a real and symmetric form under exchanging two virtual indices such that the single-line tensors of the decorated TNS are real and have a bond dimension $D = 3$. This lowers the numerical cost. We apply a gauge transformation to MPS tensors in the 2-site unit cells



$$\dots \text{---} \overset{M_A}{\square} \overset{M_B}{\square} \text{---} \dots, \quad (\text{D.39})$$

where the gauge transformation is given by

$$N = \begin{pmatrix} g & -g \\ -g & 1 \end{pmatrix}, \quad N^{-1} = \frac{1}{g(1-g)} \begin{pmatrix} 1 & g \\ g & g \end{pmatrix}. \quad (\text{D.40})$$

The real and symmetric MPS tensors in a 2-site unit cell are

$$\begin{aligned} M_A^{[0]} &= M^{[0]}N = \begin{pmatrix} 0 & 0 \\ 0 & 1-g \end{pmatrix}, \\ M_A^{[1]} &= M^{[1]}N = \begin{pmatrix} g(1-g) & 0 \\ 0 & 0 \end{pmatrix}, \\ M_B^{[0]} &= N^{-1}M^{[0]} = \frac{1}{g(1-g)} \begin{pmatrix} g & g \\ g & g \end{pmatrix}, \\ M_B^{[1]} &= N^{-1}M^{[1]} = \frac{1}{g(1-g)} \begin{pmatrix} 1 & g \\ g & g^2 \end{pmatrix}. \end{aligned} \quad (\text{D.41})$$

At $g = 0$ and 1 , because the MPS is non-injective, the gauge transformation N is not well-defined.

Next, we consider the \mathbb{Z}_2^T symmetry of the MPS tensors M_A and M_B in a unit cell. By applying the \mathbb{Z}_2^T symmetry to the MPS, we find

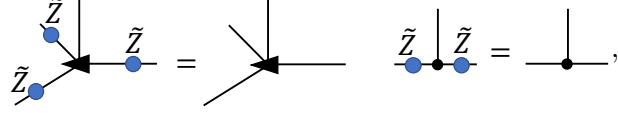
$$\begin{aligned} \sum_i (X)_{ij} \bar{M}_A^{[i]} &= \text{sign}(g) U M_A^{[j]} U^T, \\ \sum_i (X)_{ij} \bar{M}_B^{[i]} &= \text{sign}(g) (U^T)^{-1} M_B^{[j]} U^{-1}, \\ \sum_{ik} (X)_{ij} (X)_{kl} \bar{M}_A^{[i]} \bar{M}_B^{[k]} &= U M_A^{[j]} M_B^{[l]} U^{-1}, \end{aligned} \quad (\text{D.42})$$

where

$$U = \begin{pmatrix} 0 & \text{sign}(g)\sqrt{|g|} \\ 1/\sqrt{|g|} & 0 \end{pmatrix}, \quad U^{-1} = \text{sign}(g)U. \quad (\text{D.43})$$

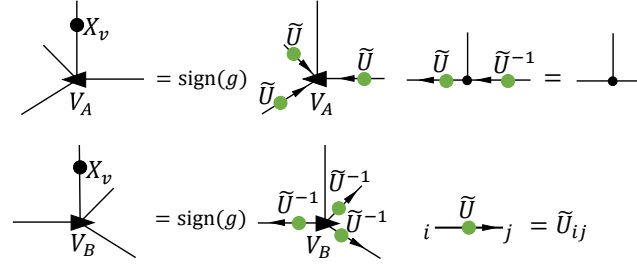
U is the representation of the symmetry operator on the virtual level. Because $U\bar{U} = \text{sign}(g)$, it is a projective representation when $g < 0$.

With the MPS tensors M_A and M_B , we can construct the tensors of the decorated TNS shown in Fig. 7.3a and Eq. (7.11). The tensors of the decorated TNS have two symmetries, one originates from the topological order and the other comes from the \mathbb{Z}_2^T symmetry. The symmetry from the topological order is



$$\begin{array}{c} \tilde{Z} \\ | \\ \bullet \\ / \quad \backslash \\ \tilde{Z} \quad \bullet \\ \backslash \quad / \\ \bullet \end{array} = \begin{array}{c} | \\ | \\ | \\ | \end{array} \quad \begin{array}{c} \tilde{Z} \\ | \\ \bullet \\ | \\ \bullet \end{array} = \begin{array}{c} | \\ | \\ | \\ | \end{array}, \quad (D.44)$$

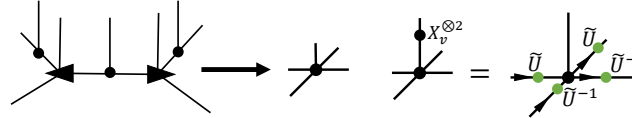
where $\tilde{Z} = 1 \oplus (-1)$. Because of Eq. (D.42), it can be found that applying the \mathbb{Z}_2^T symmetry to the decorated TNS tensor gives rise to



$$\begin{array}{c} \bullet X_v \\ | \\ \blacktriangleleft V_A \end{array} = \text{sign}(g) \begin{array}{c} \tilde{U} \\ | \\ \bullet \\ / \quad \backslash \\ \tilde{U} \quad \bullet \\ \backslash \quad / \\ \bullet \end{array} \quad \begin{array}{c} \tilde{U} \\ | \\ \bullet \\ | \\ \bullet \end{array} = \begin{array}{c} | \\ | \\ | \\ | \end{array}, \quad (D.45)$$

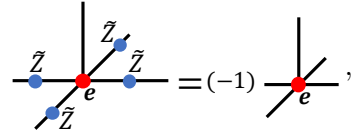
$$\begin{array}{c} \bullet X_v \\ | \\ \blacktriangleright V_B \end{array} = \text{sign}(g) \begin{array}{c} \tilde{U}^{-1} \\ | \\ \bullet \\ / \quad \backslash \\ \tilde{U}^{-1} \quad \bullet \\ \backslash \quad / \\ \bullet \end{array} \quad i \xrightarrow{\tilde{U}} j = \tilde{U}_{ij}$$

where $\tilde{U} = 1 \oplus U$. Because \tilde{U} is not a symmetric matrix, we use arrows to differentiate its row and column indices. Considering that in a unit cell, $\text{sign}(g)$ will be cancelled, we have



$$\begin{array}{c} \bullet X_v^{\otimes 2} \\ | \\ \blacktriangleleft \quad \bullet \\ | \\ \blacktriangleright \end{array} = \begin{array}{c} \bullet X_v^{\otimes 2} \\ | \\ \bullet \\ | \\ \bullet \end{array} = \begin{array}{c} \tilde{U} \\ | \\ \bullet \\ / \quad \backslash \\ \tilde{U}^{-1} \quad \bullet \\ \backslash \quad / \\ \bullet \end{array}, \quad (D.46)$$

where $X_v^{\otimes 2}$ acts on two physical degrees of freedom of two vertices. Applying the \mathbb{Z}_2^T symmetry twice, it can be found that $\tilde{U}\tilde{U} = \tilde{Z}$. Because a single-line tensor carrying an anyon \mathbf{e} satisfies



$$\begin{array}{c} \tilde{Z} \\ | \\ \bullet \\ / \quad \backslash \\ \tilde{Z} \quad \bullet \\ \backslash \quad / \\ \bullet \end{array} = (-1) \begin{array}{c} | \\ | \\ | \\ | \end{array}, \quad (D.47)$$

applying the \mathbb{Z}_2^T symmetry twice on an \mathbf{e} anyon gives rise to a minus sign. The \mathbb{Z}_2^T symmetry fractionalizes on the \mathbf{e} anyons (and also on the \mathbf{f} anyons).

Note that the decorated TNS can be made to satisfy the MPO-injectivity [218] by grouping the edge and vertex tensors appropriately. The set of virtual matrix-product-operator (MPO) symmetries corresponding to the action of the physical symmetry group, including the product MPO symmetry consisting of \tilde{U} , encodes the universal labels of the quantum phase of the system [215, 216].

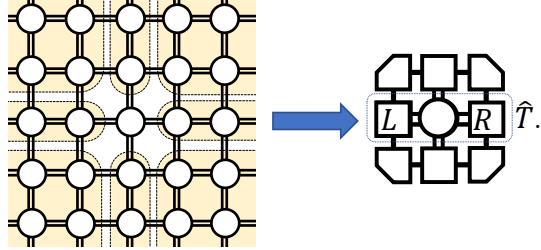
D.6. CTMRG and correlation length

In this subsection, we show the basic idea of the CTMRG algorithm and the results of the correlation length. At first, we use a simplified notation of the double tensors



$$\begin{array}{c} \bullet \\ | \\ \bullet \\ / \quad \backslash \\ \bullet \quad \bullet \\ \backslash \quad / \\ \bullet \end{array} = \begin{array}{c} | \\ | \\ | \\ | \end{array}. \quad (D.48)$$

Since the above tensor is not symmetric under exchanging left and right (or upper and lower) indices, the transfer operator of the decorated TNS is non-Hermitian. Therefore, we approximate the environment of the blocked double tensor in terms of four edge tensors and four corner tensors with a bond dimension χ [247]:


(D.49)

These edge tensors and corner tensors can be obtained using the CTMRG algorithm [248]. The correlation length $\xi_i = -1/\log(\hat{t}_i/\hat{t}_0)$ can be calculated from the largest eigenvalue \hat{t}_0 and the $(i+1)$ -th largest eigenvalue \hat{t}_i of the transfer operator \hat{T} shown in Eq. (D.49).

We scan the whole phase diagram by calculating the correlation length ξ_1 using the CTM environment with bond dimension $\chi = 20$. The results shown in Fig. D.2a clearly indicate the phase boundaries. We notice that the position of the tricritical point obtained from the correlation length is not very close to the exact result $(g, \eta) = (0, 2^{1/4}) \approx (0, 1.1892)$. This is reasonable because it is notoriously hard to numerically determine the KT phase transition point. The reason is that there is a logarithmic correction to the position of the KT phase transition point due to the finite bond dimension χ [278]:

$$\eta_c(\chi) = \eta_c + a \log[\xi_1^{-2}(\chi)], \quad (\text{D.50})$$

where $\xi_1(\chi)$ is the correlation length from a finite bond dimension χ , $\eta_c(\chi)$ is the location of the phase transition from a finite χ , and a is a constant. We can calculate the correlation length $\xi_i(\chi)$ along $g = 0$ for various large bond dimensions χ using the reduced tensor shown in Fig. D.1. As shown in Fig. D.2b, no signature of the phase transition can be found in $\xi_1(\chi)$ and we can not determine $\eta_c(\chi)$. However, we find that $\xi_2(\chi)$ exhibits peaks, which move towards the exact critical point with increasing χ (see Fig. D.2c), indicating that it could be used to determine $\eta_c(\chi)$. An alternative way to determine $\eta_c(\chi)$ is to use the entanglement entropy S from boundary MPS or corner tensors of the CTMRG environment [278, 279]. As shown in Fig. D.2d, the locations of the peaks in ξ_2 and S coincide, the differences are smaller than 0.0005. Using Eq. (D.50), the position of the tricritical point can be extrapolated, and the result is shown in Fig. D.1e, indicating that a larger bond dimension is needed to get a more accurate result.

D.7. Calculation of membrane order parameters using tensor networks

In this Appendix, we show how to simplify the calculation of the MOP shown in Eq. (7.20) using tensor networks. We define a modified double tensor that sandwiches the symmetry operator $X_v^{\otimes 2}$:


(D.51)

Since there is no canonical form, a given 2D TNS is usually unnormalized, and the MOP has to be expressed as a ratio of two tensor networks. The tensor network in the numerator

Appendix D. Appendix: Symmetry-enriched topological phase transitions in 2D tensor-network states

and the tensor network in the denominator of the ratio represents the norm of the decorated TNS:

The entries of the tensors generating the vertical matrix product operator (MPO) are

$$\begin{array}{c} 1 \\ | \\ \bullet \\ | \\ 1 \end{array} = \mathbb{1}, \quad \begin{array}{c} 2 \\ | \\ \bullet \\ | \\ 2 \end{array} = \tilde{Z},$$

and the matrices inserted along the horizontal lines are

$$\begin{array}{c} | \\ \bullet \\ | \end{array} = \begin{cases} \mathbb{1}, & \text{if } \alpha = \mathbf{1} \text{ or } \mathbf{e}, \\ \tilde{Z}, & \text{if } \alpha = \mathbf{m} \text{ or } \mathbf{f}, \end{cases} \quad , \quad \begin{array}{c} | \\ \bullet \\ | \end{array} = \begin{cases} \mathbb{1}/2, & \text{if } \alpha = \mathbf{1} \text{ or } \mathbf{m}, \\ Z/2, & \text{if } \alpha = \mathbf{e} \text{ or } \mathbf{f}. \end{cases}$$

The vertical MPO and horizontal matrices are used to generate MES in the bra and ket layers. Explicitly, a vertical MPO is a projector

$$P_{\pm} = \frac{1}{2}(\mathbb{1}^{\otimes N} \pm \tilde{Z}^{\otimes N}), \quad P_{\pm}^2 = P_{\pm}, \quad (\text{D.54})$$

where P_+ (P_-) corresponds to the red dot being $\mathbb{1}/2$ ($\tilde{Z}/2$), respectively, and N is the circumference of the cylinder.

Then we can contract the tensor networks for the numerator and denominator. We define the left fixed point σ_L and the right fixed points σ_R of the transfer operators \mathbb{T} (see Eq. (D.52)), as well as the left fixed point $\tilde{\sigma}_L$ and the right fixed points $\tilde{\sigma}_R$ of the transfer operator $\tilde{\mathbb{T}}$ (also see Eq. (D.52)). These fixed points can be approximated by the MPS

D.7. Calculation of membrane order parameters using tensor networks

where the tensor L and R come from the edge tensors of the CTM environment shown in Eq. (D.49), the tensors represented by the green dots are $\tilde{U} = 1 \oplus U$ and U is defined in Eq. D.43. The fixed points $\tilde{\sigma}_L$ and $\tilde{\sigma}_R$ of $\tilde{\mathbb{T}}$ are derived from the fixed points σ_L and σ_R of \mathbb{T} using Eq. (D.45). The matrices represented by blue boxes in Eq. (D.55) come from the two horizontal \tilde{Z} strings in Eq. (D.52). However, due to the \mathbb{Z}_2 Gauss law on every vertex tensor, the \tilde{Z} strings in the bra and ket layers cancel each other, and the matrices represented by the blue boxes become the identity matrix.

With the above fixed points, we can contract the tensor networks of the numerator and denominator in Eqs. (D.52) and (D.53) from the left and right:

(D.56)

The above tensor networks can be further simplified using the relation $P_{\pm}\sigma_{L/R} = \sigma_{L/R}P_{\pm}$:

(D.57)

The channel operators \tilde{T} and T can be defined from the above tensor networks, and it is easy to find their fixed points:

$$\begin{aligned} \langle \tilde{U}_n | \tilde{T} &= \tilde{t} \langle \tilde{U}_n |, & \tilde{T} | \tilde{D}_n \rangle &= \tilde{t} | \tilde{D}_n \rangle; \\ \langle U_n | T &= t \langle U_n |, & T | D_n \rangle &= t | D_n \rangle. \end{aligned} \quad (\text{D.58})$$

Here $t, \tilde{t} \in \mathbb{R}$ are the dominant eigenvalues of the channel operators T and \tilde{T} respectively, and we specify the degenerate channel fixed points with a subscript n . Notice that the channel fixed points have to be biorthonormalized: $\langle U_n | D_m \rangle = \delta_{nm}$. Finally, by contracting the tensor networks using the channel fixed points from above and below, the MOP can be expressed as

$$O_{\alpha} = \lim_{N \rightarrow \infty} \left[\begin{pmatrix} \tilde{t} \\ t \end{pmatrix}^N \frac{\tilde{F}_{\alpha}}{F_{\alpha}} \right]^{1/N} = \begin{cases} 0, & \text{if } \tilde{F}_{\alpha}/F_{\alpha} = 0 \\ t_v/t, & \text{if } \tilde{F}_{\alpha}/F_{\alpha} \neq 0, \end{cases} \quad (\text{D.59})$$

where

$$\tilde{F}_\alpha = \sum_n \begin{array}{c} \boxed{\tilde{U}_n} \\ \text{---} \text{---} \text{---} \text{---} \\ \text{---} \text{---} \text{---} \text{---} \\ \boxed{\tilde{D}_n} \end{array}, \quad F_\alpha = \sum_n \begin{array}{c} \boxed{U_n} \\ \text{---} \text{---} \text{---} \text{---} \\ \text{---} \text{---} \text{---} \text{---} \\ \boxed{D_n} \end{array}. \quad (\text{D.60})$$

In the trivial phase, we find that F_e and F_f are zero, which is consistent with the fact that e and f are confined and the MES is no longer well-defined: $\langle \Psi_e | \Psi_e \rangle = \langle \Psi_f | \Psi_f \rangle = 0$.

D.8. Degeneracy of entanglement spectrum and calculation of TEE using tensor networks

The key object for investigating entanglement properties of a quantum many-body wavefunction is the reduced density operator ρ from bipartition. From Ref. [280], it is known that the spectrum of a reduced density operator ρ of a TNS is identical to the spectrum of $\sigma = \sigma_L^T \sigma_R$, where σ_L and σ_R are the fixed points of the transfer operator \mathbb{T} of the TNS. The entanglement spectrum can be obtained by applying minus the logarithm to eigenvalues of σ . Moreover, considering the topological sectors, we have

$$\sigma_{\mathbf{1}} = \sigma_{\mathbf{m}} = P_+ \sigma, \quad \sigma_{\mathbf{e}} = \sigma_{\mathbf{f}} = P_- \sigma, \quad (\text{D.61})$$

where P_\pm is defined in Eq. (D.54). In the SET-TC phase, applying the \mathbb{Z}_2^T symmetry on the TNS reveals the symmetry transformations on σ_α :

$$\tilde{U}^{\otimes N} \bar{\sigma}_\alpha (\tilde{U}^{-1})^{\otimes N} = \sigma_\alpha, \quad \tilde{Z}^{\otimes N} \sigma_\alpha \tilde{Z}^{\otimes N} = \sigma_\alpha. \quad (\text{D.62})$$

Since $\tilde{Z}^{\otimes N} P_\pm = \pm P_\pm$, we have

$$\tilde{U}^{\otimes N} \tilde{U}^{\otimes N} = \begin{cases} 1, & \alpha = \mathbf{1}, \mathbf{m} \\ -1, & \alpha = \mathbf{e}, \mathbf{f} \end{cases}. \quad (\text{D.63})$$

Therefore, we can apply Kramers' theorem to σ_e and σ_f , and derive that the entanglement spectra of the e and f sectors are even-fold degenerate in the SET-TC phase.

In the following, we show a method of directly calculating the TEE in the limit $N \rightarrow \infty$, which is similar to the MOP calculation. Since the transfer operator \mathbb{T} is non-Hermitian, we calculate the second Renyi entropy using tensor networks. From Eq. (7.19), the second Renyi entropy is

$$S_\alpha^{[2]} = 2 \log \text{Tr}(\sigma_\alpha) - \log \text{Tr}(\sigma_\alpha^2), \quad (\text{D.64})$$

where there is an extra term $2 \log \text{Tr}(\sigma_\alpha)$ since usually σ_α is not normalized in tensor-network calculations. $\text{Tr}(\sigma_\alpha^2)$ can be expressed in terms of a tensor network:

$$(\text{D.65})$$

The tensor network of $\text{Tr}(\sigma_{\alpha})$ is the right hand side of Eq. (D.57). Defining another channel operator $T^{[2]}$, as shown in Eq. (D.65), its fixed points $U_n^{[2]}$, $D_n^{[2]}$ can be found

$$\langle U_n^{[2]} | T^{[2]} = t_{[2]} \langle U_n^{[2]} |, \quad T^{[2]} | D_n^{[2]} \rangle = t_{[2]} | D_n^{[2]} \rangle, \quad (\text{D.66})$$

where the subscript n specifies the degenerate fixed points and we impose the biorthonormality condition $\langle U_k^{[2]} | D_m^{[2]} \rangle = \delta_{km}$. We can contract the tensor networks of $\text{Tr}(\sigma_{\alpha}^2)$ and $\text{Tr}(\sigma_{\alpha})$ using their channel fixed points

$$\text{Tr}(\sigma_{\alpha}^2) = \lim_{N \rightarrow +\infty} t_{[2]}^N F_{\alpha}^{[2]}, \quad \text{Tr}(\sigma_{\alpha}) = \lim_{N \rightarrow +\infty} t^N F_{\alpha}, \quad (\text{D.67})$$

where

$$F_{\alpha}^{[2]} = \sum_n \begin{array}{c} \boxed{U_n^{[2]}} \\ | \\ \bullet \quad \square \quad \square \quad \square \quad \square \\ | \\ \boxed{D_n^{[2]}} \end{array} \quad (\text{D.68})$$

and F_{α} is defined in Eq. (D.60). Substituting these relations into Eq (D.64), we obtain the second Renyi entanglement entropy in the limit $N \rightarrow \infty$

$$S_{\alpha}^{[2]} = \lim_{N \rightarrow \infty} N \log \frac{t^2}{t^{[2]}} - \log \frac{F_{\alpha}^{[2]}}{F_{\alpha}^2}, \quad (\text{D.69})$$

from which we can identify the TEE $\gamma = \log F_{\alpha}^{[2]} / F_{\alpha}^2$.

E. Appendix: Efficient quantum circuits and quantum algorithms for simulating topological quantum phase transitions in 2D isometric tensor networks

E.1. The plumbing construction in 1D MPS

The plumbing method can be applied to the 1D system and we recover some of the familiar examples of quantum phase transitions in 1D matrix-product states (MPS) [242]. MPS are an ansatz class where the coefficients of a full 1D N -qubit state $|\psi\rangle$ are decomposed into products of matrices. Explicitly, for a system with open boundaries and translational invariance in the bulk

$$|\psi\rangle = \sum_{\{\sigma\}} A^{\sigma_1} B^{\sigma_2} B^{\sigma_3} \dots B^{\sigma_{n-1}} C^{\sigma_n} |\sigma_1 \sigma_2 \sigma_3 \dots \sigma_n\rangle, \quad (\text{E.1})$$

where the $\sigma_k \in \{0, 1, \dots, d\}$ indices are the physical indices and B^σ are $\chi \times \chi$ matrices with χ being the bond dimension of the MPS. The boundary tensors A^σ and C^σ are $1 \times \chi$ and $\chi \times 1$ matrices, respectively. Analogous to the main text, we employ the plumbing structure and impose the isometry condition. Namely, we require

$$B_{ij}^\sigma = \sum_{j'} \delta_{ij'}^\sigma W_{j'j}, \quad (\text{E.2})$$

where the δ -tensor takes value 1 when all indices are the same and zero otherwise. Furthermore

$$\sum_{\sigma, j'} (B_{ij'}^\sigma)^* B_{jj'}^\sigma = \delta_{ij}. \quad (\text{E.3})$$

This isometry condition is satisfied if and only if

$$\sum_j |W_{ij}|^2 = 1, \quad \forall i. \quad (\text{E.4})$$

Now suppose we take $C_i^\sigma = \delta_i^\sigma$ and A^σ is some boundary condition that can be chosen at will. The MPS in Eq. (E.1) is essentially a canonical form of the MPS, which is equivalent to a sequential quantum circuit [220].

As an example, consider a W -matrix path with $d = \chi = 2$, for $g \in [-1, 1]$

$$W(g) = \begin{pmatrix} |0\rangle & |1\rangle \\ \frac{1}{\sqrt{1+|g|}} & \text{sign}(g)\sqrt{\frac{|g|}{1+|g|}} \\ \sqrt{\frac{|g|}{1+|g|}} & \frac{1}{\sqrt{1+|g|}} \end{pmatrix} \begin{pmatrix} |0\rangle \\ |1\rangle \end{pmatrix}. \quad (\text{E.5})$$

At $g = 1$, the wavefunction $|\psi(g)\rangle$ is a simple product state $|++\dots+\rangle$ in the bulk. At $g = -1$, the state is a cluster state with $Z_i X_{i+1} Z_{i+2} |\psi(-1)\rangle = -1$ for all i in the bulk.

At these two limits, the 1D system belongs to distinct 1D SPT phases protected by anti-unitary \mathbb{Z}_2^T symmetry generated by $(\prod_i X_i)K$, where K is the complex conjugation. It can be verified that this is a symmetry for the state for all g .

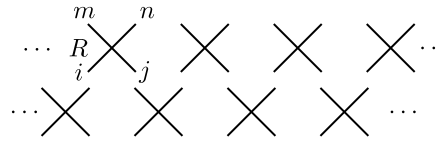
A quantum phase transition happens at $g = 0$, where the wavefunction has a long-range order and becomes the Greenberger–Horne–Zeilinger (GHZ) state $|\psi(0)\rangle = (|00\cdots 0\rangle + |11\cdots 1\rangle)/\sqrt{2}$ with the boundary tensor chosen as $A_i^\sigma = \delta_i^\sigma$. In fact, the MPS along this path is exactly the canonical form of the $\chi = 2$ MPS considered in Ref. [242], with a parent Hamiltonian

$$H(g) = g_{zzz} \sum_i Z_{i-1} X_i Z_{i+1} - g_{zz} \sum_i Z_i Z_{i+1} - g_x \sum_i X_i, \quad (\text{E.6})$$

where $g_{zzz} = (1 - g)^2$, $g_x = (1 + g)^2$ and $g_{zz} = 2(1 - g^2)$. This canonical form has been utilized to construct an efficient quantum circuit for the physical realization of this phase transition on a digital quantum computer [143].

E.2. Quantum-classical correspondence

In this section, we describe the connection between the plumbing construction and the quantum-classical correspondence in tensor networks. We note that the squared norm of the TNS wavefunction represented by the plumbed local tensor $T_{ijmn}^{\sigma\rho}$ can be expressed as the product of the transfer operators $\langle\psi|\psi\rangle = \text{Tr}(M^L)$ (assuming periodic boundary condition on an $L \times L$ system). The transfer operator $M = R_1 R_2 \cdots R_L$ is the product of the weight matrix R along each row, where $R_{ijmn} = |W_{ijmn}|^2$ and W is the W -matrix used in the plumbing procedure. One way to contract the transfer operator can be visualized as



$$\begin{array}{ccccccc} \cdots & \overset{m}{\diagup} & \overset{n}{\diagdown} & & & & \cdots \\ \cdots & R & & \times & \times & \times & \cdots \\ \cdots & \underset{i}{\diagdown} & \underset{j}{\diagup} & & & & \cdots \\ \cdots & \times & \times & \times & \times & \cdots & \end{array} \quad (\text{E.7})$$

Indeed, one can also rotate each weight matrix R by 45 degrees and contract. This is exactly the same as contracting a 2D classical partition function. As an example, consider an $L \times L$ classical spin system on a square lattice with nearest-neighbour two-body interaction $H = \sum_{\langle i,j \rangle} h(\sigma_i, \sigma_j)$. The partition function of the system $\mathcal{Z} = \text{Tr}(e^{-\beta H}) = \text{Tr}(M^L)$ can be conveniently expressed using the transfer matrix $M = R_1 R_2 \cdots R_L$, where $(R_k)_{ijmn} = \sum_\sigma \exp[-\beta(h(i, \sigma) + h(j, \sigma) + h(\sigma, m) + h(\sigma, n))]$ is the local weight matrix that carries the statistical weights associated with the coupling between the k -th spin along each row and its neighbours. The 2D classical model can thus be mapped to a 2D quantum model using the plumbing construction.

E.3. A parent Hamiltonian for the isoTNS path between SET phases

In this section, we derive the parent Hamiltonian for the isoTNS path presented in the main text. Let us consider the toric code described by the Hamiltonian defined on the same square lattice as in the main text,

$$H_{\text{TC}} = \sum_v \mathcal{A}_v + \sum_p \mathcal{B}_p, \quad (\text{E.8})$$

where $\mathcal{A}_v = (1 - \prod_{i \in v} Z_i)/2$ and $\mathcal{B}_p = (1 - \prod_{i \in p} X_i)/2$ are projectors made from products of Pauli operators around each vertex v and each plaquette p . The vertex and

E.3. A parent Hamiltonian for the isoTNS path between SET phases

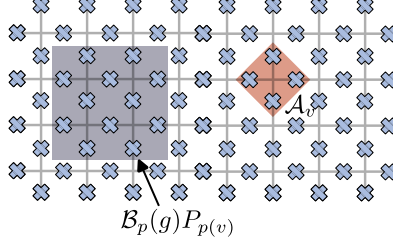


Figure E.1.: A local parent Hamiltonian for the isoTNS ground states in the main text. The Hamiltonian is frustration-free and consists of projectors around each plaquette (the shaded 12 qubits) and each vertex (shaded 4 qubits).

the plaquette operators commute with each other and the ground state $|\text{TC}\rangle$ satisfies $\mathcal{A}_v |\text{TC}\rangle = \mathcal{B}_p |\text{TC}\rangle = 0$ for all v, p . For $g > 0$, the isoTNS path between the SET phases can be obtained from the toric code ground state by an imaginary time evolution

$$|\Psi(g)\rangle = \mathcal{T}(\beta_1, \beta_2) |\text{TC}\rangle = \prod_v e^{\beta_1 P_v^{(1)} + \beta_2 P_v^{(2)}} |\text{TC}\rangle, \quad (\text{E.9})$$

where the projectors at each vertex v are defined as

$$P_v^{(1)} = \frac{1}{8}(1 + Z_{v(A)}Z_{v(B)})(1 + Z_{v(C)}Z_{v(D)})(1 + Z_{v(A)}Z_{v(D)}), \quad (\text{E.10})$$

$$P_v^{(2)} = \frac{1}{8}(1 + Z_{v(A)}Z_{v(B)})(1 + Z_{v(C)}Z_{v(D)})(1 - Z_{v(A)}Z_{v(D)}). \quad (\text{E.11})$$

Note that here we use the labeling convention

$$\begin{array}{c} D \\ | \\ A - \text{---} - C \\ | \\ B \end{array} . \quad (\text{E.12})$$

The parameters are related to g via

$$\beta_1 = \frac{1}{2}(\log 2 - \log(1 + |g|)), \quad (\text{E.13})$$

$$\beta_2 = \frac{1}{2}(\log 2 - \log(1 + |g|)) + \frac{1}{2} \log g. \quad (\text{E.14})$$

To derive a local parent Hamiltonian, we employ the method in Ref. [3]. Since $(b_p \mathcal{T} b_p \mathcal{T}^{-1} - b_p) |\Psi(g)\rangle = 0$, where $b_p = \prod_{i \in p} X_i$. It follows that

$$(e^{\Lambda_a + \Lambda_c + O_b + O_d} - b_p) |\Psi(g)\rangle = 0, \quad (\text{E.15})$$

where we use the following labeling convention for the vertices on each plaquette

$$\begin{array}{|c|c|} \hline d & c \\ \hline a & b \\ \hline \end{array} . \quad (\text{E.16})$$

The operators at each vertex are defined as

$$\begin{aligned} \Lambda_v &= -\frac{1}{4}(\beta_1 - \beta_2)(1 + Z_{v(A)}Z_{v(B)})(1 + Z_{v(C)}Z_{v(D)})Z_{v(A)}Z_{v(D)}, \\ O_v &= -\frac{1}{4}(Z_{v(A)}Z_{v(B)} + Z_{v(C)}Z_{v(D)})[(\beta_1 + \beta_2) + (\beta_1 - \beta_2)Z_{v(A)}Z_{v(D)}]. \end{aligned} \quad (\text{E.17})$$

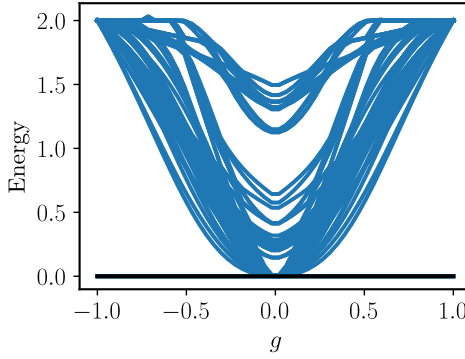


Figure E.2.: Energy spectrum from the exact diagonalization of a system with 4×2 plaquettes (16 qubits) and periodic boundary condition. The plot shows the low-lying eigenvalues of the Hamiltonian. At $g = \pm 1$, the models are fixed points of the topological phases with an energy gap $\Delta = 2$.

We can use this observation to obtain a suitable local term in the parent Hamiltonian. It is possible to choose a path slightly deviated from, but continuously connected to Eq. (E.13) such that the resulting wavefunction Eq. (E.9) is analytic in g for $g \in (-1, 1)$. The definition of the parameters β_1, β_2 can then be extended to $g < 0$ using an argument in Ref. [3] based on analytic continuation. The path Eq. (E.13) is therefore also valid for $g \in [-1, 1]$, where we define $\log g = \log |g| + i\pi$ for $g < 0$. As a sanity check, it can be verified that the imaginary time evolution at $g = -1$ is analytically continued to a finite-depth local unitary symmetric under the global spin flip, and the wavefunction Eq. (E.9) at $g = -1$ is the same as the SET isoTNS wavefunction discussed in the main text (up to an overall phase factor). Therefore, all the analysis for $g > 0$ can be straightforwardly extended to the case $g < 0$.

To proceed, note that

$$\begin{aligned} (e^{\Lambda_a + \Lambda_c + O_b + O_d} - b_p)^2 = \\ 2 \cosh(\Lambda_a + \Lambda_c + O_b + O_d) (e^{\Lambda_a + \Lambda_c + O_b + O_d} - b_p). \end{aligned} \quad (\text{E.18})$$

We can therefore define a new plaquette projector as

$$\mathcal{B}_p(g)P_{p(v)} = \frac{\text{sech}(\Lambda_a + \Lambda_c + O_b + O_d)}{2} (e^{\Lambda_a + \Lambda_c + O_b + O_d} - b_p) P_{p(v)}. \quad (\text{E.19})$$

where $P_{p(v)}$ is the projector onto the closed loop configuration around each plaquette p , i.e. $P_{p(v)} = \prod_{v \in p} (1 - \mathcal{A}_v)$. It is included to ensure that $\mathcal{B}_p(g)P_{p(v)}$ remains Hermitian and therefore a projector for $g \in [-1, 1]$. The operator hyperbolic secant function is defined as $\text{sech}(O) \equiv 1/\cosh(O)$ within the subspace $P_{p(v)} = 1$, and $\text{sech}(O) \equiv 0$ in the subspace $P_{p(v)} = 0$. A local frustration-free parent Hamiltonian is thus given by

$$H(g) = \sum_v \mathcal{A}_V + \sum_p \mathcal{B}_p(g)P_{p(v)}, \quad (\text{E.20})$$

with a ground-state energy of zero. The support of each term in $H(g)$ is depicted in Fig. E.1. When the system is defined on a torus (periodic boundary condition), $H(g)$ is gapped and the ground states are exactly four-fold degenerate for $g \neq 0$. At $g = 0$, the system is gapless. In addition, the \mathbb{Z}_2^T symmetry is satisfied, i.e. $[H(g), (\prod_i X_i) K] = 0$ for $g \in [-1, 1]$. The low-lying spectrum of the Hamiltonian on a square lattice with 4×2 plaquettes (16 qubits) is shown in Fig. E.2. Note that the parent Hamiltonian for the ground states is not unique, the one derived here is one of the possible parent Hamiltonians.

Bibliography

- [1] Yu-Jie Liu, Kirill Shtengel, and Frank Pollmann. Topological quantum phase transitions in 2d isometric tensor networks. *arXiv preprint arXiv:2312.05079*, 2023. URL <https://arxiv.org/abs/2312.05079>.
- [2] Yu-Jie Liu, Adam Smith, Michael Knap, and Frank Pollmann. Model-independent learning of quantum phases of matter with quantum convolutional neural networks. *Phys. Rev. Lett.*, 130:220603, Jun 2023. doi: 10.1103/PhysRevLett.130.220603. URL <https://link.aps.org/doi/10.1103/PhysRevLett.130.220603>.
- [3] Lukas Haller, Wen-Tao Xu, Yu-Jie Liu, and Frank Pollmann. Quantum phase transition between symmetry enriched topological phases in tensor-network states. *Phys. Rev. Res.*, 5:043078, Oct 2023. doi: 10.1103/PhysRevResearch.5.043078. URL <https://link.aps.org/doi/10.1103/PhysRevResearch.5.043078>.
- [4] Yu-Jie Liu, Kirill Shtengel, Adam Smith, and Frank Pollmann. Methods for simulating string-net states and anyons on a digital quantum computer. *PRX Quantum*, 3:040315, Nov 2022. doi: 10.1103/PRXQuantum.3.040315. URL <https://link.aps.org/doi/10.1103/PRXQuantum.3.040315>.
- [5] K. J. Satzinger, Y.-J Liu, A. Smith, C. Knapp, M. Newman, C. Jones, Z. Chen, C. Quintana, X. Mi, A. Dunsworth, C. Gidney, I. Aleiner, F. Arute, K. Arya, J. Atalaya, R. Babbush, J. C. Bardin, R. Barends, J. Basso, A. Bengtsson, A. Bilmes, M. Broughton, B. B. Buckley, D. A. Buell, B. Burkett, N. Bushnell, B. Chiaro, R. Collins, W. Courtney, S. Demura, A. R. Derk, D. Eppens, C. Erickson, L. Faoro, E. Farhi, A. G. Fowler, B. Foxen, M. Giustina, A. Greene, J. A. Gross, M. P. Harrigan, S. D. Harrington, J. Hilton, S. Hong, T. Huang, W. J. Huggins, L. B. Ioffe, S. V. Isakov, E. Jeffrey, Z. Jiang, D. Kafri, K. Kechedzhi, T. Khattar, S. Kim, P. V. Klimov, A. N. Korotkov, F. Kostritsa, D. Landhuis, P. Laptev, A. Locharla, E. Lucero, O. Martin, J. R. McClean, M. McEwen, K. C. Miao, M. Mohseni, S. Montazeri, W. Mruczkiewicz, J. Mutus, O. Naaman, M. Neeley, C. Neill, M. Y. Niu, T. E. O'Brien, A. Opremcak, B. Pató, A. Petukhov, N. C. Rubin, D. Sank, V. Shvarts, D. Strain, M. Szalay, B. Villalonga, T. C. White, Z. Yao, P. Yeh, J. Yoo, A. Zalcman, H. Neven, S. Boixo, A. Megrant, Y. Chen, J. Kelly, V. Smelyanskiy, A. Kitaev, M. Knap, F. Pollmann, and P. Roushan. Realizing topologically ordered states on a quantum processor. *Science*, 374(6572):1237–1241, 2021. doi: 10.1126/science.abi8378. URL <https://www.science.org/doi/abs/10.1126/science.abi8378>.
- [6] Simon Lieu, Yu-Jie Liu, and Alexey V. Gorshkov. Candidate for a passively protected quantum memory in two dimensions. *Phys. Rev. Lett.*, 133:030601, Jul 2024. doi: 10.1103/PhysRevLett.133.030601. URL <https://link.aps.org/doi/10.1103/PhysRevLett.133.030601>.
- [7] Yu-Jie Liu and Simon Lieu. Dissipative phase transitions and passive error correction. *Phys. Rev. A*, 109:022422, Feb 2024. doi: 10.1103/PhysRevA.109.022422. URL <https://link.aps.org/doi/10.1103/PhysRevA.109.022422>.

Bibliography

- [8] Oles Shtanko, Yu-Jie Liu, Simon Lieu, Alexey V Gorshkov, and Victor V Albert. Bounds on autonomous quantum error correction. *arXiv preprint arXiv:2308.16233*, 2023. URL <https://arxiv.org/abs/2308.16233>.
- [9] Rohit Dilip, Yu-Jie Liu, Adam Smith, and Frank Pollmann. Data compression for quantum machine learning. *Phys. Rev. Res.*, 4:043007, Oct 2022. doi: 10.1103/PhysRevResearch.4.043007. URL <https://link.aps.org/doi/10.1103/PhysRevResearch.4.043007>.
- [10] L. D. Landau. On the theory of phase transitions. *Zh. Eksp. Teor. Fiz.*, 7:19–32, 1937. doi: 10.1016/B978-0-08-010586-4.50034-1. URL <https://www.sciencedirect.com/science/article/abs/pii/B9780080105864500341?via%3Dihub>.
- [11] V. L. Ginzburg and L. D. Landau. On the Theory of superconductivity. *Zh. Eksp. Teor. Fiz.*, 20:1064–1082, 1950. doi: 10.1016/B978-0-08-010586-4.50035-3. URL <https://www.sciencedirect.com/science/article/abs/pii/B978008010586450078X?via%3Dihub>.
- [12] Zheng-Cheng Gu and Xiao-Gang Wen. Tensor-entanglement-filtering renormalization approach and symmetry-protected topological order. *Phys. Rev. B*, 80:155131, Oct 2009. doi: 10.1103/PhysRevB.80.155131. URL <https://link.aps.org/doi/10.1103/PhysRevB.80.155131>.
- [13] Frank Pollmann, Ari M. Turner, Erez Berg, and Masaki Oshikawa. Entanglement spectrum of a topological phase in one dimension. *Phys. Rev. B*, 81:064439, Feb 2010. doi: 10.1103/PhysRevB.81.064439. URL <https://link.aps.org/doi/10.1103/PhysRevB.81.064439>.
- [14] Xie Chen, Zheng-Cheng Gu, and Xiao-Gang Wen. Classification of gapped symmetric phases in one-dimensional spin systems. *Phys. Rev. B*, 83:035107, Jan 2011. doi: 10.1103/PhysRevB.83.035107. URL <https://link.aps.org/doi/10.1103/PhysRevB.83.035107>.
- [15] Norbert Schuch, David Pérez-García, and Ignacio Cirac. Classifying quantum phases using matrix product states and projected entangled pair states. *Phys. Rev. B*, 84:165139, Oct 2011. doi: 10.1103/PhysRevB.84.165139. URL <https://link.aps.org/doi/10.1103/PhysRevB.84.165139>.
- [16] Xie Chen, Zheng-Xin Liu, and Xiao-Gang Wen. Two-dimensional symmetry-protected topological orders and their protected gapless edge excitations. *Phys. Rev. B*, 84:235141, Dec 2011. doi: 10.1103/PhysRevB.84.235141. URL <https://link.aps.org/doi/10.1103/PhysRevB.84.235141>.
- [17] Frank Pollmann, Erez Berg, Ari M. Turner, and Masaki Oshikawa. Symmetry protection of topological phases in one-dimensional quantum spin systems. *Phys. Rev. B*, 85:075125, Feb 2012. doi: 10.1103/PhysRevB.85.075125. URL <https://link.aps.org/doi/10.1103/PhysRevB.85.075125>.
- [18] Xie Chen, Zheng-Cheng Gu, Zheng-Xin Liu, and Xiao-Gang Wen. Symmetry protected topological orders and the group cohomology of their symmetry group. *Phys. Rev. B*, 87:155114, Apr 2013. doi: 10.1103/PhysRevB.87.155114. URL <https://link.aps.org/doi/10.1103/PhysRevB.87.155114>.
- [19] X. G. Wen. Vacuum degeneracy of chiral spin states in compactified space. *Phys. Rev. B*, 40:7387–7390, Oct 1989. doi: 10.1103/PhysRevB.40.7387. URL <https://link.aps.org/doi/10.1103/PhysRevB.40.7387>.

- [20] X. G. Wen. Topological orders in rigid states. *Int. J. Mod. Phys. B*, 04(02):239–271, feb 1990. ISSN 0217-9792. doi: 10.1142/S0217979290000139. URL <https://www.worldscientific.com/doi/abs/10.1142/S0217979290000139>.
- [21] X. G. Wen. Mean-field theory of spin-liquid states with finite energy gap and topological orders. *Phys. Rev. B*, 44:2664–2672, Aug 1991. doi: 10.1103/PhysRevB.44.2664. URL <https://link.aps.org/doi/10.1103/PhysRevB.44.2664>.
- [22] Andrew M. Essin and Michael Hermele. Classifying fractionalization: Symmetry classification of gapped \mathbb{Z}_2 spin liquids in two dimensions. *Phys. Rev. B*, 87:104406, Mar 2013. doi: 10.1103/PhysRevB.87.104406. URL <https://link.aps.org/doi/10.1103/PhysRevB.87.104406>.
- [23] Andrej Mesaros and Ying Ran. Classification of symmetry enriched topological phases with exactly solvable models. *Phys. Rev. B*, 87:155115, Apr 2013. doi: 10.1103/PhysRevB.87.155115. URL <https://link.aps.org/doi/10.1103/PhysRevB.87.155115>.
- [24] Nicolas Tarantino, Netanel H Lindner, and Lukasz Fidkowski. Symmetry fractionalization and twist defects. *New J. Phys.*, 18(3):035006, mar 2016. doi: 10.1088/1367-2630/18/3/035006. URL <https://dx.doi.org/10.1088/1367-2630/18/3/035006>.
- [25] Yuan-Ming Lu and Ashvin Vishwanath. Classification and properties of symmetry-enriched topological phases: Chern-simons approach with applications to \mathbb{Z}_2 spin liquids. *Phys. Rev. B*, 93:155121, Apr 2016. doi: 10.1103/PhysRevB.93.155121. URL <https://link.aps.org/doi/10.1103/PhysRevB.93.155121>.
- [26] Chris Heinrich, Fiona Burnell, Lukasz Fidkowski, and Michael Levin. Symmetry-enriched string nets: Exactly solvable models for set phases. *Phys. Rev. B*, 94:235136, Dec 2016. doi: 10.1103/PhysRevB.94.235136. URL <https://link.aps.org/doi/10.1103/PhysRevB.94.235136>.
- [27] Meng Cheng, Zheng-Cheng Gu, Shenghan Jiang, and Yang Qi. Exactly solvable models for symmetry-enriched topological phases. *Phys. Rev. B*, 96:115107, Sep 2017. doi: 10.1103/PhysRevB.96.115107. URL <https://link.aps.org/doi/10.1103/PhysRevB.96.115107>.
- [28] Maissam Barkeshli, Parsa Bonderson, Meng Cheng, and Zhenghan Wang. Symmetry fractionalization, defects, and gauging of topological phases. *Phys. Rev. B*, 100:115147, Sep 2019. doi: 10.1103/PhysRevB.100.115147. URL <https://link.aps.org/doi/10.1103/PhysRevB.100.115147>.
- [29] David Aasen, Parsa Bonderson, and Christina Knapp. Characterization and classification of fermionic symmetry enriched topological phases. *arXiv preprint arXiv:2109.10911*, 2021. URL <https://arxiv.org/abs/2109.10911>.
- [30] Maissam Barkeshli, Yu-An Chen, Po-Shen Hsin, and Naren Manjunath. Classification of $(2 + 1)$ d invertible fermionic topological phases with symmetry. *Phys. Rev. B*, 105:235143, Jun 2022. doi: 10.1103/PhysRevB.105.235143. URL <https://link.aps.org/doi/10.1103/PhysRevB.105.235143>.
- [31] Steven R. White. Density matrix formulation for quantum renormalization groups. *Phys. Rev. Lett.*, 69:2863–2866, Nov 1992. doi: 10.1103/PhysRevLett.69.2863. URL <https://link.aps.org/doi/10.1103/PhysRevLett.69.2863>.

Bibliography

- [32] Steven R. White. Density-matrix algorithms for quantum renormalization groups. *Phys. Rev. B*, 48:10345–10356, Oct 1993. doi: 10.1103/PhysRevB.48.10345. URL <https://link.aps.org/doi/10.1103/PhysRevB.48.10345>.
- [33] M Suzuki. *Quantum Monte Carlo Methods in Condensed Matter Physics*. World Scientific, 1993. doi: 10.1142/2262. URL <https://www.worldscientific.com/doi/abs/10.1142/2262>.
- [34] David Deutsch and Richard Jozsa. Rapid solution of problems by quantum computation. *Proceedings of the Royal Society of London. Series A: Mathematical and Physical Sciences*, 439:553 – 558, 1992. URL <https://royalsocietypublishing.org/doi/10.1098/rspa.1992.0167>.
- [35] Daniel R. Simon. On the power of quantum computation. *Proceedings 35th Annual Symposium on Foundations of Computer Science*, pages 116–123, 1994. URL <https://ieeexplore.ieee.org/document/365701>.
- [36] Peter W. Shor. Polynomial-time algorithms for prime factorization and discrete logarithms on a quantum computer. *SIAM Rev.*, 41:303–332, 1995. URL <https://epubs.siam.org/doi/10.1137/S0097539795293172>.
- [37] Frank Arute *et al.* Quantum supremacy using a programmable superconducting processor. *Nature*, 574(7779):505–510, oct 2019. ISSN 0028-0836. doi: 10.1038/s41586-019-1666-5. URL <http://www.nature.com/articles/s41586-019-1666-5>.
- [38] Edwin Pednault, John A Gunnels, Giacomo Nannicini, Lior Horesh, and Robert Wisnieff. Leveraging secondary storage to simulate deep 54-qubit sycamore circuits. *arXiv preprint arXiv:1910.09534*, 2019. URL <https://arxiv.org/abs/1910.09534>.
- [39] Yong (Alexander) Liu, Xin (Lucy) Liu, Fang (Nancy) Li, Haohuan Fu, Yuling Yang, Jiawei Song, Pengpeng Zhao, Zhen Wang, Dajia Peng, Huarong Chen, Chu Guo, Heliang Huang, Wenzhao Wu, and Dexun Chen. Closing the "quantum supremacy" gap: achieving real-time simulation of a random quantum circuit using a new sunway supercomputer. In *Proceedings of the International Conference for High Performance Computing, Networking, Storage and Analysis*, SC '21, New York, NY, USA, 2021. Association for Computing Machinery. ISBN 9781450384421. doi: 10.1145/3458817.3487399. URL <https://doi.org/10.1145/3458817.3487399>.
- [40] Feng Pan and Pan Zhang. Simulation of quantum circuits using the big-batch tensor network method. *Phys. Rev. Lett.*, 128:030501, Jan 2022. doi: 10.1103/PhysRevLett.128.030501. URL <https://link.aps.org/doi/10.1103/PhysRevLett.128.030501>.
- [41] Markus Greiner, Olaf Mandel, Tilman Esslinger, Theodor W. Hänsch, and Immanuel Bloch. Quantum phase transition from a superfluid to a mott insulator in a gas of ultracold atoms. *Nature*, 415:39–44, 2002. URL <https://www.nature.com/articles/415039a>.
- [42] Hannes Bernien, Sylvain Schwartz, A Keesling, H Levine, Ahmed Omran, Hannes Pichler, Soonwon Choi, A. S. Zibrov, Manuel Endres, Markus Greiner, Vladan Vuletić, and Mikhail D. Lukin. Probing many-body dynamics on a 51-atom quantum simulator. *Nature*, 551:579–584, 2017. URL <https://www.nature.com/articles/nature24622>.
- [43] A. Kitaev. Fault-tolerant quantum computation by anyons. *Ann. Phys.*, 303(1):2–30, 2003. ISSN 0003-4916. doi: [https://doi.org/10.1016/S0003-4916\(02\)00018-0](https://doi.org/10.1016/S0003-4916(02)00018-0). URL <https://www.sciencedirect.com/science/article/pii/S0003491602000180>.

- [44] Michael H. Freedman. \mathbb{Z}_2 and the quantum field theory computer. *Proceedings of the National Academy of Sciences*, 95(1):98–101, 1998. doi: 10.1073/pnas.95.1.98. URL <https://www.pnas.org/doi/abs/10.1073/pnas.95.1.98>.
- [45] Sergey B Bravyi and A Yu Kitaev. Quantum codes on a lattice with boundary. *arXiv preprint quant-ph/9811052*, 1998. URL <https://arxiv.org/abs/quant-ph/9811052>.
- [46] Michael H. Freedman and David A. Meyer. Projective Plane and Planar Quantum Codes. *Found. Comput. Math.*, 1(3):325–332, jul 2001. ISSN 1615-3375. doi: 10.1007/s102080010013. URL <http://link.springer.com/10.1007/s102080010013>.
- [47] Eric Dennis, Alexei Y. Kitaev, Andrew J. Landahl, and John Preskill. Topological quantum memory. *J. Math. Phys.*, 43:4452–4505, 2001. URL <https://pubs.aip.org/aip/jmp/article-abstract/43/9/4452/230976/Topological-quantum-memory?redirectedFrom=fulltext>.
- [48] D. C. Tsui, H. L. Stormer, and A. C. Gossard. Two-dimensional magnetotransport in the extreme quantum limit. *Phys. Rev. Lett.*, 48:1559–1562, May 1982. doi: 10.1103/PhysRevLett.48.1559. URL <https://link.aps.org/doi/10.1103/PhysRevLett.48.1559>.
- [49] P.W. Anderson. Resonating valence bonds: A new kind of insulator? *Materials Research Bulletin*, 8(2):153–160, 1973. ISSN 0025-5408. doi: [https://doi.org/10.1016/0025-5408\(73\)90167-0](https://doi.org/10.1016/0025-5408(73)90167-0). URL <https://www.sciencedirect.com/science/article/pii/0025540873901670>.
- [50] R. B. Laughlin. Anomalous quantum hall effect: An incompressible quantum fluid with fractionally charged excitations. *Phys. Rev. Lett.*, 50:1395–1398, May 1983. doi: 10.1103/PhysRevLett.50.1395. URL <https://link.aps.org/doi/10.1103/PhysRevLett.50.1395>.
- [51] Daniel S. Rokhsar and Steven A. Kivelson. Superconductivity and the quantum hardcore dimer gas. *Phys. Rev. Lett.*, 61:2376–2379, Nov 1988. doi: 10.1103/PhysRevLett.61.2376. URL <https://link.aps.org/doi/10.1103/PhysRevLett.61.2376>.
- [52] Michael A. Levin and Xiao-Gang Wen. String-net condensation: A physical mechanism for topological phases. *Phys. Rev. B*, 71(4):045110, jan 2005. ISSN 1098-0121. doi: 10.1103/PhysRevB.71.045110. URL <https://link.aps.org/doi/10.1103/PhysRevB.71.045110>.
- [53] Chao-Yang Lu, Wei-Bo Gao, Otfried Gühne, Xiao-Qi Zhou, Zeng-Bing Chen, and Jian-Wei Pan. Demonstrating Anyonic Fractional Statistics with a Six-Qubit Quantum Simulator. *Phys. Rev. Lett.*, 102(3):030502, jan 2009. ISSN 0031-9007. doi: 10.1103/PhysRevLett.102.030502. URL <https://link.aps.org/doi/10.1103/PhysRevLett.102.030502>.
- [54] J. K. Pachos, W. Wieczorek, C. Schmid, N. Kiesel, R. Pohlner, and H. Weinfurter. Revealing anyonic features in a toric code quantum simulation. *New J. Phys.*, 11(8):083010, aug 2009. ISSN 1367-2630. doi: 10.1088/1367-2630/11/8/083010. URL <https://iopscience.iop.org/article/10.1088/1367-2630/11/8/083010>.
- [55] Guanru Feng, Guilu Long, and Raymond Laflamme. Experimental simulation of anyonic fractional statistics with an nmr quantum-information processor. *Phys. Rev. A*, 88:022305, Aug 2013. doi: 10.1103/PhysRevA.88.022305. URL <https://link.aps.org/doi/10.1103/PhysRevA.88.022305>.

Bibliography

- [56] Annie Jihyun Park, Emma McKay, Dawei Lu, and Raymond Laflamme. Simulation of anyonic statistics and its topological path independence using a seven-qubit quantum simulator. *New J. Phys.*, 18(4):043043, apr 2016. ISSN 1367-2630. doi: 10.1088/1367-2630/18/4/043043. URL <https://iopscience.iop.org/article/10.1088/1367-2630/18/4/043043>.
- [57] Y. P. Zhong, D. Xu, P. Wang, C. Song, Q. J. Guo, W. X. Liu, K. Xu, B. X. Xia, C.-Y. Lu, Siyuan Han, Jian-Wei Pan, and H. Wang. Emulating Anyonic Fractional Statistical Behavior in a Superconducting Quantum Circuit. *Phys. Rev. Lett.*, 117(11):110501, sep 2016. ISSN 0031-9007. doi: 10.1103/PhysRevLett.117.110501. URL <https://link.aps.org/doi/10.1103/PhysRevLett.117.110501>.
- [58] Han-Ning Dai, Bing Yang, Andreas Reingruber, Hui Sun, Xiao-Fan Xu, Yu-Ao Chen, Zhen-Sheng Yuan, and Jian-Wei Pan. Four-body ring-exchange interactions and anyonic statistics within a minimal toric-code Hamiltonian. *Nat. Phys.*, 13(12):1195–1200, dec 2017. ISSN 1745-2473. doi: 10.1038/nphys4243. URL <http://www.nature.com/articles/nphys4243>.
- [59] Zhihuang Luo, Jun Li, Zhaokai Li, Ling-Yan Hung, Yidun Wan, Xinhua Peng, and Jiangfeng Du. Experimentally probing topological order and its breakdown through modular matrices. *Nat. Phys.*, 14(2):160–165, feb 2018. ISSN 1745-2473. doi: 10.1038/nphys4281. URL <http://www.nature.com/articles/nphys4281>.
- [60] Chao Song, Da Xu, Pengfei Zhang, Jianwen Wang, Qiujiang Guo, Wuxin Liu, Kai Xu, Hui Deng, Keqiang Huang, Dongning Zheng, Shi-Biao Zheng, H. Wang, Xiaobo Zhu, Chao-Yang Lu, and Jian-Wei Pan. Demonstration of Topological Robustness of Anyonic Braiding Statistics with a Superconducting Quantum Circuit. *Phys. Rev. Lett.*, 121(3):030502, jul 2018. ISSN 0031-9007. doi: 10.1103/PhysRevLett.121.030502. URL <https://link.aps.org/doi/10.1103/PhysRevLett.121.030502>.
- [61] Chang Liu, He-Liang Huang, Chao Chen, Bi-Ying Wang, Xi-Lin Wang, Tao Yang, Li Li, Nai-Le Liu, Jonathan P. Dowling, Tim Byrnes, Chao-Yang Lu, and Jian-Wei Pan. Demonstration of topologically path-independent anyonic braiding in a nine-qubit planar code. *Optica*, 6(3):264–268, Mar 2019. doi: 10.1364/OPTICA.6.000264. URL <https://opg.optica.org/optica/abstract.cfm?URI=optica-6-3-264>.
- [62] Armin Rahmani, Kevin J. Sung, Harald Putterman, Pedram Roushan, Pouyan Ghaemi, and Zhang Jiang. Creating and manipulating a Laughlin-type $\nu = 1/3$ fractional quantum hall state on a quantum computer with linear depth circuits. *PRX Quantum*, 1:020309, Nov 2020. doi: 10.1103/PRXQuantum.1.020309. URL <https://link.aps.org/doi/10.1103/PRXQuantum.1.020309>.
- [63] Alexander Erhard, Hendrik Poulsen Nautrup, Michael Meth, Lukas Postler, Roman Stricker, Martin Stadler, Vlad Negnevitsky, Martin Ringbauer, Philipp Schindler, Hans J. Briegel, Rainer Blatt, Nicolai Friis, and Thomas Monz. Entangling logical qubits with lattice surgery. *Nature*, 589(7841):220–224, jan 2021. ISSN 0028-0836. doi: 10.1038/s41586-020-03079-6. URL <http://www.nature.com/articles/s41586-020-03079-6>.
- [64] Logan W. Clark, Nathan Schine, Claire Baum, Ningyuan Jia, and Jonathan Simon. Observation of Laughlin states made of light. *Nature*, 582(7810):41–45, June 2020. ISSN 1476-4687. doi: 10.1038/s41586-020-2318-5. URL <https://www.nature.com/articles/s41586-020-2318-5>.

- [65] G. Semeghini, H. Levine, A. Keesling, S. Ebadi, T. T. Wang, D. Bluvstein, R. Verresen, H. Pichler, M. Kalinowski, R. Samajdar, A. Omran, S. Sachdev, A. Vishwanath, M. Greiner, V. Vuletić, and M. D. Lukin. Probing topological spin liquids on a programmable quantum simulator. *Science*, 374(6572):1242–1247, 2021. doi: 10.1126/science.abi8794. URL <https://www.science.org/doi/abs/10.1126/science.abi8794>.
- [66] Can Wang, Feng-Ming Liu, Ming-Cheng Chen, He Chen, Xian-He Zhao, Chong Ying, Zhong-Xia Shang, Jian-Wen Wang, Yong-Heng Huo, Cheng-Zhi Peng, Xiaobo Zhu, Chao-Yang Lu, and Jian-Wei Pan. Realization of fractional quantum hall state with interacting photons. *Science*, 384(6695):579–584, May 2024. ISSN 1095-9203. doi: 10.1126/science.ado3912. URL <https://www.science.org/doi/10.1126/science.ado3912>.
- [67] Shibo Xu, Zheng-Zhi Sun, Ke Wang, Liang Xiang, Zehang Bao, Zitian Zhu, Fanhao Shen, Zixuan Song, Pengfei Zhang, Wenhui Ren, Xu Zhang, Hang Dong, Jinfeng Deng, Jiachen Chen, Yaozu Wu, Ziqi Tan, Yu Gao, Feitong Jin, Xuhao Zhu, Chuanyu Zhang, Ning Wang, Yiren Zou, Jiarun Zhong, Aosai Zhang, Weikang Li, Wenjie Jiang, Li-Wei Yu, Yunyan Yao, Zhen Wang, Hekang Li, Qiujiang Guo, Chao Song, H. Wang, and Dong-Ling Deng. Digital simulation of projective non-abelian anyons with 68 superconducting qubits. *Chinese Physics Letters*, 40(6):060301, June 2023. ISSN 1741-3540. doi: 10.1088/0256-307x/40/6/060301. URL <https://iopscience.iop.org/article/10.1088/0256-307X/40/6/060301>.
- [68] T. I. Andersen, Yuri D. Lensky, Kostyantyn Kechedzhi, Ilya K. Drozdov, Andreas Bengtsson, S. Hong, Alexis Morvan, Xiao Mi, Alexander Opremcak, Rajeev Acharya, Richard Allen, Markus Ansmann, Frank Arute, Kunal Arya, Abraham T. Asfaw, Juan Atalaya, Ryan Babbush, D. Bacon, Joseph C. Bardin, Gina Bortoli, Alexandre Bourassa, Jenna Bovaird, Leon Brill, Mick Broughton, Bob B Buckley, David A. Buell, Tim Burger, Brian Burkett, Nicholas Bushnell, Z. Chen, Benjamin Chiaro, David T W Chik, C. Chou, J. Zachery Cogan, Roberto Collins, P. N. Conner, William Courtney, Alexander L. Crook, Benjamin M. Curtin, Dripto M. Debroy, A. Del Toro Barba, Sean Demura, Andrew Dunsworth, Daniel Eppens, Catherine Erickson, Lara Faoro, Edward Farhi, R. Fatemi, Vinicius S. Ferreira, Leslie Flores Burgos, Ebrahim Forati, Austin G. Fowler, Brooks Foxen, William Giang, Craig Gidney, Dar Gilboa, Marissa Giustina, R. Gosula, Alejandro Grajales Dau, J. A. Gross, S. Habegger, Mary Cameron Hamilton, Matthew Hansen, Matthew P. Harrigan, Sean D. Harrington, Paula Heu, Jeremy P. Hilton, Michael J. Hoffmann, T. Huang, Ashley Huff, William J. Huggins, L. B. Ioffe, Sergei V. Isakov, Justin Iveland, Evan Jeffrey, Z. Jiang, C. Jones, Peter Juhás, Dvir Kafri, Tanuj Khatkar, Mostafa Khezri, Mária Kieferová, S. Kim, Alexei Kitaev, Paul V. Klimov, Andrey R. Klots, Alexander N. Korotkov, Fedor Kostritsa, John Mark Kreikebaum, David Landhuis, Pavel Laptev, Kim Ming Lau, Lily Laws, J. Lee, K. W. Lee, B. J. Lester, Alexander T Lill, W. Liu, Aditya Locharla, E. Lucero, Fionn D. Malone, Orion Martin, Jarrod R. McClean, Trevor McCourt, Matthew J. McEwen, Kevin C. Miao, Amanda Mieszala, Masoud Mohseni, Shirin Montazeri, E. Mount, Ramis Movassagh, Wojciech Mruczkiewicz, Ofer Naaman, Matthew Neeley, Charles J. Neill, Ani Nersisyan, Michael Newman, Jiun How Ng, Anthony Nguyen, Murray L. Nguyen, Murphy Yuezhen Niu, Thomas E. O’Brien, Seun Omonije, Andre Petukhov, Rory Potter, Leonid P. Pryadko, Chris Quintana, Charles Rocque, Nicholas C. Rubin, Negar Saei, Daniel Thomas Sank, Kannan A. Sankaragomathi, Kevin J. Satzinger, Henry F. Schurkus, C. Schuster, Martin Shearn, Aaron Shorter, Noah

Bibliography

- Shutty, Vladimir Shvarts, Jindra Skruzny, William C. Smith, R. Somma, George Sterling, Doug Strain, Marco Szalay, Alfredo Torres, Guifre Vidal, Benjamin Villalonga, C. V. Heidweiller, Theodore White, Bryan W K Woo, Chen Xing, Z. Yao, Ping Yeh, J. Yoo, Grayson Young, Adam Zalcman, Y. Zhang, Ning Zhu, Nicholas Zobrist, Hartmut Neven, Sergio Boixo, Anthony Megrant, Julian Kelly, Y. Chen, V. Smelyanskiy, E.-A. Kim, I. Aleiner, and Pedram Roushan. Non-abelian braiding of graph vertices in a superconducting processor. *Nature*, 618:264 – 269, 2022. URL <https://www.nature.com/articles/s41586-023-05954-4>.
- [69] Shibo Xu, Zheng-Zhi Sun, Ke Wang, Hekang Li, Zitian Zhu, Hang Dong, Jinfeng Deng, Xu Zhang, Jiachen Chen, Yaozu Wu, Chuanyu Zhang, Feitong Jin, Xuhao Zhu, Yu Gao, Aosai Zhang, Ning Wang, Yiren Zou, Ziqi Tan, Fanhao Shen, Jiarun Zhong, Zehang Bao, Weikang Li, Wenjie Jiang, Li-Wei Yu, Zixuan Song, Pengfei Zhang, Liang Xiang, Qiujiang Guo, Zhen Wang, Chao Song, H. Wang, and Dong-Ling Deng. Non-abelian braiding of fibonacci anyons with a superconducting processor. *Nat. Phys.*, 2024. ISSN 1745-2481. doi: 10.1038/s41567-024-02529-6. URL <https://www.nature.com/articles/s41567-024-02529-6>.
- [70] Mohsin Iqbal, Nathanan Tantivasadakarn, Ruben Verresen, Sara L. Campbell, Joan M. Dreiling, Caroline Figgatt, John P. Gaebler, Jacob Johansen, Michael Mills, Steven A. Moses, Juan M. Pino, Anthony Ransford, Mary Rowe, Peter Siegfried, Russell P. Stutz, Michael Foss-Feig, Ashvin Vishwanath, and Henrik Dreyer. Non-abelian topological order and anyons on a trapped-ion processor. *Nature*, 626 (7999):505–511, 2024. ISSN 1476-4687. doi: 10.1038/s41586-023-06934-4. URL <https://www.nature.com/articles/s41586-023-06934-4>.
- [71] F. Verstraete, J. I. Cirac, J. I. Latorre, E. Rico, and M. M. Wolf. Renormalization-group transformations on quantum states. *Phys. Rev. Lett.*, 94:140601, Apr 2005. doi: 10.1103/PhysRevLett.94.140601. URL <https://link.aps.org/doi/10.1103/PhysRevLett.94.140601>.
- [72] G. Vidal. Entanglement renormalization. *Phys. Rev. Lett.*, 99:220405, Nov 2007. doi: 10.1103/PhysRevLett.99.220405. URL <https://link.aps.org/doi/10.1103/PhysRevLett.99.220405>.
- [73] Michael Levin and Cody P. Nave. Tensor renormalization group approach to two-dimensional classical lattice models. *Phys. Rev. Lett.*, 99:120601, Sep 2007. doi: 10.1103/PhysRevLett.99.120601. URL <https://link.aps.org/doi/10.1103/PhysRevLett.99.120601>.
- [74] G. Evenbly and G. Vidal. Tensor network renormalization. *Phys. Rev. Lett.*, 115:180405, Oct 2015. doi: 10.1103/PhysRevLett.115.180405. URL <https://link.aps.org/doi/10.1103/PhysRevLett.115.180405>.
- [75] P. W. Anderson. The resonating valence bond state in La_2CuO_4 and superconductivity. *Science*, 235(4793):1196–1198, 1987. doi: 10.1126/science.235.4793.1196. URL <https://www.science.org/doi/abs/10.1126/science.235.4793.1196>.
- [76] G. Baskaran, Z. Zou, and P.W. Anderson. The resonating valence bond state and high- T_c superconductivity — a mean field theory. *Solid State Communications*, 63(11):973–976, 1987. ISSN 0038-1098. doi: [https://doi.org/10.1016/0038-1098\(87\)90642-9](https://doi.org/10.1016/0038-1098(87)90642-9). URL <https://www.sciencedirect.com/science/article/pii/0038109887906429>.

- [77] Steven A. Kivelson, Daniel S. Rokhsar, and James P. Sethna. Topology of the resonating valence-bond state: Solitons and high- T_c superconductivity. *Phys. Rev. B*, 35:8865–8868, Jun 1987. doi: 10.1103/PhysRevB.35.8865. URL <https://link.aps.org/doi/10.1103/PhysRevB.35.8865>.
- [78] V. Kalmeyer and R. B. Laughlin. Equivalence of the resonating-valence-bond and fractional quantum hall states. *Phys. Rev. Lett.*, 59:2095–2098, Nov 1987. doi: 10.1103/PhysRevLett.59.2095. URL <https://link.aps.org/doi/10.1103/PhysRevLett.59.2095>.
- [79] X. G. Wen and Q. Niu. Ground-state degeneracy of the fractional quantum hall states in the presence of a random potential and on high-genus riemann surfaces. *Phys. Rev. B*, 41:9377–9396, May 1990. doi: 10.1103/PhysRevB.41.9377. URL <https://link.aps.org/doi/10.1103/PhysRevB.41.9377>.
- [80] Jon Magne Leinaas and Jan Myrheim. On the theory of identical particles. *Il Nuovo Cimento B (1971-1996)*, 37:1–23, 1977. URL <https://link.springer.com/article/10.1007/BF02727953>.
- [81] G. A. Goldin, R. Menikoff, and D. H. Sharp. Representations of a local current algebra in nonsimply connected space and the aharonov-bohm effect. *J. Math. Phys.*, 22(8):1664–1668, 1980. ISSN 0022-2488. doi: 10.1063/1.525110. URL <https://pubs.aip.org/aip/jmp/article-abstract/22/8/1664/226300/Representations-of-a-local-current-algebra-in?redirectedFrom=fulltext>.
- [82] Frank Wilczek. Magnetic flux, angular momentum, and statistics. *Phys. Rev. Lett.*, 48:1144–1146, Apr 1982. doi: 10.1103/PhysRevLett.48.1144. URL <https://link.aps.org/doi/10.1103/PhysRevLett.48.1144>.
- [83] Frank Wilczek. Quantum mechanics of fractional-spin particles. *Phys. Rev. Lett.*, 49:957–959, Oct 1982. doi: 10.1103/PhysRevLett.49.957. URL <https://link.aps.org/doi/10.1103/PhysRevLett.49.957>.
- [84] Yong-Shi Wu. General theory for quantum statistics in two dimensions. *Phys. Rev. Lett.*, 52:2103–2106, Jun 1984. doi: 10.1103/PhysRevLett.52.2103. URL <https://link.aps.org/doi/10.1103/PhysRevLett.52.2103>.
- [85] Gregory W. Moore and Nathan Seiberg. Classical and Quantum Conformal Field Theory. *Commun. Math. Phys.*, 123:177, 1989. doi: 10.1007/BF01238857. URL <https://link.springer.com/article/10.1007/BF01238857>.
- [86] Gregory Moore and Nathan Seiberg. Polynomial equations for rational conformal field theories. *Physics Letters B*, 212(4):451–460, 1988. ISSN 0370-2693. doi: [https://doi.org/10.1016/0370-2693\(88\)91796-0](https://doi.org/10.1016/0370-2693(88)91796-0). URL <https://www.sciencedirect.com/science/article/pii/0370269388917960>.
- [87] Edward Witten. Quantum Field Theory and the Jones Polynomial. *Commun. Math. Phys.*, 121:351–399, 1989. doi: 10.1007/BF01217730. URL <https://link.springer.com/article/10.1007/BF01217730>.
- [88] F. Alexander Bais, Peter van Driel, and Mark de Wild Propitius. Quantum symmetries in discrete gauge theories. *Physics Letters B*, 280(1):63–70, 1992. ISSN 0370-2693. doi: [https://doi.org/10.1016/0370-2693\(92\)90773-W](https://doi.org/10.1016/0370-2693(92)90773-W). URL <https://www.sciencedirect.com/science/article/pii/037026939290773W>.

Bibliography

- [89] K. Fredenhagen, Karl-Henning Rehren, and B. Schroer. Superselection Sectors with Braid Group Statistics and Exchange Algebras. 1. General Theory. *Commun. Math. Phys.*, 125:201, 1989. doi: 10.1007/BF01217906. URL <https://link.springer.com/article/10.1007/BF01217906>.
- [90] J. Frohlich and F. Gabbiani. Braid statistics in local quantum theory. *Rev. Math. Phys.*, 2:251–354, 1991. doi: 10.1142/S0129055X90000107. URL <https://www.worldscientific.com/doi/abs/10.1142/S0129055X90000107>.
- [91] Vladimir G. Turaev. *Quantum Invariants of Knots and 3-Manifolds*. De Gruyter, Berlin, Boston, 1994. ISBN 9783110883275. doi: doi:10.1515/9783110883275. URL <https://doi.org/10.1515/9783110883275>.
- [92] Xiao-Gang Wen. A theory of 2+1D bosonic topological orders. *National Science Review*, 3(1):68–106, 11 2015. ISSN 2095-5138. doi: 10.1093/nsr/nwv077. URL <https://doi.org/10.1093/nsr/nwv077>.
- [93] Xie Chen, Zheng-Cheng Gu, and Xiao-Gang Wen. Local unitary transformation, long-range quantum entanglement, wave function renormalization, and topological order. *Phys. Rev. B*, 82(15):155138, oct 2010. ISSN 1098-0121. doi: 10.1103/PhysRevB.82.155138. URL <https://link.aps.org/doi/10.1103/PhysRevB.82.155138>.
- [94] Bei Zeng and Xiao-Gang Wen. Gapped quantum liquids and topological order, stochastic local transformations and emergence of unitarity. *Phys. Rev. B*, 91:125121, Mar 2015. doi: 10.1103/PhysRevB.91.125121. URL <https://link.aps.org/doi/10.1103/PhysRevB.91.125121>.
- [95] M. B. Hastings and Xiao-Gang Wen. Quasiadiabatic continuation of quantum states: The stability of topological ground-state degeneracy and emergent gauge invariance. *Phys. Rev. B*, 72:045141, Jul 2005. doi: 10.1103/PhysRevB.72.045141. URL <https://link.aps.org/doi/10.1103/PhysRevB.72.045141>.
- [96] Emanuel Knill and Raymond Laflamme. Theory of quantum error-correcting codes. *Phys. Rev. A*, 55:900–911, 1997. doi: 10.1103/PhysRevA.55.900. URL <https://link.aps.org/doi/10.1103/PhysRevA.55.900>.
- [97] Robbert Dijkgraaf and Edward Witten. Topological Gauge Theories and Group Cohomology. *Commun. Math. Phys.*, 129:393, 1990. doi: 10.1007/BF02096988. URL <https://link.springer.com/article/10.1007/BF02096988>.
- [98] Liang Kong and Zhi-Hao Zhang. An invitation to topological orders and category theory. *arXiv preprint arXiv:2205.05565*, 2022. URL <https://arxiv.org/abs/2205.05565>.
- [99] M B Hastings. An area law for one-dimensional quantum systems. *J. Stat. Mech.*, 2007(08):P08024–P08024, aug 2007. doi: 10.1088/1742-5468/2007/08/p08024. URL <https://doi.org/10.1088/1742-5468/2007/08/p08024>.
- [100] Alexei Kitaev and John Preskill. Topological Entanglement Entropy. *Phys. Rev. Lett.*, 96(11):110404, mar 2006. ISSN 0031-9007. doi: 10.1103/PhysRevLett.96.110404. URL <https://link.aps.org/doi/10.1103/PhysRevLett.96.110404>.
- [101] Michael Levin and Xiao-Gang Wen. Detecting Topological Order in a Ground State Wave Function. *Phys. Rev. Lett.*, 96(11):110405, mar 2006. ISSN 0031-9007.

- doi: 10.1103/PhysRevLett.96.110405. URL <https://link.aps.org/doi/10.1103/PhysRevLett.96.110405>.
- [102] Parsa Bonderson. PhD thesis, Caltech, May 2007.
- [103] Parsa Bonderson, Christina Knapp, and Kaushal Patel. Anyonic entanglement and topological entanglement entropy. *Ann. Phys.*, 385:399–468, 2017. ISSN 0003-4916. doi: <https://doi.org/10.1016/j.aop.2017.07.018>. URL <https://www.sciencedirect.com/science/article/pii/S0003491617302178>.
- [104] Steven T. Flammia, Alioscia Hamma, Taylor L. Hughes, and Xiao-Gang Wen. Topological Entanglement Rényi Entropy and Reduced Density Matrix Structure. *Phys. Rev. Lett.*, 103(26):261601, dec 2009. ISSN 0031-9007. doi: 10.1103/PhysRevLett.103.261601. URL <https://link.aps.org/doi/10.1103/PhysRevLett.103.261601>.
- [105] A. Elben, B. Vermersch, C. F. Roos, and P. Zoller. Statistical correlations between locally randomized measurements: A toolbox for probing entanglement in many-body quantum states. *Phys. Rev. A*, 99(5):052323, may 2019. ISSN 2469-9926. doi: 10.1103/PhysRevA.99.052323. URL <https://link.aps.org/doi/10.1103/PhysRevA.99.052323>.
- [106] Hsin Yuan Huang, Richard Kueng, and John Preskill. Predicting many properties of a quantum system from very few measurements. *Nat. Phys.*, 16:1050, 2020. ISSN 17452481. doi: 10.1038/s41567-020-0932-7. URL <https://www.nature.com/articles/s41567-020-0932-7>.
- [107] Pavel Etingof, Dmitri Nikshych, and Viktor Ostrik. On fusion categories. *Ann. Math.*, 162(2):581–642, 2005. ISSN 0003486X. doi: 10.4007/annals.2005.162.581. URL <https://annals.math.princeton.edu/2005/162-2/p01>.
- [108] Parsa Bonderson. Measuring topological order. *Phys. Rev. Research*, 3:033110, Aug 2021. doi: 10.1103/PhysRevResearch.3.033110. URL <https://link.aps.org/doi/10.1103/PhysRevResearch.3.033110>.
- [109] Parsa Bonderson, Kirill Shtengel, and J. K. Slingerland. Probing Non-Abelian Statistics with Quasiparticle Interferometry. *Phys. Rev. Lett.*, 97(1):016401, jul 2006. ISSN 0031-9007. doi: 10.1103/PhysRevLett.97.016401. URL <https://link.aps.org/doi/10.1103/PhysRevLett.97.016401>.
- [110] Liang Jiang, Gavin K. Brennen, Alexey V. Gorshkov, Klemens Hammerer, Mohammad Hafezi, Eugene Demler, Mikhail D. Lukin, and Peter Zoller. Anyonic interferometry and protected memories in atomic spin lattices. *Nat. Phys.*, 4(6):482–488, 2008. ISSN 17452481. doi: 10.1038/nphys943. URL <https://www.nature.com/articles/nphys943>.
- [111] Michael Levin and Xiao-Gang Wen. Fermions, strings, and gauge fields in lattice spin models. *Phys. Rev. B*, 67:245316, Jun 2003. doi: 10.1103/PhysRevB.67.245316. URL <https://link.aps.org/doi/10.1103/PhysRevB.67.245316>.
- [112] Erik Verlinde. Fusion rules and modular transformations in 2D conformal field theory. *Nucl. Phys. B*, 300(C):360–376, 1988. ISSN 05503213. doi: 10.1016/0550-3213(88)90603-7. URL <https://www.sciencedirect.com/science/article/abs/pii/0550321388906037>.

Bibliography

- [113] Chetan Nayak, Steven H. Simon, Ady Stern, Michael Freedman, and Sankar Das Sarma. Non-abelian anyons and topological quantum computation. *Rev. Mod. Phys.*, 80:1083–1159, Sep 2008. doi: 10.1103/RevModPhys.80.1083. URL <https://link.aps.org/doi/10.1103/RevModPhys.80.1083>.
- [114] Xiao-Gang Wen. Quantum orders in an exact soluble model. *Phys. Rev. Lett.*, 90:016803, Jan 2003. doi: 10.1103/PhysRevLett.90.016803. URL <https://link.aps.org/doi/10.1103/PhysRevLett.90.016803>.
- [115] Sergey Bravyi, Matthew B. Hastings, and Spyridon Michalakis. Topological quantum order: Stability under local perturbations. *J. Math. Phys.*, 51(9):093512, sep 2010. ISSN 0022-2488. doi: 10.1063/1.3490195. URL <http://aip.scitation.org/doi/10.1063/1.3490195>.
- [116] Alioscia Hamma, Radu Ionicioiu, and Paolo Zanardi. Ground state entanglement and geometric entropy in the kitaev model. *Physics Letters A*, 337(1):22–28, 2005. ISSN 0375-9601. doi: <https://doi.org/10.1016/j.physleta.2005.01.060>. URL <https://www.sciencedirect.com/science/article/pii/S0375960105001544>.
- [117] Robert König, Ben W. Reichardt, and Guifré Vidal. Exact entanglement renormalization for string-net models. *Phys. Rev. B*, 79(19):195123, may 2009. ISSN 1098-0121. doi: 10.1103/PhysRevB.79.195123. URL <https://link.aps.org/doi/10.1103/PhysRevB.79.195123>.
- [118] Zheng-Cheng Gu, Michael Levin, Brian Swingle, and Xiao-Gang Wen. Tensor-product representations for string-net condensed states. *Phys. Rev. B*, 79(8):085118, feb 2009. ISSN 1098-0121. doi: 10.1103/PhysRevB.79.085118. URL <https://link.aps.org/doi/10.1103/PhysRevB.79.085118>.
- [119] Liang Kong. Some universal properties of levin-wen models. In *XVIIth international congress on mathematical physics*, pages 444–455. World Scientific, 2014. URL https://www.worldscientific.com/doi/abs/10.1142/9789814449243_0042.
- [120] Tian Lan and Xiao-Gang Wen. Topological quasiparticles and the holographic bulk-edge relation in $(2 + 1)$ -dimensional string-net models. *Phys. Rev. B*, 90:115119, Sep 2014. doi: 10.1103/PhysRevB.90.115119. URL <https://link.aps.org/doi/10.1103/PhysRevB.90.115119>.
- [121] Chien-Hung Lin and Michael Levin. Generalizations and limitations of string-net models. *Phys. Rev. B*, 89(19):195130, may 2014. ISSN 1098-0121. doi: 10.1103/PhysRevB.89.195130. URL <https://link.aps.org/doi/10.1103/PhysRevB.89.195130>.
- [122] V. G. Turaev and O. Y. Viro. State sum invariants of 3-manifolds and quantum 6j-symbols. *Topology*, 31(4):865–902, oct 1992. doi: 10.1016/0040-9383(92)90015-a. URL <https://www.sciencedirect.com/science/article/pii/004093839290015A>.
- [123] Michael Freedman, Chetan Nayak, Kirill Shtengel, Kevin Walker, and Zhenghan Wang. A class of p,t-invariant topological phases of interacting electrons. *Ann. Phys.*, 310(2):428–492, 2004. ISSN 0003-4916. doi: <https://doi.org/10.1016/j.aop.2004.01.006>. URL <https://www.sciencedirect.com/science/article/pii/S0003491604000260>.

- [124] Robert König, Greg Kuperberg, and Ben W. Reichardt. Quantum computation with Turaev-Viro codes. *Ann. Phys.*, 325(12):2707–2749, 2010. ISSN 00034916. doi: 10.1016/j.aop.2010.08.001. URL <https://www.sciencedirect.com/science/article/abs/pii/S0003491610001375>.
- [125] S. Bravyi, M. B. Hastings, and F. Verstraete. Lieb-Robinson Bounds and the Generation of Correlations and Topological Quantum Order. *Phys. Rev. Lett.*, 97(5):050401, jul 2006. ISSN 0031-9007. doi: 10.1103/PhysRevLett.97.050401. URL <https://link.aps.org/doi/10.1103/PhysRevLett.97.050401>.
- [126] Michael Freedman, Alexei Kitaev, and Zhenghan Wang. Simulation of topological field theories by quantum computers. *Commun. Math. Phys.*, 227(3):587–603, Jun 2002. ISSN 1432-0916. doi: 10.1007/s002200200635. URL <https://doi.org/10.1007/s002200200635>.
- [127] Miguel Aguado and Guifré Vidal. Entanglement Renormalization and Topological Order. *Phys. Rev. Lett.*, 100(7):070404, feb 2008. ISSN 0031-9007. doi: 10.1103/PhysRevLett.100.070404. URL <https://link.aps.org/doi/10.1103/PhysRevLett.100.070404>.
- [128] Michael P. Zaletel and Frank Pollmann. Isometric Tensor Network States in Two Dimensions. *Phys. Rev. Lett.*, 124(3):037201, jan 2020. ISSN 0031-9007. doi: 10.1103/PhysRevLett.124.037201. URL <https://link.aps.org/doi/10.1103/PhysRevLett.124.037201>.
- [129] Tomohiro Soejima, Karthik Siva, Nick Bultinck, Shubhayu Chatterjee, Frank Pollmann, and Michael P. Zaletel. Isometric tensor network representation of string-net liquids. *Phys. Rev. B*, 101(8):085117, feb 2020. ISSN 2469-9950. doi: 10.1103/PhysRevB.101.085117. URL <https://link.aps.org/doi/10.1103/PhysRevB.101.085117>.
- [130] Zhi-Yuan Wei, Daniel Malz, and J. Ignacio Cirac. Sequential generation of projected entangled-pair states. *Phys. Rev. Lett.*, 128:010607, Jan 2022. doi: 10.1103/PhysRevLett.128.010607. URL <https://link.aps.org/doi/10.1103/PhysRevLett.128.010607>.
- [131] Lucas Slattery and Bryan K Clark. Quantum circuits for two-dimensional isometric tensor networks. *arXiv preprint arXiv:2108.02792*, 2021. URL <https://arxiv.org/abs/2108.02792>.
- [132] M. Aguado, G. K. Brennen, F. Verstraete, and J. I. Cirac. Creation, Manipulation, and Detection of Abelian and Non-Abelian Anyons in Optical Lattices. *Phys. Rev. Lett.*, 101(26):260501, dec 2008. ISSN 0031-9007. doi: 10.1103/PhysRevLett.101.260501. URL <https://link.aps.org/doi/10.1103/PhysRevLett.101.260501>.
- [133] G. K. Brennen, M. Aguado, and J. I. Cirac. Simulations of quantum double models. *New J. Phys.*, 11(5):053009, may 2009. ISSN 1367-2630. doi: 10.1088/1367-2630/11/5/053009. URL <https://iopscience.iop.org/article/10.1088/1367-2630/11/5/053009>.
- [134] Yi Zhang, Tarun Grover, Ari Turner, Masaki Oshikawa, and Ashvin Vishwanath. Quasiparticle statistics and braiding from ground-state entanglement. *Phys. Rev. B*, 85:235151, Jun 2012. doi: 10.1103/PhysRevB.85.235151. URL <https://link.aps.org/doi/10.1103/PhysRevB.85.235151>.

Bibliography

- [135] Sergey Bravyi, Isaac Kim, Alexander Kliesch, and Robert Koenig. Adaptive constant-depth circuits for manipulating non-abelian anyons. *arXiv preprint arXiv:2205.01933*, 2022. URL <https://arxiv.org/abs/2205.01933>.
- [136] N. E. Bonesteel and D. P. DiVincenzo. Quantum circuits for measuring levin-wen operators. *Phys. Rev. B*, 86:165113, Oct 2012. doi: 10.1103/PhysRevB.86.165113. URL <https://link.aps.org/doi/10.1103/PhysRevB.86.165113>.
- [137] Adriano Barenco, Charles H. Bennett, Richard Cleve, David P. DiVincenzo, Norman Margolus, Peter Shor, Tycho Sleator, John A. Smolin, and Harald Weinfurter. Elementary gates for quantum computation. *Phys. Rev. A*, 52:3457–3467, Nov 1995. doi: 10.1103/PhysRevA.52.3457. URL <https://link.aps.org/doi/10.1103/PhysRevA.52.3457>.
- [138] Vivek V. Shende and Igor L. Markov. On the cnot-cost of toffoli gates. *Quantum Info. Comput.*, 9(5):461–486, May 2009. ISSN 1533-7146. doi: 10.26421/QIC8.5-6-8. URL <https://arxiv.org/abs/0803.2316>.
- [139] Christopher Chamberland, Guanyu Zhu, Theodore J. Yoder, Jared B. Hertzberg, and Andrew W. Cross. Topological and subsystem codes on low-degree graphs with flag qubits. *Phys. Rev. X*, 10:011022, Jan 2020. doi: 10.1103/PhysRevX.10.011022. URL <https://link.aps.org/doi/10.1103/PhysRevX.10.011022>.
- [140] Oliver Buerschaper and Miguel Aguado. Mapping Kitaev’s quantum double lattice models to Levin and Wen’s string-net models. *Phys. Rev. B*, 80(15):155136, oct 2009. ISSN 1098-0121. doi: 10.1103/PhysRevB.80.155136. URL <https://link.aps.org/doi/10.1103/PhysRevB.80.155136>.
- [141] Zoltán Kádár, Annalisa Marzuoli, and Mario Rasetti. Microscopic description of 2d topological phases, duality, and 3d state sums. *Adv. Math. Phys.*, page 671039, 2010. ISSN 16879120. doi: 10.1155/2010/671039. URL <https://www.hindawi.com/journals/amp/2010/671039/>.
- [142] Iris Cong, Soonwon Choi, and Mikhail D. Lukin. Quantum convolutional neural networks. *Nat. Phys.*, 15(12):1273–1278, 2019. ISSN 17452481. doi: 10.1038/s41567-019-0648-8. URL <https://www.nature.com/articles/s41567-019-0648-8>.
- [143] Adam Smith, Bernhard Jobst, Andrew G. Green, and Frank Pollmann. Crossing a topological phase transition with a quantum computer. *Phys. Rev. Research*, 4:L022020, Apr 2022. doi: 10.1103/PhysRevResearch.4.L022020. URL <https://link.aps.org/doi/10.1103/PhysRevResearch.4.L022020>.
- [144] Marcus Cramer, Martin B. Plenio, Steven T. Flammia, Rolando Somma, David Gross, Stephen D. Bartlett, Olivier Landon-Cardinal, David Poulin, and Yi-Kai Liu. Efficient quantum state tomography. *Nat. Commun.*, 1(1):149, dec 2010. ISSN 2041-1723. doi: 10.1038/ncomms1147. URL <http://www.nature.com/articles/ncomms1147>.
- [145] B. P. Lanyon, C. Maier, M. Holzäpfel, T. Baumgratz, C. Hempel, P. Jurcevic, I. Dhand, A. S. Buyskikh, A. J. Daley, M. Cramer, M. B. Plenio, R. Blatt, and C. F. Roos. Efficient tomography of a quantum many-body system. *Nat. Phys.*, 13(12):1158–1162, 2017. ISSN 17452481. doi: 10.1038/nphys4244. URL <https://www.nature.com/articles/nphys4244>.

- [146] Dong-Ling Deng, Xiaopeng Li, and S. Das Sarma. Quantum entanglement in neural network states. *Phys. Rev. X*, 7:021021, May 2017. doi: 10.1103/PhysRevX.7.021021. URL <https://link.aps.org/doi/10.1103/PhysRevX.7.021021>.
- [147] S. J. van Enk and C. W. J. Beenakker. Measuring $\text{Tr}\rho^n$ on single copies of ρ using random measurements. *Phys. Rev. Lett.*, 108:110503, Mar 2012. doi: 10.1103/PhysRevLett.108.110503. URL <https://link.aps.org/doi/10.1103/PhysRevLett.108.110503>.
- [148] A. Elben, B. Vermersch, M. Dalmonte, J. I. Cirac, and P. Zoller. Rényi entropies from random quenches in atomic hubbard and spin models. *Phys. Rev. Lett.*, 120:050406, Feb 2018. doi: 10.1103/PhysRevLett.120.050406. URL <https://link.aps.org/doi/10.1103/PhysRevLett.120.050406>.
- [149] Tiff Brydges, Andreas Elben, Petar Jurcevic, Benoît Vermersch, Christine Maier, Ben P. Lanyon, Peter Zoller, Rainer Blatt, and Christian F. Roos. Probing rényi entanglement entropy via randomized measurements. *Science*, 364(6437):260–263, 2019. doi: 10.1126/science.aau4963. URL <https://www.science.org/doi/abs/10.1126/science.aau4963>.
- [150] Zhi-Yuan Wei, J. Ignacio Cirac, and Daniel Malz. Generation of photonic tensor network states with circuit qed. *Phys. Rev. A*, 105:022611, Feb 2022. doi: 10.1103/PhysRevA.105.022611. URL <https://link.aps.org/doi/10.1103/PhysRevA.105.022611>.
- [151] Austin G. Fowler, Matteo Mariantoni, John M. Martinis, and Andrew N. Cleland. Surface codes: Towards practical large-scale quantum computation. *Phys. Rev. A*, 86(3):032324, sep 2012. ISSN 1050-2947. doi: 10.1103/PhysRevA.86.032324. URL <https://link.aps.org/doi/10.1103/PhysRevA.86.032324>.
- [152] Clare Horsman, Austin G. Fowler, Simon Devitt, and Rodney Van Meter. Surface code quantum computing by lattice surgery. *New J. Phys.*, 14(12):123011, dec 2012. ISSN 1367-2630. doi: 10.1088/1367-2630/14/12/123011. URL <https://iopscience.iop.org/article/10.1088/1367-2630/14/12/123011>.
- [153] Alexis Schotte, Guanyu Zhu, Lander Burgelman, and Frank Verstraete. Quantum error correction thresholds for the universal fibonacci turaev-viro code. *Phys. Rev. X*, 12:021012, Apr 2022. doi: 10.1103/PhysRevX.12.021012. URL <https://link.aps.org/doi/10.1103/PhysRevX.12.021012>.
- [154] Robert König. Composite anyon coding and the initialization of a topological quantum computer. *Phys. Rev. A*, 81:052309, May 2010. doi: 10.1103/PhysRevA.81.052309. URL <https://link.aps.org/doi/10.1103/PhysRevA.81.052309>.
- [155] Benjamin Nachman, Miroslav Urbanek, Wibe A. de Jong, and Christian W. Bauer. Unfolding quantum computer readout noise. *npj Quantum Information*, 6(1):84, Sep 2020. ISSN 2056-6387. doi: 10.1038/s41534-020-00309-7. URL <https://doi.org/10.1038/s41534-020-00309-7>.
- [156] Alexei Kitaev. Anyons in an exactly solved model and beyond. *Ann. Phys.*, 321(1):2–111, jan 2006. ISSN 00034916. doi: 10.1016/j.aop.2005.10.005. URL <http://linkinghub.elsevier.com/retrieve/pii/S0003491605002381><https://linkinghub.elsevier.com/retrieve/pii/S0003491605002381>.

Bibliography

- [157] A. Elben, B. Vermersch, M. Dalmonte, J. I. Cirac, and P. Zoller. Rényi entropies from random quenches in atomic hubbard and spin models. *Phys. Rev. Lett.*, 120:050406, Feb 2018. doi: 10.1103/PhysRevLett.120.050406. URL <https://link.aps.org/doi/10.1103/PhysRevLett.120.050406>.
- [158] Christian Schwemmer, Lukas Knips, Daniel Richart, Harald Weinfurter, Tobias Moroder, Matthias Kleinmann, and Otfried Gühne. Systematic errors in current quantum state tomography tools. *Phys. Rev. Lett.*, 114:080403, Feb 2015. doi: 10.1103/PhysRevLett.114.080403. URL <https://link.aps.org/doi/10.1103/PhysRevLett.114.080403>.
- [159] B. Vermersch, A. Elben, M. Dalmonte, J. I. Cirac, and P. Zoller. Unitary n -designs via random quenches in atomic hubbard and spin models: Application to the measurement of rényi entropies. *Phys. Rev. A*, 97:023604, Feb 2018. doi: 10.1103/PhysRevA.97.023604. URL <https://link.aps.org/doi/10.1103/PhysRevA.97.023604>.
- [160] Zak Webb. The clifford group forms a unitary 3-design. *Quantum Info. Comput.*, 16(15–16):1379–1400, November 2016. ISSN 1533-7146. URL <https://dl.acm.org/doi/abs/10.5555/3179439.3179447>.
- [161] Huangjun Zhu. Multiqubit clifford groups are unitary 3-designs. *Phys. Rev. A*, 96:062336, Dec 2017. doi: 10.1103/PhysRevA.96.062336. URL <https://link.aps.org/doi/10.1103/PhysRevA.96.062336>.
- [162] Tim Adye. Unfolding algorithms and tests using RooUnfold. In *Proc. PHYSTAT 2011 Work. Stat. Issues Relat. to Discov. Claims Search Exp. Unfolding*, 2011. ISBN 9789290833673. doi: 10.5170/CERN-2011-006.313.
- [163] Joel J. Wallman and Joseph Emerson. Noise tailoring for scalable quantum computation via randomized compiling. *Phys. Rev. A*, 94:052325, Nov 2016. doi: 10.1103/PhysRevA.94.052325. URL <https://link.aps.org/doi/10.1103/PhysRevA.94.052325>.
- [164] Sergey Bravyi and Alexei Kitaev. Universal quantum computation with ideal Clifford gates and noisy ancillas. *Phys. Rev. A*, 71(2):022316, feb 2005. ISSN 1050-2947. doi: 10.1103/PhysRevA.71.022316. URL <https://link.aps.org/doi/10.1103/PhysRevA.71.022316>.
- [165] Robert Raussendorf and Jim Harrington. Fault-tolerant quantum computation with high threshold in two dimensions. *Phys. Rev. Lett.*, 98:190504, May 2007. doi: 10.1103/PhysRevLett.98.190504. URL <https://link.aps.org/doi/10.1103/PhysRevLett.98.190504>.
- [166] Zijun Chen, Kevin J. Satzinger, Juan Atalaya, Alexander N. Korotkov, Andrew Dunsworth, Daniel Sank, Chris Quintana, Matt McEwen, Rami Barends, Paul V. Klimov, Sabrina Hong, Cody Jones, Andre Petukhov, Dvir Kafri, Sean Demura, Brian Burkett, Craig Gidney, Austin G. Fowler, Alexandru Paler, Harald Putterman, Igor Aleiner, Frank Arute, Kunal Arya, Ryan Babbush, Joseph C. Bardin, Andreas Bengtsson, Alexandre Bourassa, Michael Broughton, Bob B. Buckley, David A. Buell, Nicholas Bushnell, Benjamin Chiaro, Roberto Collins, William Courtney, Alan R. Derk, Daniel Eppens, Catherine Erickson, Edward Farhi, Brooks Foxen, Marissa Giustina, Ami Greene, Jonathan A. Gross, Matthew P. Harrigan, Sean D. Harrington, Jeremy Hilton, Alan Ho, Trent Huang, William J. Huggins,

- L. B. Ioffe, Sergei V. Isakov, Evan Jeffrey, Zhang Jiang, Kostyantyn Kechedzhi, Seon Kim, Alexei Kitaev, Fedor Kostritsa, David Landhuis, Pavel Laptev, Erik Lucero, Orion Martin, Jarrod R. McClean, Trevor McCourt, Xiao Mi, Kevin C. Miao, Masoud Mohseni, Shirin Montazeri, Wojciech Mruczkiewicz, Josh Mutus, Ofer Naaman, Matthew Neeley, Charles Neill, Michael Newman, Murphy Yuezhen Niu, Thomas E. O'Brien, Alex Opremcak, Eric Ostby, Bálint Pató, Nicholas Redd, Pedram Roushan, Nicholas C. Rubin, Vladimir Shvarts, Doug Strain, Marco Szalay, Matthew D. Trevithick, Benjamin Villalonga, Theodore White, Z. Jamie Yao, Ping Yeh, Juhwan Yoo, Adam Zalcman, Hartmut Neven, Sergio Boixo, Vadim Smelyanskiy, Yu Chen, Anthony Megrant, and Julian Kelly. Exponential suppression of bit or phase errors with cyclic error correction. *Nature*, 595(7867): 383–387, July 2021. ISSN 1476-4687. doi: 10.1038/s41586-021-03588-y. URL <https://www.nature.com/articles/s41586-021-03588-y>.
- [167] Michael Levin and Xiao-Gang Wen. Fermions, strings, and gauge fields in lattice spin models. *Phys. Rev. B*, 67:245316, Jun 2003. doi: 10.1103/PhysRevB.67.245316. URL <https://link.aps.org/doi/10.1103/PhysRevB.67.245316>.
- [168] Marcel den Nijs and Koos Rommelse. Preroughening transitions in crystal surfaces and valence-bond phases in quantum spin chains. *Phys. Rev. B*, 40:4709–4734, Sep 1989. doi: 10.1103/PhysRevB.40.4709. URL <https://link.aps.org/doi/10.1103/PhysRevB.40.4709>.
- [169] Tom Kennedy and Hal Tasaki. Hidden $Z_2 \times Z_2$ symmetry breaking in haldane-gap antiferromagnets. *Phys. Rev. B*, 45:304–307, Jan 1992. doi: 10.1103/PhysRevB.45.304. URL <https://link.aps.org/doi/10.1103/PhysRevB.45.304>.
- [170] D. Pérez-García, M. M. Wolf, M. Sanz, F. Verstraete, and J. I. Cirac. String order and symmetries in quantum spin lattices. *Phys. Rev. Lett.*, 100:167202, Apr 2008. doi: 10.1103/PhysRevLett.100.167202. URL <https://link.aps.org/doi/10.1103/PhysRevLett.100.167202>.
- [171] Xie Chen, Zheng-Cheng Gu, and Xiao-Gang Wen. Complete classification of one-dimensional gapped quantum phases in interacting spin systems. *Phys. Rev. B*, 84(23):235128, dec 2011. ISSN 1098-0121. doi: 10.1103/PhysRevB.84.235128. URL <https://link.aps.org/doi/10.1103/PhysRevB.84.235128>.
- [172] Frank Pollmann and Ari M. Turner. Detection of symmetry-protected topological phases in one dimension. *Phys. Rev. B*, 86:125441, Sep 2012. doi: 10.1103/PhysRevB.86.125441. URL <https://link.aps.org/doi/10.1103/PhysRevB.86.125441>.
- [173] Jutho Haegeman, David Pérez-García, Ignacio Cirac, and Norbert Schuch. Order parameter for symmetry-protected phases in one dimension. *Phys. Rev. Lett.*, 109:050402, Jul 2012. doi: 10.1103/PhysRevLett.109.050402. URL <https://link.aps.org/doi/10.1103/PhysRevLett.109.050402>.
- [174] Andreas Elben, Jinlong Yu, Guanyu Zhu, Mohammad Hafezi, Frank Pollmann, Peter Zoller, and Benoît Vermersch. Many-body topological invariants from randomized measurements in synthetic quantum matter. *Science Advances*, 6(15):eaaz3666, 2020. doi: 10.1126/sciadv.aaz3666. URL <https://www.science.org/doi/abs/10.1126/sciadv.aaz3666>.
- [175] Peter Broecker, Juan Carrasquilla, Roger G. Melko, and Simon Trebst. Machine learning quantum phases of matter beyond the fermion sign problem. *Scientific*

Bibliography

- Reports*, 7(1):8823, Aug 2017. ISSN 2045-2322. doi: 10.1038/s41598-017-09098-0. URL <https://doi.org/10.1038/s41598-017-09098-0>.
- [176] Patrick Huembeli, Alexandre Dauphin, and Peter Wittek. Identifying quantum phase transitions with adversarial neural networks. *Phys. Rev. B*, 97:134109, Apr 2018. doi: 10.1103/PhysRevB.97.134109. URL <https://link.aps.org/doi/10.1103/PhysRevB.97.134109>.
- [177] Xiao-Yu Dong, Frank Pollmann, and Xue-Feng Zhang. Machine learning of quantum phase transitions. *Phys. Rev. B*, 99:121104, Mar 2019. doi: 10.1103/PhysRevB.99.121104. URL <https://link.aps.org/doi/10.1103/PhysRevB.99.121104>.
- [178] Annabelle Bohrdt, Christie S. Chiu, Geoffrey Ji, Muqing Xu, Daniel Greif, Markus Greiner, Eugene Demler, Fabian Grusdt, and Michael Knap. Classifying snapshots of the doped hubbard model with machine learning. *Nat. Phys.*, 15(9):921–924, jul 2019. doi: 10.1038/s41567-019-0565-x. URL <https://www.nature.com/articles/s41567-019-0565-x>.
- [179] Giuseppe Carleo, Ignacio Cirac, Kyle Cranmer, Laurent Daudet, Maria Schuld, Naf-tali Tishby, Leslie Vogt-Maranto, and Lenka Zdeborová. Machine learning and the physical sciences. *Rev. Mod. Phys.*, 91:045002, Dec 2019. doi: 10.1103/RevModPhys.91.045002. URL <https://link.aps.org/doi/10.1103/RevModPhys.91.045002>.
- [180] Hsin-Yuan Huang, Richard Kueng, Giacomo Torlai, Victor V. Albert, and John Preskill. Provably efficient machine learning for quantum many-body problems. *Science*, 377(6613):eabk3333, 2022. doi: 10.1126/science.abk3333. URL <https://www.science.org/doi/abs/10.1126/science.abk3333>.
- [181] Saverio Monaco, Oriol Kiss, Antonio Mandarino, Sofia Vallecorsa, and Michele Grossi. Quantum phase detection generalization from marginal quantum neural network models. *Phys. Rev. B*, 107:L081105, Feb 2023. doi: 10.1103/PhysRevB.107.L081105. URL <https://link.aps.org/doi/10.1103/PhysRevB.107.L081105>.
- [182] Nicolas Sadoune, Giuliano Giudici, Ke Liu, and Lode Pollet. Unsupervised interpretable learning of phases from many-qubit systems. *Phys. Rev. Res.*, 5:013082, Feb 2023. doi: 10.1103/PhysRevResearch.5.013082. URL <https://link.aps.org/doi/10.1103/PhysRevResearch.5.013082>.
- [183] Johannes Herrmann, Sergi Masot Llima, Ants Remm, Petr Zapletal, Nathan A. McMahon, Colin Scarato, François Swiadek, Christian Kraglund Andersen, Christoph Hellings, Sebastian Krinner, Nathan Lacroix, Stefania Lazar, Michael Kerschbaum, Dante Colao Zanuz, Graham J. Norris, Michael J. Hartmann, Andreas Wallraff, and Christopher Eichler. Realizing quantum convolutional neural networks on a superconducting quantum processor to recognize quantum phases. *Nat. Commun.*, 13(1):4144, Jul 2022. doi: 10.1038/s41467-022-31679-5. URL <https://www.nature.com/articles/s41467-022-31679-5>.
- [184] Edward Farhi, Jeffrey Goldstone, Sam Gutmann, and Michael Sipser. Quantum computation by adiabatic evolution. *arXiv:quant-ph/0001106*, 2000. URL <https://arxiv.org/abs/quant-ph/0001106>.
- [185] Yimin Ge, Jordi Tura, and J. Ignacio Cirac. Faster ground state preparation and high-precision ground energy estimation with fewer qubits. *J. Math. Phys.*, 60(2):022202, 2019. doi: 10.1063/1.5027484. URL <https://doi.org/10.1063/1.5027484>.

- [186] Alberto Peruzzo, Jarrod McClean, Peter Shadbolt, Man-Hong Yung, Xiao-Qi Zhou, Peter J. Love, Alán Aspuru-Guzik, and Jeremy L. O'Brien. A variational eigenvalue solver on a photonic quantum processor. *Nat. Commun.*, 5(1):4213, Jul 2014. ISSN 2041-1723. doi: 10.1038/ncomms5213. URL <https://doi.org/10.1038/ncomms5213>.
- [187] Jarrod R McClean, Jonathan Romero, Ryan Babbush, and Alán Aspuru-Guzik. The theory of variational hybrid quantum-classical algorithms. *New J. Phys.*, 18(2):023023, feb 2016. doi: 10.1088/1367-2630/18/2/023023. URL <https://doi.org/10.1088%2F1367-2630%2F18%2F2%2F023023>.
- [188] Arthur Pesah, M. Cerezo, Samson Wang, Tyler Volkoff, Andrew T. Sornborger, and Patrick J. Coles. Absence of barren plateaus in quantum convolutional neural networks. *Phys. Rev. X*, 11:041011, Oct 2021. doi: 10.1103/PhysRevX.11.041011. URL <https://link.aps.org/doi/10.1103/PhysRevX.11.041011>.
- [189] Diederik P Kingma and Jimmy Ba. Adam: A method for stochastic optimization. *arXiv:1412.6980*, 2014. URL <https://arxiv.org/abs/1412.6980>.
- [190] Pietro Smacchia, Luigi Amico, Paolo Facchi, Rosario Fazio, Giuseppe Florio, Saverio Pascazio, and Vlatko Vedral. Statistical mechanics of the cluster ising model. *Phys. Rev. A*, 84:022304, Aug 2011. doi: 10.1103/PhysRevA.84.022304. URL <https://link.aps.org/doi/10.1103/PhysRevA.84.022304>.
- [191] Ruben Verresen, Roderich Moessner, and Frank Pollmann. One-dimensional symmetry protected topological phases and their transitions. *Phys. Rev. B*, 96:165124, Oct 2017. doi: 10.1103/PhysRevB.96.165124. URL <https://link.aps.org/doi/10.1103/PhysRevB.96.165124>.
- [192] G. Vidal. Classical simulation of infinite-size quantum lattice systems in one spatial dimension. *Phys. Rev. Lett.*, 98:070201, Feb 2007. doi: 10.1103/PhysRevLett.98.070201. URL <https://link.aps.org/doi/10.1103/PhysRevLett.98.070201>.
- [193] Connor Shorten and Taghi M. Khoshgoftaar. A survey on image data augmentation for deep learning. *Journal of Big Data*, 6(1):60, Jul 2019. ISSN 2196-1115. doi: 10.1186/s40537-019-0197-0. URL <https://doi.org/10.1186/s40537-019-0197-0>.
- [194] Michael P. Zaletel. Detecting two-dimensional symmetry-protected topological order in a ground-state wave function. *Phys. Rev. B*, 90:235113, Dec 2014. doi: 10.1103/PhysRevB.90.235113. URL <https://link.aps.org/doi/10.1103/PhysRevB.90.235113>.
- [195] Nathanan Tantivasadakarn, Ryan Thorngren, Ashvin Vishwanath, and Ruben Verresen. Long-range entanglement from measuring symmetry-protected topological phases. *arXiv:2112.01519*, 2021. URL <https://arxiv.org/abs/2112.01519>.
- [196] Dolev Bluvstein, Harry Levine, Giulia Semeghini, Tout T. Wang, Sepehr Ebadi, Marcin Kalinowski, Alexander Keesling, Nishad Maskara, Hannes Pichler, Markus Greiner, Vladan Vuletić, and Mikhail D. Lukin. A quantum processor based on coherent transport of entangled atom arrays. *Nature*, 604(7906):451–456, apr 2022. doi: 10.1038/s41586-022-04592-6. URL <https://doi.org/10.1038%2Fs41586-022-04592-6>.
- [197] Evert P. L. van Nieuwenburg, Ye-Hua Liu, and Sebastian D. Huber. Learning phase transitions by confusion. *Nat. Phys.*, 13(5):435–439, February 2017. doi: 10.1038/nphys4037. URL <https://www.nature.com/articles/nphys4037>.

Bibliography

- [198] Ethan Lake, Shankar Balasubramanian, and Soonwon Choi. Exact quantum algorithms for quantum phase recognition: Renormalization group and error correction. *arXiv:2211.09803*, 2022. URL <https://arxiv.org/abs/2211.09803>.
- [199] Johannes Jakob Meyer, Marian Mularski, Elies Gil-Fuster, Antonio Anna Mele, Francesco Arzani, Alissa Wilms, and Jens Eisert. Exploiting symmetry in variational quantum machine learning. *arXiv:2205.06217*, 2022. URL <https://arxiv.org/abs/2205.06217>.
- [200] Martín Larocca, Frédéric Sauvage, Faris M. Sbahi, Guillaume Verdon, Patrick J. Coles, and M. Cerezo. Group-invariant quantum machine learning. *PRX Quantum*, 3:030341, Sep 2022. doi: 10.1103/PRXQuantum.3.030341. URL <https://link.aps.org/doi/10.1103/PRXQuantum.3.030341>.
- [201] Michael A. Nielsen and Isaac L. Chuang. *Quantum Computation and Quantum Information: 10th Anniversary Edition*. Cambridge University Press, 2011. ISBN 9781107002173. URL <https://www.amazon.com/Quantum-Computation-Information-10th-Anniversary/dp/1107002176?SubscriptionId=AKIAIOBINVZYXZQZ2U3A&tag=chimbiori05-20&linkCode=xm2&camp=2025&creative=165953&creativeASIN=1107002176>.
- [202] C. D. Batista and Zohar Nussinov. Generalized elitzur’s theorem and dimensional reductions. *Phys. Rev. B*, 72:045137, Jul 2005. doi: 10.1103/PhysRevB.72.045137. URL <https://link.aps.org/doi/10.1103/PhysRevB.72.045137>.
- [203] Zohar Nussinov and Gerardo Ortiz. A symmetry principle for topological quantum order. *Ann. Phys.*, 324(5):977–1057, 2009. ISSN 0003-4916. doi: <https://doi.org/10.1016/j.aop.2008.11.002>. URL <https://www.sciencedirect.com/science/article/pii/S0003491608001711>.
- [204] Davide Gaiotto, Anton Kapustin, Nathan Seiberg, and Brian Willett. Generalized global symmetries. *Journal of High Energy Physics*, 2015(2):1–62, 2015. URL [https://link-springer-com.eaccess.tum.edu/article/10.1007/JHEP02\(2015\)172](https://link-springer-com.eaccess.tum.edu/article/10.1007/JHEP02(2015)172).
- [205] Xiao-Gang Wen. Emergent anomalous higher symmetries from topological order and from dynamical electromagnetic field in condensed matter systems. *Phys. Rev. B*, 99:205139, May 2019. doi: 10.1103/PhysRevB.99.205139. URL <https://link.aps.org/doi/10.1103/PhysRevB.99.205139>.
- [206] Salvatore D. Pace and Xiao-Gang Wen. Exact emergent higher-form symmetries in bosonic lattice models. *Phys. Rev. B*, 108:195147, Nov 2023. doi: 10.1103/PhysRevB.108.195147. URL <https://link.aps.org/doi/10.1103/PhysRevB.108.195147>.
- [207] John McGreevy. Generalized symmetries in condensed matter. *Annual Review of Condensed Matter Physics*, 14(1):57–82, 2023. doi: 10.1146/annurev-conmatphys-040721-021029. URL <https://doi.org/10.1146/annurev-conmatphys-040721-021029>.
- [208] Andrés M. Somoza, Pablo Serna, and Adam Nahum. Self-dual criticality in three-dimensional \mathbb{Z}_2 gauge theory with matter. *Phys. Rev. X*, 11:041008, Oct 2021. doi: 10.1103/PhysRevX.11.041008. URL <https://link.aps.org/doi/10.1103/PhysRevX.11.041008>.
- [209] Klaus Fredenhagen and Mihail Marcu. Charged states in z_2 gauge theories. *Commun. Math. Phys.*, 92, 1983. URL <https://link.springer.com/article/10.1007/BF01206315#citeas>.

- [210] Mihail Marcu. (uses of) an order parameter for lattice gauge theories with matter fields. *Lattice Gauge Theory: A Challenge in Large-Scale Computing*, pages 267–278, 1986.
- [211] Jürg Frölich Jean Bricmont. An order parameter distinguishing between different phases of lattice gauge theories with matter fields. *Physics Letters B*, 122(1):73–77, 1983. ISSN 0370-2693. doi: [https://doi.org/10.1016/0370-2693\(83\)91171-1](https://doi.org/10.1016/0370-2693(83)91171-1). URL <https://www.sciencedirect.com/science/article/pii/0370269383911711>.
- [212] John B. Kogut. An introduction to lattice gauge theory and spin systems. *Rev. Mod. Phys.*, 51:659–713, Oct 1979. doi: 10.1103/RevModPhys.51.659. URL <https://link.aps.org/doi/10.1103/RevModPhys.51.659>.
- [213] Frank Verstraete and J Ignacio Cirac. Renormalization algorithms for quantum-many body systems in two and higher dimensions. *arXiv preprint cond-mat/0407066*, 2004. URL <https://arxiv.org/abs/cond-mat/0407066>.
- [214] J. Ignacio Cirac, David Pérez-García, Norbert Schuch, and Frank Verstraete. Matrix product states and projected entangled pair states: Concepts, symmetries, theorems. *Rev. Mod. Phys.*, 93:045003, Dec 2021. doi: 10.1103/RevModPhys.93.045003. URL <https://link.aps.org/doi/10.1103/RevModPhys.93.045003>.
- [215] Dominic J. Williamson, Nick Bultinck, Michael Mariën, Mehmet B. Şahinoğlu, Jutho Haegeman, and Frank Verstraete. Matrix product operators for symmetry-protected topological phases: Gauging and edge theories. *Phys. Rev. B*, 94:205150, Nov 2016. doi: 10.1103/PhysRevB.94.205150. URL <https://link.aps.org/doi/10.1103/PhysRevB.94.205150>.
- [216] Dominic J Williamson, Nick Bultinck, and Frank Verstraete. Symmetry-enriched topological order in tensor networks: Defects, gauging and anyon condensation. *arXiv preprint arXiv:1711.07982*, 2017. URL <https://doi.org/10.48550/arXiv.1711.07982>.
- [217] Sujeet K. Shukla, M. Burak Şahinoğlu, Frank Pollmann, and Xie Chen. Boson condensation and instability in the tensor network representation of string-net states. *Phys. Rev. B*, 98(12):125112, sep 2018. ISSN 2469-9950. doi: 10.1103/PhysRevB.98.125112. URL <https://link.aps.org/doi/10.1103/PhysRevB.98.125112>.
- [218] Mehmet Burak Şahinoğlu, Dominic Williamson, Nick Bultinck, Michael Mariën, Jutho Haegeman, Norbert Schuch, and Frank Verstraete. Characterizing Topological Order with Matrix Product Operators. *Annales Henri Poincaré*, 22(2):563–592, 2021. doi: 10.1007/s00023-020-00992-4. URL <https://link.springer.com/article/10.1007/s00023-020-00992-4>.
- [219] David Perez-Garcia, Frank Verstraete, Michael M. Wolf, and J. Ignacio Cirac. Matrix product state representations. *Quant. Inf. Comput.*, 7(5-6):401–430, 2007. doi: 10.26421/QIC7.5-6-1. URL <https://dl.acm.org/doi/10.5555/2011832.2011833>.
- [220] C. Schön, E. Solano, F. Verstraete, J. I. Cirac, and M. M. Wolf. Sequential generation of entangled multiqubit states. *Phys. Rev. Lett.*, 95:110503, Sep 2005. doi: 10.1103/PhysRevLett.95.110503. URL <https://link.aps.org/doi/10.1103/PhysRevLett.95.110503>.
- [221] Norbert Schuch, Michael M. Wolf, Frank Verstraete, and J. Ignacio Cirac. Computational complexity of projected entangled pair states. *Phys. Rev. Lett.*, 98:140506,

Bibliography

- Apr 2007. doi: 10.1103/PhysRevLett.98.140506. URL <https://link.aps.org/doi/10.1103/PhysRevLett.98.140506>.
- [222] Xie Chen, Arpit Dua, Michael Hermele, David T. Stephen, Nathanan Tantivasadakarn, Robijn Vanhove, and Jing-Yu Zhao. Sequential quantum circuits as maps between gapped phases. *Phys. Rev. B*, 109:075116, Feb 2024. doi: 10.1103/PhysRevB.109.075116. URL <https://link.aps.org/doi/10.1103/PhysRevB.109.075116>.
- [223] Xiao-Gang Wen. Colloquium : Zoo of quantum-topological phases of matter. *Rev. Mod. Phys.*, 89(4):041004, dec 2017. ISSN 0034-6861. doi: 10.1103/RevModPhys.89.041004. URL <https://link.aps.org/doi/10.1103/RevModPhys.89.041004>.
- [224] F. A. Bais and J. K. Slingerland. Condensate-induced transitions between topologically ordered phases. *Phys. Rev. B*, 79:045316, Jan 2009. doi: 10.1103/PhysRevB.79.045316. URL <https://link.aps.org/doi/10.1103/PhysRevB.79.045316>.
- [225] José Garre-Rubio, Sofyan Iblisdir, and David Pérez-García. Symmetry reduction induced by anyon condensation: A tensor network approach. *Phys. Rev. B*, 96:155123, Oct 2017. doi: 10.1103/PhysRevB.96.155123. URL <https://link.aps.org/doi/10.1103/PhysRevB.96.155123>.
- [226] Michael Levin and Zheng-Cheng Gu. Braiding statistics approach to symmetry-protected topological phases. *Phys. Rev. B*, 86:115109, Sep 2012. doi: 10.1103/PhysRevB.86.115109. URL <https://link.aps.org/doi/10.1103/PhysRevB.86.115109>.
- [227] Xie Chen, Yuan-Ming Lu, and Ashvin Vishwanath. Symmetry-protected topological phases from decorated domain walls. *Nat. Commun.*, 5(1):3507, 2014. doi: 10.1038/ncomms4507. URL <https://doi.org/10.1038/ncomms4507>.
- [228] Wei Li, Shuo Yang, Meng Cheng, Zheng-Xin Liu, and Hong-Hao Tu. Topology and criticality in the resonating affleck-kennedy-lieb-tasaki loop spin liquid states. *Phys. Rev. B*, 89:174411, May 2014. doi: 10.1103/PhysRevB.89.174411. URL <https://link.aps.org/doi/10.1103/PhysRevB.89.174411>.
- [229] Ching-Yu Huang, Xie Chen, and Frank Pollmann. Detection of symmetry-enriched topological phases. *Phys. Rev. B*, 90:045142, Jul 2014. doi: 10.1103/PhysRevB.90.045142. URL <https://link.aps.org/doi/10.1103/PhysRevB.90.045142>.
- [230] Daniel Ben-Zion, Diptarka Das, and John McGreevy. Exactly solvable models of spin liquids with spinons, and of three-dimensional topological paramagnets. *Phys. Rev. B*, 93:155147, Apr 2016. doi: 10.1103/PhysRevB.93.155147. URL <https://link.aps.org/doi/10.1103/PhysRevB.93.155147>.
- [231] Nobuya Maeshima, Yasuhiro Hieida, Yasuhiro Akutsu, Tomotoshi Nishino, and Kouichi Okunishi. Vertical density matrix algorithm: A higher-dimensional numerical renormalization scheme based on the tensor product state ansatz. *Phys. Rev. E*, 64:016705, Jun 2001. doi: 10.1103/PhysRevE.64.016705. URL <https://link.aps.org/doi/10.1103/PhysRevE.64.016705>.
- [232] Nathanan Tantivasadakarn, Ryan Thorngren, Ashvin Vishwanath, and Ruben Verresen. Pivot hamiltonians as generators of symmetry and entanglement. *SciPost Physics*, 14(2):012, 2023. URL <https://scipost.org/SciPostPhys.14.2.012>.

- [233] Eddy Ardonne, Paul Fendley, and Eduardo Fradkin. Topological order and conformal quantum critical points. *Ann. Phys.*, 310(2):493–551, 2004. ISSN 0003-4916. doi: <https://doi.org/10.1016/j.aop.2004.01.004>. URL <https://www.sciencedirect.com/science/article/pii/S0003491604000247>.
- [234] Lincoln Carr. *Understanding quantum phase transitions*. CRC press, 2010. doi: 10.1201/b10273-10.
- [235] F. Verstraete, M. M. Wolf, D. Perez-Garcia, and J. I. Cirac. Criticality, the area law, and the computational power of projected entangled pair states. *Phys. Rev. Lett.*, 96:220601, Jun 2006. doi: 10.1103/PhysRevLett.96.220601. URL <https://link.aps.org/doi/10.1103/PhysRevLett.96.220601>.
- [236] Wen-Tao Xu and Guang-Ming Zhang. Tensor network state approach to quantum topological phase transitions and their criticalities of \mathbb{Z}_2 topologically ordered states. *Phys. Rev. B*, 98:165115, Oct 2018. doi: 10.1103/PhysRevB.98.165115. URL <https://link.aps.org/doi/10.1103/PhysRevB.98.165115>.
- [237] Guo-Yi Zhu and Guang-Ming Zhang. Gapless coulomb state emerging from a self-dual topological tensor-network state. *Phys. Rev. Lett.*, 122:176401, Apr 2019. doi: 10.1103/PhysRevLett.122.176401. URL <https://link.aps.org/doi/10.1103/PhysRevLett.122.176401>.
- [238] Wen-Tao Xu, Qi Zhang, and Guang-Ming Zhang. Tensor network approach to phase transitions of a non-abelian topological phase. *Phys. Rev. Lett.*, 124:130603, Apr 2020. doi: 10.1103/PhysRevLett.124.130603. URL <https://link.aps.org/doi/10.1103/PhysRevLett.124.130603>.
- [239] Qi Zhang, Wen-Tao Xu, Zi-Qi Wang, and Guang-Ming Zhang. Non-hermitian effects of the intrinsic signs in topologically ordered wavefunctions. *Communications Physics*, 3(1):209, 2020. URL <https://doi.org/10.1038/s42005-020-00479-y>.
- [240] Wen-Tao Xu and Norbert Schuch. Characterization of topological phase transitions from a non-abelian topological state and its galois conjugate through condensation and confinement order parameters. *Phys. Rev. B*, 104:155119, Oct 2021. doi: 10.1103/PhysRevB.104.155119. URL <https://link.aps.org/doi/10.1103/PhysRevB.104.155119>.
- [241] Wen-Tao Xu, Jose Garre-Rubio, and Norbert Schuch. Complete characterization of non-abelian topological phase transitions and detection of anyon splitting with projected entangled pair states. *Phys. Rev. B*, 106:205139, Nov 2022. doi: 10.1103/PhysRevB.106.205139. URL <https://link.aps.org/doi/10.1103/PhysRevB.106.205139>.
- [242] Michael M. Wolf, Gerardo Ortiz, Frank Verstraete, and J. Ignacio Cirac. Quantum phase transitions in matrix product systems. *Phys. Rev. Lett.*, 97:110403, Sep 2006. doi: 10.1103/PhysRevLett.97.110403. URL <https://link.aps.org/doi/10.1103/PhysRevLett.97.110403>.
- [243] Nick G. Jones, Julian Bibo, Bernhard Jobst, Frank Pollmann, Adam Smith, and Ruben Verresen. Skeleton of matrix-product-state-solvable models connecting topological phases of matter. *Phys. Rev. Research*, 3:033265, Sep 2021. doi: 10.1103/PhysRevResearch.3.033265. URL <https://link.aps.org/doi/10.1103/PhysRevResearch.3.033265>.

Bibliography

- [244] Claudio Castelnovo and Claudio Chamon. Quantum topological phase transition at the microscopic level. *Phys. Rev. B*, 77:054433, Feb 2008. doi: 10.1103/PhysRevB.77.054433. URL <https://link.aps.org/doi/10.1103/PhysRevB.77.054433>.
- [245] Claudio Castelnovo, Simon Trebst, and Matthias Troyer. Topological order and quantum criticality. *arXiv preprint arXiv:0912.3272*, 2009. URL <https://arxiv.org/abs/0912.3272v2>.
- [246] Zheng-Cheng Gu, Michael Levin, and Xiao-Gang Wen. Tensor-entanglement renormalization group approach as a unified method for symmetry breaking and topological phase transitions. *Phys. Rev. B*, 78:205116, Nov 2008. doi: 10.1103/PhysRevB.78.205116. URL <https://link.aps.org/doi/10.1103/PhysRevB.78.205116>.
- [247] Tomotoshi Nishino and Kouichi Okunishi. Corner transfer matrix renormalization group method. *Journal of the Physical Society of Japan*, 65(4):891–894, 1996. URL <https://doi.org/10.1143/JPSJ.65.891>.
- [248] Philippe Corboz, T. M. Rice, and Matthias Troyer. Competing states in the t - j model: Uniform d -wave state versus stripe state. *Phys. Rev. Lett.*, 113:046402, Jul 2014. doi: 10.1103/PhysRevLett.113.046402. URL <https://link.aps.org/doi/10.1103/PhysRevLett.113.046402>.
- [249] Bernard Nienhuis. Exact critical point and critical exponents of $O(n)$ models in two dimensions. *Phys. Rev. Lett.*, 49:1062–1065, Oct 1982. doi: 10.1103/PhysRevLett.49.1062. URL <https://link.aps.org/doi/10.1103/PhysRevLett.49.1062>.
- [250] Murray T. Batchelor and Henk W. J. Blöte. Conformal invariance and critical behavior of the $o(n)$ model on the honeycomb lattice. *Phys. Rev. B*, 39:2391–2402, Feb 1989. doi: 10.1103/PhysRevB.39.2391. URL <https://link.aps.org/doi/10.1103/PhysRevB.39.2391>.
- [251] David Senechal Philippe Di Francesco, Pierre Mathieu. *Conformal Field Theory*. Springer-Verlag New York, Inc, 1997.
- [252] Michael Freedman, Chetan Nayak, and Kirill Shtengel. Line of critical points in $2 + 1$ dimensions: Quantum critical loop gases and non-abelian gauge theory. *Phys. Rev. Lett.*, 94:147205, Apr 2005. doi: 10.1103/PhysRevLett.94.147205. URL <https://link.aps.org/doi/10.1103/PhysRevLett.94.147205>.
- [253] Eduardo Fradkin and Joel E. Moore. Entanglement entropy of 2d conformal quantum critical points: Hearing the shape of a quantum drum. *Phys. Rev. Lett.*, 97:050404, Aug 2006. doi: 10.1103/PhysRevLett.97.050404. URL <https://link.aps.org/doi/10.1103/PhysRevLett.97.050404>.
- [254] Thomas Scaffidi, Daniel E. Parker, and Romain Vasseur. Gapless symmetry-protected topological order. *Phys. Rev. X*, 7:041048, Nov 2017. doi: 10.1103/PhysRevX.7.041048. URL <https://link.aps.org/doi/10.1103/PhysRevX.7.041048>.
- [255] Ruben Verresen, Mikhail D. Lukin, and Ashvin Vishwanath. Prediction of toric code topological order from Rydberg blockade. *Phys. Rev. X*, 11:031005, Jul 2021. doi: 10.1103/PhysRevX.11.031005. URL <https://link.aps.org/doi/10.1103/PhysRevX.11.031005>.

- [256] Nathanan Tantivasadakarn, Ruben Verresen, and Ashvin Vishwanath. Shortest route to non-abelian topological order on a quantum processor. *Phys. Rev. Lett.*, 131:060405, Aug 2023. doi: 10.1103/PhysRevLett.131.060405. URL <https://link.aps.org/doi/10.1103/PhysRevLett.131.060405>.
- [257] Jong Yeon Lee, Wenjie Ji, Zhen Bi, and Matthew Fisher. Decoding measurement-prepared quantum phases and transitions: from ising model to gauge theory, and beyond. *arXiv preprint arXiv:2208.11699*, 2022. URL <https://arxiv.org/abs/2208.11699>.
- [258] Guo-Yi Zhu, Nathanan Tantivasadakarn, Ashvin Vishwanath, Simon Trebst, and Ruben Verresen. Nishimori’s cat: Stable long-range entanglement from finite-depth unitaries and weak measurements. *Phys. Rev. Lett.*, 131:200201, Nov 2023. doi: 10.1103/PhysRevLett.131.200201. URL <https://link.aps.org/doi/10.1103/PhysRevLett.131.200201>.
- [259] R. J. Baxter. *Exactly solved models in statistical mechanics*. 1982. ISBN 978-0-486-46271-4. doi: 10.1142/9789814415255_0002.
- [260] Matthieu Vanicat, Lenart Zadnik, and Toma ž Prosen. Integrable trotterization: Local conservation laws and boundary driving. *Phys. Rev. Lett.*, 121:030606, Jul 2018. doi: 10.1103/PhysRevLett.121.030606. URL <https://link.aps.org/doi/10.1103/PhysRevLett.121.030606>.
- [261] Aaron J. Friedman, Amos Chan, Andrea De Luca, and J. T. Chalker. Spectral statistics and many-body quantum chaos with conserved charge. *Phys. Rev. Lett.*, 123:210603, Nov 2019. doi: 10.1103/PhysRevLett.123.210603. URL <https://link.aps.org/doi/10.1103/PhysRevLett.123.210603>.
- [262] Pavel Kos, Bruno Bertini, and Toma ž Prosen. Chaos and ergodicity in extended quantum systems with noisy driving. *Phys. Rev. Lett.*, 126:190601, May 2021. doi: 10.1103/PhysRevLett.126.190601. URL <https://link.aps.org/doi/10.1103/PhysRevLett.126.190601>.
- [263] Michael Foss-Feig, David Hayes, Joan M. Dreiling, Caroline Figgatt, John P. Gaebler, Steven A. Moses, Juan M. Pino, and Andrew C. Potter. Holographic quantum algorithms for simulating correlated spin systems. *Phys. Rev. Res.*, 3:033002, Jul 2021. doi: 10.1103/PhysRevResearch.3.033002. URL <https://link.aps.org/doi/10.1103/PhysRevResearch.3.033002>.
- [264] John C. Napp, Rolando L. La Placa, Alexander M. Dalzell, Fernando G. S. L. Brandão, and Aram W. Harrow. Efficient classical simulation of random shallow 2d quantum circuits. *Phys. Rev. X*, 12:021021, Apr 2022. doi: 10.1103/PhysRevX.12.021021. URL <https://link.aps.org/doi/10.1103/PhysRevX.12.021021>.
- [265] Daniel Haag, Flavio Baccari, and Georgios Styliaris. Typical correlation length of sequentially generated tensor network states. *PRX Quantum*, 4:030330, Aug 2023. doi: 10.1103/PRXQuantum.4.030330. URL <https://link.aps.org/doi/10.1103/PRXQuantum.4.030330>.
- [266] Sagar Vijay, Jeongwan Haah, and Liang Fu. Fracton topological order, generalized lattice gauge theory, and duality. *Phys. Rev. B*, 94:235157, Dec 2016. doi: 10.1103/PhysRevB.94.235157. URL <https://link.aps.org/doi/10.1103/PhysRevB.94.235157>.

Bibliography

- [267] Austin G Fowler and Craig Gidney. Low overhead quantum computation using lattice surgery. *arXiv preprint arXiv:1808.06709*, 2018. URL <https://arxiv.org/abs/1808.06709>.
- [268] Sergey Bravyi, Sarah Sheldon, Abhinav Kandala, David C. McKay, and Jay M. Gambetta. Mitigating measurement errors in multi-qubit experiments. *arXiv*, jun 2020. ISSN 23318422. URL <http://arxiv.org/abs/2006.14044>.
- [269] John Tukey. Bias and confidence in not quite large samples. *Ann. Math. Statist.*, 29:614, 1958. URL <https://projecteuclid.org/journals/annals-of-mathematical-statistics/volume-29/issue-2/Abstracts-of-Papers/10.1214/aoms/1177706647.full>.
- [270] Bradley Efron and Robert J. Tibshirani. *An Introduction to the Bootstrap*. Number 57 in Monographs on Statistics and Applied Probability. Chapman & Hall/CRC, Boca Raton, Florida, USA, 1993.
- [271] Stefanie J. Beale, Arnaud Carignan-Dugas, Dar Dahlen, Joseph Emerson, Ian Hincks, Pavithran Iyer, Aditya Jain, David Hufnagel, Egor Ospadov, Jordan Saunders, Andrew Stasiuk, Joel J. Wallman, and Adam Winick. True-q, 2020. URL <https://doi.org/10.5281/zenodo.3945250>.
- [272] Erwin L Hahn. Spin echoes. *Phys. rev.*, 80(4):580, 1950. URL <https://journals.aps.org/pr/abstract/10.1103/PhysRev.80.580>.
- [273] Herman Y Carr and Edward M Purcell. Effects of diffusion on free precession in nuclear magnetic resonance experiments. *Phys. rev.*, 94(3):630, 1954. URL <https://journals.aps.org/pr/abstract/10.1103/PhysRev.94.630>.
- [274] Saul Meiboom and David Gill. Modified spin-echo method for measuring nuclear relaxation times. *Review of scientific instruments*, 29(8):688–691, 1958. URL <https://aip.scitation.org/doi/10.1063/1.1716296>.
- [275] Terry Gullion, David B Baker, and Mark S Conradi. New, compensated carr-purcell sequences. *Journal of Magnetic Resonance (1969)*, 89(3):479–484, 1990. URL <https://www.sciencedirect.com/science/article/abs/pii/0022236490903313>.
- [276] Jonas Bylander, Simon Gustavsson, Fei Yan, Fumiki Yoshihara, Khalil Harrabi, George Fitch, David G Cory, Yasunobu Nakamura, Jaw-Shen Tsai, and William D Oliver. Noise spectroscopy through dynamical decoupling with a superconducting flux qubit. *Nat. Phys.*, 7(7):565–570, 2011. URL <https://www.nature.com/articles/nphys1994>.
- [277] Brooks Foxen, Charles Neill, Andrew Dunsworth, Pedram Roushan, Ben Chiaro, Anthony Megrant, Julian Kelly, Zijun Chen, Kevin Satzinger, Rami Barends, et al. Demonstrating a continuous set of two-qubit gates for near-term quantum algorithms. *Phys. Rev. Lett.*, 125(12):120504, 2020. URL <https://journals.aps.org/prl/abstract/10.1103/PhysRevLett.125.120504>.
- [278] Zi-Qian Li, Li-Ping Yang, Z. Y. Xie, Hong-Hao Tu, Hai-Jun Liao, and T. Xiang. Critical properties of the two-dimensional q -state clock model. *Phys. Rev. E*, 101:060105, Jun 2020. doi: 10.1103/PhysRevE.101.060105. URL <https://link.aps.org/doi/10.1103/PhysRevE.101.060105>.

- [279] Roman Krčmár, Andrej Gendiar, and Tomotoshi Nishino. Phase transition of the six-state clock model observed from the entanglement entropy. *arXiv preprint arXiv:1612.07611*, 2016. URL <https://arxiv.org/abs/1612.07611>.
- [280] J. Ignacio Cirac, Didier Poilblanc, Norbert Schuch, and Frank Verstraete. Entanglement spectrum and boundary theories with projected entangled-pair states. *Phys. Rev. B*, 83:245134, Jun 2011. doi: 10.1103/PhysRevB.83.245134. URL <https://link.aps.org/doi/10.1103/PhysRevB.83.245134>.

Yu-Jie Liu

München, 19.07.2024